Preparation, Manipulation, and Spectroscopy of Cold Trapped Beryllium Ions and Molecular Hydrogen Ions

Inaugural-Dissertation

zur Erlangung des Doktorgrades (Dr. rer. nat.)
der Mathematisch-Naturwissenschaftlichen Fakultät
der Heinrich-Heine-Universität Düsseldorf

vorgelegt von

Jianwei Shen

aus Düsseldorf

Düsseldorf, Oktober 2022

Aus dem Institut für Experimentalphysik
der Heinrich-Heine Universität Düsseldorf

Gedruckt mit der Genehmigung
der Mathematisch-Naturwissenschaftlichen Fakultät
der Heinrich-Heine-Universität Düsseldorf

Referent: Prof. S. Schiller, Ph.D.
Koreferent: Prof. Dr. M. Büscher

Tag der mündlichen Prüfung: 04.10.2022

Contents

List of Figures

List of Tables

1 Introduction

1.1 Motivation

The trapping and cooling of neutral and charged particles is undoubtedly one of the fields in physics with the most rapid development and the most brilliant achievements during the last few decades, accompanied by the Nobel Prizes in physics in the years 1989, 1997, 2001, and 2005. Afterwards, constant improvements of technology of ultracold quantum physics have moved into focus that have led to new insights into many-body systems, quantum mechanical effects, and frequency metrology.

The technique of laser cooling has been proved to be effective and successful for reducing the temperature of atoms, however, it cannot be applied to molecular particles directly, due to the lack of closed optical transitions of molecules or the lack of suitable laser sources for excitations. Alternatively, indirectly cooling methods have been developed in the past few years, such as buffer gas cooling based on elastic collisions with cold helium gas [1], formation of cold molecules through photoassociation of laser-cooled neutral atoms [2], deceleration of supersonic beams by a switched sequence of electrostatic field gradients [3], implantation of molecules into helium nanodroplets [4], creation of ultracold molecules via Feshbach resonances [5], selection of molecules with small velocities from a gaseous ensemble [6], and creation of neutral molecular Bose-Einstein condensation (BEC) [7, 8]. However, those methods are mainly restricted to some particular species, or depend on the internal structure of the particles, or limited to some specific circumstances such as strong magnetic fields.

Followed by the first demonstration of ions in Penning traps [9, 10], we make use of another powerful universal cooling method: the so-called sympathetic cooling technique. First, atomic ions confined in a radio frequency (RF) ion trap are laser cooled to a temperature of millikelvin. Then, the translational temperature of the molecular ions that are simultaneously confined in the same trap would be reduced to a similar temperature as the atomic ions, due to the strong long-range Coulomb interaction.

This technique is independent of the internal structures of the involved particles, e.g. magnetic or electric moments or their energy level structures, and thus can be applied to a large variety of molecular species, ranging from the simplest of all molecules, e.g. the hydrogen molecule H_2^+ and its isotopomers HD^+ and D_2^+, to massive and complex molecules, e.g. proteins and polymers.

Currently, strong efforts towards cold molecule production, translational and internal cooling, spectroscopy, and detection are underway, since the cold and ultracold molecules systems provide a new insight of studying light-molecule and molecule-molecule interactions in a low-temperature regime that was inaccessible previously, and thus represent a new frontier in the fields of quantum optics, fundamental physics, molecular physics, chemical physics, and precision metrology.

Spectroscopic measurements of cold molecules lead to a wide range of possible applications, such as: the metrology of fundamental constants [11], tests of time invariance of fundamental constants [12], validation of the molecular theories [13], establishment of an molecular frequency standard [14], and quantum computing [15, 16], etc.

Among all the measurement techniques, the high-resolution rotational spectroscopy of molecules plays an important role in molecular physics, which provides extensive information on and insight into the structure and dynamics of molecules with various applications, e.g. the identification of molecular species in interstellar clouds. In the past few years, appropriate terahertz radiation sources with useful power levels have been extensively developed, causing the reachable spectral region of molecular spectroscopy to expand from the microwave region to the terahertz (submillimeter wavelength) region. Among them, continuous-wave, narrow-linewidth terahertz radiation, especially appropriate for high-resolution molecular spectroscopy, is available from backward-wave oscillators or via frequency upconversion using Schottky diodes [17, 18] or semiconductor superlattices [19, 20].

Improvement of the resolution of molecular rotational spectroscopy beyond the Doppler limit has been achieved by various methods, such as two-photon spectroscopy [21], Lamb-dip spectroscopy, velocity-class selection [22] and molecular beams [23]. For instance, sub-Doppler spectral lines with widths of approx. 15 kHz at 100 GHz [24] and several 10 kHz around $0.7 \sim 1$ THz [25, 26] have been reported.

However, the resolution of such techniques is limited by pressure broadening and/or transition time broadening. With the intention of eventually conquering these limitations, it is of interest to investigate a fundamentally different regime: trapping cold molecules in an ultra-high vacuum (UHV) environment (interaction-free) with the molecular temperature reduced as low as 1 K, and confining to submillimeter extension. In this case, Doppler broadening and pressure broadening, as well as transition time broadening, would be reduced significantly or even altogether eliminated. This regime could be achieved with cold molecular ions stored in RF traps or with cold neutral molecules captured in e.g. optical traps. The techniques of cold molecule production have been reviewed elsewhere (see e.g. Refs. [27, 28]).

In this work, as one of the simplest molecules, the molecular hydrogen ion HD^+, that consists of only a hydrogen nucleon, a deuteron nucleon and a single electron, has been chosen for investigation. Due to the shifted center of mass with respect to the center of charge, the HD^+ molecular ion possesses electric dipole-allowed rotational transitions [29], which makes it different from its isotopomers H_2^+ and D_2^+, and plays an important role in the field of molecular quantum mechanics [30, 31, 32, 33, 34].

In detail, experimentally, the HD^+ ions were sympathetically cooled to a secular temperature as low as $10 \sim 15$ mK by laser-cooled Be^+ ions and strongly confined in the ion trap. To analyze the Zeeman shift of HD^+ hyperfine transitions, the magnetic field in the ion trap was determined by performing Raman spectroscopy of Be^+ ions. Subsequently, high-resolution rotational spectroscopy of HD^+ ions by using two experimental methods was carried out. To increase the signal-to-noise ratio, rotational laser cooling was employed and several fundamental rotational transitions in the microwave regime were observed for the first time in our laboratory which strongly motivated further development. For higher-resolution spectroscopy in the future, the hyperfine pumping by the quantum cascade laser (QCL) is highly demanded to realize the quantum state preparation in the rovibrational ground level. For this purpose, a transportable transfer cavity system was developed to control and stabilize the frequency of the QCL precisely. The experimental results show that the system could be applied to other lasers for frequency controlling purposes as well. For demonstration, based on this system, together with a frequency-tunable optical parametric oscillator (OPO), spectroscopy of doubly-spin-forbidden rovibrational transitions of HD^+ ions was performed which shows that we are now able to realize the quantum state preparation and excite not only strong but also very weak transitions.

1.2 Outline

This work is organized as follows:

Chapter 2: the theory, as well as the experimental setup of ion trapping and cooling, is introduced.

Chapter 3: Raman transitions of Be^+ ions under various laser polarization and magnetic fields are analyzed, then the Raman spectroscopy of Be^+ ions by using a novel cooling laser source with the intention of local magnetic field determination is presented.

Chapter 4: the involved theory of HD^+ molecular ion is provided.

Chapter 5: spectroscopic results of the fundamental rotational transition of HD^+ ions by using a terahertz radiation source are reported and discussed.

Chapter 6: the development of a transportable transfer cavity is described.

Chapter 7: doubly-spin-forbidden rovibrational transitions of HD^+ ions by using the transfer cavity are studied and the results are discussed.

Chapter 8: a summary of the work.

2 Ion trapping and cooling

In this work, trapping, cooling, and spectroscopy of charged particles were realized in a linear Paul trap placed in an UHV chamber (2×10^{-11} mbar). As a key apparatus in our experiment, the trap is studied in this chapter. The basic theory of this type of trap including the radial and axial confinement, as well as the ion motion, is introduced in section 2.1. In order to sustain cold ion ensembles in the trap, an effective cooling procedure is required. Thus, a brief overview of various cooling techniques is given in section 2.2. Afterwards, the fundamentals of Doppler laser cooling and sympathetic cooling applied in our trap are shown. In section 2.3, based on the time-independent pseudo-potential and mutual Coulomb interaction that determine the ion motion in the trap, a description of the Coulomb ion crystals characterized by the plasma coupling parameter, as well as the corresponding cloud-liquid-solid phase transition of the ion ensembles in our experiment, is presented. Finally, an analysis of the ion crystals with various sizes is provided.

2.1 Theory of the linear Paul trap

2.1.1 Radial confinement

A quadrupole mass filter [35] consists of four parallel hyperbolic electrodes and is often replaced in the laboratory by four cylindrical electrodes, which shows a very similar electromagnetic performance in the center of the setup.

Figure 2.1 shows the structure and the electric circuit of a standard quadrupole mass filter that is the key element of the molecular ion source applied in this work. If one pair of oppositely placed electrodes is supplied with a radio frequency (RF) potential $+(U - V\cos \varOmega t)/2$ while the other pair with $-(U - V\cos \varOmega t)/2$, then the quadrupole saddle potential is generated as follows:

$$\phi(x,\, y,\, t) = \frac{x^2 - y^2}{2r_0^2}(U - V\cos \varOmega t). \tag{2.1}$$

Here, U is the DC amplitude. V and $\varOmega$ are the amplitude and angular frequency of the radio frequency, respectively. $r_0 = \sqrt{x_0^2 + y_0^2}$ represents the distance between the center of the setup and the surface of electrodes.

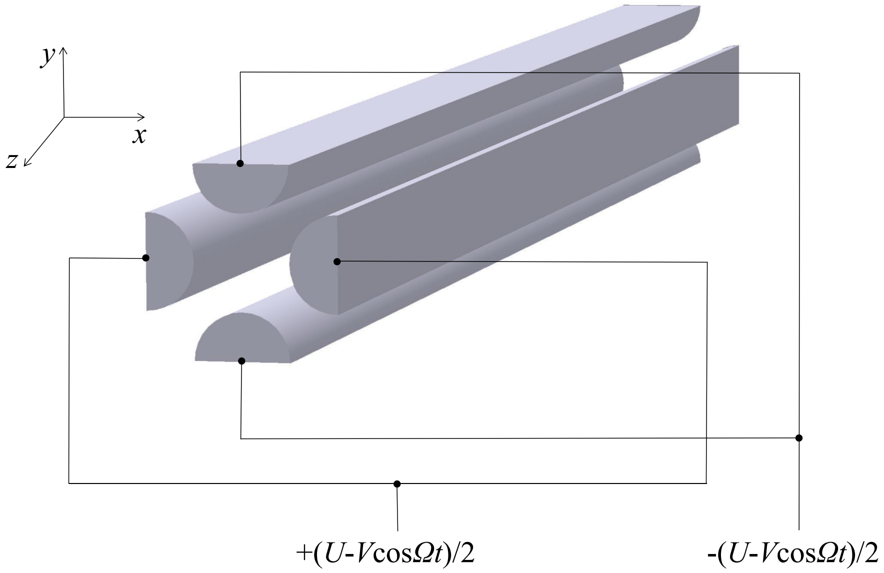

Figure 2.1: Structure of a quadrupole mass filter [35]. In order to simplify the setup, the hyperbolic electrodes are replaced by cylindrical electrodes.

In this case, the equations of two-dimensional motion of a particle of charge Q and mass m are expressed as:

$$\frac{d^2x}{dt^2} + \frac{Q}{mr_0^2}(U - V\cos\Omega t)\,x = 0, \tag{2.2}$$

$$\frac{d^2y}{dt^2} - \frac{Q}{mr_0^2}(U - V\cos\Omega t)\,y = 0. \tag{2.3}$$

If the definitions of the dimensionless parameters are introduced as follows:

$$a = \frac{4QU}{mr_0^2\Omega^2}, \qquad q = \frac{4QV}{mr_0^2\Omega^2}, \qquad \varsigma = \frac{\Omega t}{2}, \tag{2.4}$$

Equation 2.2 and 2.3 can be transformed to:

$$\frac{d^2x}{d\varsigma^2} + (a - 2q\cos 2\varsigma)\,x = 0, \tag{2.5}$$

$$\frac{d^2y}{d\varsigma^2} - (a - 2q\cos 2\varsigma)\,y = 0, \tag{2.6}$$

which are called Mathieu differential equations.

Stable solutions of the equations could be found only for certain values of the parameters a and q with limited amplitudes in the x- and y-directions less than r_0. Figure 2.2 shows the regions of stable motion in the x- or y-direction of the quadrupole mass filter. The stable radial motion of the ion in the xy-plane is characterized by parameter pairs (a, q) in the overlap regions. As Figure 2.2 (b) shows, only those ions with the maximum and minimum mass m_1 and m_2 that are determined by the intersections between the radial stability region and the line with a slope of $a/q = 2U/V$ could be radially confined. Thus, the quadrupole mass filter is regarded as a band-pass filter that traps ions with $m_2 \leq m \leq m_1$ and filters out the ions outside this mass range.

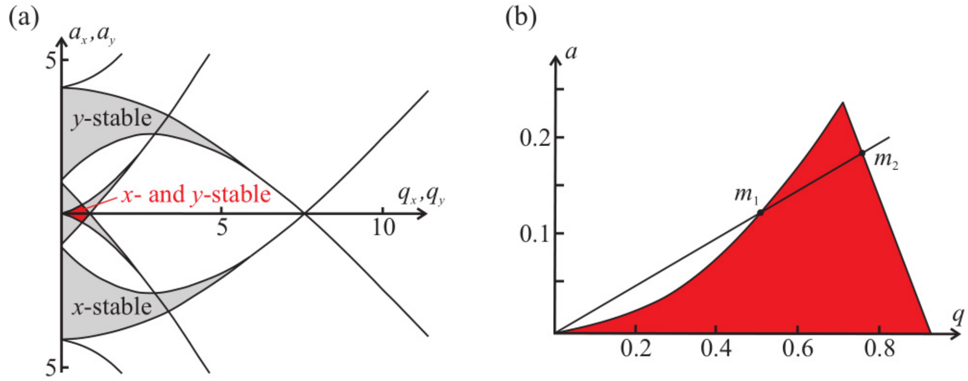

Figure 2.2: Stability diagram of the quadrupole mass filter [36]. (a) Regions of stable motion in the x- or y-direction are shown in gray, while the overlap regions that stand for stable motion in the xy-plane are colored in red. (b) Stable regions in the xy-plane (positive part) in detail.

2.1.2 Axial confinement

The axial confinement of ions could be realized by applying static electric fields in the axial direction of a quadrupole mass filter. In this work, a linear Paul trap is used to trap the ions. As shown in Figure 2.3, a static endcap voltage U_{EC} is applied to eight quadrupole electrodes that are added to the mass filter. The created axial potential close to the trap axis is given by [37]:

$$\phi(z) = \kappa U_{EC} z^2, \tag{2.7}$$

where the coefficient κ is a constant ($\kappa \approx 3 \times 10^{-3}\ mm^{-2}$ for our Paul trap)[38] that is determined by the geometry and distance of the endcap electrodes [39, 40]. In the radial direction, the endcap potential has a defocusing effect to some extent. In most applications and also for this work, the total radial trap potential can be expressed as:

$$\phi(x, y, t) = -\frac{V \cos \Omega t}{2r_0^2}(x^2 - y^2) - \frac{1}{2}\kappa U_{EC}(x^2 + y^2). \tag{2.8}$$

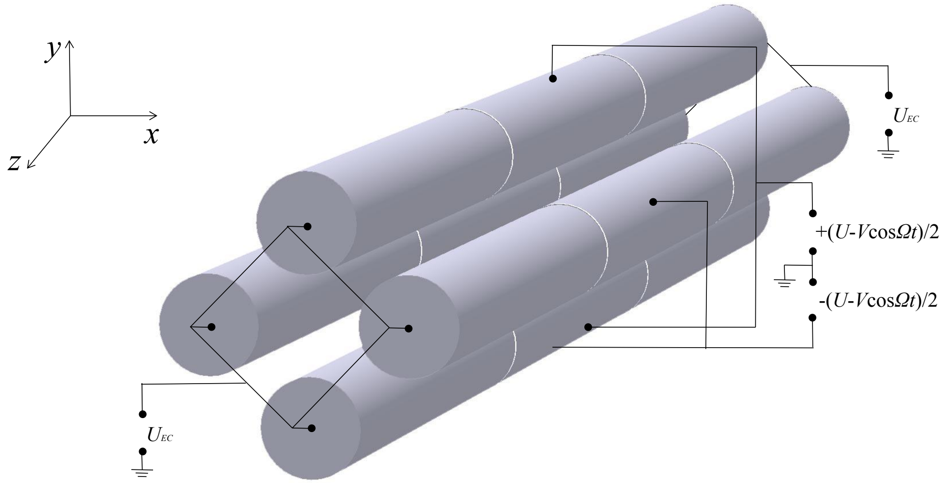

Figure 2.3: Structure of our linear Paul trap [37]. A static endcap voltage is applied to eight quadrupole electrodes that are added to the mass filter.

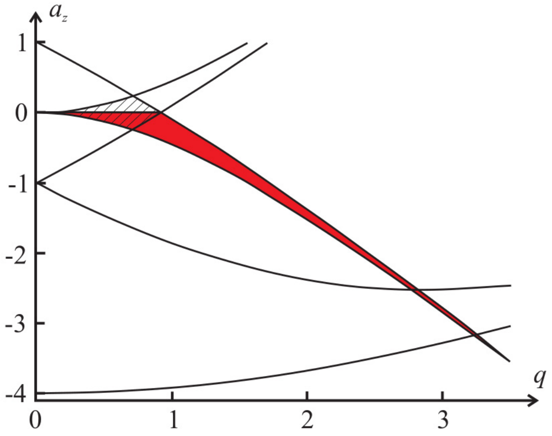

Figure 2.4: Stability diagram of the linear Paul trap [39]. For positively charged ions, the first radial stability region of the linear Paul trap is shown in red, while the first radial stability region of the quadrupole mass filter is illustrated in hatching for comparison.

By using the following dimensionless parameters:

$$\tau = \frac{1}{2}\Omega t,\ a_z = -\frac{4\kappa Q U_{EC}}{m\Omega^2},\ q = q_x = -q_y = \frac{2QV}{mr_0^2\Omega^2}, \tag{2.9}$$

the equations in the xy-plane can be transformed into the Mathieu differential equations as follows:

$$\frac{\partial^2 u}{\partial \tau^2} + (a_z - 2q_u \cos 2\tau)u = 0, \quad \text{with} \;\; u = x, y. \tag{2.10}$$

Thus, the stability region of the linear Paul trap differs slightly from that of the quadrupole mass filter. As shown in Figure 2.4, concerning the axial direction, the positively charged ions can be stably trapped only under the condition of $a_z < 0$ (i.e. $U_{EC} > 0$). In principle, as long as the absolute value of a_z is sufficiently high by applying an appropriate endcap voltage U_{EC} accordingly, the ions with an arbitrary high q-value (i.e. arbitrary low mass) can be trapped.

2.1.3 Ion motion in the linear Paul trap

The ion motion in the radial direction of the linear Paul trap is expressed by the solutions of the Mathieu differential equations as follows:

$$u(t) = u_{max}(1 + \frac{q}{2}\cos\mathit{\Omega} t)\cos\omega_r t, \quad \text{with} \;\; u = x, y \quad (\text{for} \; -a_z, q \ll 1). \tag{2.11}$$

Here, the parameter ω_r is called radial secular frequency:

$$\omega_r = \frac{\mathit{\Omega}}{2}\sqrt{\frac{q^2}{2} + a_z}. \tag{2.12}$$

Depending on a_z, the radial secular frequency will be reduced along with the increase of the static field of the endcap electrodes. Thus, a so-called ion secular motion of low frequency $\omega_r \ll \mathit{\Omega}$ with the amplitude u_{max} that is the dominant motion of the ion in the linear Paul trap is described by Equation 2.11 and 2.12.

In addition, superposed to this secular motion, a so-called ion micromotion (fast jitter motion) is oscillating at the trap radio frequency $\mathit{\Omega}$ with a small amplitude (for $q \ll 1$) that is proportional to the distance to the trap axis. Thus, the ion motion can be considered as a time average of this integration and can be expressed by a time-independent harmonic pseudo-potential:

$$\phi_{ps}(x, y) = \frac{1}{8} qV \frac{x^2 + y^2}{r_0^2} - \frac{1}{2}\kappa U_{EC}(x^2 + y^2). \tag{2.13}$$

For the three-dimensional space, this pseudo-potential can be expressed by:

$$\phi_{ps}(r, z) = \frac{m}{2Q}\omega_r^2 r^2 + \frac{m}{2Q}\omega_z^2 z^2, \tag{2.14}$$

with $r = \sqrt{x^2 + y^2}$ and the axial secular frequency as follows:

$$\omega_z = \frac{\mathit{\Omega}}{2}\sqrt{-2a_z}. \tag{2.15}$$

In the center of the trap (i.e. at the position $z = 0$), the pseudo-potential is:

$$\phi_0 = \frac{QV}{8}q, \tag{2.16}$$

which implies that the ions with kinetic energy higher than ϕ_0 will be released from the trap.

It is necessary to point out that the strict form of expressions for radial secular frequency ω_r and axial secular frequency ω_z obtained in this section are valid only for one single trapped ion. If more ions are confined in the trap simultaneously, the space charge effects and coupling effects between different ion species that lead to significantly shifted resonance frequencies sometimes should be considered [41].

When the collisions between ions with residual gas particles or other trapped ions are taking into consideration, the kinetic energy from the ions' micromotion can be transferred to the secular motion irreversibly. Superimposed to this disturbance, electric noise takes place as well, which eventually leads to ions' motion getting out of phase with the trap RF field. This kinetic energy can be regarded as an indicator of ions' temperature that would be increased due to this so-called RF heating interference.

The RF heating rate is influenced by various factors, e.g. the trap parameters, the number of trapped ions, etc., which has been investigated elsewhere using molecular dynamics (MD) simulations [42, 43, 44].

2.2 Cooling of trapped ions

As mentioned in section 2.1, via kinetic energy transfer by collisions with residual gas particles, RF heating, and even electric noise on the trap electrodes, the trapped ions are constantly heated up with increased kinetic energy. In the case of the kinetic energy exceeds the trap potential depth (Equation 2.16), the trapped ions will be released from the trap. Hence, it is necessary to introduce a constant and sufficient cooling procedure to ensure effective trapping of the ions and to sustain cold ion ensembles.

Several cooling techniques, e.g. buffer gas cooling [45], resistive cooling [46, 47], laser cooling [48, 49, 50, 51], sympathetic cooling [9, 52, 53], etc., are applied according to various situations, where the last two mentioned techniques for translational cooling of atomic and molecular ions are used in this work.

2.2.1 Cooling techniques

2.2.1.1 Laser cooling

The basic idea of laser cooling (see Figure 2.5, a detailed treatment follows in subsection 2.2.2) is a deceleration of particles by momentum transfer based on a repeated procedure of absorption of directed photons and emission of photons in arbitrary directions. In each cycle of photon scattering, the momentum of the particle is reduced by a photon momentum of $\hbar\vec{k}_L$. The particle returns to the initial ground level immediately at the end of each scattering process and is ready for the next absorption and emission cycle.

This laser cooling method is only applicable to those particles with closed optical transitions and is unsuitable for most other atom or ion species, especially molecules that usually possess numerous rovibrational levels, sometimes with radiationless relaxations or long lifetimes. Alternatively, a so-called sympathetic cooling technique opens a new way of indirectly cooling the favored molecule species, which will be introduced in the following subsection.

2.2.1.2 Sympathetic cooling

The basic principle of sympathetic cooling is as follows: when one ion species is trapped in an ion trap and is laser cooled, the other ion species that is together trapped in the ion trap will be cooled down as well due to the Coulomb interaction. In this procedure of elastic Coulomb collisions, the kinetic energy is transferred from the non-laser-cooled ion species to the laser-cooled ion species and is then dissipated via laser cooling, which leads to a thermal equilibrium between these two ion species.

Compared with other cooling methods that are not applicable to the molecules due to the lack of closed optical transitions or matching laser sources, the sympathetic cooling technique can be applied to any kind of atomic or molecular ions, as long as they can be stably trapped together with the laser-cooled atomic ions. This is suitable especially for molecular ions.

Unlike buffer gas cooling, with which the mass of the interacting species is a restricting factor, there is no such restriction for sympathetic cooling, which makes it applicable for a large number of molecular ion species. In other words, the non-laser-cooled ion species can be sympathetically cooled by laser-cooled ion species of higher mass, as well as the one of lower mass.

MD simulations [54] have shown that the efficiency of sympathetic cooling significantly depends on the mass-to-charge ratio of the laser-cooled and sympathetically cooled ions, and much less on their mass ratio.

In a linear Paul trap, as will be shown in section 2.3, ion species of different mass-to-charge ratios separate radially. This radial separation determines the sympathetic cooling efficiency. Due to Coulomb interaction, the spatially closer an ion species is to the laser-cooled ion species, the higher is the efficiency of sympathetic cooling. In other words, the most efficient of sympathetic cooling is for ion species of a mass-to-charge ratio similar to that of the laser-cooled ion species. Hence, in our group, HD^+ ions are sympathetically cooled by laser-cooled Be^+ ions in an ion trap apparatus (mass-to-charge ratio = 3 Da).

2.2.2 Fundamentals of Doppler laser cooling

Based on the law of momentum conservation, Doppler laser cooling can be applied to cool suitable neutral or charged particles effectively and reduce their translational temperatures below 1 K. During the process of scattering a photon, a particle experiences a recoil and shifts its resonance frequency due to the Doppler effect.

Assume a single atom described by a closed two-level energy system with the ground level $|g\rangle$ and the excited level $|e\rangle$. The energy interval is:

$$E_e - E_g = \hbar\omega_A, \tag{2.17}$$

where ω_A is the frequency of the dipole transition $|g\rangle \rightarrow |e\rangle$.

Further assume a monochromatic laser wave with the expression:

$$\vec{E}_L(\vec{r}, t) = \vec{e}_L(\vec{r})\hat{E}(\vec{r})\cos(\omega_L t + \vec{k}_L \cdot \vec{r}), \tag{2.18}$$

where $\vec{e}_L(\vec{r})$, $\hat{E}(\vec{r})$, ω_L, and $\vec{k}_L$ represent the polarization, amplitude, frequency, and wave vector of the laser field in $\vec{r}$, respectively.

As shown in Figure 2.5, when the atom is exposed in this slightly red-detuned laser field (i. e. $\omega_L < \omega_A$) and moves with the velocity $\vec{v}$ towards the laser beam, for the atom, the laser frequency appears increased by a Doppler shift of $\vec{k}_L \cdot \vec{v}$ and the resonance will occur under the condition of $\omega_A - \vec{k}_L \cdot \vec{v} = \omega_L$. By absorption of a photon, the atom gains the photon momentum $\hbar\vec{k}_L$ in the direction of the laser beam and is therefore decelerated. In contrast, an atom moving in the same direction of laser propagation is off-resonant with the laser beam, thus it will not absorb a photon to change its momentum, namely the acceleration of atoms in the same direction of a red-detuned laser field is not possible.

After the absorption of a photon, the atom returns to the ground level by spontaneous emission and is ready for the next cycle of absorption and emission. The recoil effect due to spontaneous emission can be neglected because spontaneous emission is in an arbitrary direction, it cancels each other out over numerous cycles of absorption and emission. Therefore, the only remaining consequence is the deceleration of the atom. Thus, the atom is laser cooled.

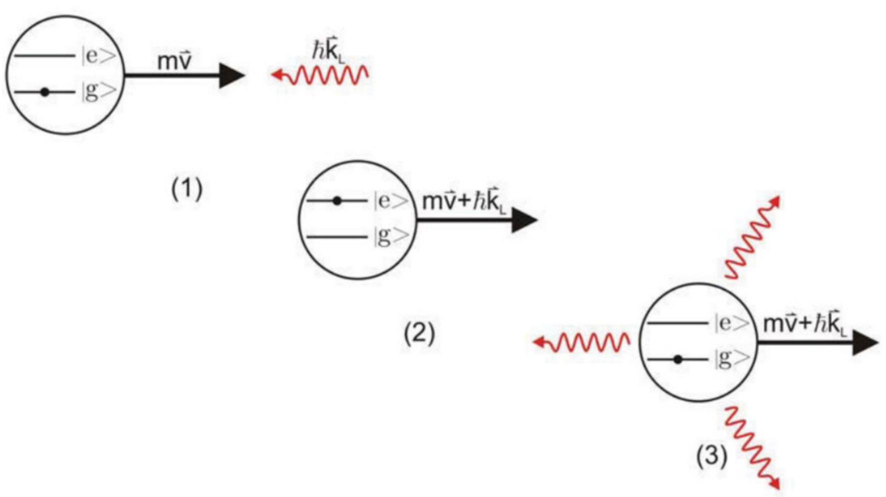

Figure 2.5: Schematic illustration of a Doppler laser cooling cycle [55]. (1) In the beginning, an atom in the ground level $|g\rangle$ with a momentum $m\vec{v}$ moves against a photon with a momentum $\hbar\vec{k}_L$. (2) The atom is excited to the level $|e\rangle$ by absorption of the photon, with its momentum reduced to $m\vec{v}+\hbar\vec{k}_L$. (3) Finally, the atom relaxes to the initial ground level by spontaneous emission of a photon in an arbitrary direction and is ready for the next cycle of absorption and emission.

By using a semi-classical model that describes the atom as a two-level system quantum-mechanically and its motion classically, Doppler laser cooling can be treated quantitatively. The main results of laser cooling will be presented in this subsection and the detailed treatment can be found in [55, 56, 57].

Based on the above-mentioned assumptions, the atom in the excited level $|e\rangle$ relaxes to the ground level $|g\rangle$ by spontaneous emission with the rate:

$$\varGamma = \frac{1}{\tau}, \tag{2.19}$$

where τ is the lifetime of the excited level.

The light force that acts on the atom can be described as [56]:

$$F_{light} = \text{photonmomentum} \cdot \text{photonscattering rate} = \hbar\vec{k}_L \cdot \varGamma\rho_e. \tag{2.20}$$

By solving the optical Bloch equations (OBE), the population of the excited level ρ_e is given as follows:

$$\rho_e = \frac{\varOmega_R^2}{4\varDelta^2 + 2\varOmega_R^2 + \varGamma^2}, \tag{2.21}$$

where Ω_R is the Rabi frequency that determines the interaction strength between the atom and the light field, and $\Delta = \omega_L - \omega_A$ is the light wave detuning from the atomic transition.

According to Equation 2.20, when the atom moves with the velocity $\vec{v}$, an additional Doppler shift $\vec{k}_L \cdot \vec{v}$ should be considered. Thus, the light force can be expressed by:

$$F_{light} = \hbar k_L \Gamma \frac{\Omega_R^2}{4\left(\Delta - \vec{k}_L \cdot \vec{v}\right)^2 + 2\Omega_R^2 + \Gamma^2}. \tag{2.22}$$

For low velocities v, a Taylor expansion of Equation 2.22 is given by:

$$F_{light} = F_{light,0} + \beta v + \mathcal{O}(v^2). \tag{2.23}$$

Here, the light force carries two contributions: a constant force $F_{light,0}$ that is typically on the order of 10^{-20} N and a damping force βv that depends on the velocity of the atom with the damping coefficient:

$$\beta = \hbar k_L^2 \frac{4S_0 \frac{\Delta}{\Gamma}}{\left[1 + S_0 + \left(\frac{2\Delta}{\Gamma}\right)^2\right]^2}. \tag{2.24}$$

Here, S_0 is the saturation parameter on resonance with the dipole transition $|g\rangle \rightarrow |e\rangle$ in a light field intensity I, which can be expressed as:

$$S_0 = \frac{I}{I_s} = \frac{2\Omega_R^2}{\Gamma^2}, \tag{2.25}$$

where the saturation intensity is:

$$I_s = \frac{2\pi^2 \hbar c \Gamma}{3\lambda_L^3}, \tag{2.26}$$

for which the population of the excited level $|e\rangle$ is 25%.

Assume an ensemble of atomic ions with the above criteria (two-level energy system, dipole transition frequency ω_A, etc.) confined in a linear Paul trap, and exposed to a monochromatic light wave of frequency ω_L propagating along the trap axis, some effects on the ions due to the light force should be considered as follows:

A shift of the ions that is typically by a few micrometers from the trap center in the light propagation direction is caused by the constant force $F_{light,0}$. When the damping coefficient β is negative, the ions will be decelerated against the light propagation direction ($v < 0$) due to the velocity-dependent damping force βv. This is the case for the negative values of detuning $\varDelta$, i.e. red-detuned laser light. On the contrary, the ions will be accelerated for the case $\varDelta > 0$.

Figure 2.6 shows the damping coefficient β as a function of detuning $\varDelta$ for various values of saturation parameters S_0. In the case of $\varDelta = -\varGamma/2$ and $S_0 = 2$, the strongest damping is achieved.

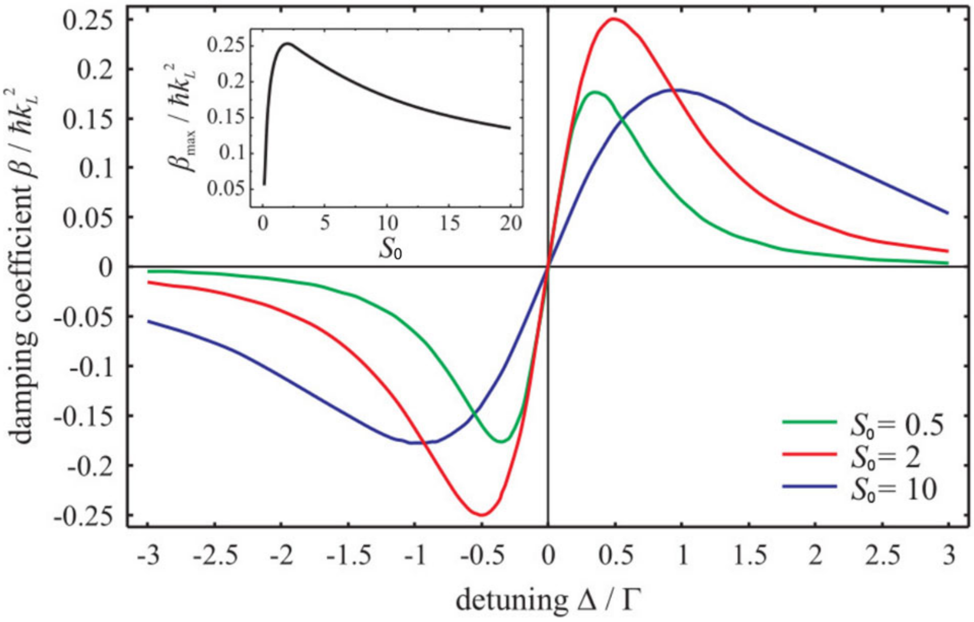

Figure 2.6: Damping coefficient β in a two-level energy system that is depending on the detuning $\varDelta$ for different saturation parameters S_0. The maximum value of β as a function of S_0 is shown in the inset. For a red-detuned laser light with half the transition linewidth of $\varDelta = -\varGamma/2$, the damping coefficient β reaches its absolute maximum value with a light field intensity $I = 2I_s$ (an intensity I that is twice as high as the saturation intensity I_s) [56].

Note that a single laser beam for cooling the ions is sufficient in an ion trap apparatus. Although only the motion along the propagation direction of the laser light is damped, an effective translational cooling in all three dimensions is achieved due to the interaction of the ions and the trap confinement that couples the ion motion.

As described above, with Doppler laser cooling, spontaneous emission of the atom is isotropic in space, which yields a random walk performance of the atom's motion in momentum space [56]. Thus, the minimum reachable temperature of an atom is limited even if all possible heating effects are neglected. This temperature limit of laser cooling is the so-called Doppler temperature, which is given by:

$$T_{Doppler} = \frac{\hbar\varGamma}{2\kappa_B}. \tag{2.27}$$

For laser-cooled beryllium (Be^+) ions ($\mathit{\Gamma} = 2\pi \cdot 19.4$ MHz [58]) used in this work, the Doppler limit is at $T_{Doppler} = 0.47$ mK [40, 58], which is only reachable under ideal conditions for a single atomic ion in the center of the trap, and all possible heating effects reducing to the minimum. A detailed description about laser cooling of beryllium ions will be presented in the following subsections.

2.2.3 Doppler laser cooling of beryllium ions

As the lightest atomic ion that is suitable for laser cooling, the beryllium ion is chosen in this work for sympathetic cooling of other light molecules, e.g. HD^+ ion. The properties of the beryllium ion in more detail are shown in Table 2.1.

Atomic data	
symbol	${}^{9}_{4}Be^+$
configuration	$1s^2 2s^1$
nuclear spin	$I = 3/2$

Data of laser cooling	
atomic transition	${}^2S_{1/2}(F=2) - {}^2P_{3/2}$
wavelength	$\lambda_A = 313.1327$ nm
linewidth	$\mathit{\Gamma} = 2\pi \cdot 19.4$ MHz
Doppler temperature	$T_{Doppler} = 0.47$ mK
saturation intensity	$I_s = 83$ mW/cm^2
recoil velocity	$v_{recoil} = 0.14$ m/s

Table 2.1: Data of Be^+ ion [40].

The properties of an atomic mass of 9 a.u., a closed $1s$ shell, and a single electron in the $2s$ shell make the beryllium ion the lightest hydrogen-like atomic ion. Therefore it possesses a relatively simple energy level scheme as presented in Figure 2.7.

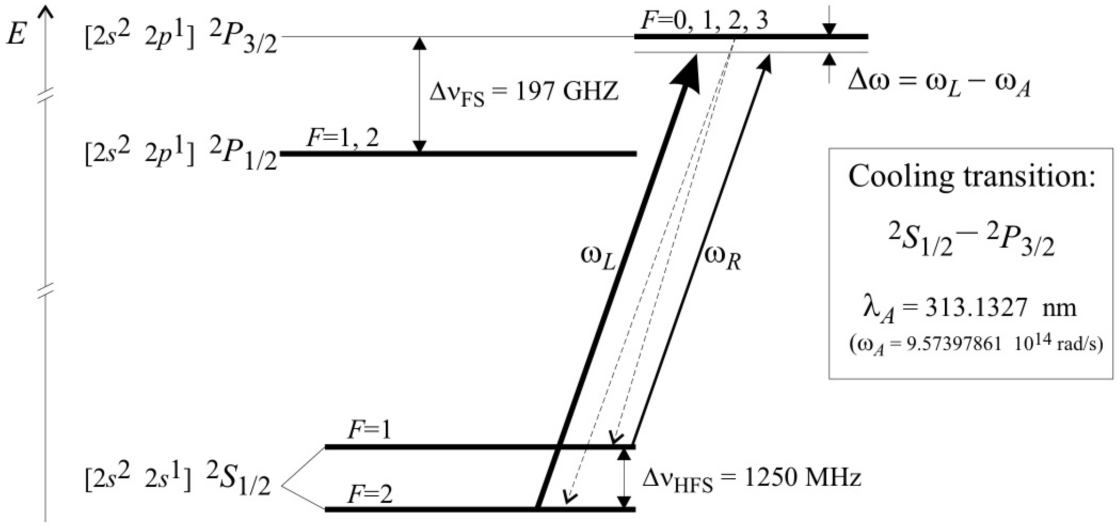

Figure 2.7: Level scheme of the relevant laser cooling transitions of Be^+ ion [40].

Laser cooling of the Be$^+$ ions is performed on the atomic transition of $^2S_{1/2}(F = 2) - {}^2P_{3/2}$. The nuclear spin $I = 3/2$ yields hyperfine splittings of the energy levels. A hyperfine splitting of $\Delta\nu_{HFS} = 1250$ MHz occurs in the $^2S_{1/2}$ ground level, while the splittings in the excited levels $^2\mathrm{P}_{1/2}$ and $^2\mathrm{P}_{3/2}$ vanish in the natural linewidth of the levels. When Be$^+$ ions are excited to the $^2\mathrm{P}_{3/2}$ level at a wavelength of $\lambda_A = 313.1327$ nm, they can decay into either hyperfine states $^2S_{1/2}(F = 1)$ or $^2S_{1/2}(F = 2)$ of the ground level. Thus, a "repumper" at a frequency detuning of $\Delta\nu_{HFS}$ from the main cooling laser frequency that excites the residual population to the $^2\mathrm{P}_{3/2}$ level is required.

2.2.4 Taking advantage of the laser polarization

Several factors, i.e. the initial population of the ground level, the polarization of the cooling laser, and the branching ratio of the spontaneous emission from the $^2\mathrm{P}_{3/2}$ level, determine the required intensity of the repumping beam.

The dipole coupling strength of two substates can be expressed by the square of Clebsch-Gordan coefficient [59, 60] that depends on the laser polarization and the magnetic quantum numbers. By changing the magnetic quantum numbers, a series of the Clebsch-Gordan coefficients can be obtained. Among them only some coefficients of the hyperfine transitions are non-zero according to the following selection rules:

$$\begin{cases} \Delta F & = 0,\ \pm 1 \\ \Delta m_F & = 0,\ \pm 1 \text{ (for } \pi\text{-, } \sigma^{\pm}\text{-polarized light).} \end{cases} \tag{2.28}$$

By using Racah algebra, the following matrix elements can be expanded into computable 3j and 6j symbols:

$$\langle d \rangle = \left\langle F, m_f \mid C_q^{(1)} \mid F', m_f' \right\rangle . \tag{2.29}$$

Thus, the relative oscillator strength of all related hyperfine transitions can be calculated.

As shown in Figure 2.8, first, the initial populations in both states of the ground level $^2S_{1/2}$ can be assumed to be equal, since the ground level splitting of 1250 MHz is relatively small. Then, the branching ratios can be computed by using the calculated oscillator strength $\langle d \rangle$. After an excitation and emission cycle, the probability of finding the Be$^+$ ion in a $F = 2$ state is 62.5% and 60% when using π-polarized and $\sigma^{\pm}$-polarized laser, respectively, which shows only a slight difference.

It can be seen that a Be$^+$ ion that is excited from a $F = 2$ state will decay back to a $F = 2$ state with the probability of ca. 80%, which is similar to the one that is excited from a $F = 1$ state and decays back to $F = 1$ state with the probability of

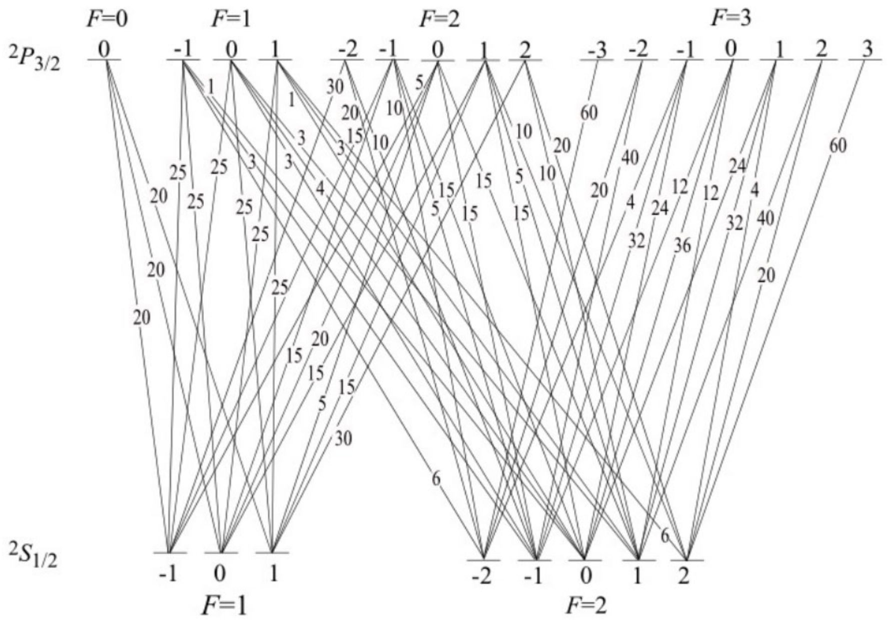

Figure 2.8: Relative squared oscillator strength $\langle d \rangle^2$ of hyperfine transitions $^2S_{1/2}(F = 1, 2) - {}^2P_{3/2}(F = 0, 1, 2, 3)$ of Be$^+$ ion (normalized to 60 for decay, and to 120 for excitation, respectively) [40].

ca. 70%. These ratios indicate that a similar intensity of the repumping laser as the one of the main laser is required.

However, when using σ^+-polarized laser, the ions will be pumped to the transition $|F = 2, m_F = 2\rangle - |F = 3, m_F = 3\rangle$ after several cycles. Decay from the hyperfine substate $|F = 3, m_F = 3\rangle$ to the $F = 1$ state is forbidden according to the selection rules (Equation 2.28), therefore, in principle, no repumping laser would be required in this case.

Concretely, caused by Larmor precession during the lifetime Γ, the transitions within some other excited hyperfine states, e.g. $|F = 3, m_F = 3\rangle - |F = 3, m_F = 2\rangle$, cannot be avoided, due to the imperfection of the laser polarization and the residual magnetic fields. Nevertheless, by rough estimations of these effects, a repumping laser intensity with only a few percent of the main cooling laser should be sufficient, as long as the circular polarization is applied.

As a result, experimentally, the preferred cooling procedure of Be$^+$ ions is as follows: A σ^+-polarized laser light is used to excite the Be$^+$ ions from the ground state $^2S_{1/2}(F = 2, m_F = 2)$ to the excited state $^2P_{3/2}(F = 3, m_F = 3)$ with a natural linewidth $\Gamma = 2\pi \cdot 19.4$ MHz [86]. By detuning the frequency of the main cooling laser light via generating a sideband at 1250 MHz, an optical "repumping" takes place. In addition, taking the Doppler broadening effect (see subsection 2.2.2) into consideration, both the main cooling laser and the repumping laser are frequency broadened to achieve the most effective cooling of the Be$^+$ ions.

In this work, by taking advantage of the laser polarization, Raman spectroscopy of Be^+ ions was performed and the local magnetic field was determined consequently. The details will be described in chapter 3.

2.3 Coulomb ion crystals

As described in subsection 2.1.3, the motion of trapped ions is determined by the three-dimensional time-independent pseudo-potential (Equation 2.14) and the following mutual Coulomb interaction:

$$\phi_{C,i} = \frac{1}{4\pi\varepsilon_0} \sum_j \frac{Q_j}{r_{ij}}. \tag{2.30}$$

Here, $\phi_{C,i}$ represents the electric potential felt by an ion i that is generated by all the neighboring ions j with a charge of Q_j and a distances of r_{ij} from the ion i. Confined in the center of the trap, all the ions repulse each other electrostatically due to the same charges and thus form a diffuse ion "cloud". Without cooling, all the ions in the cloud would move in disordered directions with various thermal velocities.

When a proper cooling laser is applied, the ion ensemble reduces the translational energy and changes its state from a disordered ion cloud to an ordered ion crystal, i.e. a liquid-solid phase transition of the ion ensemble occurs. For the appearance of this so-called Coulomb crystallization, the particles' mutual interaction (Equation 2.30) over their disturbing translational motion is a dominant factor, which can be determined by the plasma coupling parameter:

$$\varUpsilon = \frac{1}{\kappa_B T} \frac{Q^2}{4\pi\varepsilon_0 a_{WS}}, \tag{2.31}$$

which represents the Coulomb energy of interaction among all the ions and the thermal energy per degree of freedom. The parameter a_{WS} is called Wigner-Seitz radius:

$$a_{WS} = \left(\frac{3}{4\pi n_0}\right), \tag{2.32}$$

which is used to describe the ions' mean distance in the ion crystal, where n_0 is the ion density of the ensemble. Here, at the translational temperature of about 3 mK, the typical value of the mean ion distance is $a_{WS} \approx 30$ μm [61].

In general, the coupling parameter $\varUpsilon$ is crucial for a non-neutral plasma, e.g. a trapped ion ensemble. For $\varUpsilon < 1$, the ensemble is in a gaseous state. For $\varUpsilon \gtrsim 1$, a strongly coupled plasma state will be referred. For $\varUpsilon \gtrsim 2$, a phase transition from the plasma state to a liquid state, characterized by a short-range order, will occur which is derived from the MD simulations of infinite non-neutral plasmas [62, 63]. In the case of $\Upsilon > 170$, a further phase transition from the liquid state to a structured solid state, described by a long-range order, is predicted by the MD simulations and thermodynamic approaches [63, 64].

Figure 2.9 shows a typical experimental setup of ion trapping and laser cooling in this work (details of the apparatus will be described in chapter 3). Figure 2.10 shows the CCD images of the phase transition of the Be^+ ensemble that is exposed longitudinally to the cooling laser beam. The ions are trapped in the center of a linear Paul trap apparatus and are initially in a diffuse gaseous state or a so-called plasma state (ion "cloud"). By tuning the frequency of cooling laser towards Be^+ resonance, the phase transition of the ion ensemble takes place from the plasma state as shown in panel (a) of Figure 2.10 into a liquid state (b) and eventually into a solid state (c). If further adjusting the laser frequency very close to resonance, the fluorescence intensity of the ion crystal increases dramatically, as shown in panel (d) with high brightness.

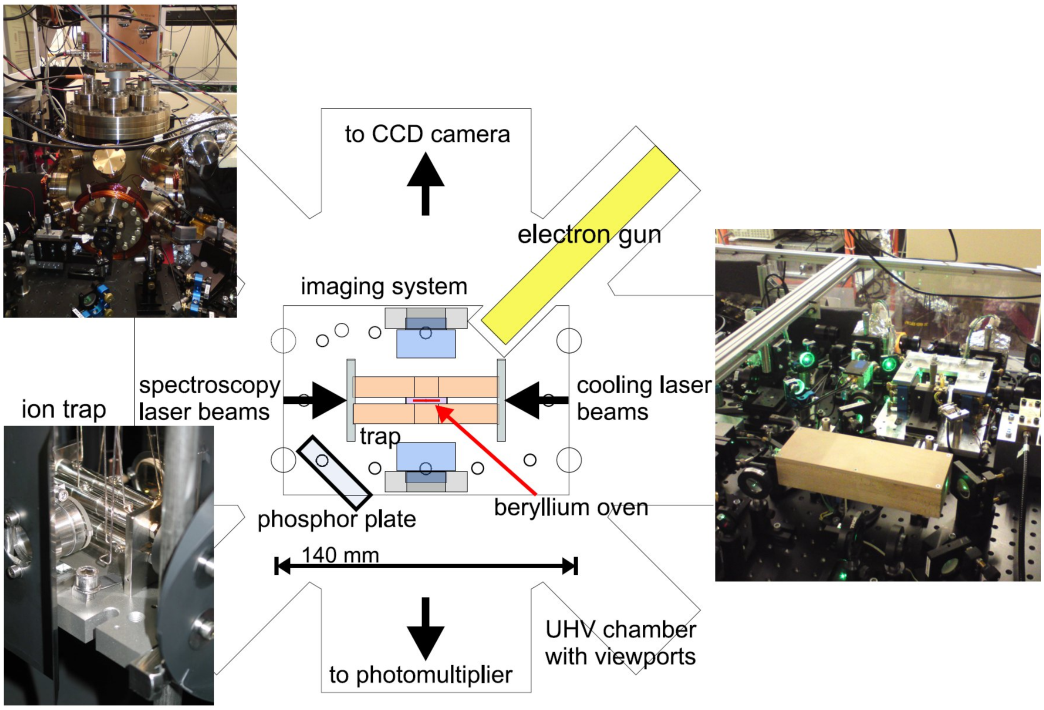

Figure 2.9: Typical experimental setup of ion trapping and cooling. Upper left: UHV chamber; bottom left: ion trap [65]; middle: schematic view of horizontal cross-section of the experimental UHV setup [40]; right: cooling laser. The charge-coupled device (CCD) camera is used to image the beryllium crystal and the photomultiplier tube (PMT) is used to detect the Be^+ fluorescence.

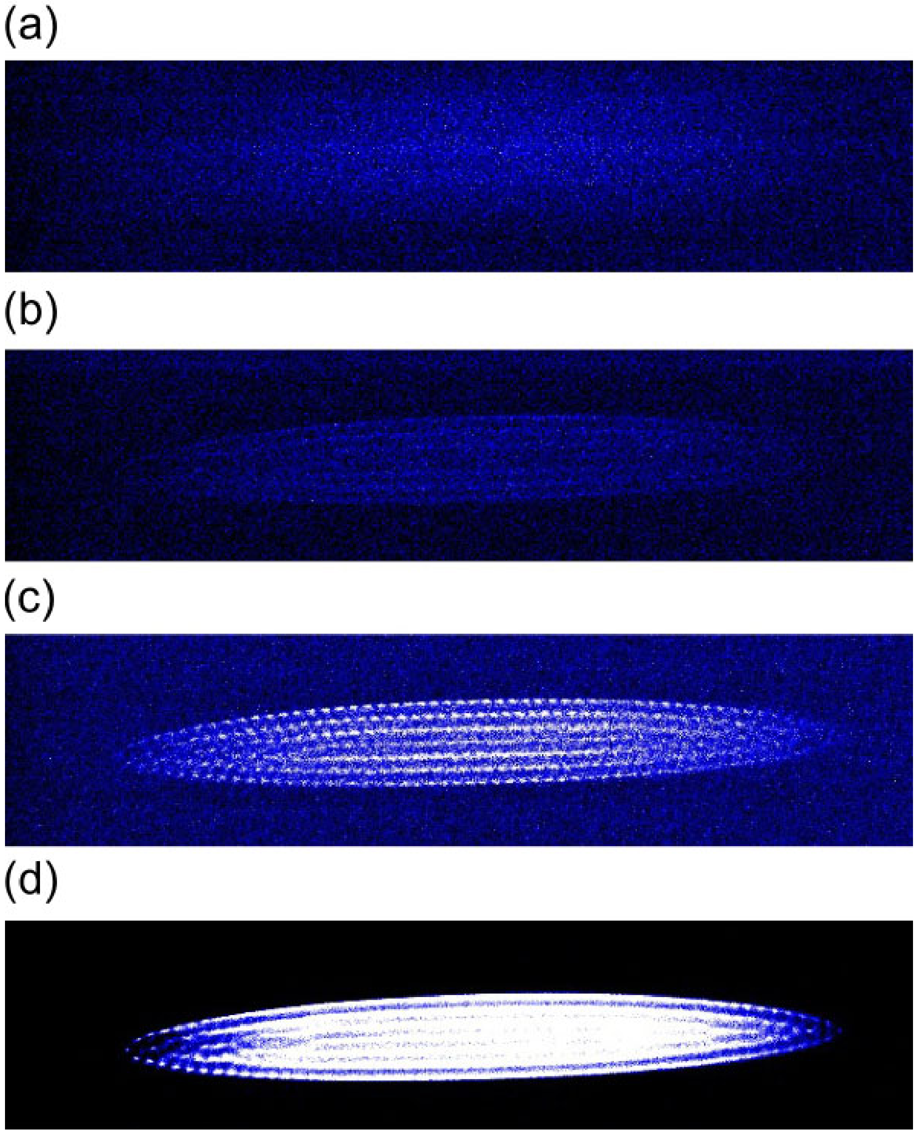

Figure 2.10: Coulomb crystallization of a Be^+ ensemble. By tuning the frequency of the cooling laser towards Be^+ resonance, an initially diffuse cloud of Be^+ ions is cooled down from a gaseous state (a) to a liquid state (b) and further to a solid state (c). The panel (d) shows the ion crystal in a solid state by adjusting cooling laser frequency very close to Be^+ resonance.

In this work, the Be^+ ions are used ultimately for the spectroscopic studies of HD^+ ions by analyzing the intensity change of spontaneous fluorescence emission from the Be^+ ions that are proportional to the number of remained HD^+ ions during the process of secular excitation. So in principle, the Be^+ crystal in the state (d) seems to be a better solution for spectroscopic purposes due to the higher fluorescence intensity that can improve the signal-to-noise ratio. However, this leads to a saturation of the Be^+ fluorescence detector. In addition, the ion crystal in the state (d) turns out to be unstable during the process of loading and sympathetic cooling HD^+ ions, due to the strong Coulomb interaction. Therefore, the Be^+ crystal in the solid state (c) is chosen for spectroscopy, in which the Be^+ ensemble is much more stable and has sufficient "strength" to cool down the HD^+ ions. Since the fluorescence change of the Be^+ crystal in the state (c) for spectroscopy of HD^+ ions is not as high as the one in the state (d), a medium-sized Be^+ crystal instead of a small crystal is preferable to compensate the relatively low fluorescence intensity. The details will be described in chapter 3 and chapter 5.

The procedure of loading a Be^+ crystal with sympathetically cooled HD^+ ions is as follows: first, beryllium atoms are evaporated from an oven that contains a beryllium filament and is positioned close to the linear Paul trap electrodes in the trap center. Then the atoms are ionized by an electron gun to Be^+ ions and cooled down by a UV cooling laser at a wavelength of 313 nm. After the Be^+ ensemble is stable which can be monitored by a CCD camera, the loading and cooling of HD^+ ions take place (see subsection 5.4.1 for a detailed description).

To achieve the most effective sympathetic cooling, it is crucial to trap both laser-cooled and sympathetically cooled ions simultaneously with a good spatial overlap. According to the Mathieu (stability) parameters in Equation 2.9, the condition of stable trapping is given by:

$$q = q_x = -q_y = \frac{2QV}{mr_0^2\Omega^2} < 0.9. \tag{2.33}$$

Since the ions located closer to the trap axis possess lower heating rate, small q-parameters are favored. In order to obtain a good spatial overlap between laser-cooled and sympathetically cooled ions, trap potentials $U_{trap,\,LC}$ and $U_{trap,\,SC}$ for each ion species need to be adjusted to the similar values in the radial direction to fulfill the following condition [66]:

$$\frac{Q_{LC}^2}{m_{LC}} \approx \frac{Q_{SC}^2}{m_{SC}}, \tag{2.34}$$

where the parameters Q_{LC}, Q_{SC}, m_{LC}, and m_{SC} represent the charges and masses of laser-cooled and sympathetically cooled ions, respectively.

A schematic diagram of the effective trap potential for various values of Q^2/m is shown in Figure 2.11. Thus, the light Be^+ ions are favorable to sympathetically cool light- (e.g. HD^+ ions) and medium-sized atomic and molecular ions.

By precise controlling during the loading of Be^+ ions and HD^+ ions, ion crystals with various sizes can be obtained. It is obvious that the more laser-cooled Be^+ ions loaded in the trap, the more HD^+ ions would be sympathetically cooled due to the Coulomb interaction. Generally, a large ion crystal contains about 2500 laser-cooled Be^+ ions, a medium-sized crystal normally contains about 1500 Be^+ ions, and a small crystal contains about several hundred ions or even less.

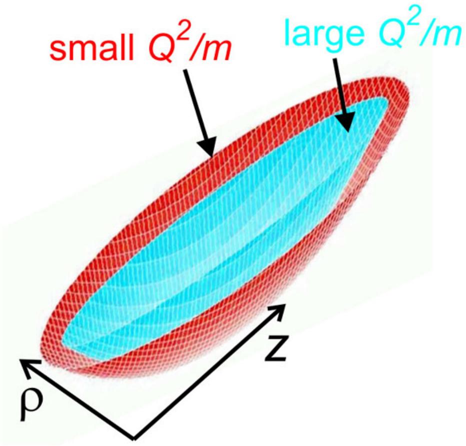

Figure 2.11: Sketch of the effective trap potential for various values of Q^2/m. Here $\rho = \sqrt{x^2 + y^2}$ and z are the radial and axial trap coordinates, respectively [66]. An essential condition of effective sympathetic cooling is $Q^2_{LC}/m_{LC} \approx Q^2_{SC}/m_{SC}$.

Figure 2.12 shows a CCD image of a typical medium-sized Coulomb crystal that is used for our measurements with mixed species: about 1500 laser-cooled Be^+ ions and 200 $\sim$ 250 sympathetically cooled HD^+ ions at 10 $\sim$ 15 mK translational temperature. According to the mass-to-charge ratio, the sympathetically cooled particles (HD^+) separate from the atomic coolants (Be^+) radially. The trap potential for HD^+ ions is steeper, due to the smaller mass-to-charge ratio. Thus, compared with the Be^+ atomic coolants, the HD^+ ions are located closer to the trap axis, which can be distinguished from the appearance of a dark core (non-fluorescing) in the initially pure Be^+ crystal.

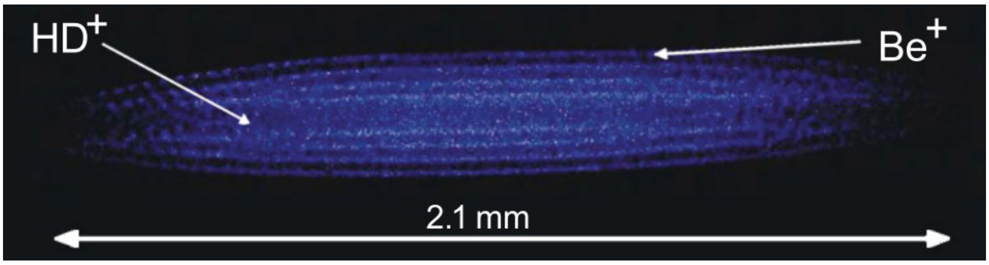

Figure 2.12: CCD image of a typical Coulomb crystal, containing about 1500 laser-cooled Be^+ ions and 200 $\sim$ 250 sympathetically cooled HD^+ ions at 10 $\sim$ 15 mK translational temperature [66]. It is suitable for spectroscopy of HD^+ ions in this work. The trap axis z is horizontal.

In the field of quantum optics, ion crystal with fewer numbers of particles is favorable. In this work, small Coulomb crystals were loaded and studied as well. Figure 2.13 shows the images recorded by a CCD camera.

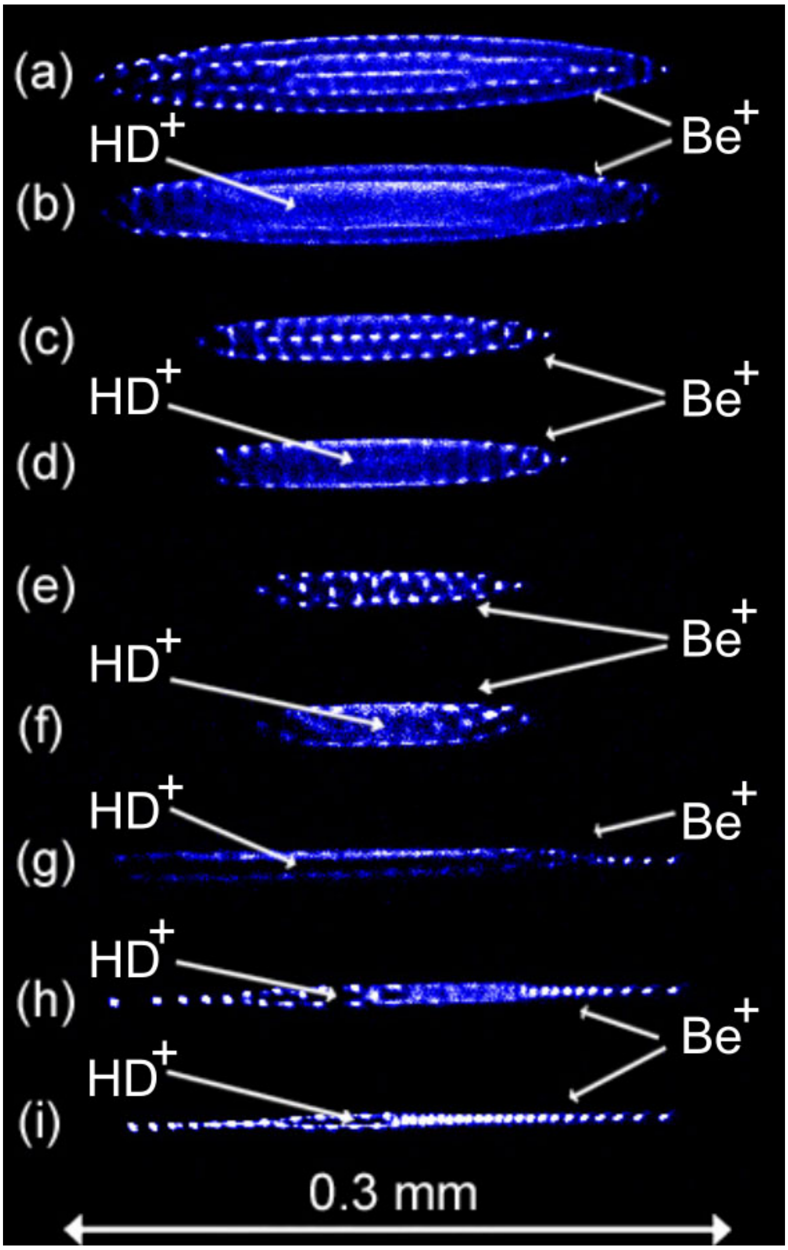

Figure 2.13: CCD images of small Coulomb crystals: (a) pure crystal containing about 150 ~ 200 cooled Be^+ ions; (b) mixed-species crystal containing about 150 ~ 200 cooled Be^+ ions and 20 HD^+ ions; (c) pure crystal containing about 70 cooled Be^+ ions; (d) mixed-species crystal containing about 70 cooled Be^+ ions and 10 HD^+ ions; (e) pure crystal containing about 40 cooled Be^+ ions; (f) mixed-species crystal containing about 40 cooled Be^+ ions and about 6 HD^+ ions; (g) mixed-species ion chain containing about 40 cooled Be^+ ions and about 6 HD^+ ions; (h) and (i) mixed-species linear ion chains containing about 40 cooled Be^+ ions and 3 HD^+ ions. The trap axis is horizontal. The cooling laser beam direction is to the right.

Panels (a), (c), and (e) of Figure 2.13 show the pure crystals containing about 150 $\sim$ 200, 70, and 40 cooled Be^+ ions, respectively, while panels (b), (d), and (f) show the corresponding mixed-species crystals containing about 20, 10, and 6 sympathetically cooled HD^+ ions, respectively. Based on the ion crystal that is shown in panel (f), by reducing the endcap voltage of the trap electrodes, the ion crystal changes its form to an ion chain (g). Panels (h) and (i) show the two-species linear ion chains containing about 40 cooled Be^+ ions and 3 HD^+ ions. Such a mixed-species linear ion chain could be used for the molecular quantum state preparation for quantum information processing [67] by implementing new cooling schemes for the vibrational motion of the extended ion chain. Furthermore, the vibrational trap mode spectrum of the two-species ion chain could be studied by using quantum logic techniques [68].

Towards this direction, by further improving the trap apparatus and the controlling system for ion loading procedure, a “Coulomb-pair” that is composed of only one single laser-cooled Be^+ ion and one single sympathetically cooled HD^+ ion is in principle achievable. In that case, the space charge effects, Doppler effects, coupling effects, as well as collisions between Be^+ and HD^+ ion species that occasionally lead to the resonance frequency shift and line broadening, would be significantly reduced.

3 Raman spectroscopy of Be^+ ions

Precise spectroscopy of cold molecules requires understanding and controlling the local magnetic field. To obtain the information of the magnetic field without opening the vacuum chamber, one approach is measuring the Zeeman shifts of the trapped cold particles (e.g. HD^+, Be^+, etc.). Compared with the resonance-enhanced multi-photon dissociation (REMPD, see subsection 5.5.2) method of the HD^+ particles, the detection scheme of Be^+ particles is more appropriate for this purpose, since it is non-destructive and is thus more efficient.

In this chapter, the experimental scheme and procedure of Raman spectroscopy of Be^+ ions are firstly given in section 3.1, followed by the description of the setup of the compact frequency-stabilized tunable UV laser at 313 nm in section 3.2. Then, the analysis results of the Raman transitions of Be^+ ions with various laser polarization and magnetic fields, as well as the conditions of the near-zero magnetic field obtained from a large number of test experiments, are presented in section 3.3. Based on this, the results of the Raman spectroscopy of Be^+ ions by varying the current of only one pair of Helmholtz coils each time and the conditions of the zero magnetic field, as well as the relations between the magnetic fields and the currents of Helmholtz coils in the respective X-, Y-, and Z-directions, are reported in section 3.4. At last, a comparison of the results obtained from the Raman spectroscopy of Be^+ ions and the ones from the measurement by using a magnetic sensor is provided and discussed.

3.1 Experimental scheme and procedure

The setup of Raman spectroscopy of beryllium ions is shown in Figure 3.1. The UHV chamber houses a linear ion trap driven at 14.2 MHz. A cooling laser beam at $\lambda = 313$ nm from a home-made UV source is employed propagating along the trap-axis (Z-direction) to cool the beryllium ions. It is phase modulated by a fiber-optic electro-optic modulator (EOM) with the driving power of +33 dBm (+3 dBm from a microwave synthesizer and +30 dBm from a laboratory self-made RF amplifier). A sideband at around 1250 MHz away from its carrier is generated and acts as a repumping laser. A power meter is installed at the position Pc after the laser passing through the vacuum chamber to monitor the laser power and beam alignment. It should be mentioned that the laser power mentioned in this whole chapter is not the real power of the cooling laser but only a value read out from the power meter as a reference.

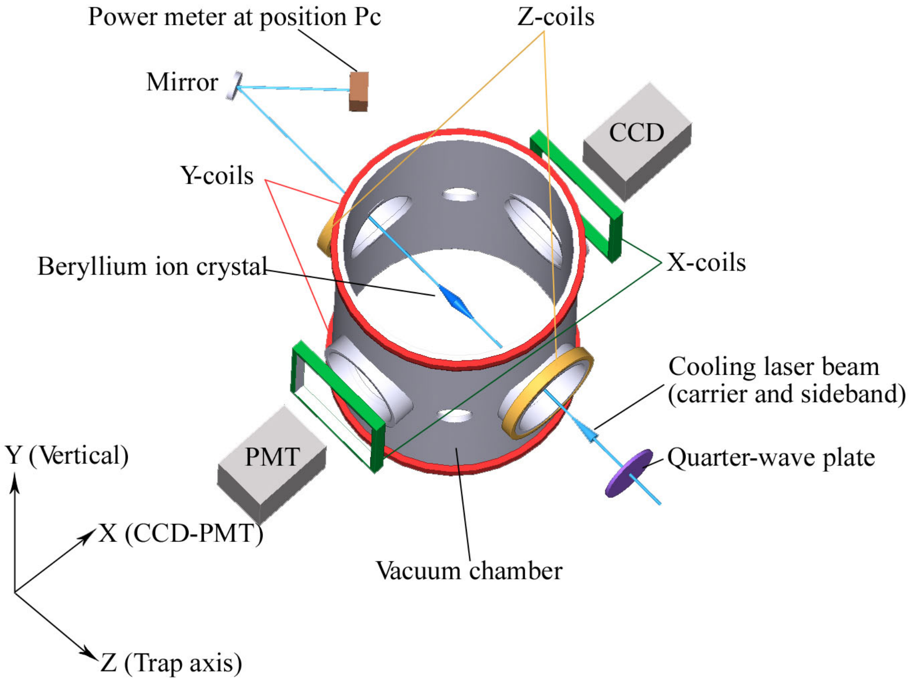

Figure 3.1: Schematic of the Raman spectroscopy of Be$^+$ ions [69]. The ions are cooled by the cooling laser beam that contains both the main carrier and the sideband. The power meter is installed at the position Pc to record the laser power. The local magnetic field is generated by three pairs of Helmholtz coils. The CCD camera is used to image the beryllium crystal and the PMT is used to detect the Be$^+$ fluorescence.

Initially, the cooling laser is frequency stabilized to an iodine absorption line and is about $1 \sim 2$ GHz red detuned from resonance. After the beryllium ions are loaded to form an ion cloud, the carrier frequency of the laser is tuned smoothly towards resonance until hundreds of MHz away from it and then locked to the iodine absorption line again, causing a corresponding cloud-liquid-solid phase transition of the ion ensemble. Subsequently, the cooling laser power is decreased to tens of micro Watt and the RF input of the EOM for the sideband generation is decreased to +10 dBm. Thus, the system is ready for spectroscopy, during which, the carrier frequency remains constant, while the sideband frequency is swept repeatedly. Meanwhile, the Be$^+$ fluorescence is recorded by the PMT and the beryllium crystal is imaged by the CCD camera.

In this work, the local magnetic field is generated by three pairs of Helmholtz coils. Each of them generates a magnetic field in one direction. For clarity, these three pairs of coils are denoted as X-, Y-, and Z-coils, respectively. To investigate the Zeeman splitting effect, in each measurement group, the induced magnetic field is varied only in one direction (e.g. X-direction) and kept constant in the other two directions (i.e. Y- and Z-directions).

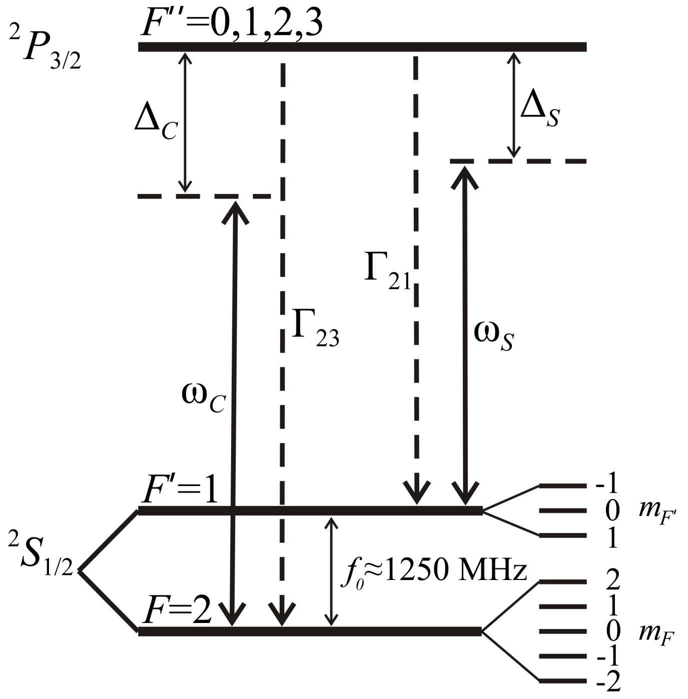

Figure 3.2: Relevant level scheme of Be$^+$ ion in detail [69].

Figure 3.2 shows the relevant level scheme of Be$^+$ ion that can be treated as a lambda-type three-level structure. Due to the nuclear spin of $I = 3/2$, the ground level $^2S_{1/2}$ splits into two hyperfine states $^2S_{1/2}(F = 1)$ and $^2S_{1/2}(F = 2)$, with a frequency splitting of around 1250 MHz. The excited level $^2P_{3/2}$ splits into four hyperfine energy states $^2P_{3/2}(F = 0, 1, 2, 3)$. ω_c stands for the frequency of main pumping laser wave $E_c(t) = E_c\cos(\omega_c t + \varphi_c)$ ("carrier wave"), while ω_s denotes the frequency of the repumping laser wave $E_s(t) = E_s\cos(\omega_s t + \varphi_s)$ ("sideband wave"), which is one of the sidebands that are generated by the EOM in the cooling laser setup. Here, E_c and E_s are the field amplitudes, while φ_c and φ_s are the phases of the carrier wave and sideband wave, respectively. $\varDelta_c = \omega_{31} - \omega_c$ and $\varDelta_s = \omega_{32} - \omega_s$ represent field detunings from the atomic resonances. $\varGamma_{31}$ and $\varGamma_{32}$ are radiative decay rates, respectively.

The timing sequence of the Be$^+$ spectroscopy is shown in Figure 3.3. During the whole experiment, the carrier of the cooling laser remains on constantly to keep the beryllium ions in a good cooling state. Before each measurement starts, the laser sideband is tuned at 1250 MHz for 20 seconds and then switched off (not shown in Figure 3.3) to repopulate the Be$^+$ ions to the same initial state, thus the current measurement will not be affected by the previous one. During the measurement runs, the sideband is switched on and off alternatively with its frequency swept from $f_{mod,1}$ to $f_{mod,n}$ $(n = 2, 3, 4...)$. The corresponding fluorescence levels of signal and background are recorded as $N_{f,i}$ and $N_{b,i}$ $(i = 1, 2, 3...)$, respectively. To avoid the influences by the long-term laser power fluctuation and beryllium ions loss that

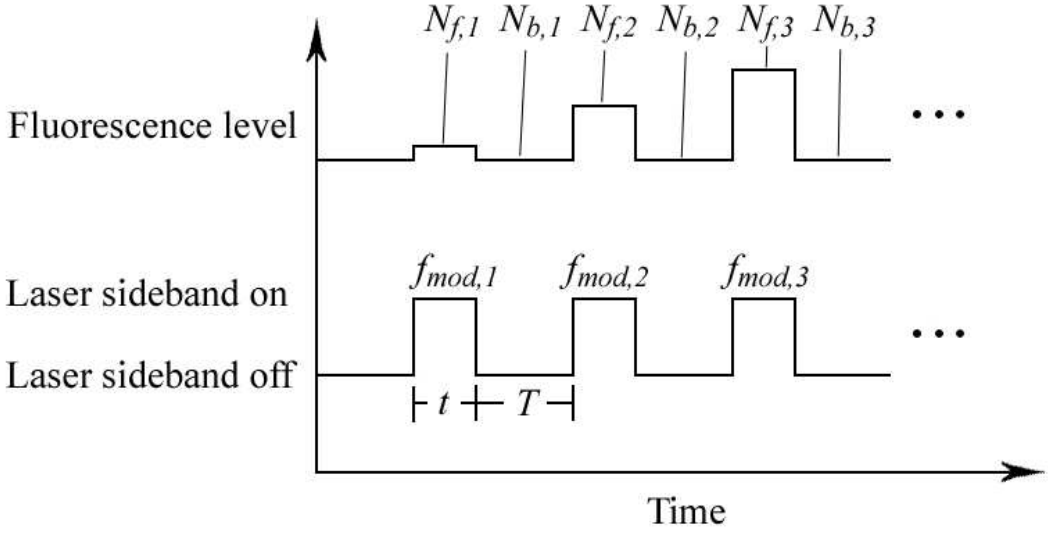

Figure 3.3: Timing sequence of the Raman spectroscopy of Be$^+$ ions [69]. Laser carrier (not shown here) remains on constantly, while the sideband is switched on and off alternatively with its frequency swept from $f_{mod,1}$ to $f_{mod,n}$ ($n = 2, 3, 4...$). The corresponding fluorescence levels of signal and background are recorded as $N_{f,i}$ and $N_{b,i}$ ($i = 1, 2, 3...$), respectively. The time interval of sideband generation on and off are denoted as t and T, respectively. In this experiment, both t and T are set to 500 ms.

causing the fluorescence change as well, the effective signal generated by the laser sideband at a frequency $f_{mod,i}$ is calculated as $(N_{f,i} - N_{b,i})/N_{b,i}$.

3.2 Compact UV source for laser cooling of Be$^+$ ions

Previously in our laboratory, the Be$^+$ ions were laser cooled by a cumbersome UV radiation system that took a lot of space. Due to long-distance laser propagation, the laser beam was extremely sensitive to the alignment with a large number of mirrors. In addition, the occurrence of insufficient power to the trap and the occasional mode jump was an obstacle for long-term experimentation.

In order to perform an effective and stable laser cooling of the atomic ions, a compact frequency-stabilized tunable UV source at 313 nm with high power up to 100 mW was developed [70]. The system is based on the frequency quintupling of a standard C-band telecom laser at a wavelength of 1565 nm that is amplified in a fiber amplifier. The output at the third-harmonic wavelength of 522 nm is used for frequency stabilization to the molecular iodine transitions.

Figure 3.4 shows the experimental setup of the compact cooling laser source that is used throughout the whole work of spectroscopic measurements. A metal box houses

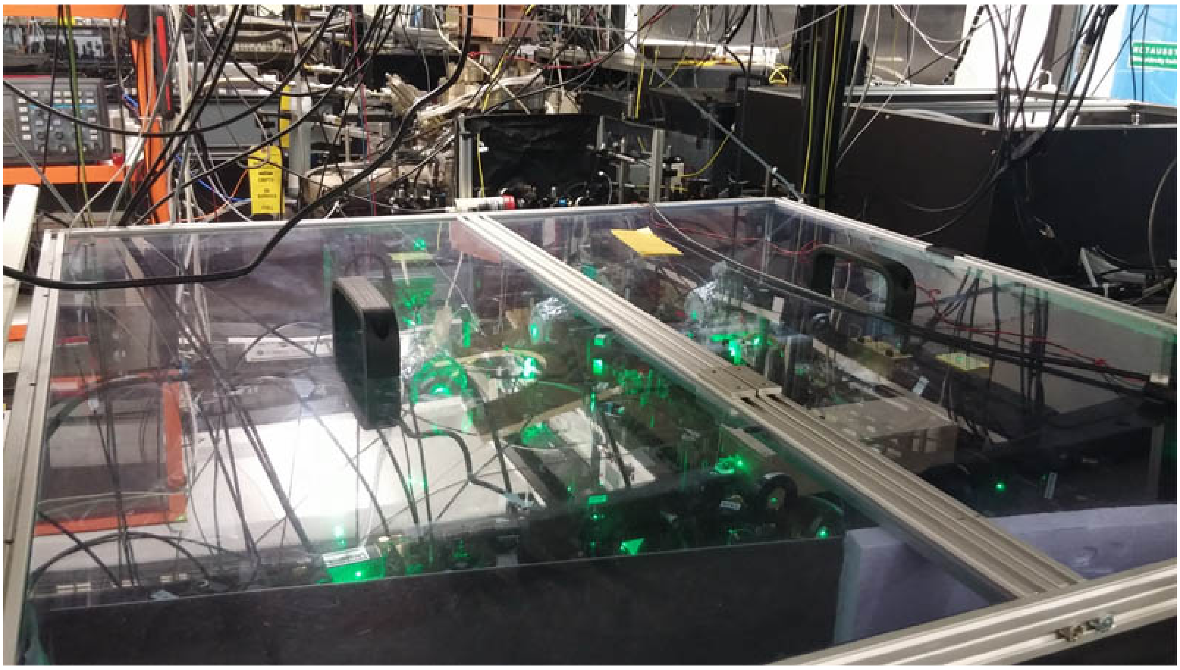

Figure 3.4: Photograph of the experimental setup of the compact and high-power 313 nm laser source.

the whole setup for thermal and acoustic isolation. The output of the 313 nm laser beam is positioned very close to the vacuum chamber in order to shorten the beam propagation distance. Compared with the previous 313 nm UV radiation system, this novel and high-power laser source is much more stable and easier to operate, which makes the laser cooling of beryllium ions appreciably more effective.

3.2.1 Laser setup

Figure 3.5 illustrates the schematic of the UV laser setup. A master laser (a single-frequency erbium-doped distributed-feedback (DFB) fiber laser module, Koheras K80-153-12) produces a standard C-band telecom laser at a wavelength of 1565 nm with a power of 10 mW. A fiber-optic phase modulator (EOM, Photline Technologies, type MPX-LN-05) is applied to generate two sets of sidebands, one of which is used for producing a repumping wave for Be^+ cooling (modulation frequency: 1250 MHz), and the other is for the frequency locking to an enhancement cavity (modulation frequency: 20 MHz). Afterwards, the laser carrier and sidebands are amplified by a 15-W polarization-maintaining erbium-doped fiber amplifier (EDFA, type: IPG EAR-15K-C- LP-SF-UD).

Frequency conversion from the fundamental frequency (ν) to the fifth-harmonic (5ν) is realized as follows: (i) single-pass SHG ($\nu + \nu \rightarrow 2\nu$) in a cascade of two 50-mm long PPLN crystals (Deltronic), which could increase the SHG efficiency up to a factor of 4 [71, 72]; (ii) single-pass SFG ($\nu + 2\nu \rightarrow 3\nu$) in the 30-mm long PPSLT crystal (HCP); (iii) SFG ($2\nu + 3\nu \rightarrow 5\nu$) in a 10-mm long BBO crystal (Ekspla) that is placed in an enhancement cavity in order to increase the output power of the fifth harmonic generation at the wavelength of 313 nm.

For the resonant SFG, a standard bow-tie enhancement cavity with two plane and two curved mirrors (50 mm radius of curvature) is employed. The cavity that is designed to resonate only with the second harmonic at 783 nm, whereas the single-pass third-harmonic is delivered to the frequency stabilization system, is locked to the master laser by the sideband of 20 MHz using the standard Pound-Drever-Hall technique (PDH, see section 6.1).

At the EDFA power of 15 W, the maximum second-harmonic (2ν) power of 7.7 W with 53% pump conversion efficiency, the third-harmonic (3ν) power of 1.2 W corresponds to 8% conversion efficiency, and consequently, the fifth-harmonic (5ν) power of 100 mW are achieved. Note that this UV power level is a tremendous advantage for the laser cooling of beryllium ions since a typical UV power of only several mW is required.

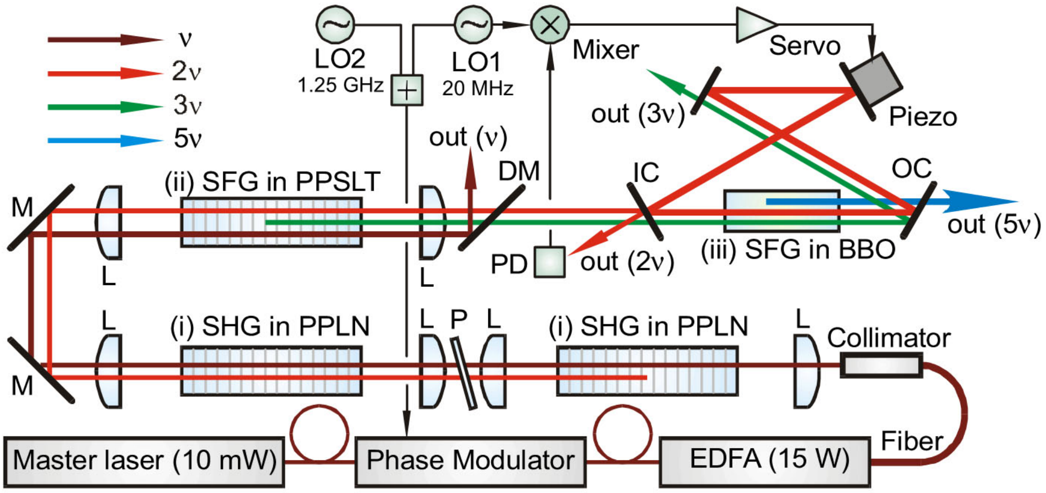

Figure 3.5: Schematic of the novel UV radiation system [70]. M: mirror; L: lens; P: Brewster plate; PD: photodetector; DM: dichroic mirror; PPLN: periodically poled lithium niobate crystal; PPSLT: periodically poled stoichiometric lithium tantalite crystal; BBO: barium borate crystal; SHG: second harmonic generation; SFG: sum frequency generation; EDFA: erbium-doped fiber amplifier; IC/OC: input/ output coupler of the enhancement cavity; out ($\nu, 2\nu, 3\nu, 5\nu$): output laser beams at the fundamental, second, third and fifth-harmonic frequency. All nonlinear crystals are stabilized within a temperature of 0.1 °C. Plano-convex (PCX) lenses are used for the collimation and focusing of the laser beam. A Brewster plate is used to compensate and adjust the phase mismatch.

3.2.2 Frequency stabilization

By using the method of Doppler-free frequency modulation transfer spectroscopy (FMTS) with a 15-cm long temperature stabilized iodine cell, the frequency stabilization and tuning of the UV laser source were realized. As shown in Figure 3.6, the output beam of the enhancement cavity at the third-harmonic frequency 3ν is split by PBC1 and delivered to the double-pass acousto-optic modulator AOM1 (max. frequency shift $\mathit{\Delta}_m = 200$ MHz, bandwidth ±50 MHz). Subsequently, the frequency-shifted laser beam ($3\nu + 2\mathit{\Delta}$) is sent to the AOM2 (max. frequency shift $\delta_m = 80$ MHz) to generate the pump beam and probe inputs for the setup of FMTS, one of which, the pump beam is modulated at 1 MHz by the EOM, with the demodulated error signal fed back to the master laser via a servo amplifier. Thus, via the third-harmonic output 3ν, the master laser is frequency stabilized to the hyperfine structure (hfs) components of the iodine molecule absorption line.

Ultimately, the frequency of the 313 nm UV source (i.e. the fifth-harmonic 5ν) is determined by the followed equation:

$$f_{5\nu} = \frac{5}{3}\left(\nu_{I2} - 2\mathit{\Delta} - \frac{\delta}{2}\right), \tag{3.1}$$

where ν_{I2} represents the frequency of the iodine hfs component (a list of the involved hfs components is shown in Table 3.1), while $\mathit{\Delta}$ and δ stand for the modulation frequency of AOM1 and AOM2, respectively.

To perform the frequency tuning of the UV output laser at 313 nm, a combination of coarse adjustment and fine tuning is implemented. Initially, the master laser is frequency locked to one of the selected iodine hfs component in Table 3.1 that is close to the desired frequency, leading to a subsequent phase transition of the laser-cooled Be$^+$ ion ensemble in the trap, as shown in Figure 2.10. Afterwards, by regulating the frequency $\mathit{\Delta}$ of AOM1 (fine tuning), the initial fluorescence intensity of Be$^+$ ions could be adjusted to a low level to avoid saturation of the photodetector during spectroscopic measurements.

hfs line	Freq. (GHz)	hfs line	Freq. (GHz)	hfs line	Freq. (GHz)
1	574437.959	6	574438.318	11	574438.600
2	574438.110	7	574438.373	12	574438.631
3	574438.212	8	574438.448	13	574438.702
4	574438.273	9	574438.485	14	574438.735
5	574438.281	10	574438.525	15	574438.809

Table 3.1: Frequency list of the involved hfs components of iodine molecule transitions [70]. The uncertainty of the frequency values is estimated at about 500 kHz.

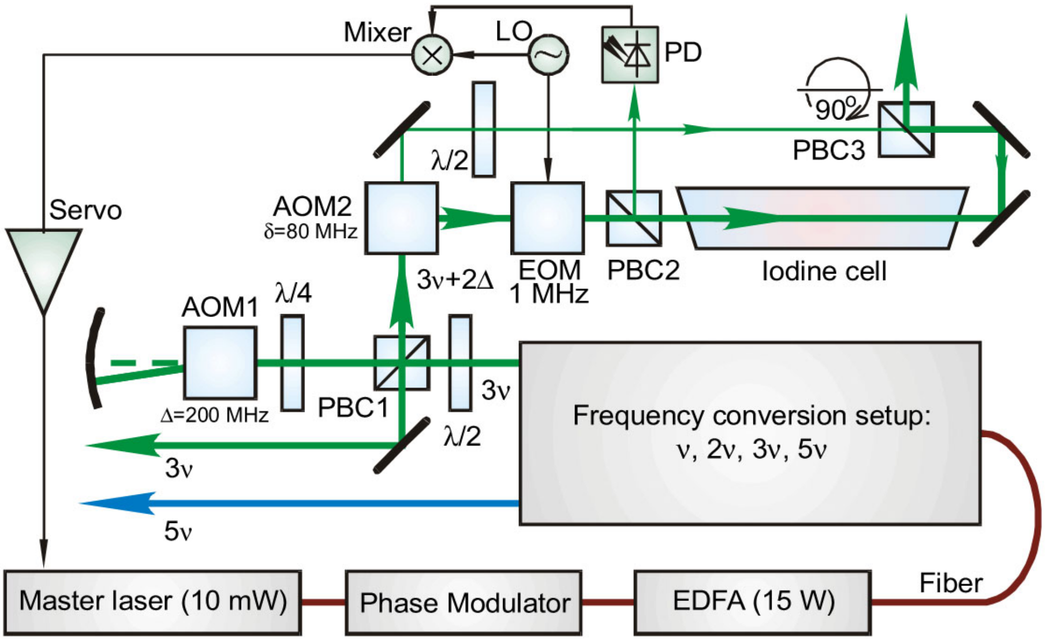

Figure 3.6: Schematic of frequency stabilization and tuning of the novel UV laser source [70]. 3ν and 5ν: the output beams at third and fifth-harmonic frequency; PBC: polarization beam splitter cubes (the PBC3 is rotated by 90° with respect to the PBC2, to reflect the pump beam and transmit the probe beam); $\lambda/2$ and $\lambda/4$: wave plates; AOM: acousto-optic modulator; EOM: electro-optic modulator; PD: photodetector.

3.3 Laser polarization- and magnetic field-dependent Raman transitions

Figure 3.7 shows the Zeeman splittings of Be$^+$ ion in the levels of $^2S_{1/2}$ and $^2P_{3/2}$ in a non-zero magnetic field. Mathematically, the Zeeman splitting of a state with magnetic quantum number m_F in a magnetic field B can be expressed as:

$$E_{mag} \quad = \quad g_F m_F \mu_B B \quad \approx \quad g_F m_F B (1.400\,\text{MHz/G}) \ , \tag{3.2}$$

with the g_F factor:

$$g_F \quad \approx \quad g_J \frac{F(F+1) - I(I+1) + J(J+1)}{2F(F+1)} \ , \tag{3.3}$$

where the g_J factor is:

$$g_J \quad \approx \quad \frac{3}{2} + \frac{S(S+1) - L(L+1)}{2J(J+1)} \ . \tag{3.4}$$

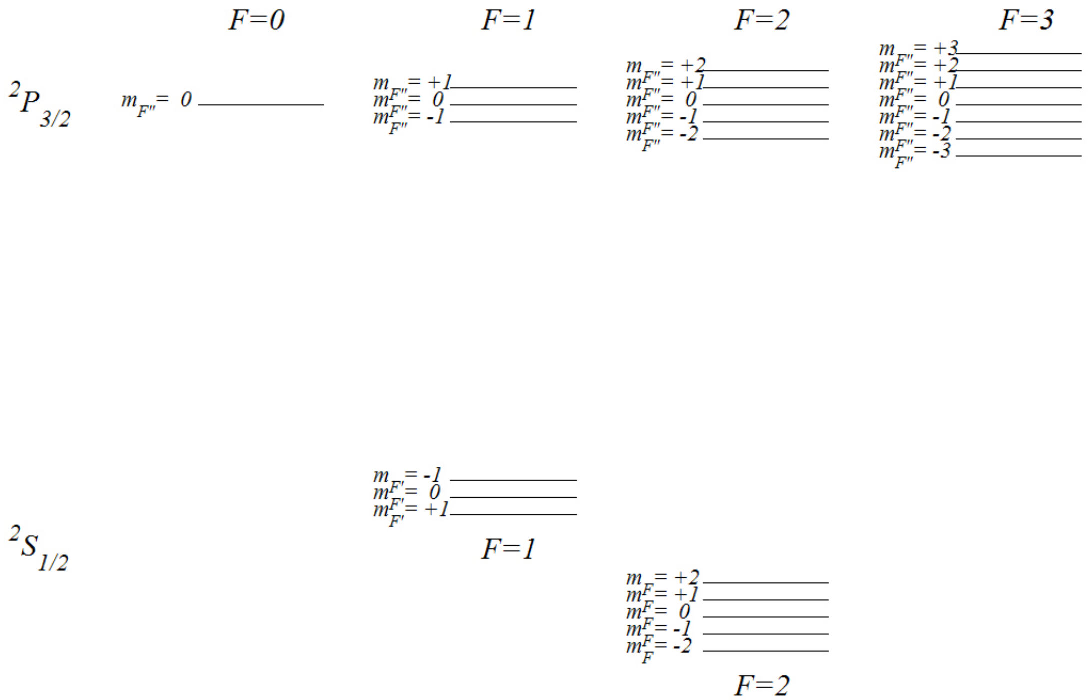

Figure 3.7: Zeeman splittings of Be$^+$ ion in the levels of $^2S_{1/2}$ and $^2P_{3/2}$. The energy level differences are not to scale.

In the case of Be$^+$ ion, the relevant Zeeman splittings are:

$$\begin{array}{lcl} P_{3/2}(\text{all } F) & : & g_F = +2/3, \\ S_{1/2}(F=1) & : & g_F = -1/2, \\ S_{1/2}(F=2) & : & g_F = +1/2. \end{array} \tag{3.5}$$

Here, μ_B is the Bohr magneton and equals to $5.78838263(52) \times 10^{-11}$ MeV/T. In terms of frequency, it should be divided by the Planck's constant $h = 4.135669 \times 10^{-21}\text{MeV} \cdot \text{s}$ and turns out to be 1.400 MHz/G.

As mentioned above, this experiment is aiming at the determination of the magnetic field in the trap. According to Equation 3.2, the energetic positions of the Zeeman sub-components have a direct relation with the magnetic field. Thus, by measuring these positions precisely, the magnetic field could be determined accordingly.

In this case, the selection rules for the optical transitions are:

$$\begin{cases} \varDelta F & = 0,\ \pm 1 \\ \varDelta m_F & = -1,\ 0,\ +1 \text{ (for } \sigma^-\text{-, } \pi\text{-, and } \sigma^+\text{-polarized light).} \end{cases} \tag{3.6}$$

Experimentally, the cooling laser beam has been adjusted to be circularly polarized for both the main carrier and the sideband from the identical UV laser source. Thus, its projection is either σ^+ or σ^- polarized in the Z-direction, and is a mixture of σ^+,

σ^-, and π polarized in both the X- and Y-direction. In the following subsections, the corresponding Raman transitions are analyzed.

3.3.1 Raman transitions with the σ^+ or σ^- polarization

From Figure 3.2 and 3.3, we can get a physical picture as follows: during the quantum state preparation time, only the laser carrier is performed on the transition $^2S_{1/2}(F = 2) \to {}^2P_{3/2}$ with a frequency detuning $\varDelta_c$. The Be$^+$ ions in the excited level $^2P_{3/2}$ can decay into one of the hyperfine Zeeman substates of either $^2S_{1/2}(F = 2)$ or $^2S_{1/2}(F = 1)$ state, e.g. $^2S_{1/2}(F = 1, m_F = 0, \pm 1)$, as shown in Figure 3.7. Subsequently, the laser sideband generation is alternatively switched on and off with its frequency swept from $f_{mod,1}$ to $f_{mod,n}$ $(n = 2, 3, 4...)$, while the laser carrier remains consistently with a constant frequency.

As shown in Figure 3.8, if both the laser carrier and sideband are σ^+ polarized, the ions are finally pumped to the substate $^2S_{1/2}(F = 1, m_F = +1)$. When the condition $\varDelta_c = \varDelta_s = \varDelta$ is fulfilled during the sweeping of sideband frequency, the system will reach a situation of the two-photon resonance, as shown in Figure 3.8 (b). Here, the corresponding transition is the so-called Raman transition.

It should be mentioned that the laser sideband in the experiment is generated from the main carrier by the EOM in the laser setup. The so-called “sideband frequency” in this whole chapter is the frequency difference from the carrier frequency. From Figure 3.8 (b), it can be clearly seen that this sideband frequency represents exactly the energy interval between the Zeeman substates $^2S_{1/2}(F = 1, m_F = +1)$ and $^2S_{1/2}(F = 2, m_F = +1)$. When the magnetic field changes its value, this energy interval varies accordingly due to the Zeeman splitting effect and the Raman transition frequency or the “sideband frequency” that fits the two-photon resonance shifts consequently.

It can be derived from Figure 3.8 that with the σ^+ polarization of both the carrier and sideband, the corresponding Zeeman shift in a magnetic field B is:

$$\begin{aligned} \varDelta E_{\sigma+} &= [1/2 \times 1 - (-1/2) \times 1)] \times 1.4\,\mathrm{MHz}\,(B/1\mathrm{G}) \\ &= 1 \times 1.4\,\mathrm{MHz}\,(B/1\mathrm{G}). \end{aligned} \tag{3.7}$$

Similarly, the Zeeman shift with σ^- polarization of both the carrier and sideband is:

$$\begin{aligned} \varDelta E_{\sigma-} &= [1/2 \times (-1) - (-1/2) \times (-1)] \times 1.4\,\mathrm{MHz}\,(B/1\mathrm{G}) \\ &= -1 \times 1.4\,\mathrm{MHz}\,(B/1\mathrm{G}). \end{aligned} \tag{3.8}$$

Thus, the magnetic field can be determined by measuring the frequency shifts of the Raman transitions.

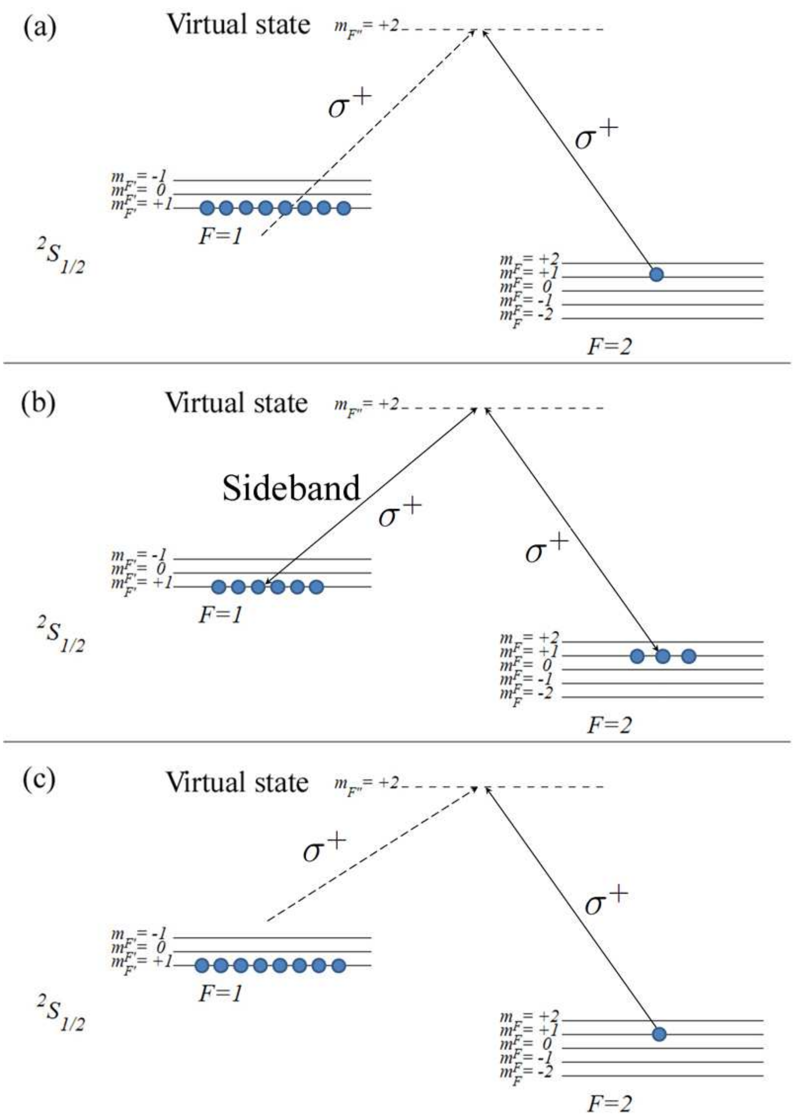

Figure 3.8: Raman transition with the σ^+ polarization of both the carrier and sideband. The energy level differences are not to scale. (a) The sideband frequency is blue detuned. (b) The system reaches a situation of the two-photon resonance. (c) The sideband frequency is red detuned. Bullets of various numbers represent the population distribution in different Zeeman substates. The virtual state has a frequency detuning of $\mathit{\Delta}_c = \mathit{\Delta}_s = \mathit{\Delta}$ from the corresponding atomic resonance, as shown in Figure 3.2.

3.3.2 Raman transitions with the mixture of σ^+, σ^-, and π polarizations

If both the laser carrier and sideband possess a mixture of σ^+, σ^-, and π polarizations, all the ions will be pumped to the Zeeman substates of ${}^2S_{1/2}(F = 1)$ state

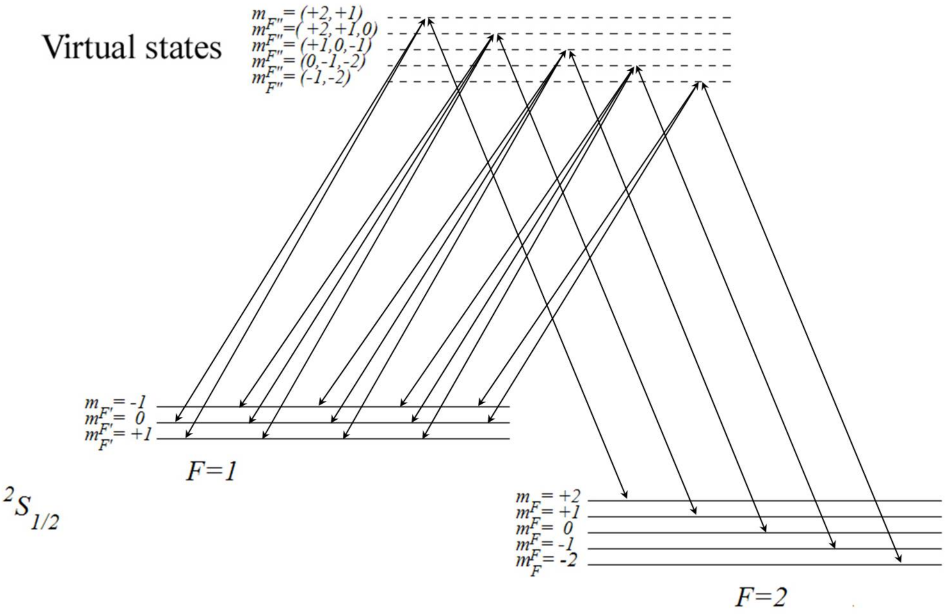

Figure 3.9: Raman transitions with the mixture of σ^+, σ^-, and π polarizations. The energy level differences are not to scale. The virtual states have a detuning of $\Delta_c = \Delta_s = \Delta$ from the corresponding atomic resonances, as shown in Figure 3.2.

after the quantum preparation time. Figure 3.9 shows the corresponding Raman transitions. According to the selection rules of Equation 3.6, the Zeeman shifts in this case are as follows:

$^2S_{1/2}(F = 2,\, m_F = +2) \rightarrow {}^2S_{1/2}(F' = 1,\, m_{F'} = (0,\, +1))$:

$$\begin{aligned} \Delta E_{mix,\, m_F=+2} &= [1/2 \times 2 - (-1/2) \times m_{F'}] \times 1.4\,\mathrm{MHz}\,(B/1\mathrm{G}) \\ &= (1,\, 3/2) \times 1.4\,\mathrm{MHz}\,(B/1\mathrm{G}); \end{aligned} \tag{3.9}$$

$^2S_{1/2}(F = 2,\, m_F = +1) \rightarrow {}^2S_{1/2}(F' = 1,\, m_{F'} = (0,\, \pm 1))$:

$$\begin{aligned} \Delta E_{mix,\, m_F=+1} &= [1/2 \times 1 - (-1/2) \times m_{F'}] \times 1.4\,\mathrm{MHz}\,(B/1\mathrm{G}) \\ &= (0,\, 1/2,\, 1) \times 1.4\,\mathrm{MHz}\,(B/1\mathrm{G}); \end{aligned} \tag{3.10}$$

$^2S_{1/2}(F = 2,\, m_F = 0) \rightarrow {}^2S_{1/2}(F' = 1,\, m_{F'} = (0,\, \pm 1))$:

$$\begin{aligned} \Delta E_{mix,\, m_F=0} &= [1/2 \times 0 - (-1/2) \times m_{F'}] \times 1.4\,\mathrm{MHz}\,(B/1\mathrm{G}) \\ &= (-1/2,\, 0,\, 1/2) \times 1.4\,\mathrm{MHz}\,(B/1\mathrm{G}); \end{aligned} \tag{3.11}$$

$^2S_{1/2}(F = 2,\, m_F = -1) \rightarrow {}^2S_{1/2}(F' = 1,\, m_{F'} = (0,\, \pm 1))$:

$$\begin{aligned} \Delta E_{mix,\, m_F=-1} &= [1/2 \times (-1) - (-1/2) \times m_{F'}] \times 1.4\,\mathrm{MHz}\,(B/1\mathrm{G}) \\ &= (-1,\, -1/2,\, 0) \times 1.4\,\mathrm{MHz}\,(B/1\mathrm{G}); \end{aligned} \tag{3.12}$$

$^2S_{1/2}(F = 2,\, m_F = -2) \rightarrow {}^2S_{1/2}(F' = 1,\, m_{F'} = (0,\, -1))$:

$$\begin{aligned} \Delta E_{mix,\, m_F=-2} &= [1/2 \times (-2) - (-1/2) \times m_{F'}] \times 1.4\,\mathrm{MHz}\,(B/1\mathrm{G}) \\ &= (-3/2,\, -1) \times 1.4\,\mathrm{MHz}\,(B/1\mathrm{G}). \end{aligned} \tag{3.13}$$

Altogether, the possible Zeeman shifts are:

$$\Delta E_{mix} = (-3/2,\, -1,\, -1/2,\, 0,\, 1/2,\, 1,\, 3/2) \times 1.4\,\mathrm{MHz}\,(B/1\mathrm{G}). \tag{3.14}$$

3.4 Raman Spectroscopy of Be$^+$ ions and determination of the magnetic field

To understand the behavior of the Be$^+$ Raman transitions in our experiment, in the initial phase, it is favorable to perform a large number of measurements over a wide frequency range under various conditions. The experimental scheme and procedure are already shown in section 3.1. The laser carrier and sideband are kept circularly polarized in the whole measurements. It is found that the magnetic field in the trap center is close to zero under the following conditions:

$$\begin{aligned} I_X &= I_{X,0} &= 0.93\ \mathrm{A}, \\ I_Y &= I_{Y,0} &= 1.70\ \mathrm{A}, \\ I_Z &= I_{Z,0} &= 0.14\ \mathrm{A}, \end{aligned} \tag{3.15}$$

where the I_X, I_Y, and I_Z represent the currents of X-, Y-, and Z-coils, respectively.

Based on these settings, Raman transitions of beryllium ions are studied by varying the current of only one pair of Helmholtz coils each time. Subsequently, the relations between the magnetic fields and the currents of Helmholtz coils in the respective X-, Y-, and Z-directions are derived from the Raman spectra. Finally, the conditions of the zero magnetic field are found and can be expressed as follows:

$$\begin{aligned} I_X &= I'_{X,0} &= 0.921\ \mathrm{A}, \\ I_Y &= I'_{Y,0} &= 1.681\ \mathrm{A}, \\ I_Z &= I'_{Z,0} &= -0.166\ \mathrm{A}. \end{aligned} \tag{3.16}$$

The detailed procedures of obtaining this result are presented in the following subsections.

3.4.1 Raman spectra of Be$^+$ ions in the near-zero magnetic field

With the settings of Equation 3.15, a spectrum with the frequency range from 1240 MHz to 1260 MHz was obtained, as shown in Figure 3.10. The sweeping step size of the sideband frequency is 8 kHz. It can be seen that only one single peak close to 1250 MHz appears. In case I_X (or I_Y) drifts from $I_{X,0}$ (or $I_{Y,0}$), more than one peak will appear (see Figure 3.12 in subsection 3.4.2) indicating that the Zeeman splitting occurs, while in case I_Z deviates from $I_{Z,0}$, the peak will shift correspondingly with the main profile of the spectrum remaining the same.

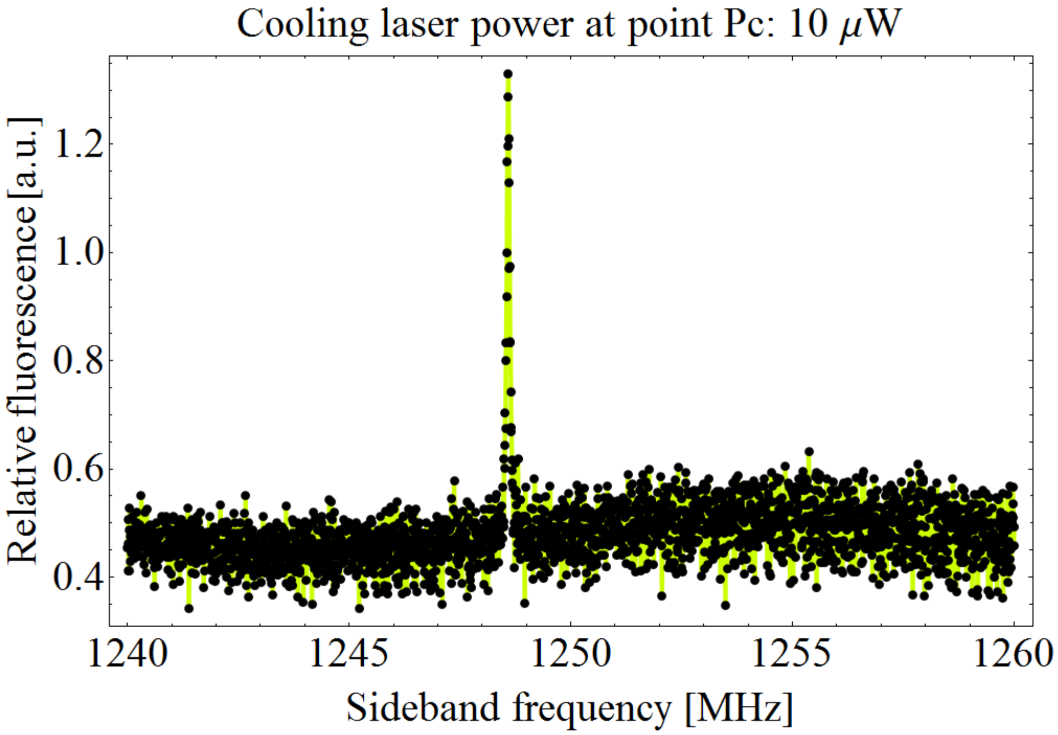

Figure 3.10: Raman spectrum of Be$^+$ ions in the near-zero magnetic field with the laser power of 10 μW. The sweeping step size of the sideband frequency is 8 kHz.

Based on this result, a series of Raman spectra of Be$^+$ ions in the near-zero magnetic field with various cooling laser power levels of 10 μW, 5 μW, and 3 μW were obtained (see Figure 3.11), indicating a strong dependence of the peak's linewidth on the cooling laser power. The lower the laser power is, the narrower the linewidth is. When the laser power is 3 μW, the linewidth is less than 40 kHz. This is a piece of important evidence that the physical process in this situation is not a coherent absorption at the atomic resonance frequency that normally possesses a natural linewidth of around 20 MHz, but a phenomenon of the two-photon resonance with Raman transitions as analyzed in section 3.3. This statement is also supported by the fact of the large detuning of the sideband frequency from resonance.

In addition, it can be seen that the peak experiences a shift towards higher frequency along with the increase of the laser power that is caused by the light pressure. According to Equation 3.7, the local magnetic field gradient is estimated to be 0.04 MHz/(1 × 1.4 MHz/G) = 0.029 G = 29 mG.

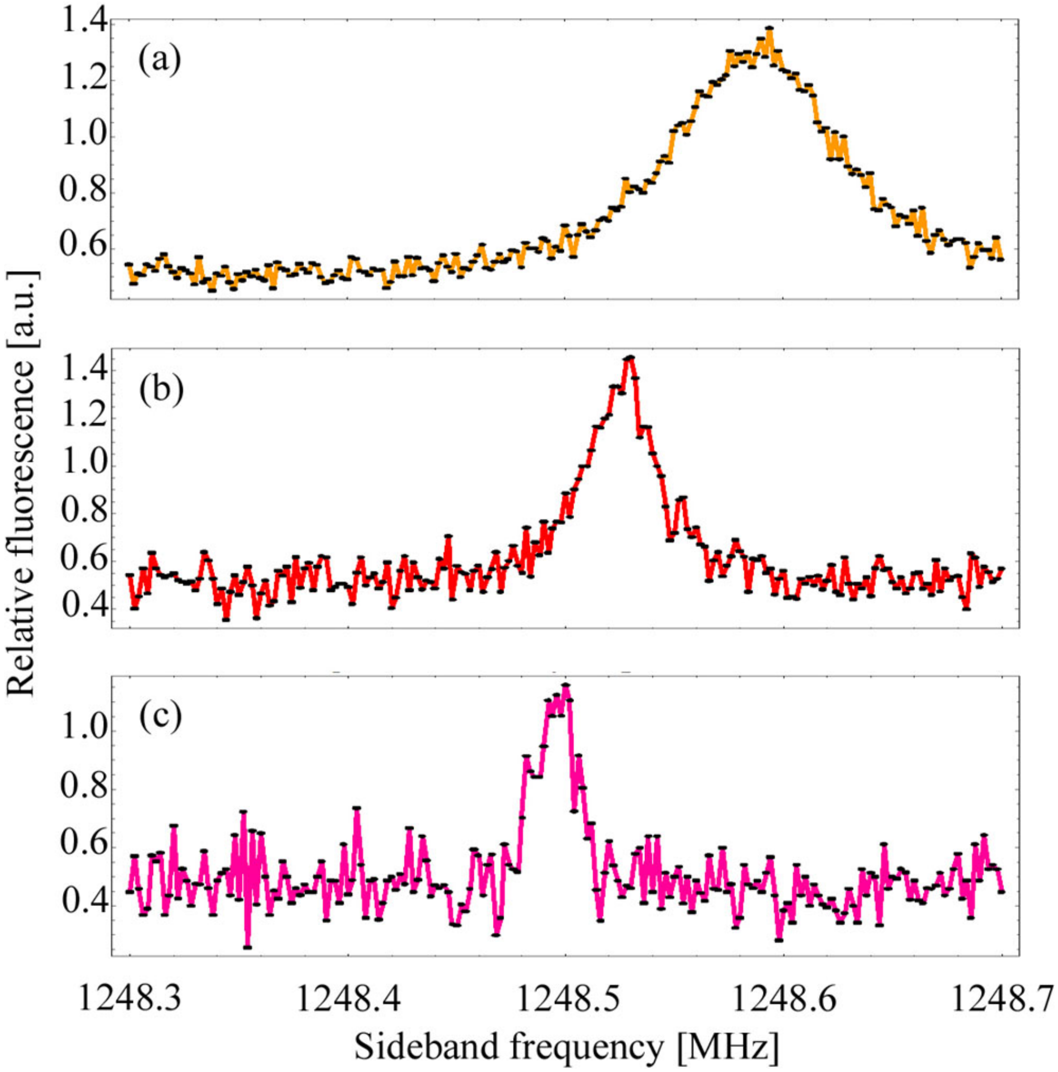

Figure 3.11: Raman spectra of Be$^+$ ions in the near-zero magnetic field with various laser power levels of (a) 10 μW; (b) 5 μW; (c) 3 μW. The sweeping step size of the sideband frequency is 2 kHz to ensure a sufficient frequency resolution.

3.4.2 Variation of the magnetic field along X-direction

In this series of measurements, only the current of X-coils I_X varies, while I_Y and I_Z remain at $I_{Y,0}$ and $I_{Z,0}$, respectively.

When I_X is set to $I_{X,0}$, only one peak appears in the spectrum, as is already shown in Figure 3.10, which implies that there is almost no Zeeman splitting. When I_X is tuned away from $I_{X,0}$, the Zeeman splitting effect occurs. A typical spectrum in this case is shown in Figure 3.12. Each data point with the error bar results from five individual measurements. The transition peaks are marked as “H1”, “L1”, “H2”, “L2”, etc. In order to determine the positions of these peaks precisely, the spectrum is divided into four parts and then fitted mathematically by using either a two-peak Lorentzian profile function or a single-peak Lorentzian profile function (see Figure 3.13 for example).

When I_X varies, the positions of those peaks shift accordingly. The result is shown in Figure 3.14 (top). Each data point comes from four individual spectra. When fitting these data points, the following expression is used:

$$f_X = \; j \cdot \sqrt{B_X^2 + B_Y^2 + B_Z^2} \; + f_{X,\mathit{offset}}. \tag{3.17}$$

Here, j [MHz/G] is the parameter of $(-2.1, -1.4, -0.7, 0, 0.7, 1.4, 2.1)$ MHz/G in Equation 3.14 for H1, L1, H2, L2, H3, L3, and H4, respectively. B_X [G] $= K_X \cdot (I_X - I'_{X,0})$ is the relation between magnetic field in the X-direction and the current of X-coils with a ratio of K_X [G/A], where $I'_{X,0}$ [A] represents the current of X-coils when B_X is zero. B_Y [G] and B_Z [G] stand for the magnetic fields in the Y- and Z-directions, respectively. $f_{X,\mathit{offset}}$ [MHz] is the common frequency offset in X-direction.

Notice that the fitting curves in Figure 3.14 are nearly mirror-imaged, which is not a coincidence. The electric field of the circularly-polarized laser beam has both components parallel and perpendicular to the laser propagation direction. In this case, since both the laser beam and the dominant magnetic field are in the X-direction, the electric field of the laser does not “see” the difference whether the magnetic field direction is reversed. In addition, the magnetic field in the Y-Z plane is calculated as $\sqrt{B_Y^2 + B_Z^2} = 0.755 \pm 0.039$ G, which is reflected by the “waist” of the curves.

By a great number of measurements, it is found that when I_Y and I_Z are tuned to $I'_{Y,0}$ and $I'_{Z,0}$, respectively, the peaks of L1, L2, and L3 disappear and this “waist” of the curves vanishes, indicating that the magnetic fields in the Y- and Z-directions are almost zero (see Figure 3.14 (bottom)).

From the fittings of the curves by using Equation 3.17, the relation between the magnetic field in the X-direction and the current of X-coils was obtained as follows:

$$B_X \;=\; (0.367 \pm 0.002)\,\mathrm{G/A} \times [I_X - (0.921 \pm 0.030)]\,\mathrm{A}\ . \tag{3.18}$$

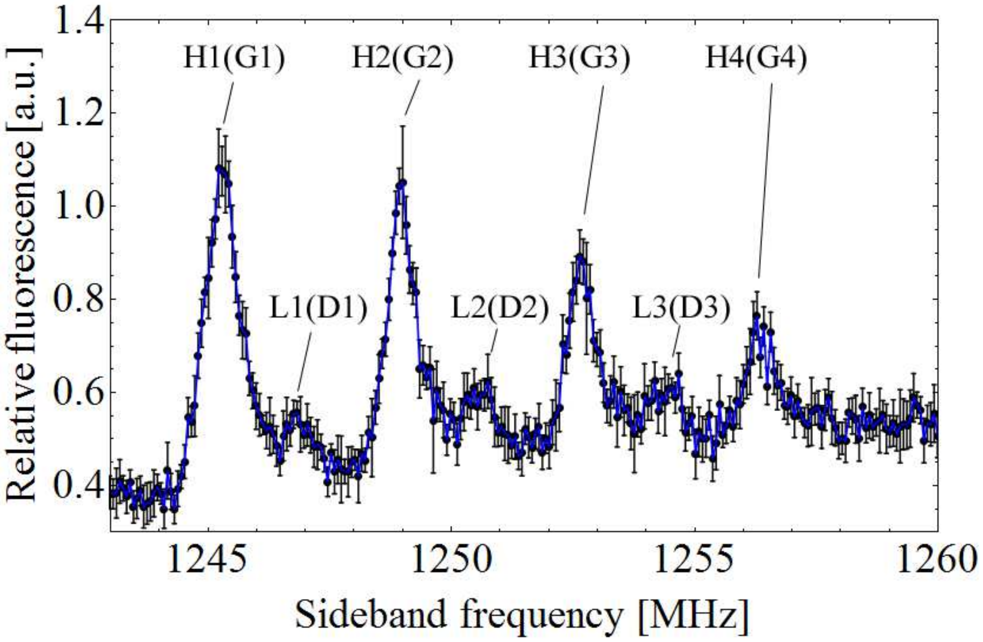

Figure 3.12: Typical Raman spectrum of Be$^+$ ions when I_X (or I_Y) is set away from $I_{X,0}$ (or $I_{Y,0}$) with the laser power of 70 μW [69]. The laser beam is circularly polarized. The peaks are labeled as Hi and Li ($i = 1, 2, 3...$) when the transition frequency shifts with respect to the current of X-coils are studied, and are marked as Gi and Di ($i = 1, 2, 3...$) when the transition frequency shifts with respect to the current of Y-coils are studied.

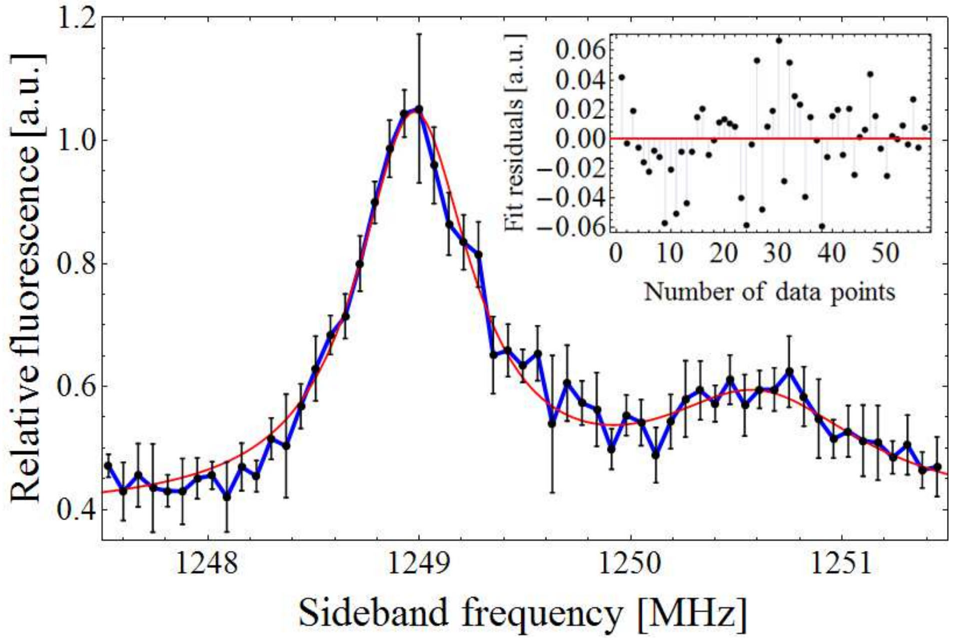

Figure 3.13: Example of a zoomed spectrum from Figure 3.12. The smooth curve in red represents a fit by using a two-peak Lorentzian profile function with the fit residuals shown in the inset.

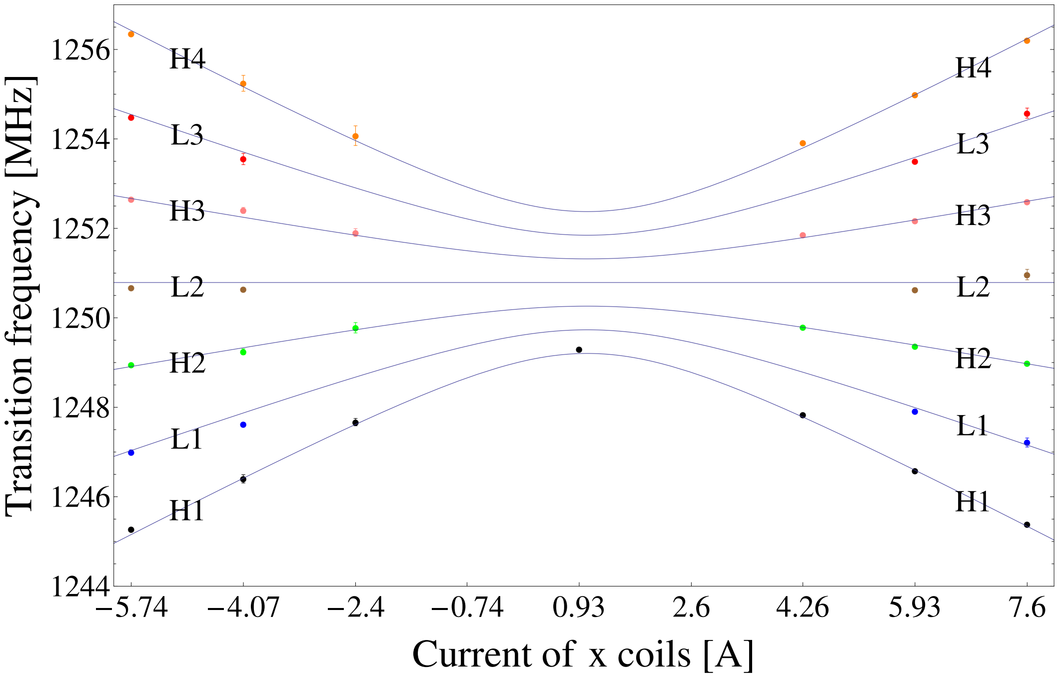

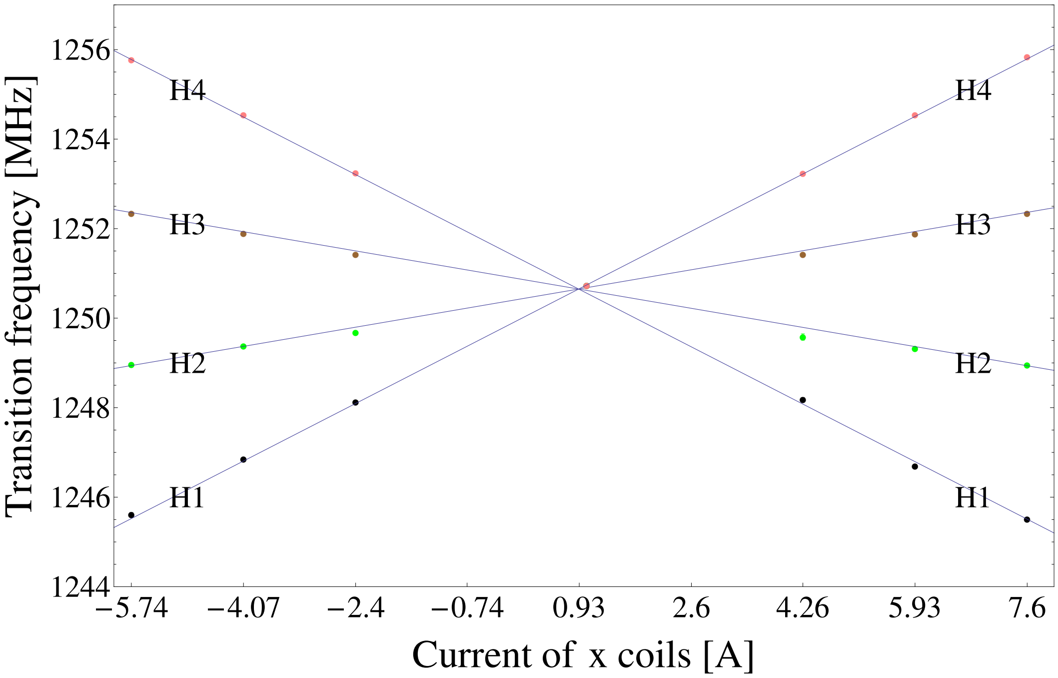

Figure 3.14: Raman transition frequencies as a function of the current of X-coils. Each data point results from four individual spectra. The curves are derived from the global fittings by using the theoretical model of Equation 3.17. Top: I_Y and I_Z are kept at $I_{Y,0}$ and $I_{Z,0}$, respectively. Bottom: I_Y and I_Z remain at $I'_{Y,0}$ and $I'_{Z,0}$, respectively [69].

3.4.3 Variation of the magnetic field along Y-direction

In this series of measurements, only the current of Y-coils I_Y varies, while I_X and I_Z are kept at $I'_{X,0}$ and $I'_{Z,0}$, respectively.

An inspection with a multimeter shows different current values of both ends of the Y-coils, especially when I_Y is higher than 5 A, indicating a current leakage in the Y-coils. Nevertheless, it is found that the leakage problem can be neglected when I_Y is lower than 4 A. In this special case, the I_Y mentioned here is the value measured at the "+" end of the Y-coils.

By using a similar procedure as introduced in subsection 3.4.2, the Raman spectra were obtained when the magnetic field in the Y-direction is varied. A typical spectrum is shown in Figure 3.12 with the corresponding transition peaks denoted in this case as "G1", "D1", "G2", and "D2", etc. Since the variation range of I_Y is relatively short due to the above-mentioned reason, the shifts of those peaks are small. Thus, only the corresponding transition frequency shift of the peak G4 (as shown in Figure 3.15) that has the largest shift among all the peaks is chosen for analysis.

When fitting these data points, the following expression is used:

$$f_Y = \ 2.1 \cdot \sqrt{B_X^2 + B_Y^2 + B_Z^2} \ + f_{Y,offset}, \tag{3.19}$$

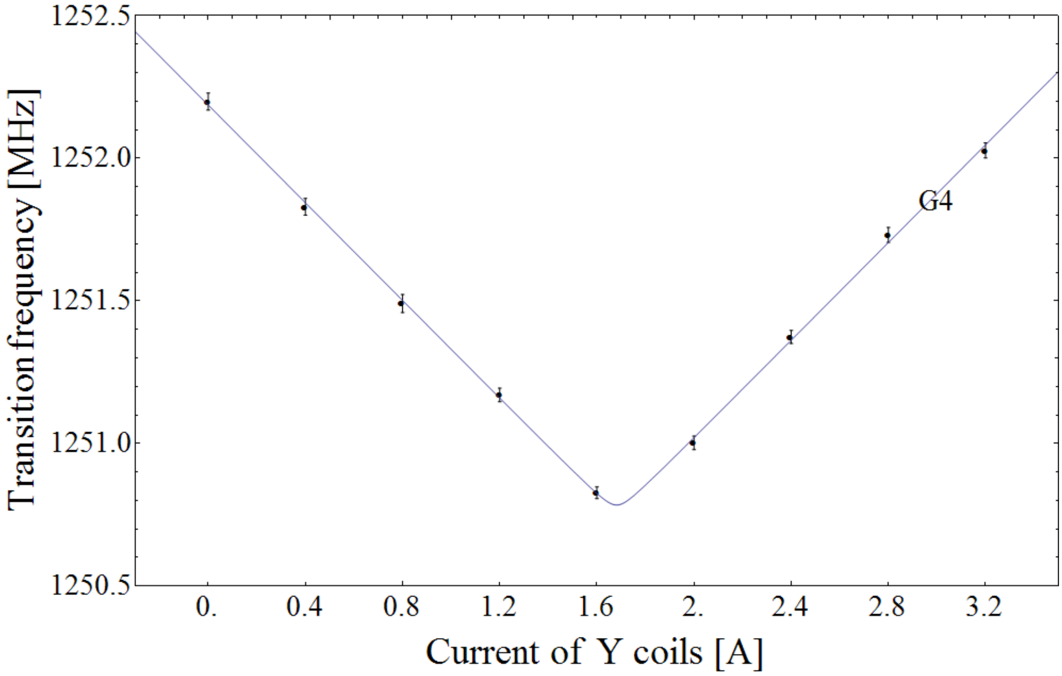

Figure 3.15: Raman transition frequency as a function of the current of Y-coils. Each data point is obtained from four individual spectra.

Here, 2.1 MHz/G is the coefficient of Equation 3.14 for the peak G4. The relation between magnetic field in the Y-direction and the current of Y-coils is $B_Y = K_Y \cdot (I_Y - I'_{Y,0})$ with a ratio of K_Y [G/A].

From the fitting of the curve, the results were obtained as follows:

$$\begin{aligned} B_Y &= (0.408 \pm 0.010)\,\mathrm{G/A} \times [I_Y - (1.681 \pm 0.009)]\,\mathrm{A}, \\ \sqrt{B_X^2 + B_Z^2} &= 0.019 \pm 0.036\ \mathrm{G}. \end{aligned} \tag{3.20}$$

It can be seen that when I_X and I_Z are kept at $I'_{X,0}$ and $I'_{Z,0}$, respectively, the magnetic fields in the X- and Z-directions are almost zero.

3.4.4 Variation of the magnetic field along Z-direction

In this series of measurements, only the current of Z-coils I_Z varies, while I_X and I_Y remain at $I_{X,0}$ and $I_{Y,0}$, respectively. The typical spectrum profile is shown in Figure 3.10 with only one appearing single peak. When the value of I_Z varies, the peak shifts accordingly.

In order to find the conditions of the zero magnetic in the Z-direction, the measurements were performed initially by using the σ^+ polarization of the laser beam and then repeated by using σ^- polarization with the UV laser power set to 70 μW. In both cases, the positions of the peak are recorded, as shown in Figure 3.16 (top). The data points are linearly fitted. The same procedure was repeated by reducing the laser power to a low level of 3 μW with the result shown in Figure 3.16 (bottom).

From both figures, it can be concluded that, with the same laser power, the peak position is independent of laser polarization when I_Z is tuned to -0.172 A (the cross point of the two lines), indicating that the magnetic field in the Z-direction at this point is zero. In addition, it is noticed that the position of this cross point locates always at -0.172 A which is independent of the laser power, and shifts from 1250.907 ± 0.082 MHz to 1250.069 ± 0.022 MHz when the laser power changes from 70 μW to 3 μW due to the light pressure effect.

For a more precise investigation, a repeated measurement in a short range of I_Z was carried out. The laser power is adjusted to 6 μW. I_X and I_Y are set to $I'_{X,0}$ and $I'_{Y,0}$, respectively. The result is shown in Figure 3.17 with the cross point of I_Z at -0.166 A, which is consistent with the value in Figure 3.16.

By using Equation 3.7 and 3.8, the relation between the magnetic field in the Z-direction and the current of Z-coils was derived and can be expressed as follows:

$$B_Z = (3.753 \pm 0.028)\,\mathrm{G/A} \times [I_Z + (0.166 \pm 0.001)]\,\mathrm{A}. \tag{3.21}$$

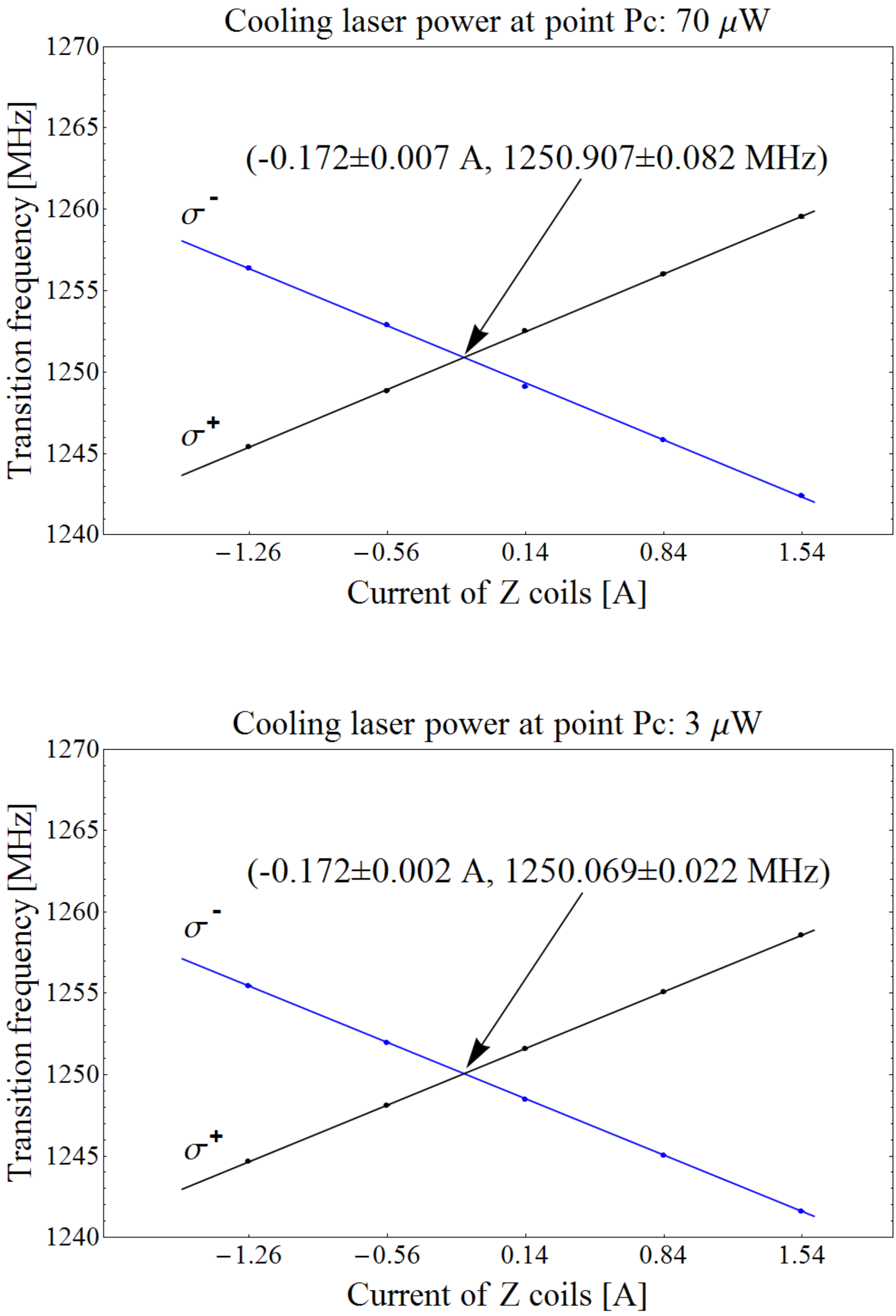

Figure 3.16: Raman transition frequencies as a function of the current of Z-coils with the laser power levels of 70 μW (top) and 3 μW (bottom). Each data point is the average of four individual measurements as shown in Figure 3.10. The measurements were carried out initially by using the σ^+ polarization of the laser beam and then repeated by using σ^- polarization. Data points are fitted linearly. I_X and I_Y are kept at $I_{X,0}$ and $I_{Y,0}$, respectively.

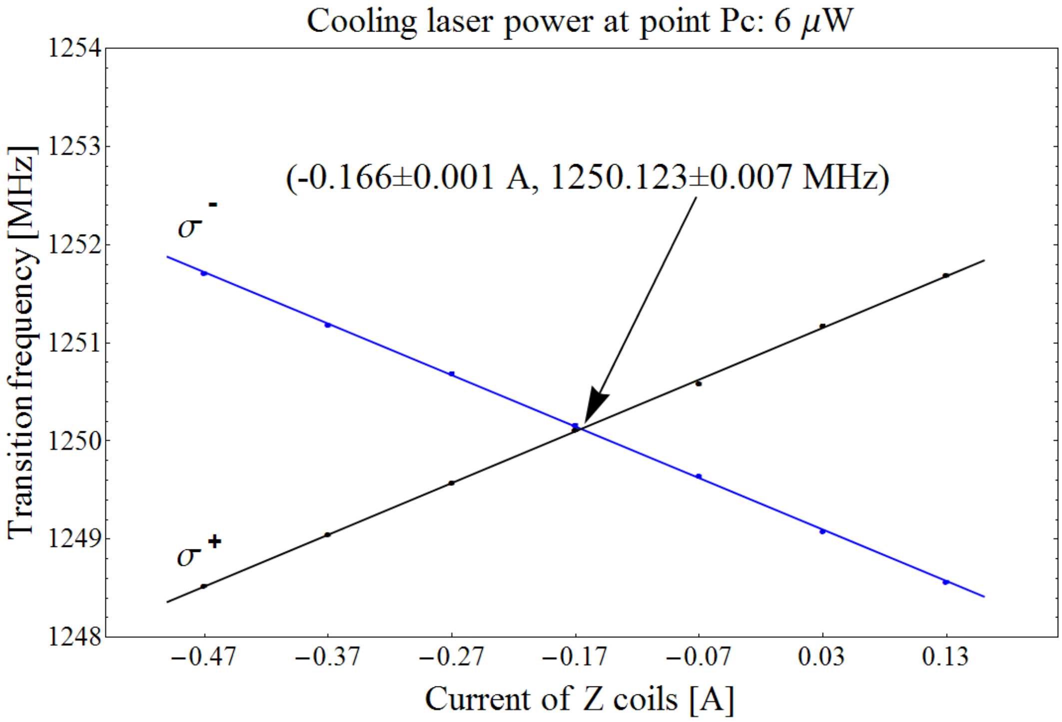

Figure 3.17: Raman transition frequencies as a function of the current of Z-coils (in a short range) with the laser power of 6 μW [69]. I_X and I_Y are kept at $I'_{X,0}$ and $I'_{Y,0}$, respectively. Experimental method and data processing are the same as Figure 3.16.

3.4.5 Transition frequency and FWHM in the zero magnetic field

From the experiments described in the previous subsections, the conditions of zero magnetic field in the trap center (see Equation 3.16) were finally acquired. Under such conditions, by varying the UV laser power, a series of the Raman spectra of Be$^+$ ions were obtained and the profiles near 1250 MHz are presented in Figure 3.18, while the corresponding transition frequency and the full width at half maximum (FWHM) of the peak are summarized in Figure 3.19. A typical Raman spectrum in the zero magnetic field with a wide frequency range is demonstrated in Figure 3.20.

It can be seen that as the laser power increases, the transition frequency shifts linearly towards higher frequency and the FWHM also expands linearly. This phenomenon can be described by the linear susceptibility $\chi^{(1)}$ that is an important parameter to represent the linear response of a particle exposed to an external optical field [73]:

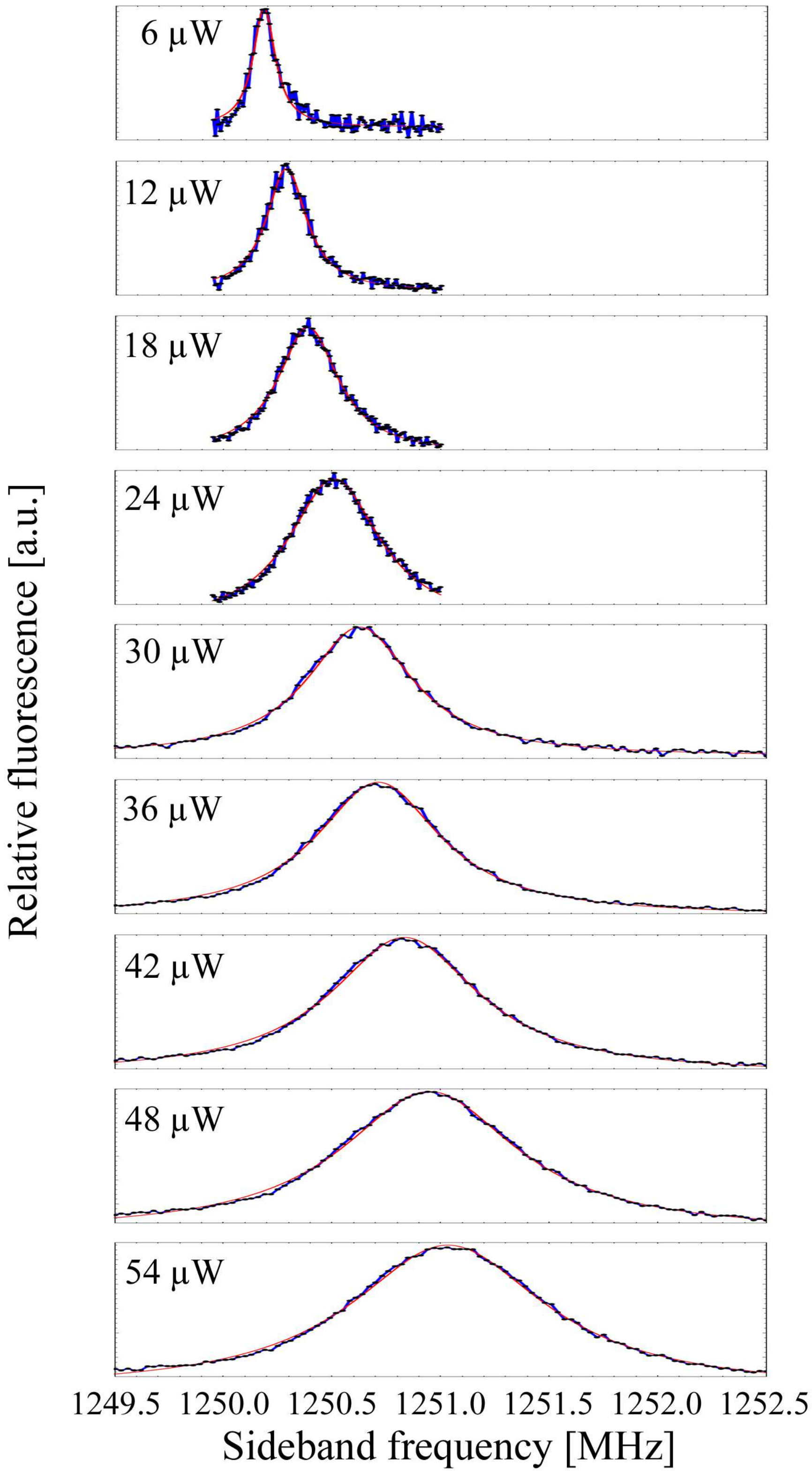

Figure 3.18: Raman spectra of Be$^+$ ions with various laser power levels in the zero magnetic field. Blue: original data; red: Lorentzian fit.

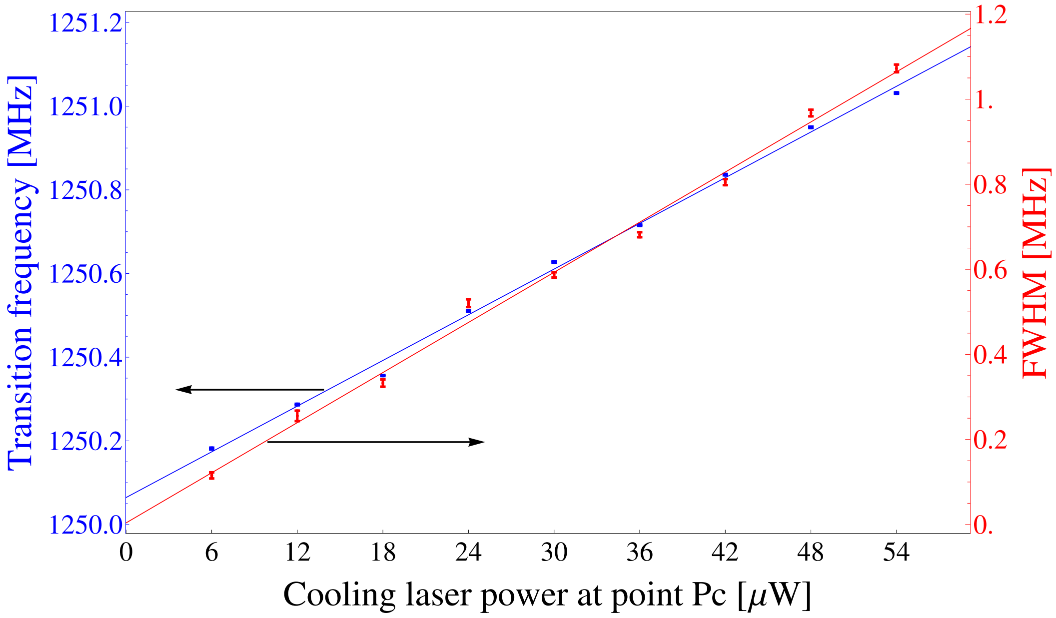

Figure 3.19: Raman transition frequency and FWHM of the peak (corresponding to Figure 3.18) as a function of the cooling laser power in the zero magnetic field. Each data point is the average of four individual measurements [69].

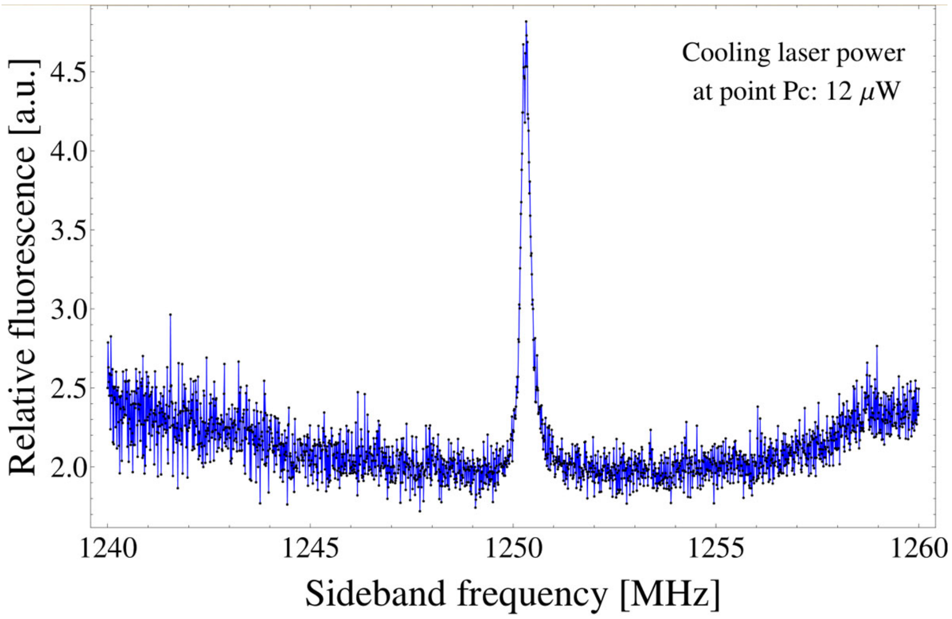

Figure 3.20: Typical Raman spectrum of Be$^+$ ions in the zero magnetic field with a wide frequency range [69].

$$\begin{aligned}\chi^{(1)}(-\omega_s,\omega_s) &= \frac{\mid \mu_{23}\mid^2 \varrho}{\epsilon_0 \hbar} \\ &\times \left[\frac{4\delta(\mid \Omega_c \mid^2 - 4\delta\Delta) - 4\Delta\gamma_{21}^2}{\mid\mid \Omega_c \mid^2 + (\gamma_{32} + i2\Delta)(\gamma_{21} + i2\delta)\mid^2}\right. \\ &\left. + i\frac{8\delta^2\gamma_{32} + 2\gamma_{21}(\mid \Omega_c \mid^2 + \gamma_{21}\gamma_{32})}{\mid\mid \Omega_c \mid^2 + (\gamma_{32} + i2\Delta)(\gamma_{21} + i2\delta)\mid^2}\right].\end{aligned} \tag{3.22}$$

Here, ω_s is the frequency of the repumping laser wave that is already introduced in Figure 3.2. μ_{23} is the transition electronic dipole moment between energy levels $|2\rangle$ and $|3\rangle$. ϱ is the particle density. ϵ_0 is the permittivity. $\hbar$ is the reduced Planck's constant. $\Omega_c = \mu_{13} \cdot E_c/\hbar$ is Rabi frequency of the laser carrier with μ_{13} being the transition electronic dipole moment between energy levels $|1\rangle$ and $|3\rangle$, and E_c being the amplitude of the electric field. $\delta = \Delta_s - \Delta_c$ is the two-photon detuning, while $\Delta = \Delta_s = \omega_{32} - \omega_s$ is the single-photon detuning with γ_{21} and γ_{32} being the corresponding coherence decay rates.

Equation 3.22 reveals both the real and imaginary part of the linear susceptibility. Its real part stands for the refractive index, while its imaginary part governs the dissipation and absorption of the field. Under the condition of $\gamma_{21} \ll \gamma_{32}$, the peak transition frequency and the linewidth can be derived as follows:

$$\delta = \frac{\Omega_c^2}{4\Delta}, \tag{3.23}$$

$$\mathrm{FWHM} = \frac{\gamma_{32}\Omega_c^2}{\gamma_{32}^2 - 4\Delta^2}, \tag{3.24}$$

which show clearly that both the transition frequency and the FWHM are proportional to the term Ω_c^2, i.e. the power of laser carrier that occupies more than 90% of the total laser power in this spectroscopic work. Thus, the almost linearly pressure-induced frequency shift and line broadening are explained.

From Figure 3.19, it can be derived that by the absence of the light pressure, i.e. $\Omega_c = 0$ and $\delta = \Delta_s - \Delta_c = 0$, the transition frequency is 1250.065 ± 0.013 MHz, which represents the splitting frequency in the ground level $^2S_{1/2}$ of Be$^+$ ion. This result agrees well with both the theoretical calculations ($2\times625.08(2)$ MHz when the magnetic moment of the nucleus $\mu(^9\mathrm{Be}) = -1.177432$, and $2\times625.11(3)$ MHz when $\mu(^9\mathrm{Be}) = -1.177492$) by V.A.Yerokhin [74] and the experimental value of $2 \times 625.008837048(10)$ MHz by Wineland *et al* [75].

3.5 Conclusion

The magnetic field determination by measurements of Raman transitions of Be$^+$ ions has been realized. The spectroscopy involved here is treated as a phenomenon of the two-photon resonance process. From the spectra, the relations between the magnetic fields and the currents of Helmholtz coils in the respective X-, Y-, and Z-directions were obtained and can be expressed by:

$$\begin{aligned} B_X = &\ (0.367 \pm 0.002)\,\mathrm{G/A} \times [I_X - (0.921 \pm 0.030)]\,\mathrm{A}, \\ B_Y = &\ (0.408 \pm 0.010)\,\mathrm{G/A} \times [I_Y - (1.681 \pm 0.009)]\,\mathrm{A}, \\ B_Z = &\ (3.753 \pm 0.028)\,\mathrm{G/A} \times [I_Z + (0.166 \pm 0.001)]\,\mathrm{A}, \end{aligned} \tag{3.25}$$

from which, the conditions of the zero magnetic field can be found and are already shown in Equation 3.16.

In this work, the current fluctuation in the Helmholtz coils is in the order of 5 mA, thus the uncertainty of the magnetic field controlling is about 20 mG. In order to reduce the influence from this fluctuation, each measurement of Raman spectroscopy in this work has been repeated at least three times.

Previously, with a magnetic sensor positioned near the trap center after opening the vacuum chamber, an independent measurement of the magnetic field has been executed in our group as well. The results are shown as follows:

$$\begin{aligned} B'_X &= 0.34\ \mathrm{G/A} \times (I_X - 0.68)\ \mathrm{A}, \\ B'_Y &= 0.25\ \mathrm{G/A} \times (I_Y - 1.16)\ \mathrm{A}, \\ B'_Z &= 3.28\ \mathrm{G/A} \times (I_Z + 0.13)\ \mathrm{A}. \end{aligned} \tag{3.26}$$

In principle, the information of the magnetic field from Equation 3.25 and 3.26 are basically in the same order of magnitude. However, locationally, compared with the conventional measurement that strongly depends on the position and orientation of the sensor, the result obtained in this work is intrinsically more precise, since it is derived directly from the Raman spectra of the trapped beryllium ions.

In addition, another advantage of this Raman spectroscopy is the unnecessity of opening the vacuum chamber, which potentially brings pollutants into the vacuum chamber and takes weeks long to pump to the same ultra-high vacuum condition of approx. 2×10^{-11} mbar.

In conclusion, this experiment shows an alternative approach aiming at the determination of the local magnetic field. It provides the information of the present local magnetic field in the trap center, the conditions of zero magnetic field, and the relations between the magnetic fields and the currents of Helmholtz coils in all three dimensions, which is of extreme importance in our group for further experimental spectroscopic studies on other particles in the trap, e.g. HD$^+$ ions.

4 The HD$^+$ molecular ion

In the field of quantum optics, ultracold molecules are attractive systems for high-precision spectroscopy of fundamental constants such as nuclear properties [76], particle mass ratios [32, 77], parity violation in enantiomers [78], QED effects [13], Lorentz invariance [79], and permanent electric dipole moment of the electron [3].

As one of the simplest molecules, the hydrogen ion HD$^+$ possesses electric dipole-allowed rotational transitions, which makes it different from its isotopomers H$_2^+$ and D$_2^+$. It is thus of fundamental importance and has been chosen for spectroscopic measurements in this work.

Theoretical description of this ion has been well developed previously [80]. Based on the calculations of non-relativistic energies, the relativistic and radiative corrections were reported by Korobov [30] which are important steps towards high-precision rovibrational states calculations. This chapter presents the basic molecular theory that could be applied to HD$^+$ molecular ion for spectroscopic purposes.

4.1 Quantum numbers

As shown in Figure 4.1, the HD$^+$ molecular ion consists of only a deuteron (d), a proton (p), and a single electron (e). Due to the shifted center of mass, it possesses a permanent electric dipole moment and is thus a good test system for fundamental physics and molecular quantum mechanics.

The coupling scheme of the angular momenta in HD$^+$ is visualized in Figure 4.2 and is given by [38, 81]:

$$\mathbf{F} = \mathbf{I}_p + \mathbf{s}_e, \qquad \mathbf{S} = \mathbf{F} + \mathbf{I}_d, \qquad \mathbf{J} = \mathbf{L} + \mathbf{S}, \tag{4.1}$$

where $\mathbf{I}_p$, $\mathbf{s}_e$, and $\mathbf{I}_d$ denote the spin of the proton, electron, and deuteron, respectively. $\mathbf{F}$ is the sum of proton and electron spin. $\mathbf{S}$ is the total spin. $\mathbf{L}$ stands for the rotational angular momentum. In the situation of the zero magnetic field, the molecular total angular momentum $\mathbf{J}$ and its projection in z-axis J_z are preferable quantum numbers. Thus, an energy eigenstate of HD$^+$ is noted by $|L\ F\ S\ J\ J_z\rangle$.

This type of coupling scheme is fulfilled in the $1s\sigma_g$ ground level of the molecular hydrogen ion, which will be shown in Figure 4.3 in the next section. It is worthy to mention that for high rotational angular momentum **L**, the **LS** coupling scheme breaks due to the strong electron-spin-orbit coupling.

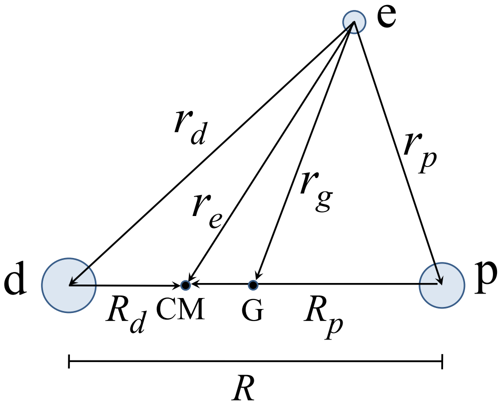

Figure 4.1: Coordinates of the molecular hydrogen ion HD$^+$ with a center-of-mass frame. m_d, m_p, and m_e denote the mass of deuteron (d), proton (p), and electron (e), respectively. P_d, P_p, and P_e stand for the momenta. $r_d = r_e - R_d$, $r_p = r_e - R_p$, and $R = R_p - R_d$, where R_d, R_p, and r_e are the coordinates with respect to the center of mass (CM). r_g is the electron coordinate regarding the geometrical center (G). $Z_d = Z_p = 1$ are the nuclear charges [38]. All the notations mentioned here will be used throughout this whole chapter.

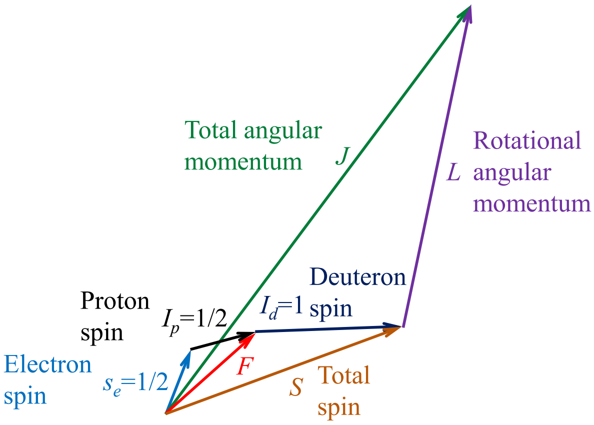

Figure 4.2: Coupling scheme of the angular momenta [38].

4.2 Potential energy curves of HD$^+$ molecular ion

The energy levels of the molecular hydrogen ion could be obtained by solving the time-independent Schrödinger equation [40]. The nuclear and electronic motions are then separated from which the electronic potential energy curves and the separated electronic states are calculated.

The complete time-independent non-relativistic Hamiltonian Schrödinger equation is given by:

$$\left[-\hbar^2\left(\frac{\nabla_g^2}{2m_e}+\frac{\nabla_R^2}{2\mu}+\frac{\nabla_g^2}{8\mu}+\frac{\nabla_g\cdot\nabla_R}{2\mu_a}\right)+V\right]\Psi(r_g;R)=E\Psi(r_g;R), \tag{4.2}$$

where

$$V=\frac{e^2}{4\pi\varepsilon_0}\left(\frac{1}{R}-\frac{1}{r_p}-\frac{1}{r_d}\right), \tag{4.3}$$

$$\frac{1}{\mu}=\frac{1}{m_d}+\frac{1}{m_p}, \tag{4.4}$$

$$\frac{1}{\mu_a}=\frac{1}{m_d}-\frac{1}{m_p}. \tag{4.5}$$

The Hamiltonian may be written in the following form:

$$\mathcal{H}=\mathcal{H}_{\mathrm{BO}}+\mathcal{H}_{\mathrm{ad}}+\mathcal{H}_{\mathrm{gu}}, \tag{4.6}$$

where the items of $\mathcal{H}_{\mathrm{BO}}$, $\mathcal{H}_{\mathrm{ad}}$, and $\mathcal{H}_{\mathrm{gu}}$ represent the contributions from Born-Oppenheimer approach, adiabatic and non-adiabatic approach, respectively, which can be expressed as:

$$\mathcal{H}_{\mathrm{BO}}=\frac{-\hbar^2\nabla_g^2}{2m_e}+V, \tag{4.7}$$

$$\mathcal{H}_{\mathrm{ad}}=-\hbar^2\left(\frac{\nabla_g^2}{8\mu}+\frac{\nabla_R^2}{2\mu}\right), \tag{4.8}$$

$$\mathcal{H}_{\mathrm{gu}}=\frac{-\hbar^2\nabla_g\cdot\nabla_R}{2\mu_a}. \tag{4.9}$$

In order to simplify the solution, the Born-Oppenheimer approximation is applied, leading to the so-called Born-Oppenheimer problem as follows:

$$\mathcal{H}_{\mathrm{BO}}\phi_t(r_g;R) = E_t(R)\phi_t(r_g;R), \tag{4.10}$$

where the energy eigenvalue $E_t(R)$ could be specified by any given internuclear distance R. Thus, the electronic potential energy curve $U(R) = E_t(R)$ as shown in Figure 4.3 is obtained, where any interaction between electron and nuclear is neglected.

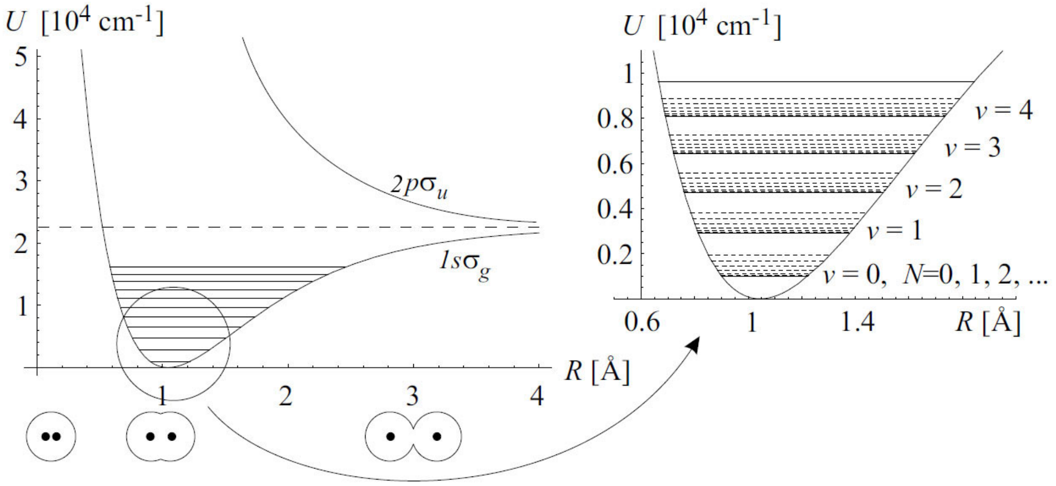

Figure 4.3: Born-Oppenheimer potential energy curves as a function of the internuclear distance R of the HD$^+$ molecular ion. The enlargement of the electronic ground level shows the rovibrational states [40].

To describe the nuclear motion, the radial Schrödinger equation by using the potential term $U(R)$ is:

$$\left[-\frac{d^2}{dR^2} + \frac{2\mu}{\hbar^2}\left(U(R) - E_{v,L}\right) + \frac{L(L+1)}{R^2}\right]\chi_{v,L}(R) = 0, \tag{4.11}$$

where $E_{v,L}$ and $\chi_{v,L}(R)$ stand for the rovibrational eigenenergies and eigenstates, respectively. The parameters v and L are the vibrational and rotational quantum numbers, respectively.

In order to determine the rovibrational energy levels, a model in which the vibrational motion as in an anharmonic potential, the rotational motion as a rigid rotator is applied. Thus, Equation 4.11 is transformed to the following equation:

$$\begin{aligned}\frac{E_{v,L}}{hc} &= \overline{\nu}_e\left(v+\frac{1}{2}\right) - x_e\overline{\nu}_e\left(v+\frac{1}{2}\right)^2 \\ &\quad + B_e L(L+1) - \alpha_e\left(v+\frac{1}{2}\right)L(L+1),\end{aligned} \tag{4.12}$$

where the parameters are given as follows: the harmonic potential frequency $\overline{\nu}_e = 1995\ \mathrm{cm}^{-1}$, the potential anharmonicity $x_e = 0.022$, the rotation constant $B_e = 23\ \mathrm{cm}^{-1}$, and the rovibrational coupling constant $\alpha_e = 0.93\ \mathrm{cm}^{-1}$. The solution of Equation 4.12 is shown in the enlargement of Figure 4.3.

The Born-Oppenheimer approach is a first-order approximation in solving the three-body problem. It is based on the assumption that the electron moves much faster than the nuclei due to the much smaller mass, and can therefore follow the motion of nuclear quasi-instantaneously. The next level of approximation is by using the adiabatic approach, which is based on the response of the nuclei to the instantaneous motion of the electron. This results in the uniformity maintenance of the molecular center of mass motion. The non-adiabatic approach is based on various preconditions as the electron follows the nuclei: for the heavy nuclei, the electron can follow almost completely, while for the light nuclei, such following has a certain delay, which is included in the treatment. More details of the theoretical work have been well reviewed in Refs. [33, 40, 80].

4.3 Relativistic and radiative corrections

4.3.1 Leading-order relativistic corrections

The Breit-Pauli Hamiltonian is used to describe the leading-order relativistic corrections ($R_\infty\alpha^2$) [30, 38].

The major contribution of the bound electron is:

$$E^{(2)}_{\mathrm{rc}} = \alpha^2 \left\langle -\frac{p_e^4}{8m_e^3} + \frac{4\pi}{8m_e^2}\left[Z_d\delta(r_d) + Z_p\delta(r_p)\right] \right\rangle . \tag{4.13}$$

By taking the finite mass of nuclei into account, the additional correction can be expressed as follows:

$$\begin{aligned} E^{(2)}_{\text{tr-ph}} \quad = \quad & \frac{\alpha^2 Z_d}{2m_e m_d}\left\langle \frac{p_e P_d}{r_d} + \frac{r_d(r_d p_e)P_d}{r_d^3} \right\rangle \\ & + \frac{\alpha^2 Z_p}{2m_e m_p}\left\langle \frac{p_e P_p}{r_p} + \frac{r_p(r_p p_e)P_p}{r_p^3} \right\rangle \\ & - \frac{\alpha^2 Z_d Z_p}{2m_d m_p}\left\langle \frac{P_d P_p}{R} + \frac{R(RP_d)P_p}{R^3} \right\rangle , \end{aligned} \tag{4.14}$$

which is called recoil correction. Note that the first term of Equation 4.14 is called transverse photon exchange, and the last term has a contribution of about 10% to $E^{(2)}_{\text{tr-ph}}$ that is not ignorable for further consideration.

For heavy particles, the expression of the relativistic kinetic energy contribution is:

$$E_{\mathrm{kin}}^{(2)} = -\alpha^2 \left\langle \frac{P_d^4}{8m_d^3} + \frac{P_p^4}{8m_p^3} \right\rangle . \tag{4.15}$$

The further contribution of the order $(R_\infty \alpha^2)$ can be expressed by:

$$E_{\mathrm{Darwin}}^{(2)} = \frac{\alpha^2 4\pi Z_p}{8m_p^2} \left\langle \delta(r_p) \right\rangle , \tag{4.16}$$

where the nuclear spin of the proton $(I_p = 1/2)$ has to be taken into account, whereas the term of deuteron $(I_d = 1)$ vanishes.

The final contribution that should be considered is called the leading-order electric charge finite-size correction, which is given (both for proton and deuteron) by:

$$E_{\mathrm{nuc}}^{(2)} = \sum_{i=d,p} \frac{2\pi Z_i (R_i/a_0)^2}{3} \left\langle \delta(r_i) \right\rangle , \tag{4.17}$$

where the R_i stands for the root-mean-square (rms) radius of nuclear electric charge distribution, which is related with the internal structure of the complex particles.

Thus, the total expression described by the Breit-Pauli Hamiltonian can be characterized as follows:

$$E_{\alpha^2} = E_{\mathrm{rc}}^{(2)} + E_{\text{tr-ph}}^{(2)} + E_{\mathrm{kin}}^{(2)} + E_{\mathrm{Darwin}}^{(2)} + E_{\mathrm{nuc}}^{(2)} . \tag{4.18}$$

4.3.2 Leading-order radiative corrections

To describe the radiative corrections of the order $(R_\infty \alpha^3)$ for a one electron molecular system, the contributions in different terms that are similar with Equation 4.18 are presented in this subsection, where only the spin-independent part is considered [30, 38].

The contribution from the one-loop self-energy correction is given by:

$$E_{\mathrm{se}}^{(3)} = \frac{4\alpha^3}{3m_e^3} \left(\ln \frac{1}{\alpha^2} - \beta(L, v) + \frac{5}{6} - \frac{3}{8} \right) \left\langle Z_d \delta(r_d) + Z_p \delta(r_p) \right\rangle , \tag{4.19}$$

where the Bethe logarithm is:

$$\beta(L, v) = \frac{\left\langle \mathbf{J}(H_0 - E_0) \ln \left[(H_0 - E_0)/R_\infty \right] \mathbf{J} \right\rangle}{\left\langle \left[\mathbf{J}, \left[H_0, \mathbf{J} \right] \right] / 2 \right\rangle} , \tag{4.20}$$

which includes the most difficult numerical problems in calculation of QED corrections considering the three-body bound states. The operator $\mathbf{J} = \Sigma_a z_a \mathbf{p}_a/m_a$ in Equation 4.20 is called the electric current density operator.

The contribution from the anomalous magnetic moment of the order $(R_\infty \alpha^3)$ is:

$$E^{(3)}_{\text{anom}} = \frac{\pi\alpha^2}{m_e^2}\left[\frac{1}{2}\left(\frac{\alpha}{\pi}\right)\right]\langle Z_d\delta(r_d) + Z_p\delta(r_p)\rangle\,. \tag{4.21}$$

The contribution from the one-loop vacuum polarization of the order $(R_\infty\alpha^3)$ can be expressed by:

$$E^{(3)}_{\text{vp}} = \frac{4\alpha^3}{3m_e^2}\left(-\frac{1}{5}\right)\langle Z_d\delta(r_d) + Z_p\delta(r_p)\rangle\,. \tag{4.22}$$

The final contribution is from the one transverse photon exchange, which is given by:

$$E^{(3)}_{\text{tr-ph}} = \alpha^3\sum_{i=d,p}\left[\frac{2Z_i^2}{3m_e m_i}\left(-\ln\alpha - 4\beta(L,v) + \frac{31}{3}\right)\langle\delta(r_i)\rangle - \frac{14Z_i^2}{3m_e m_i}Q(r_i)\right], \tag{4.23}$$

where the $Q(r)$ term is:

$$Q(r) = \lim_{\rho\to 0}\left\langle\frac{\Theta(r-p)}{4\pi r^3} + (\ln\rho + \gamma_E)\delta(\mathbf{r})\right\rangle, \tag{4.24}$$

which was introduced by Araki [82] and Sucher [83].

Thus, the total expression to describe the radiative corrections of the order $(R_\infty\alpha^3)$ is:

$$E_{\alpha^3} = E^{(3)}_{\text{se}} + E^{(3)}_{\text{anom}} + E^{(3)}_{\text{vp}} + E^{(3)}_{\text{tr-ph}}. \tag{4.25}$$

Higher-order relativistic corrections of the order $(R_\infty\alpha^4 \sim m_e c^2\alpha^6)$ and radiative corrections of the order $(R_\infty\alpha^5)$ for H_2^+ and HD^+ can be found in [31].

4.4 Spin-interaction Hamiltonian

For the energy stages $L \leq 4$ and $v \leq 4$ of the molecular hydrogen ion, a precision of 1 kHz has been achieved by using the leading-order relativistic and radiative corrections that are already introduced in the previous section. The next important calculation is the hyperfine states of the ion. So far, this calculation has been performed by using the adiabatic [84] and two-state adiabatic [85] approaches in which the electron-nuclear spin-spin and the electron-spin-rotation interactions are included. The theoretical calculations were in agreement with the experimental spectroscopic studies on cold HD$^+$ ions [29, 33], however, there was a slight disagreement when comparing the approximate theory with the precise RF measurement [33] leading to a further improvement of the theory by using a complete spin-dependent Breit-Pauli Hamiltonian [81].

Taking the electromagnetic interaction of its constituents into account, the spectrum of the HD$^+$ molecular ion has been calculated by using a Hamiltonian with the following form:

$$H = H^{NR} + V^{sh} + V^{spin}, \tag{4.26}$$

where H^{NR} represents the non-relativistic three-body Hamiltonian, while the correction term V^{sh} describes the contribution of the spin-independent interaction that has been calculated up to an order of $m\alpha^6$ by using the relativistic and radiative corrections and up to $m\alpha^7$ by introducing some most important terms with a relative accuracy of 3×10^{-10}, respectively [30, 31]. The other contribution V^{spin} stands for the spin-interaction Hamiltonian and can be expressed as:

$$V^{spin} = V_{ep} + V_{ed} + V_{pd}, \tag{4.27}$$

where V_{ep}, V_{ed}, and V_{pd} represent the electron-proton, electron-deuteron, and proton-deuteron interactions, respectively. Their expressions are given as follows:

$$\begin{aligned} V_{ep} \;=\; \alpha^2 \Bigg\{ & \frac{1+2\kappa_e}{2m_e^2} \frac{(\mathbf{r}_p \times \mathbf{p}_e)\,\mathbf{s}_e}{r_p^3} - \frac{1+\kappa_e}{m_e m_p} \frac{(\mathbf{r}_p \times \mathbf{P}_p)\,\mathbf{s}_e}{r_p^3} \\ & - \frac{2\mu_p - 1}{2m_p^2} \frac{(\mathbf{r}_p \times \mathbf{P}_p)\,\mathbf{I}_p}{r_p^3} \\ & + \frac{\mu_p}{m_e m_p} \frac{(\mathbf{r}_p \times \mathbf{p}_e)\,\mathbf{I}_p}{r_p^3} - \frac{8\pi}{3} \frac{\mu_e \mu_p}{m_e m_p} \delta(\mathbf{r}_p)\,(\mathbf{s}_e \cdot \mathbf{I}_p) \\ & + \frac{\mu_e \mu_p}{m_e m_p} \frac{r_p^2\,(\mathbf{s}_e \cdot \mathbf{I}_p) - 3\,(\mathbf{r}_p \cdot \mathbf{s}_e)\,(\mathbf{r}_p \cdot \mathbf{I}_p)}{r_p^5} \Bigg\}, \end{aligned} \tag{4.28}$$

$$\begin{aligned} V_{ed} = \alpha^2 \Bigg\{ & \frac{1+2\kappa_e}{2m_e^2} \frac{(\mathbf{r}_d \times \mathbf{p}_e)\, \mathbf{s}_e}{r_d^3} - \frac{1+\kappa_e}{m_e m_d} \frac{(\mathbf{r}_d \times \mathbf{P}_d)\, \mathbf{s}_e}{r_d^3} \\ & - \frac{1}{m_d} \left[\frac{\mu_d}{2m_p} - \frac{1}{2m_d} \right] \frac{(\mathbf{r}_d \times \mathbf{P}_d)\, \mathbf{I}_d}{r_d^3} + \frac{\mu_d}{2m_e m_p} \frac{(\mathbf{r}_d \times \mathbf{p}_e)\, \mathbf{I}_d}{r_d^3} \\ & - \frac{4\pi}{3} \frac{\mu_e \mu_d}{m_e m_p} \delta(\mathbf{r}_d)\, (\mathbf{s}_e \cdot \mathbf{I}_d) \\ & + \frac{\mu_e \mu_d}{2m_e m_p} \frac{r_d^2\, (\mathbf{s}_e \cdot \mathbf{I}_p) - 3\, (\mathbf{r}_d \cdot \mathbf{s}_e)\, (\mathbf{r}_d \cdot \mathbf{I}_d)}{r_d^5} \Bigg\} \\ & + \frac{Q_d}{2} \frac{r_d^2 \mathbf{I}_d^2 - 3\, (\mathbf{r}_d \cdot \mathbf{I}_d)^2}{r_d^5}, \end{aligned} \tag{4.29}$$

$$\begin{aligned} V_{pd} = \alpha^2 \Bigg\{ & -\frac{2\mu_p - 1}{2m_p^2} \frac{[\mathbf{R} \times \mathbf{P}_p]\, \mathbf{I}_p}{R^3} + \frac{\mu_p}{m_p m_d} \frac{[\mathbf{R} \times \mathbf{P}_d]\, \mathbf{I}_p}{R^3} \\ & + \frac{1}{m_d} \left[\frac{\mu_d}{2m_p} - \frac{1}{2m_d} \right] \frac{[\mathbf{R} \times \mathbf{P}_d]\, \mathbf{I}_p}{R^3} - \frac{\mu_d}{2m_p^2} \frac{[\mathbf{R} \times \mathbf{P}_p]\, \mathbf{I}_d}{R^3} \\ & - \frac{4\pi}{3} \frac{\mu_p \mu_d}{m_p^2} \delta(\mathbf{R})\, (\mathbf{I}_d \cdot \mathbf{I}_p) \\ & + \frac{\mu_p \mu_d}{2m_p^2} \frac{R^2\, (\mathbf{I}_d \cdot \mathbf{I}_p) - 3\, (\mathbf{R} \cdot \mathbf{I}_d)\, (\mathbf{R} \cdot \mathbf{I}_p)}{R^5} \Bigg\} \\ & - \frac{Q_d}{2} \frac{R^2 \mathbf{I}_d^2 - 3\, (\mathbf{R} \cdot \mathbf{I}_d)^2}{R^5}, \end{aligned} \tag{4.30}$$

where the notations $\mathbf{R}_d$, $\mathbf{R}_p$, and $\mathbf{r}_e$ are the coordinates of deuteron, proton, and electron in the frame of center-of-mass, respectively, with $\mathbf{r}_d = \mathbf{r}_e - \mathbf{R}_d$, $\mathbf{r}_p = \mathbf{r}_e - \mathbf{R}_p$, and $\mathbf{R} = \mathbf{R}_p - \mathbf{R}_d$. The notations $\mathbf{I}_d$, $\mathbf{I}_p$, and $\mathbf{s}_e$ are the spins, while $\mathbf{P}_d$, $\mathbf{P}_p$, and $\mathbf{p}_e$ are the momenta, respectively. $\mu_e = -(1+\kappa_e)$ stands for the magnetic moment of an electron in Bohr magnetons, μ_p and μ_d represent the magnetic moments of proton and deuteron in the nuclear magnetons, and the notation Q_d is the quadrupole moment of deuteron. Here, the nuclear spin-spin contact interaction is tiny and thus negligible.

The effective spin Hamiltonian is derived from the average of Equation 4.28, 4.29, and 4.30 over spatial degrees of freedom:

$$\begin{aligned} H_{\mathit{eff}}^{\mathit{hfs}} &= E_1(\mathbf{L}\cdot\mathbf{s}_e)+E_2(\mathbf{L}\cdot\mathbf{I}_p)+E_3(\mathbf{L}\cdot\mathbf{I}_d)+E_4(\mathbf{I}_p\cdot\mathbf{s}_e)+E_5(\mathbf{I}_d\cdot\mathbf{s}_e)\\ &\quad +E_6\left\{2\mathbf{L}^2(\mathbf{I}_p\cdot\mathbf{s}_e)-3\left[(\mathbf{L}\cdot\mathbf{I}_p)(\mathbf{L}\cdot\mathbf{s}_e)+(\mathbf{L}\cdot\mathbf{s}_e)(\mathbf{L}\cdot\mathbf{I}_p)\right]\right\}\\ &\quad +E_7\left\{2\mathbf{L}^2(\mathbf{I}_d\cdot\mathbf{s}_e)-3\left[(\mathbf{L}\cdot\mathbf{I}_d)(\mathbf{L}\cdot\mathbf{s}_e)+(\mathbf{L}\cdot\mathbf{s}_e)(\mathbf{L}\cdot\mathbf{I}_d)\right]\right\}\\ &\quad +E_8\left\{2\mathbf{L}^2(\mathbf{I}_p\cdot\mathbf{I}_d)-3\left[(\mathbf{L}\cdot\mathbf{I}_p)(\mathbf{L}\cdot\mathbf{I}_d)+(\mathbf{L}\cdot\mathbf{I}_d)(\mathbf{L}\cdot\mathbf{I}_p)\right]\right\}\\ &\quad +E_9\left[\mathbf{L}^2\mathbf{I}_d^2-\frac{3}{2}(\mathbf{L}\cdot\mathbf{I}_d)-3(\mathbf{L}\cdot\mathbf{I}_d)^2\right]. \end{aligned} \tag{4.31}$$

By considering the effect of an external magnetic field up to 1 G, which is a typical value in our present ion trap, an improvement of this theory has been reported [86]. The details will be discussed in section 4.6.

4.5 Electric dipole transitions

4.5.1 Selection rules of electric dipole transitions

In respect of spectroscopy in quantum optics, it is crucial to investigate the transitions between various rovibrational levels of particles precisely. In addition, when the particles are cooled sympathetically by other atomic coolants, the cooling of the internal degrees of freedom should also be considered.

The asymmetry of diatomic molecules, e.g. HD$^+$ ions, where the center of charge differs from the center of mass, leads to a permanent electric dipole moment which is independent of the electronic state of the molecule:

$$\mu(R) = Q\frac{m_1-m_2}{m_1+m_2}R, \tag{4.32}$$

where m_1 and m_2 stand for the masses of the isotopes with the electric charge $Q=e$ for both and a distance R from each other.

Compared with homonuclear diatomic molecules with no dipole moment, e.g. H_2^+ and D_2^+, the heteronuclear diatomic molecule HD$^+$ has been chosen for spectroscopy since the corresponding excitation rates are about 8 orders of magnitude higher and the rovibrational decay times are in the range of milliseconds to a few seconds.

Within the same electronic level of HD$^+$, it is allowed only for those electric dipole transitions between the states of different symmetry. For all rotational transitions with $\mathit{\Delta} L=\pm1$, the selection rule of the total angular momentum is:

$$\mathit{\Delta} J = \pm 1. \tag{4.33}$$

While for all vibrational transitions, the selection rule is:

$$\varDelta v = 0, \pm 1, \pm 2, \pm 3, \cdots . \tag{4.34}$$

The fundamental vibrational transition $\varDelta v = \pm 1$ is also allowed in the harmonic approximation of the potential, while the overtones $\varDelta v = \pm 2, \pm 3, \cdots$ result from the anharmonicity of Equation 4.12 with decreased intensities.

4.5.2 Einstein coefficients

When an atom or molecule is exposed to an external radiation, the processes of absorption, spontaneous and stimulated emission of light between two energy levels should be distinguished. To describe the probability of these referred processes, the Einstein coefficients are applied.

Assume n and m are two allowed energy levels of a particle with $E_n > E_m$, the Einstein coefficient A_{nm} is related to the probability per second for the particle participating in a spontaneous decay, while the other Einstein coefficient B_{nm} refers to the probability to experience an absorption process that is proportional to the spectral energy density of the radiation. For stimulated emission, the Einstein coefficient B_{mn} can be applied correspondingly in a similar way. As long as the statistical weights of the levels n and m are identical, B_{mn} can be set as equal as B_{nm}.

The Einstein coefficients between two degenerate states can be expressed in SI units as follows [47]:

$$A_{nm} = \frac{\hbar\omega^3}{\pi^2 c^3} B_{nm} \quad \text{and} \quad B_{nm} = \frac{\pi \left| \vec{M}_{n,m} \right|^2}{3 g_n \varepsilon_0 \hbar^2}. \tag{4.35}$$

Here, the parameter $\vec{M}_{n,m}$ is the transition dipole matrix element of a degenerate state which is given by:

$$\vec{M}_{n_\xi, m_\mu} = \int \psi^*_{n_\xi} \vec{p} \psi_{m_\mu} dr_e dr_c, \tag{4.36}$$

where ψ_{n_ξ} and ψ_{m_μ} are the wave functions for the two states, respectively. Since $\vec{M}_{n_\xi, m_\mu}$ stands for a combined nuclear-electronic transition moment for allowed electronic transitions, the dipole operator $\vec{p}$ can be divided into two parts: an electronic and a nuclear part, with the expression of $\vec{p} = \vec{p}_e + \vec{p}_c$.

In the Born-Oppenheimer approximation, the wave function $\psi_{j,e}\chi_{j,c}$ is used instead of ψ_j, where $\psi_{j,e}$ and $\chi_{j,c}$ are the electronic and nuclear wave functions, respectively. Thus, the transition dipole matrix element can be expressed in another form:

$$\begin{aligned}\vec{M}_{n_\xi,m_\mu} &= \int \chi^*_{n_\xi,c}\left[\int \psi^*_{n_\xi,e}\vec{p}_e\psi_{m_\mu,e}dr_e\right]\chi_{m_\xi,c}dr_c \\ &+ \int \chi^*_{n_\xi,c}\vec{p}_c\left[\int \psi^*_{n_\xi,e}\psi_{m_\mu,e}dr_e\right]\chi_{m_\mu,c}dr_c. \end{aligned} \tag{4.37}$$

The first term in Equation 4.37 will be vanished for pure rovibrational transitions ($\psi_{n_\xi,e} = \psi_{m_\mu,e}$), whereas the second term vanishes for the changes of nuclear position or of electronic state ($\psi_{n_\xi,e} \neq \psi_{m_\mu,e}$).

4.5.3 Rovibrational transitions of HD$^+$

The theoretical calculation of the transition moments $M_{v''L'';v'L'} = \langle v'L'|\,\mu\,|v''L''\rangle$ for the electronic rovibrational dipole transition $|e\rangle = |v'L'\rangle \leftrightarrow |g\rangle = |v''L''\rangle$ of HD$^+$ ion was reported by Colbourn and Bunker [87]. As shown in Table 4.1, the R- and P-branch indicate the rotational transitions of $L' - L'' = +1$ and $L' - L'' = -1$, respectively. The matrix elements in the table are given in a CGS unit of Debye (1 Debye $\approx$ $3.3 \cdot 10^{-30}$ cm $\approx$ 0.2 eÅ).

	$v' = 1 - v'' = 0$		$v' = 2 - v'' = 0$		$v' = 4 - v'' = 0$		$v' = 4 - v'' = 2$	
L''	R	P	R	P	R	P	R	P
0	0.0861		-0.0111		-0.00075		-0.0272	
1	0.0820	0.0943	-0.0109	-0.0113	-0.00076	-0.00073	-0.0267	-0.0279
2	0.0780	0.0986	-0.0108	-0.0114	-0.00076	-0.00072	-0.0262	-0.0282
3	0.0741	0.1028	-0.0106	-0.0115	-0.00077	-0.00071	-0.0257	-0.0285
4	0.0702	0.1071	-0.0104	-0.0116	-0.00077	-0.00069	-0.0251	-0.0287
5		0.1114		-0.0116		-0.00068		-0.0289

Table 4.1: Transition moments $M_{v''L'';v'L'} = \langle v'L'|\,\mu\,|v''L''\rangle$ of the electronic rovibrational dipole transition $|e\rangle = |v'L'\rangle \leftrightarrow |g\rangle = |v''L''\rangle$ of HD$^+$ ion [87].

The radiative relaxation times of rovibrational dipole transitions for the electronic ground level of HD$^+$ ion were computed by Amitay *et al.* in 1994 [88]. The radiative lifetime $\tau_{v'L'}$ of a rovibrational level is:

$$\tau_{v'L'} = \frac{1}{A_{v'L'}}. \tag{4.38}$$

Here, $A_{v'L'}$ represents the total Einstein coefficient and is performed by superimposing all probabilities $A_{v'L';v''L''}$ over all dipole allowed spontaneous transitions between two rovibrational levels $|v'L'\rangle \leftrightarrow |v''L''\rangle$, which can be expressed by:

$$A_{v'L'} = \sum_{v''L''} A_{v'L';v''L''}, \tag{4.39}$$

where the probabilities $A_{v'L';v''L''}$ can be obtained from the given electronic rovibrational dipole transition moments $M_{v'L';v''L''}$ (see Table 4.1) by:

$$A_{v'L';v''L''} = 7.2356 \cdot 10^{-6} \cdot \Delta E^3_{v'L';v''L''} \cdot |M_{v'L';v''L''}|^2 \, . \tag{4.40}$$

Here, the transition probability $A_{v'L';v''L''}$ is in the unit of s^{-1}, the energy difference $\Delta E_{v'L';v''L''}$ in cm^{-1} and $M_{v'L';v''L''}$ in eÅ.

Table 4.2 shows the lifetimes τ_{vL} of some selected rovibrational levels of HD^+ that are relevant for spectroscopy. In contrast to typical dipole transitions in atoms, due to the smaller transition frequency and the weaker transition moments between the rovibrational levels of HD^+, the lifetimes here are substantially longer.

It can be expected that all molecular HD^+ ions to be in the vibrational ground level when the temperature is sufficiently low, according to the fact that the radiative relaxation to the vibrational ground level is on the order of 100 ms. However, the full rotational relaxation of HD^+ is one order of magnitude longer, since their transition frequencies are lower.

	$L=0$	$L=1$	$L=2$	$L=3$	$L=4$	$L=5$
$v=0$		140.24	14.61	4.04	1.64	0.823
$v=1$	0.059	0.059	0.058	0.057	0.055	0.052
$v=2$	0.032	0.032	0.031	0.031	0.031	0.029
$v=3$	0.023	0.023	0.023	0.022	0.022	0.021
$v=4$	0.019	0.019	0.018	0.018	0.018	0.017
$v=5$	0.016	0.016	0.016	0.016	0.015	0.015

Table 4.2: Lifetimes τ_{vL} in seconds of some selected rovibrational levels of HD^+ ion [88].

4.6 Zeeman effect of hyperfine states

To study the transition frequencies more precisely, many systematic effects during measurements have to be taken into account. Particular attention should be made to the Zeeman effect caused by an external magnetic field, i.e. background or applied magnetic fields.

Typically, a small magnetic field is applied to the trapped ions to split the Zeeman components in purpose. Along with the running of the experimental apparatus of the ion trap, undesired time-dependent magnetic fields may also be in existence, due to inevitable alternating currents flowing in the ion trap.

To calculate the Zeeman energies of HD^+ ion in a constant external magnetic field, a Breit-type Hamiltonian could be used to characterize the electromagnetic interactions, and the high-accuracy variational non-relativistic Coulomb wave functions could be introduced as an initial approximation. For the magnetic field strength below 10 G, the contribution of the relativistic $\mathcal{O}(\alpha^2)$ corrections from the interaction with magnetic field is tiny and negligible [81, 89]. Thus, a first-order perturbative evaluation of the Zeeman structure of a rovibrational level (v, L) can be performed.

Taking the interaction with an external magnetic field $\mathbf{B}$ into consideration, Equation 4.26 is extended with an additional term V^{mag} into the following form:

$$H = H^{NR} + V^{sh} + V^{spin} + V^{mag}, \tag{4.41}$$

where in the leading-order approximation, V^{mag} is expressed as:

$$V^{mag} = -\mathbf{m} \cdot \mathbf{B}, \;\text{ with }\; \mathbf{m} = \sum_i \frac{eZ_i}{2M_i c} \left(\mathbf{L} i + \frac{\mu_i}{s_i} \mathbf{s}_i \right). \tag{4.42}$$

The summation is over the three constituents of HD$^+$ ion $(i = p, d, e)$. Z_i and M_i are the electric charge (in units e) and the mass of particle i, respectively. μ_i and s_i are the magnetic moment in units $e\hbar/2M_i c$ and the spin (1/2 for the proton and electron, and 1 for the deuteron), respectively. The operators $\mathbf{s}_i$ and $\mathbf{L}_i = \mathbf{R}_i \times \mathbf{P}_i$ are the spin and orbital momentum, where $\mathbf{R}_i$ and $\mathbf{P}_i$ are the position vector and momentum in the frame of center-of-mass, respectively.

Based on the effective Hamiltonian $H_{\mathit{eff}}^{\mathit{hfs}}$ of HD$^+$ in the absence of the magnetic field that is obtained in Equation 4.31, by averaging $V^{spin} + V^{mag}$ over the spatial degrees of freedom, the state-dependent effective spin Hamiltonian H_{eff}^{tot} is given by:

$$\begin{aligned} H_{\mathit{eff}}^{tot} &= H_{\mathit{eff}}^{\mathit{hfs}} + E_{10}(\mathbf{L} \cdot \mathbf{B}) + E_{11}(\mathbf{s}_p \cdot \mathbf{B}) \\ &\quad + E_{12}(\mathbf{s}_d \cdot \mathbf{B}) + E_{13}(\mathbf{s}_e \cdot \mathbf{B}). \end{aligned} \tag{4.43}$$

Here, the coefficients E_{11}, E_{12}, and E_{13} are derived from Equation 4.42 in the adopted approximation, and could be characterized in terms of masses and magnetic moments of particles as follows:

$$\begin{aligned} E_{11} &= -\frac{e\mu_p}{M_p c} = -4.2577 \text{ kHz/G}, \\ E_{12} &= -\frac{e\mu_d}{2M_p c} = -0.6536 \text{ kHz/G}, \\ E_{13} &= \frac{e\mu_e}{M_e c} = 2.8025 \text{ MHz/G}, \end{aligned} \tag{4.44}$$

while by using the variational non-relativistic wave functions of HD$^+$ [30], the coefficient E_{10} can be expressed as:

$$E_{10} = -\mu_B \sum_i \frac{Z_i M_e}{M_i} \frac{\langle vL \,||\mathbf{L}_i||\, vL \rangle}{\sqrt{L(L+1)(2L+1)}}, \tag{4.45}$$

with the numerical values shown in Table 4.3.

$L \setminus v$	0	1	2	3	4
1	−0.558 26	−0.553 71	−0.548 86	−0.543 66	−0.538 11
2	−0.558 13	−0.553 56	−0.548 69	−0.543 49	−0.537 92
3	−0.557 92	−0.553 34	−0.548 45	−0.543 22	−0.537 63
4	−0.557 64	−0.553 04	−0.548 13	−0.542 87	−0.537 25

Table 4.3: Calculated results of the coefficient E_{10} (in the unit of kHz/G) in the effective spin Hamiltonian of the lower rovibrational levels of HD$^+$ ion. E_{10} is zero for $L = 0$ [86].

By diagonalizing the matrix of H_{eff}^{tot}, the spin splittings of the energy states of HD$^+$ could be defined. Note that $\mathbf{I}_d \equiv \mathbf{s}_d$ and $\mathbf{I}_p \equiv \mathbf{s}_p$, the coupling scheme is identical to Equation 4.1:

$$\mathbf{F} = \mathbf{s}_p + \mathbf{s}_e, \quad \mathbf{S} = \mathbf{F} + \mathbf{s}_d, \quad \mathbf{J} = \mathbf{L} + \mathbf{S}. \tag{4.46}$$

The z-axis projection J_z of $\mathbf{J}$ is the only exact quantum number for the non-zero magnetic field $\mathbf{B}$, except for the “stretched” states with $F = s_p + s_e = 1$, $S = F + s_d = 2$, $J = L + S = L + 2$, and $J_z = \pm J$, for which F, S, and J are also the exact quantum numbers.

To label the eigenstates of H_{eff}^{tot}, an additional index n is introduced. Thus, corresponding to the “spinless” energies E^{vL}, the energy hyperfine states of HD$^+$ are sketched by the eigenvalues ΔE^{vLnJ_z}, which could be calculated from the system equation as follows:

$$\sum_{F'S'J'} \left\langle LFSJJ_z \left| H_{\mathit{eff}}^{tot} \right| LF'S'J'J_z \right\rangle \beta_{F'S'J'}^{vLnJ_z} = \Delta E^{vLnJ_z} \beta_{FSJ}^{vLnJ_z}, \tag{4.47}$$

where the coefficients $\beta_{FSJ}^{vLnJ_z}$ of the corresponding state vectors in the basis set $\mathcal{F}$ are given by:

$$|vLnJ_z\rangle = \sum_{FSJ} \beta_{FSJ}^{vLnJ_z} |LFSJJ_z\rangle . \tag{4.48}$$

In the absence of a magnetic field, the hyperfine states of HD$^+$ are distinguished with the quantum number $n = (F, S, J)$, whereas in the presence of a magnetic field, these hyperfine states split into substates that could be labeled with the additional quantum number J_z.

In the case of a low magnetic field, e.g. 1 G, which is the typical situation in our ion trap, the dependence of the eigenvalues ΔE^{vLnJ_z} on the magnetic field $\mathbf{B}$ may be approximated expressed with the following quadratic form:

$$\left(\Delta E^{vLnJ_z}(B) - \Delta E^{vLnJ_z}(0)\right)/h \approx t^{vLn} \cdot J_z \cdot \mathbf{B} + \left(q^{vLn} + r^{vLn} \cdot J_z^2\right) \cdot \mathbf{B}^2. \tag{4.49}$$

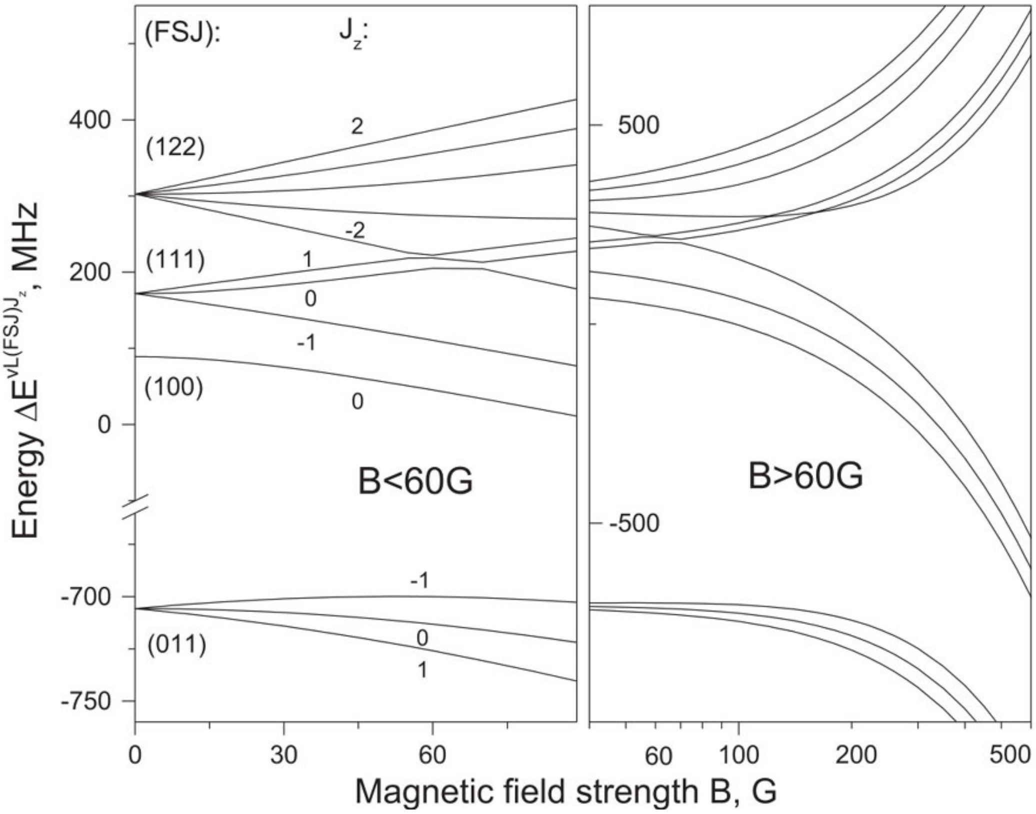

Figure 4.4: Energies $\varDelta E^{vL(FSJ)J_z}$ of the hyperfine splittings of the ground fundamental rovibrational level ($v = 0, L = 0$) of HD$^+$ molecular ion as a function of the magnetic field $\mathbf{B}$ at low ($B < 60$ G, left) and high ($B > 60$ G, right) magnetic field strength. The two "stretched states" are the top and bottom substates at approx. 300 MHz [86].

By using this approximation, the exact values with a relative error below 10^{-6} could be derived with the exception for the Zeeman components of the $L = 1$ states with $F = 1, S = 2, J = 2, 3$ and for those very close hyperfine states, in which the third order contribution with the magnetic field cannot be ignored. The values of t^{vLn}, q^{vLn}, and r^{vLn} for the lower rovibrational levels of HD$^+$ with $v \leqslant 4$ and $L \leqslant 4$ refer to table 2 of Refs. [86]. In Equation 4.49, the quadratic term in $\mathbf{B}$ is of significant interest mainly for those hyperfine states with $J_z = 0$, from which a conspicuous contribution for the remaining levels at $B > 0.1$ G could be obtained. In the case of $B > 60$ G, a rearrangement of the spectrum occurs as the spectrum acquires doublet form since the term $E_{13}(\mathbf{s}_e \cdot \mathbf{B})$ is predominant in H_{eff}^{tot} of Equation 4.43, while the small splitting results from the term $E_{11}(\mathbf{s}_p \cdot \mathbf{B})$. The dependence on $\mathbf{B}$ of the energies $\varDelta E^{vL(FSJ)J_z}$ of the hyperfine splittings for the fundamental rovibrational ground level ($v = 0, L = 0$) of HD$^+$ molecular ion is illustrated in Figure 4.4.

In this work, the determination of the magnetic field in the trap center by the measurements of Raman spectra of Be$^+$ ions has been realized (see section 3.5). By adjusting the currents of the three pairs of Helmholtz coils, a typical magnetic field intensity of 1 G was applied, in which the hyperfine interactions predominate over the interaction with the external field. Based on this, by taking the Zeeman effect into consideration, precise spectroscopy of the fundamental rotational transition (see chapter 5) and the doubly-spin-forbidden transitions (see chapter 7) of HD^+ have been accomplished.

5 Spectroscopy of the fundamental rotational transition of HD^+ ions

High-resolution rotational spectroscopy of molecules is an advanced and very well-developed technique in molecular physics, which provides the opportunity to investigate the external and internal structures and dynamics of molecules with various applications, including the identification of molecular species in interstellar clouds. Thanks to the development of appropriate terahertz radiation sources with useful power levels, the achievable spectral region could be extended from the microwave region to the terahertz (submillimeter wavelength) region.

In this work, as one of the most fundamental molecules, the molecular hydrogen ions HD^+ that were sympathetically cooled by laser-cooled atomic Be^+ ions to a temperature as low as approximately 10 mK have been chosen for spectroscopic measurements. Excitation of the fundamental rotational transition $(v = 0, L = 0) \rightarrow (v' = 0, L' = 1)$ of HD^+ at 1.3 THz was performed and significant transition frequencies were recorded successfully for the first time. This transition is of the utmost importance, since it is the most fundamental dipole-allowed rotational transition of any molecule, and has not been observed before. In addition, the black-body-radiation-induced (BBR) rotational excitation was also observed.

It should be mentioned that, in order to increase the signal-to-noise ratio, an important aspect of this work is the employment of laser rotational cooling by using a quantum cascade laser (QCL) at the wavelength of 5.5 μm and a distributed feedback laser (DFB) at the wavelength of 2.7 μm that drive the transitions $(v = 0, L = 2) \rightarrow (v' = 1, L' = 1)$ and $(v = 0, L = 1) \rightarrow (v' = 2, L' = 0)$, respectively. With this scheme, the difference in fractional population of the lower and upper levels of spectroscopy has been improved impressively, i.e. from 0.15 in thermal equilibrium to approx. -0.65, and consequently the detectable signal has been increased dramatically. For signal detection, a method of resonance-enhanced multi-photon dissociation (REMPD) was used.

In section 5.1, the terahertz spectroscopic scheme with the theoretical calculation is shown. In section 5.2, the hyperfine states and the Zeeman effect are analyzed. In section 5.3, the detection scheme of the rotational transition is reported. In section 5.4, the experimental apparatus including the terahertz source is described. In section 5.5, the signal detection procedure is provided. In section 5.6, the spectroscopy results are presented. In the end, the conclusion and discussion are given in section 5.7.

5.1 Terahertz spectroscopic scheme

The *ab initio* high precision calculation of the rovibrational transition frequencies of the molecular hydrogen ion HD$^+$ [30, 31] facilitates our experimental research work greatly. $(v = 0,\ L = 0) \rightarrow (v' = 0,\ L' = 1)$ is the fundamental rotational transition of HD$^+$, and is thus very interesting to us. With the consideration of the relativistic corrections (ca. 48.8 MHz, order α^2) and QED corrections (ca. -9.4 MHz, order α^3), the spinless value (hyperfine energy contributions excluded) of this transition studied in this work has been calculated to be $f_{0,theor} = 1\,314\,925.752$ MHz with an estimated theoretical error of approximately 2 kHz [90].

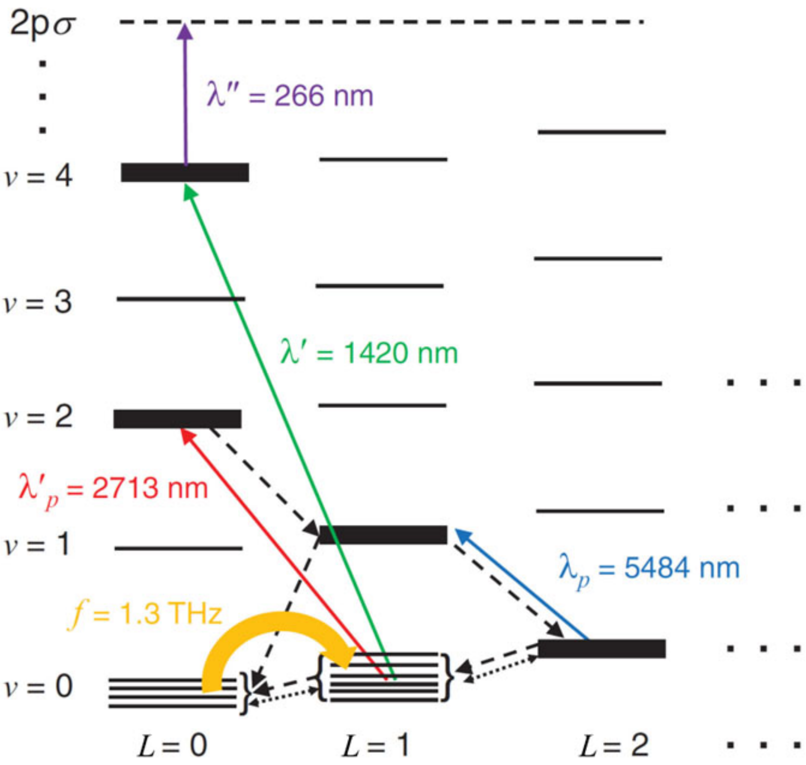

Figure 5.1: Simplified energy level scheme of HD$^+$ ion with transitions relevant to this work [91]. Full thin arrows represent laser-induced transitions; dashed arrows stand for some transitions of relevant spontaneous emission; dotted double arrows show the transitions of relevant BBR. The energy level differences are not to scale. Hyperfine structure is indicated schematically by several thin lines for the levels $(v = 0, L = 0)$ and $(v' = 0, L' = 1)$, and by thick lines for some other participating levels. The spectral linewidths of the waves at λ_p, λ'_p, λ', and λ'' are relatively large in order to cover all the hyperfine states in the relevant energy levels.

Experimentally, the sympathetically cooled HD$^+$ ions are translationally and vibrationally cold due to the energies and decay times of high vibrational levels. However, they are expected to be rotationally warm due to the inevitable BBR between rotational levels and the absence of strong coupling between the external and internal degrees of freedom, i.e. under normal circumstances, the molecular population is distributed among several rotational levels in the $v = 0$ manifold.

To solve this problem, rotational laser cooling that could transfer most population into the rovibrational ground level ($v = 0, L = 0$) and nearly empty the target level ($v' = 0, L' = 1$) was employed in this work. Thus, the HD$^+$ ions are expected to be rotationally cold and are ready for spectroscopy. As shown in the schematic diagram of Figure 5.1, for each measurement cycle of spectroscopy, the HD$^+$ ions are firstly rotational cooled by using a QCL radiation ($\lambda_p = 5.5$ μm) and a DFB radiation ($\lambda'_p = 2.7$ μm), and are excited from the hyperfine states of rovibrational ground level ($v = 0, L = 0$) to the corresponding hyperfine states of the rotationally excited level ($v' = 0, L' = 1$) by the frequency-detuned-terahertz wave (yellow-colored, thick arrow in Figure 5.1). Further, the ions are transferred to a vibrationally excited level ($v'' = 4, L'' = 0$) by a resonant laser radiation ($\lambda' = 1420$ nm), and finally to the electronically excited level $2p\sigma$ (shown in Figure 4.3) by a non-resonant UV radiation ($\lambda'' = 266$ nm) to be photodissociated.

5.2 Hyperfine states with Zeeman effect

In order to perform rotational spectroscopy, the hyperfine states and the Zeeman effect should be taken into account. As Figure 5.2 shows, the rovibrational ground level ($v = 0$, $L = 0$) of HD$^+$ possesses four hyperfine states with twelve magnetic substates (with magnetic quantum number J_z). In our trap apparatus, the magnetic field in the ion's region is non-zero, and thus the magnetic degeneracy is lifted.

As shown in Figure 5.3, the theoretical stick spectrum contains a large number of transitions in the frequency range with relatively large transition dipole moments. In a magnetic field of 1 G (assumed), most transitions will shift by ca. 100 kHz or more, except for five strong $J_z = 0 \rightarrow J'_z = 0$ transitions, whose quadratic Zeeman shifts are less than 6.2 kHz [81]. For each lower hyperfine substate there exists at least one such transition with small Zeeman shift, while the energy substate ($F = 0$, $S = 1$, $J = 1$, $J_z = 0$) possesses two. Three of them are pointed out by the first, third, and fourth arrows in Figure 5.2. A fourth hyperfine transition is ($F = 1$, $S = 1$, $J = 1$, $J_z = 0$)$\rightarrow$($F' = 1$, $S' = 1$, $J' = 2$, $J'_z = 0$) with its transition frequency at $f = f_{0,theor} + 11.78$ MHz. However, this frequency is close to some other transition frequencies and is not suitable for this work. Instead, an alternative transition ($F = 1$, $S = 1$, $J = 1$, $J_z = 0$) $\rightarrow$ ($F' = 1$, $S' = 1$, $J' = 0$, $J'_z = 0$) that is indicated by the second arrow from the top in Figure 5.2 is chosen, although this transition has a substantial quadratic Zeeman shift (78 kHz at 1 G). Due to the magnetic field gradient in the trap center where the ions are cooled and stored, some line broadening in the spectrum could be expected.

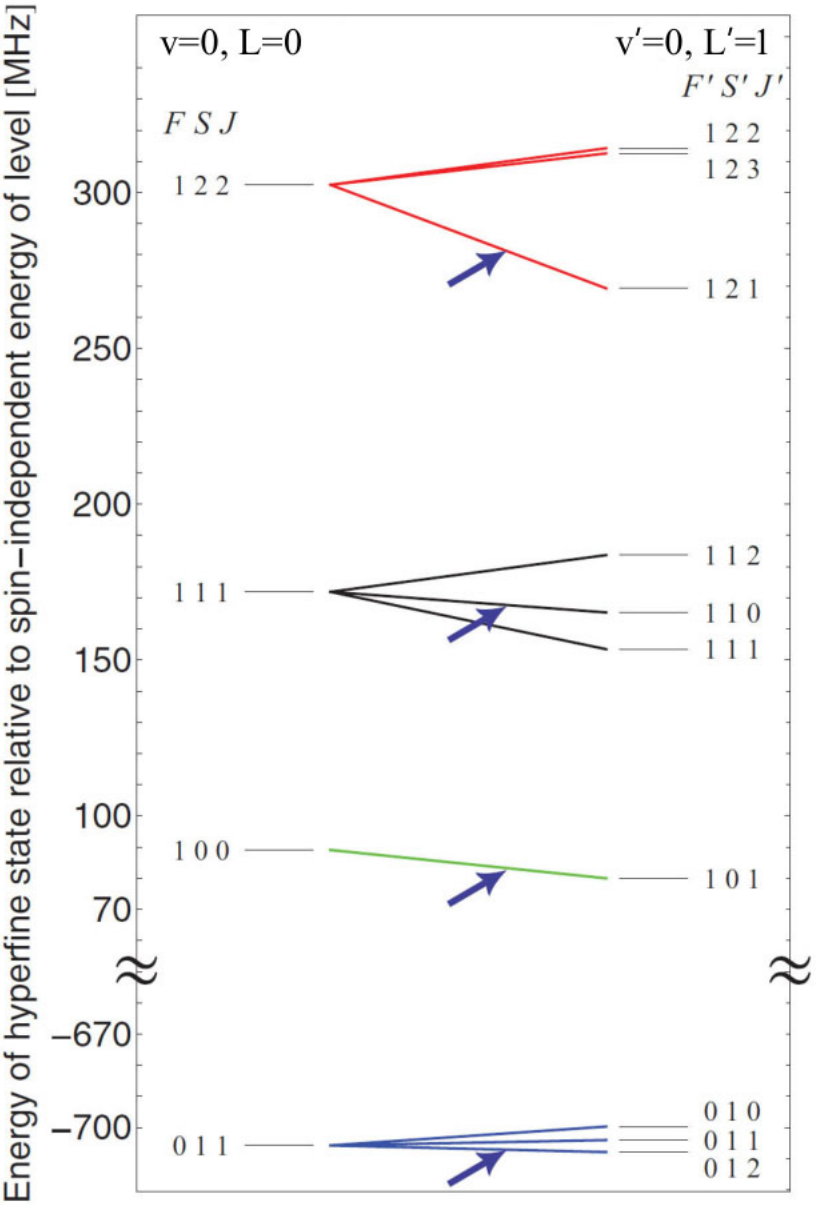

Figure 5.2: Energy diagram of the hyperfine states of HD^+ ion with the main electric-dipole-allowed transitions in the zero magnetic field [91]. Left side: rovibrational ground level ($v = 0$, $L = 0$); right side: rotationally excited level ($v' = 0$, $L' = 1$). The hyperfine states are labeled by the quantum numbers (F, S, J) with a degeneracy factor of $(2J + 1)$ for each. Transitions that not changing the quantum numbers F, S are relatively strong and are marked, from top to bottom, in red, black, green, and blue.

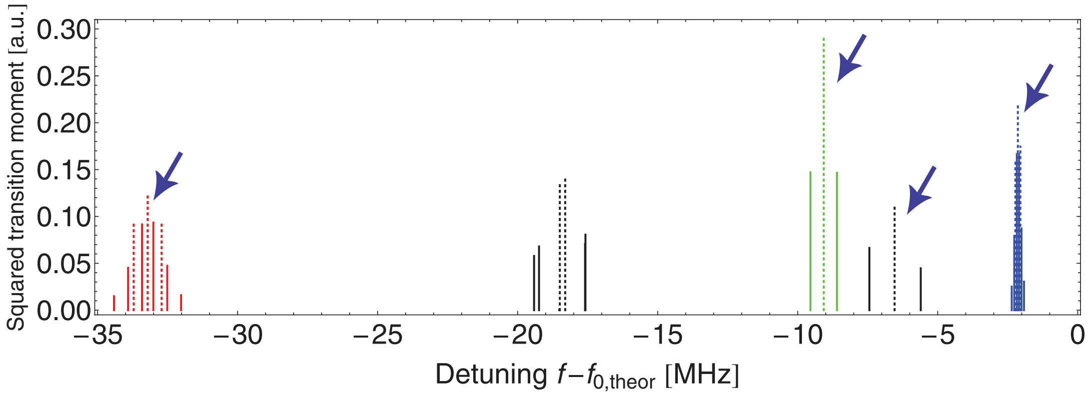

Figure 5.3: Theoretical stick spectrum of the $(v = 0,\ L = 0) \rightarrow (v' = 0,\ L' = 1)$ rotational transition, including Zeeman shifts [91]. The magnetic field involved here is set to 1 G. The σ transitions are shown in full lines, while the π transitions are in dashed lines. The spinless theoretical transition frequency $f_{0,theor}$ is calculated to be 1 314 925.752 MHz. The terahertz frequencies indicated by arrows are shown in list A (see Table 5.1). The colors of red, green, black, and blue are corresponding to those used in Figure 5.2.

5.3 Detection scheme of the rotational transition

According to the Boltzmann distribution regarding the thermal equilibrium with BBR at a secular temperature of 300 K, all the sympathetically cooled HD$^+$ ions are initially in the $v = 0$ vibrational level with an internal population distribution of 0.10, 0.25, 0.27, 0.20, 0.11, and 0.04 for the rotational levels $(0, 0)$, $(0, 1)$, $(0, 2)$, $(0, 3)$, $(0, 4)$, and $(0, 5)$ that are labeled by the quantum numbers (v, L), respectively, while each hyperfine state of those levels contains only a fraction of the population [92].

To increase the population in the rovibrational ground level $(v = 0,\ L = 0)$, the rotational cooling scheme was implemented by using a QCL at the wavelength of 5.5 μm and a DFB laser at the wavelength of 2.7 μm that drive the transitions $(v = 0, L = 2) \rightarrow (v' = 1, L' = 1)$ and $(v = 0, L = 1) \rightarrow (v' = 2, L' = 0)$, respectively. With this scheme, the fractional population of the lower $(v = 0,\ L = 0)$ and upper $(v' = 0,\ L' = 1)$ levels of the terahertz spectroscopy has been redistributed to approx. 0.8 and 0.15, respectively, i.e. the difference has been improved impressively from 0.15 in thermal equilibrium to approx. −0.65.

Nevertheless, detecting the individual hyperfine transitions is still challenging due to the low corresponding population. Each substate would contain statistically 1/12 of the population in the $(v = 0,\ L = 0)$ level, i.e. the fraction being typically 20 to 30 HD$^+$ ions. In addition, the population distribution in these individual substates varies substantially in time, which requires an averaging of substantial data.

In order to obtain a sufficiently strong signal, an alternative strategy was applied. As shown in Table 5.1, several strong hyperfine transitions on terahertz frequencies were selected to irradiate the molecular hydrogen ions sequentially. Various frequency sets were used, in which each frequency in a list was irradiated for 200 ms and was meanwhile frequency-modulated by ±2 kHz at a rate of 5 Hz. In each measurement cycle, only one list from Table 5.1 was implemented. The frequencies in the list were repeated sequentially for 3 seconds or more, depending on the excitation scheme used.

	Frequency $f_i - f_{0,\,\mathrm{theor}}$ (MHz)						
Lower hyperfine level (F, S, J)	(1,2,2)	(1,1,1)				(1,0,0)	(0,1,1)
List A'	−33.211	−6.597	−6.578	−6.558	−6.539	−9.069	−2.138
List A	−33.211	−6.539				−9.069	−2.138
List B	−34.993	−7.850				−9.773	−2.465
List C	−31.408	−5.096				−8.355	−1.812
List D	−34.102	−7.194				−9.421	−2.301
List E	−32.310	−5.817				−8.712	−1.975
500-MHz detuning	500						

Table 5.1: Frequency lists used for the rotational excitation of HD$^+$ [91]. f_i is the terahertz frequency.

Each frequency list includes three of the five above-mentioned low-Zeeman-shift $J_z = 0 \to J'_z = 0$ transitions, originating from three of the four hyperfine states of the rovibrational ground level $(v = 0, L = 0)$. The respective frequency values of these transitions were chosen corresponding to an assumed magnetic field of 1 G. As mentioned above, the transition originating from the fourth hyperfine state $(F = 1,\ S = 1,\ J = 1)$ has a significant quadratic Zeeman shift. Due to the lack of knowledge of the precise magnetic field distribution in the trap, four distinct frequencies corresponding to the magnetic field strengths 0.25, 0.5, 0.75, and 1 G (the detuning for 0 G is −6.617 MHz), were applied as compensation. Overall, four of the twelve Zeeman substates should be nominally excited by the frequency set that is labeled as list A'. However, by taking the above-mentioned Doppler broadening into consideration, more substates (with larger Zeeman shifts) would be addressed. The essential frequencies to excite all the Zeeman substates of the ground hyperfine states fall into ranges of approx. ±0.5, ±1, 0, ±0.22 MHz at 1 G, relative to the frequencies of the list A'. At higher molecular temperatures ($100 \sim 200$ mK), these spreads have a partial overlap with the Doppler broadening. Nevertheless, at lower temperatures ($10 \sim 15$ mK) when the ion ensemble is in the crystallized state, this effect is minimized.

To obtain information about frequency detuning dependence of the rotational excitation, the "detuned frequency lists" were also applied. As shown in Table 5.1, relative to list A', smaller and larger frequency detunings were used, denoted by B and C, respectively. The detunings of list B are −1.782, −1.311, −0.704, −0.327 MHz, while the ones of list C are 1.803, 1.443, 0.714, 0.326 MHz. These detunings are larger than their respective Zeeman shifts in an assumed magnetic field of 1 G. The relative detunings of Lists D and E are approximately half of the values of lists B and C, respectively. The relative detunings of list D are -0.891, -0.655, -0.352, -0.163 MHz, while the ones of list E are 0.901, 0.722, 0.357, 0.163 MHz. Finally, as a variation (simplified version) of list A', list A was applied as well. In all cases, frequency modulation was employed.

5.4 Experimental apparatus

5.4.1 Overview

A typical procedure of one terahertz spectroscopic measurement cycle starts routinely by the loading of Be$^+$ crystal, followed by the generating and cleaning process of HD$^+$. Afterwards, the data acquisition process takes place by applying rotational cooling, terahertz excitation, and REMPD sequentially. Finally, the residual HD$^+$ and product ions are removed from the trap by a "cleaning" process that ends the measurement cycle.

Figure 5.4 shows a schematic of the apparatus in the experiment. Initially, a beryllium ion crystal is produced in the center of the linear ion trap and cooled (see chapter 3) by a 313 nm cooling laser that enters from the right viewport of the vacuum chamber. By using a hyperfine transition of the molecular iodine as a reference, the frequency of the UV cooling laser could be detuned and stabilized from a few 100 MHz to the red of the Be$^+$ atomic transition to a few tens of MHz to the red, causing a phase transition of the cold ion ensemble from liquid to crystallized state for optimal Be$^+$ cooling (see Figure 2.10 in section 2.3).

At the beginning of each measurement cycle, the ion ensemble is transformed to the liquid state. Then, the HD gas is loaded into the vacuum chamber by controlling a piezoelectric valve, after which the HD molecules are ionized to HD$^+$ ions by an electron gun that is positioned towards the ion trap. During this process, both HD$^+$ ions as well as the heavy impurity ions are produced, trapped, and subsequently sympathetically cooled by the Be$^+$ ions. For removal of the impurity ions, the DC quadrupole potential of the trap is briefly increased, which reduces the trap quasi-potential in one transverse direction. Thus, the heavy ions are ejected from the ion trap. Consequently, the ion ensemble is transformed back into the crystallized state, which ends the molecular preparation procedure. Typically, the generated cold HD$^+$ sample contains approx. 250 molecular ions, as shown in Figure 2.12 in section 2.3.

For rotational cooling purposes, the radiations from a QCL with $\lambda_p = 5484$ nm and a DFB laser with $\lambda'_p = 2713$ nm are employed diagonally into the ion trap.

For the process of REMPD, two lasers are applied entering from the left. The first REMPD laser is a diode laser propagating at the wavelength of 1420 nm and is used to drive the $(v = 0, L = 1) \rightarrow (v' = 4, L' = 0)$ transition of HD$^+$. The second

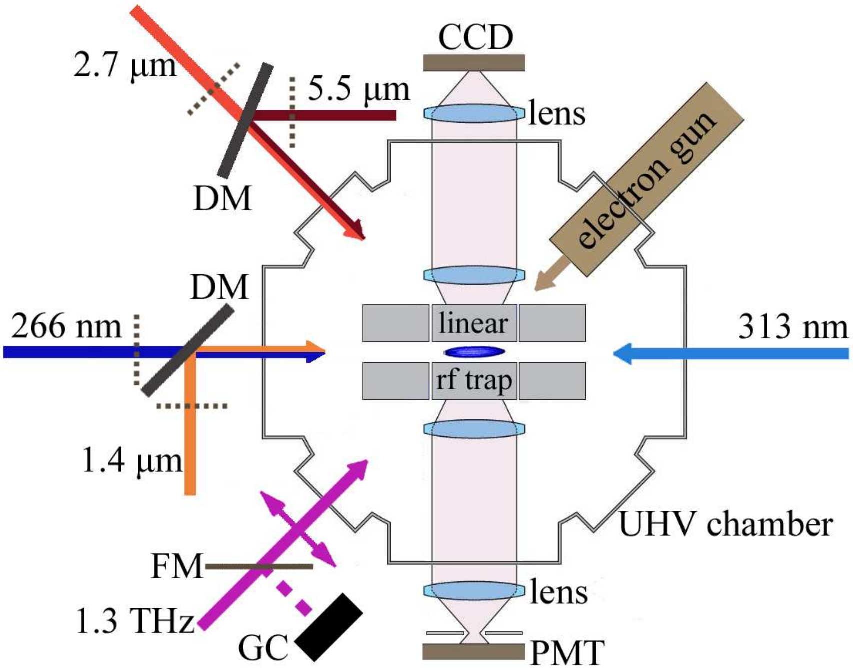

Figure 5.4: Schematic of the setup and beams for terahertz spectroscopy of HD^+ ions [91]. DM: dichroic mirror; FM: flip mirror; GC: Golay cell; CCD: charge-coupled device; PMT: photomultiplier tube. Dotted lines stand for laser beam shutters controlled by computers. The double arrow that is perpendicular to the terahertz radiation direction indicates the terahertz wave polarization. Dimensions are not to scale.

REMPD laser at the wavelength of 266 nm is provided by a resonantly frequency-doubled 532 nm laser and is used for photon dissociation of HD^+ with non-resonant excitation.

For detection purposes, a CCD camera is installed to monitor the beryllium crystal with HD^+ ions, and a PMT is used to record the fluorescence of Be^+ ions for further analysis.

5.4.2 Terahertz source

The terahertz source is the key element for this spectroscopy work. It is positioned close to the vacuum chamber emitting radiation at a frequency of 1.3 THz with a linewidth below 100 Hz and a subhertz absolute frequency stability. For driving the fundamental rotational transition $(v = 0, L = 0) \to (v' = 0, L' = 1)$ of HD^+, the source is driven at the 72nd subharmonic of the desired frequency, near 18 GHz, provided by a microwave synthesizer that is frequency locked to a global positioning system (GPS)-referenced hydrogen maser. In order to obtain a good spatial overlap between the radiation and sympathetically cooled HD^+ ions, its wave is focused into the trap center by a concave parabolic mirror oriented at the right angle to the beam. For the purpose of power-monitoring, the wave of the terahertz radiation could be sent to a Golay cell detector by switching a flip mirror manually. Figure 5.5 shows the terahertz source that is applied in this spectroscopic experiment. This source has been described previously in [93] but was not yet in use for spectroscopic purposes due to some limitations. In this work, the narrow-band terahertz source is fully utilized by several significant improvements, e.g. a replacement of a new microwave synthesizer (E8241A from Agilent Technologies) with much lower phase noise and frequency jitter than the previous one, a better frequency stabilization technique to a GPS-referenced hydrogen maser in our laboratory, and a better spatial overlap with HD$^+$ ions, etc.

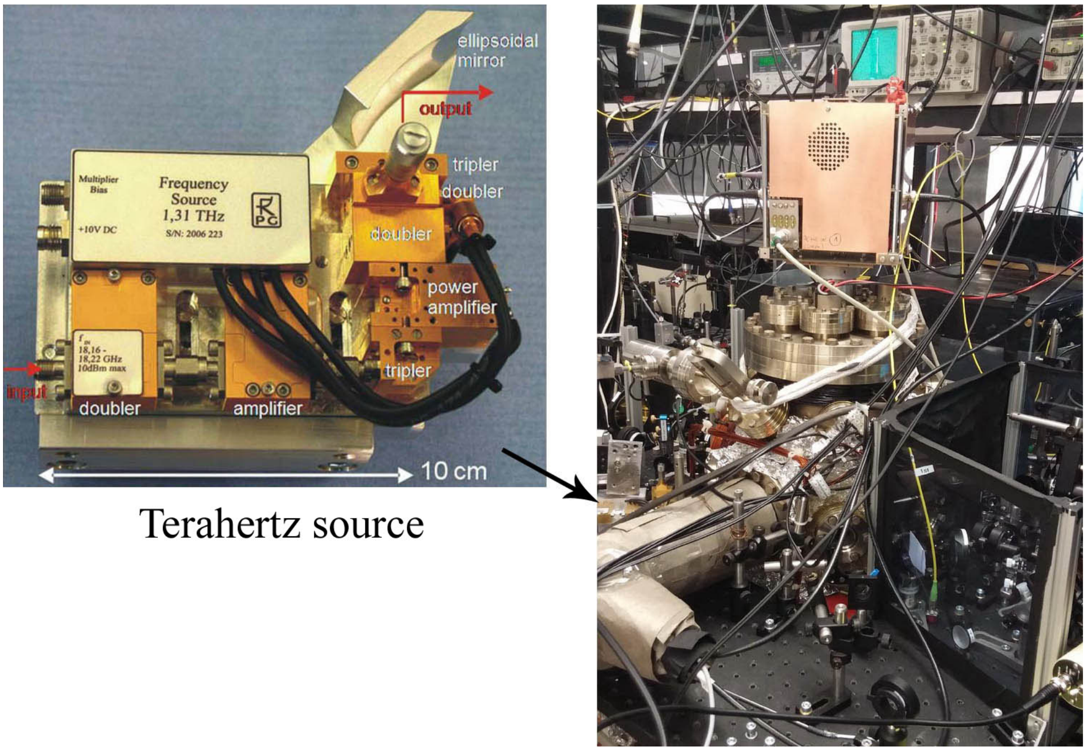

Figure 5.5: Photograph of the apparatus. Left: the terahertz source (bias and power supplies not shown) that is applied in this work [93]; right: the UHV chamber in our HD$^+$-laboratory for the experiment.

5.5 Signal detection procedure

5.5.1 Secular excitation

To detect the HD$^+$ ions that are sympathetically cooled by Be$^+$ ions effectively, one takes the advantage of the induced transfer of ions' kinetic energy from the micromotion to the secular motion, which is described in subsection 2.1.3. By applying a low AC voltage to the electrode (plate) that is positioned perpendicular to the trap axis, a shift of the ion motion out of phase with the trap RF field occurs. Thus, the HD^+ ions obtain an additional kinetic energy in form of micromotion, which is then transferred to its secular motion and further to the secular motion of Be^+ ions, due to the Coulomb interaction between these two ion species. By using the PMT, the corresponding changes in the fluorescence intensity of Be^+ ions are recorded.

Quantitatively, for a laser-cooled beryllium crystal with sympathetically cooled HD^+ ions that is in steady state, the cooling rate $\mathit{\Gamma}_c$ is identical to the heating rate $\mathit{\Gamma}_h$. In the first approximation, the Be^+ fluorescence rate $\mathit{\Gamma}_f$ (below saturation) is proportional to the cooling rate $\mathit{\Gamma}_c$.

Thus, in the absence of secular excitation, the fluorescence rate can be characterized by:

$$\mathit{\Gamma}_f \propto \mathit{\Gamma}_c = \mathit{\Gamma}_h = \mathit{\Gamma}_0, \tag{5.1}$$

where $\mathit{\Gamma}_0$ stands for the Be^+ background heating rate that is independent of the number of HD^+ ions.

In comparison, the corresponding fluorescence rate $\mathit{\Gamma}'_f$ in the presence of secular excitation can be expressed by:

$$\mathit{\Gamma}'_f \propto \mathit{\Gamma}'_c = \mathit{\Gamma}'_h = (\mathit{\Gamma}_0 + \mathit{\Gamma}_N), \tag{5.2}$$

where $\mathit{\Gamma}_N$ represents the induced additional heating rate of the Be^+ ions that is proportional to the number of remained HD^+ ions in the trap.

5.5.2 Resonance-enhanced multi-photon dissociation (REMPD)

For spectroscopic measurements of HD^+ ions, a destructive one, resonance-enhanced multi-photon dissociation (REMPD) technique [66] is introduced. The particular implementation used in this work is $1 + 1' + 1''$ procedure, where the HD^+ absorbs sequentially three photons of different energies.

As is depicted schematically in Figure 5.6, the molecules are firstly excited with the 1.3 THz radiation from the rovibrational ground level ($v = 0, L = 0$) to the rotationally excited level ($v' = 0, L' = 1$) and are transferred further to the vibrationally excited level ($v'' = 4, L'' = 0$) by a tunable infrared diode laser ($\lambda' = 1420$ nm), from which, the molecules are ultimately dissociated by the 266 nm laser radiation (approx. 30 mW):

$$\mathrm{HD}^+(v'' = 4) + h\nu_{266} = \mathrm{H} + \mathrm{D}^+ \text{ or } \mathrm{D} + \mathrm{H}^+. \tag{5.3}$$

As a consequence of different Franck-Condon wave function overlap, the UV absorption cross section calculated from the $v'' = 4$ level ($\sim 2.4 \times 10^{-17}$ cm^2) is approx. 7 orders of magnitude larger than the one from the $v = 0$ level [94].

As the REMPD is a destructive detection method, at the end of each cycle of measurement, the residual HD$^+$ and product ions H + D$^+$ or D + H$^+$ are removed from the trap by applying a "cleaning" procedure as follows: first, the 313 nm cooling laser is detuned by a few 100 MHz to the red of the Be$^+$ atomic transition, which leads to a phase transition of the Coulomb crystal from the crystallized state to the liquid state with a "dark core" inside of it. Then, a frequency scan of secular excitation with a moderate amplitude covering the frequencies of HD$^+$ and all lighter ions is switched on. By alternatively blocking and unblocking the cooling laser beam briefly for several times, the residual HD$^+$ and light ions thereby escape from the trapping region, leaving a pure and clean Be$^+$ crystal that can be monitored from the disappearance of the "dark core" in the real-time image of the CCD camera. Finally, the secular excitation is switched off and the system is ready for a new measurement cycle starting with new HD$^+$ loading.

Typically, reloading of Be$^+$ ions is not required, since the same Be$^+$ ion crystal maintains in the trap and can be used for several hours of experimentation.

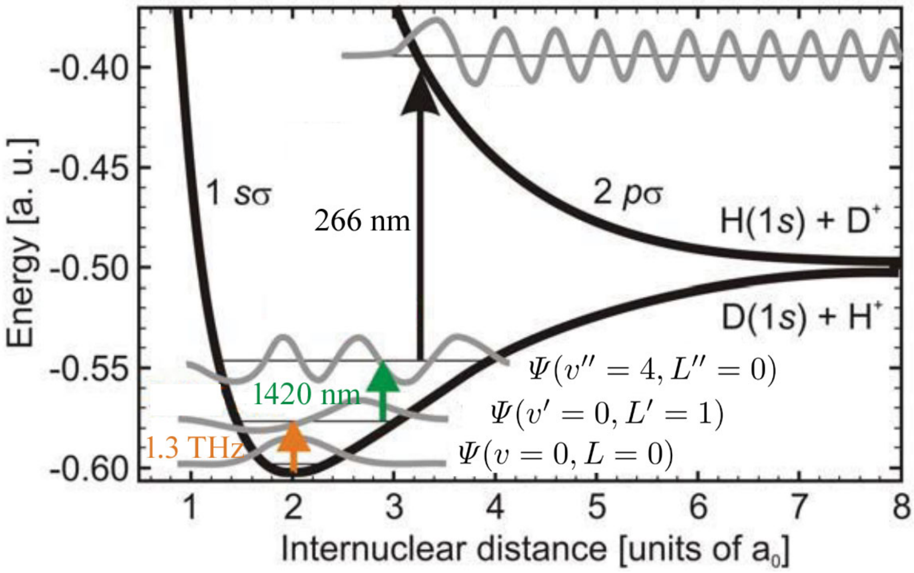

Figure 5.6: Principle of $1 + 1' + 1''$ REMPD procedure of HD$^+$ ions. Energy values stand for total binding energies of HD$^+$. This scheme is depicted based on the Born-Oppenheimer potential energy curves as shown in Figure 4.3, which is favorable and widely used for detection of HD$^+$ ions (see e.g. Ref. [38] with other rovibrational transition frequencies of HD$^+$ in our laboratory system).

5.5.3 Data acquisition

In this work, two independent measurement methods for one data point were implemented.

5.5.3.1 Method I

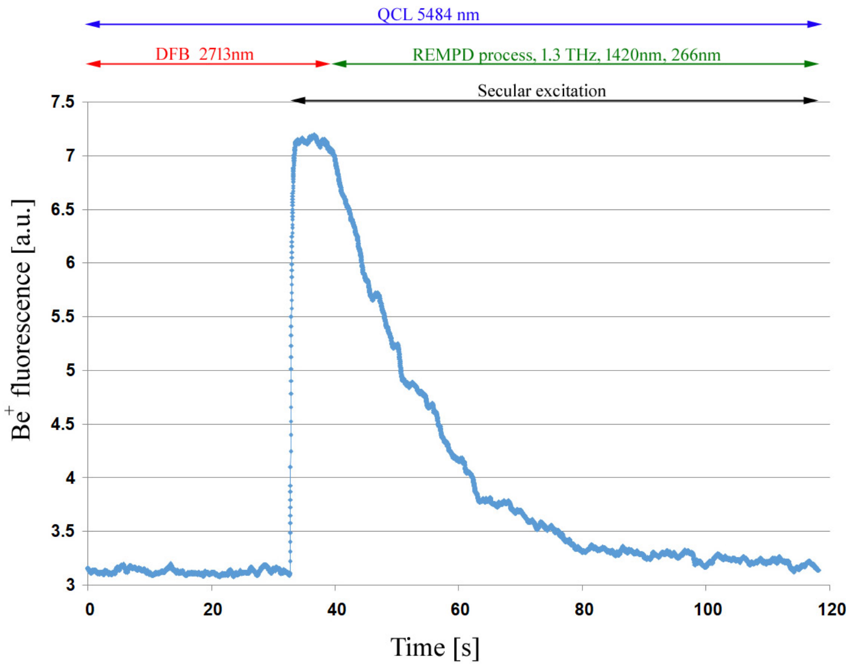

Figure 5.7: A typical procedure of method I of the terahertz spectroscopic measurements.

(i) At first, the terahertz radiation is effectively kept off by detuning the frequency by 500 MHz of the rotational resonant transition $(v = 0, L = 0) \rightarrow (v' = 0, L' = 1)$ of HD$^+$, and the REMPD lasers (i.e. 1420 nm and 266 nm) are blocked. (ii) The rotational cooling (QCL at 5484 nm and DFB at 2713 nm) takes place for a duration of 40 seconds, after which the DFB rotational cooling laser is blocked whereas the QCL remains on. (iii) The REMPD lasers are unblocked and the desired terahertz frequency scan is activated simultaneously. (iv) 5 seconds before step (iii) starts, a repeated secular frequency scan ($740 \sim 900$ kHz) is initiated and kept on during the remainder of the measurement cycle. Thus, the Be$^+$ fluorescence is stabilized initially and reduced dramatically as a function of time as soon as the REMPD process starts, due to the decrease of heating caused by the loss of HD$^+$ molecular ions. Essentially, for a terahertz-frequency-dependent duration (typically approximately one minute), the fluorescence signal finally reaches the background level in the absence of HD$^+$, which ends one measurement cycle.

The process for the whole duration is illustrated in Figure 5.7 and the contained fluorescence signal decay curve is extracted for analysis (see Figure 5.13).

5.5.3.2 Method II

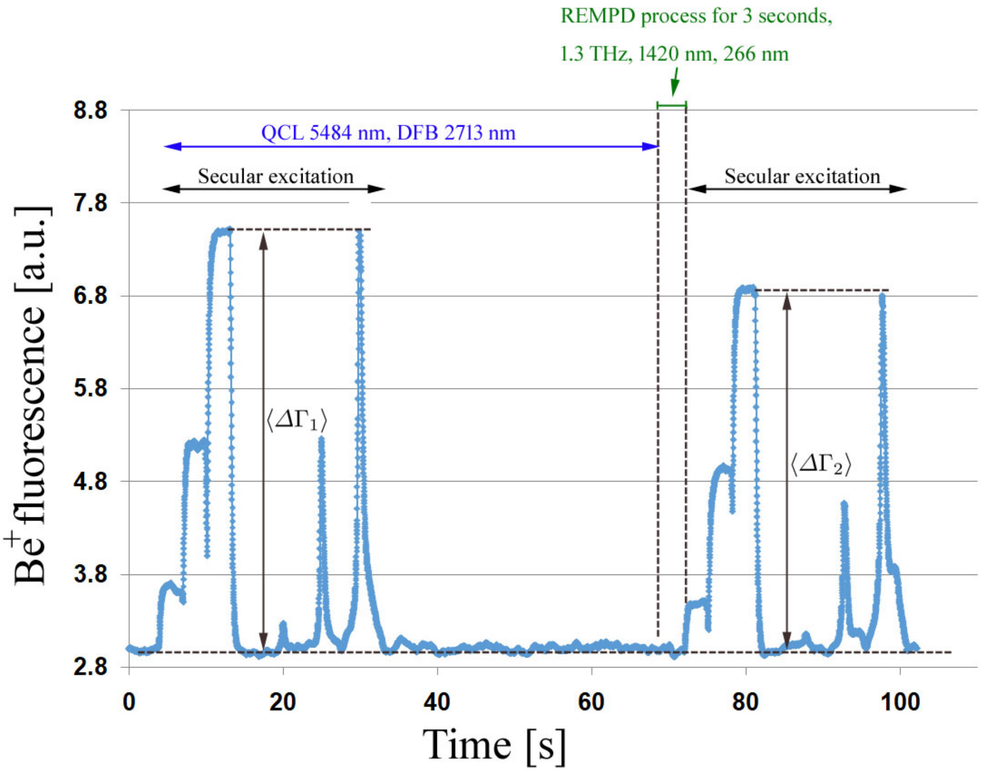

Figure 5.8: A typical procedure of method II of the terahertz spectroscopic measurements.

(i) Initially, to determine the number of HD$^+$ ions before spectroscopy, a continuous secular excitation that is followed by a discrete secular excitation sequence for reliability and validity evaluation is launched. During this process, the rotational cooling (QCL at 5484 nm and DFB at 2713 nm) is applied and last for 60 seconds to effectively transfer almost all the population to the rovibrational ground level (initial level) and nearly deplete the population in the target level, which is favorable for the terahertz spectroscopy, whereas the terahertz radiation is kept off, and the REMPD lasers are blocked. (ii) Both rotational cooling lasers are blocked, whereas the desired terahertz frequency scan is activated and meanwhile the REMPD lasers are unblocked. Thus, the $1 + 1' + 1''$ REMPD sequence only for 3 seconds is implemented. Immediately afterwards, in step (iii) the same secular excitation as described in step (i) is switched on again and the reduced Be$^+$ fluorescence level is recorded. Consequently, the information of the terahertz transition signal and the relative decrease in HD$^+$ number after REMPD is defined by the ratio of the two fluorescence levels.

A typical spectroscopic measurement cycle by using Method II is illustrated in Figure 5.8. According to the difference of Equation 5.1 and 5.2, the following relations can be derived:

$$\Delta\Gamma_f = (\Gamma_f' - \Gamma_f) \propto \Gamma_N \propto N, \tag{5.4}$$

which indicates that the HD$^+$ number N scales with the difference of Be$^+$ fluorescence rates by presence and absence of secular excitation. Hence, the determination of $\Delta\Gamma_f$ gives information on the fractional population of HD$^+$ that is addressed by the terahertz transition:

$$S_s = \frac{\langle\Delta\Gamma_1\rangle - \langle\Delta\Gamma_2\rangle}{\langle\Delta\Gamma_1\rangle} = 1 - \frac{N_2}{N_1}, \tag{5.5}$$

where the bracket stands for the mean value defined from the fluctuated fluorescence level, while the indices 1 and 2 represent the situations before and after the REMPD process.

In addition, it has to be taken into account that the background HD$^+$ loss S_b without being influenced by REMPD should be determined by using the same procedure as shown in Figure 5.8 (with the exception that in step (ii), all REMPD lasers should be blocked), and subtracted from S_s. Thus, a background-corrected detection signal can be expressed as:

$$S_{sb} = S_s - S_b. \tag{5.6}$$

After one spectroscopic measurement cycle by using method II, a single data point in the terahertz spectrum (see e.g. Figure 5.10) is generated.

5.6 Spectroscopy results

According to the theoretical analysis of Figure 5.3, the relatively strong hyperfine transitions between ($v = 0$, $L = 0$) and ($v' = 0$, $L' = 1$) levels of the molecular hydrogen ions are -2.138 MHz, -9.069 MHz, -33.211 MHz, and -6.539 MHz detunings from the spinless theoretical transition frequency $f_{0,theor}$. In this work, for clarity, two experimental methods were applied to study those transitions.

First, by using the individual-hyperfine-transition-detection scheme (subsection 5.6.1), the former three transitions were successfully observed but the latter one around -6.539 MHz detuning was not clearly distinguished from the background noise. Instead, based on the theoretical calculation in a larger frequency detuning range than the one in Figure 5.3 (see the stick spectrum in Figure 5.9), another relatively strong transition around 6.051 MHz detuning corresponding to the transition ($v = 0,\ L = 0,\ F = 0,\ S = 1,\ J = 1$)→($v' = 0,\ L' = 1,\ F' = 0,\ S' = 1,\ J' = 0$) has been detected.

Then, an alternative strategy with frequency sweeping (subsection 5.6.2) was implemented as a double check of those transitions observation. Since the transitions around −2.138 MHz and 6.051 MHz detunings start from the same lower quantum state ($v = 0,\ L = 0,\ F = 0,\ S = 1,\ J = 1$) and cannot be driven simultaneously, the −6.539 MHz detuning instead of 6.051 MHz detuning was used in the sweeping list.

5.6.1 Observation of individual hyperfine transitions

By using the method II (see subsubsection 5.5.3.2), a very first spectrum of measured hyperfine rotational transitions between ($v = 0,\ L = 0$) and ($v' = 0,\ L' = 1$) levels of the molecular hydrogen ion ensemble in the crystallized state (10 ∼ 15 mK) was obtained as an overview, since in the initial phase of this measurement, to the best of our knowledge, no reports about this spectrum range could be found. As Figure 5.9 shows, the measured spectrum (right side) agrees with the stick spectrum (left side) that refers to the theoretical transition frequencies in a relatively large frequency scale.

Based on this coarse spectrum, a first set of delicate measurements with the terahertz wave frequency detuned around −2.138 MHz, −9.069 MHz, 6.051 MHz, and −33.211 MHz from $f_{0,theor}$ was carried out. The results are presented in Figure 5.10 ∼ Figure 5.12.

Each data point with an error bar in all these spectra is the average of at least three individual measurements. As one example, the red data points in Figure 5.10 (a) represent the results of all the individual measurements for each frequency detuning. In other plots, the red points are not shown for simplicity. It should be mentioned that some data points are so close to others that they almost overlap in the plot, e.g. by −2.143 MHz detuning, the data of −0.183794 is almost overlapped with another data of −0.182986. To distinguish them from each other, they are plotted with a slight horizontal offset.

In addition, since each measurement of one complete spectrum lasts for several hours, a routine background signal check took place during the whole measurement period in order to ensure long-term stability. Taking the measurement in panel (j) of Figure 5.12 for example, the magenta points with error bars stand for the background signal as the terahertz wave frequency detuned by 4 MHz from $f_{0,theor}$ where no transition line exists. These background signals were recorded right after the measurements of 6.253 MHz, 6.258 MHz, and 6.262 MHz detunings and are plotted beside those frequencies accordingly for comparison purposes.

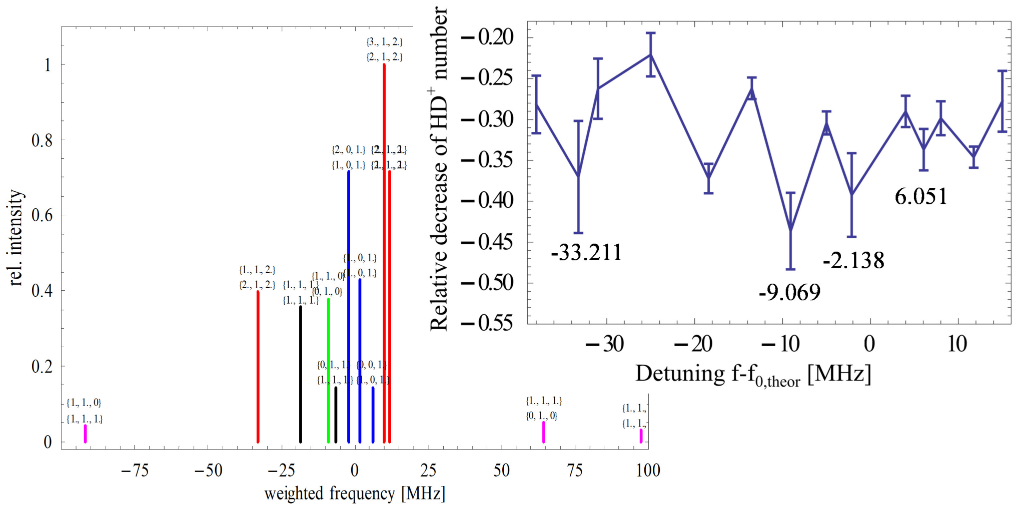

Figure 5.9: Spectrum in large scale of the $(v = 0,\ L = 0) \rightarrow (v' = 0,\ L' = 1)$ rotational transition of the molecular hydrogen ions. Left side: theoretical stick spectrum which is computed by Prof. S. Schiller. The values are weighted over m_F_{upper} and m_F_{lower} with the intensity cutoff of 0.007. The Quantum numbers are: top-$\{F_u, F_{1u}, F_{2u}\}$, bottom-$\{F_l, F_{1l}, F_{2l}\}$. Right side: a very first measured spectrum between $(v = 0,\ L = 0)$ and $(v' = 0,\ L' = 1)$ levels as an overview.

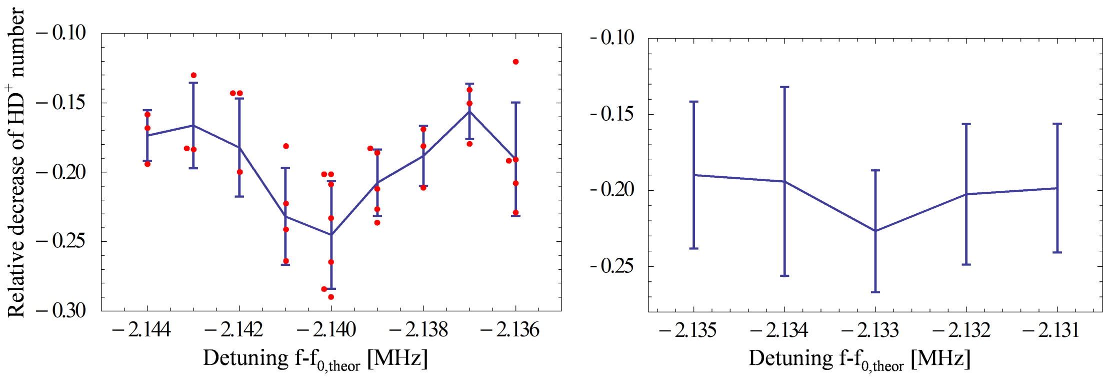

(a) (b)

Figure 5.10: Measured hyperfine rotational transitions between $(v = 0,\ L = 0)$ and $(v' = 0,\ L' = 1)$ levels of the molecular hydrogen ions. The corresponding terahertz radiation frequency detunings are: (a) -2.144 MHz $\sim$ -2.136 MHz; (b) -2.135 MHz $\sim$ -2.131 MHz. Each data point with an error bar in all the spectra presented in this section is the average of at least three individual measurements. As one example, the red data points in panel (a) represent the results of all the individual measurements for each frequency detuning. In other plots, the red points are not shown for simplicity.

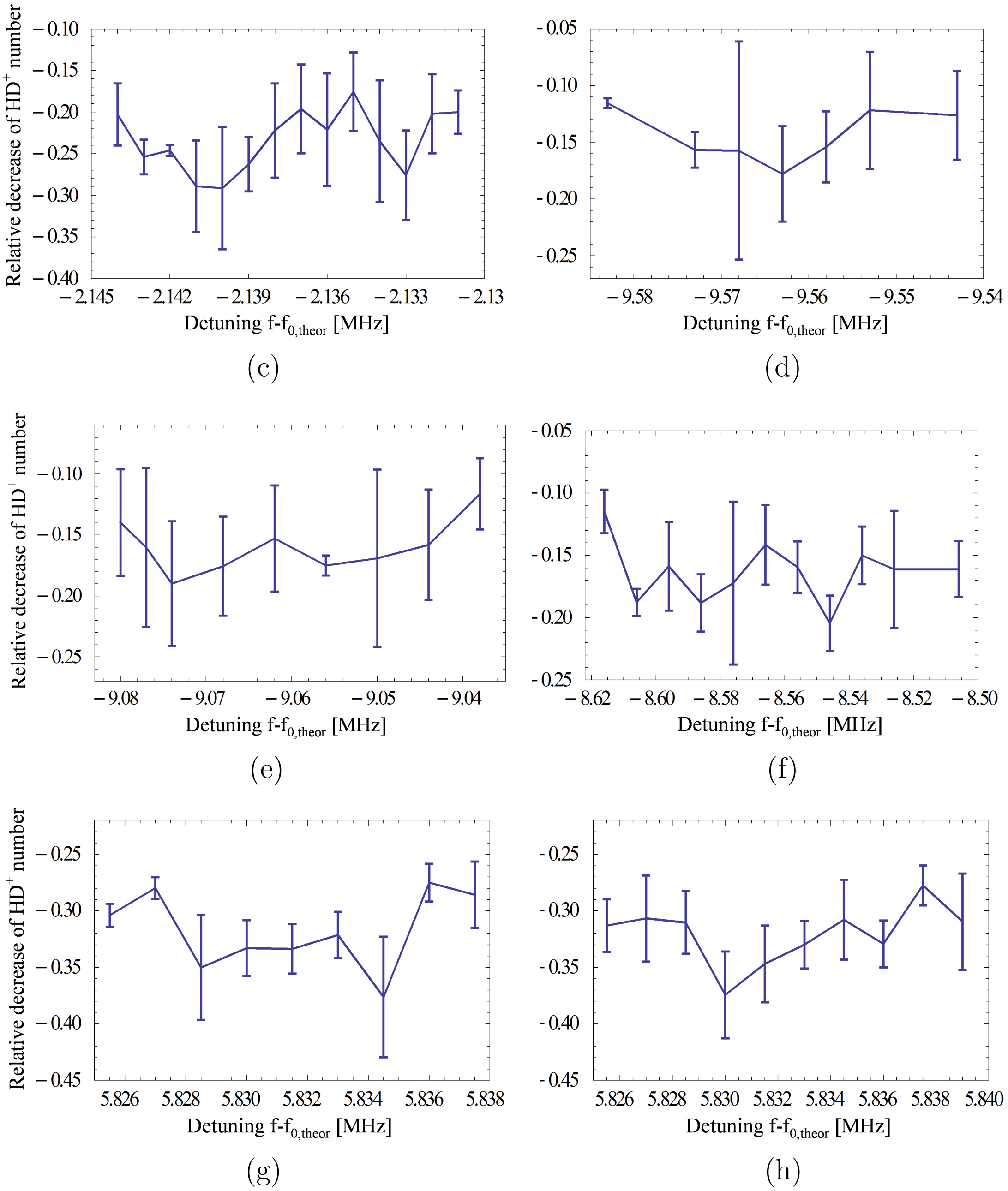

(c) (d)

(e) (f)

(g) (h)

Figure 5.11: Measured hyperfine rotational transitions between ($v = 0$, $L = 0$) and ($v' = 0$, $L' = 1$) levels of the molecular hydrogen ions. The corresponding terahertz radiation frequency detunings are: (c) -2.144 MHz $\sim$ -2.131 MHz; (d) -9.080 MHz $\sim$ -9.038 MHz; (e) -9.583 MHz $\sim$ -9.543 MHz; (f) -8.616 MHz $\sim$ -8.506 MHz; (g) 5.8255 MHz $\sim$ 5.8375 MHz; (h) 5.8255 MHz $\sim$ 5.839 MHz.

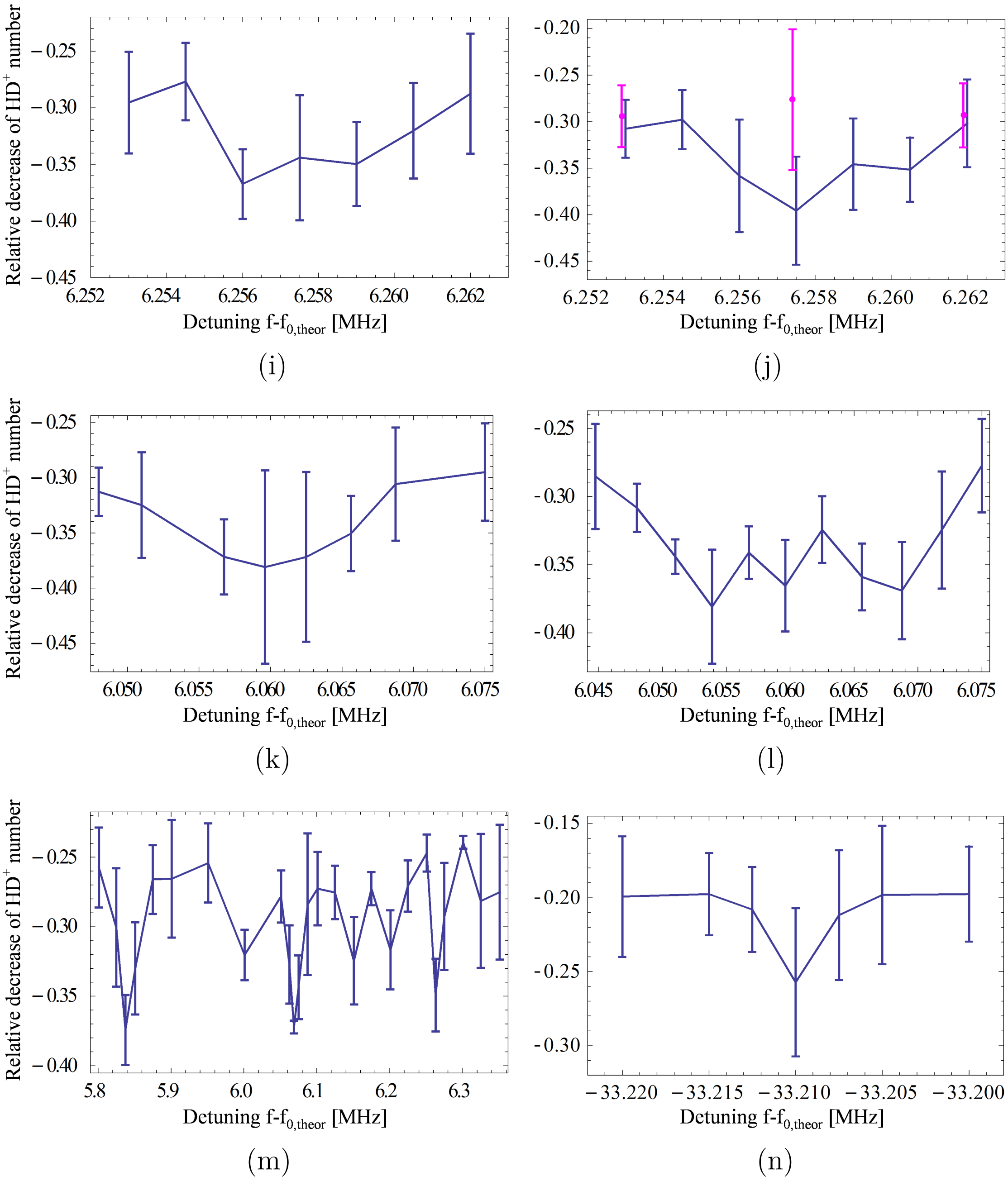

(i) (j)

(k) (l)

(m) (n)

Figure 5.12: Measured hyperfine rotational transitions between ($v = 0$, $L = 0$) and ($v' = 0$, $L' = 1$) levels of the molecular hydrogen ions. The corresponding terahertz radiation frequency detunings are: (i) 6.253 MHz ∼ 6.262 MHz; (j) 6.253 MHz ∼ 6.262 MHz; (k) 6.048 MHz ∼ 6.075 MHz; (l) 6.045 MHz ∼ 6.075 MHz; (m) 5.800 MHz ∼ 6.350 MHz; (n) −33.220 MHz ∼ −33.200 MHz. The magenta points with error bars in panel (j) stand for the background signal as the terahertz wave frequency detuned by 4 MHz.

The spectroscopic results show that the experimental measurements are consistent with the theoretical calculation. The spectra of -2.144 MHz $\sim$ -2.136 MHz and -2.135 MHz $\sim$ -2.131 MHz detunings, corresponding to the hyperfine transition $(v = 0,\ L = 0,\ F = 0,\ S = 1,\ J = 1) \rightarrow (v' = 0,\ L' = 1,\ F' = 0,\ S' = 1,\ J' = 2)$ which are indicated by the fourth arrow from the top in Figure 5.2 are presented in Figure 5.10 (a) and (b). Each plot shows a peak in the center of the spectrum. The measurement was repeated in the frequency detuning rang of -2.144 MHz $\sim$ -2.131 MHz. As Figure 5.11 (c) confirms, the measurement is repeatable and could be comparable with the detailed spectra of Figure 5.10 (a) and (b).

The spectra of -9.583 MHz $\sim$ -9.543 MHz, -9.080 MHz $\sim$ -9.038 MHz, and -8.660 MHz $\sim$ -8.515 MHz detunings are presented in Figure 5.11 (d) $\sim$ (f), respectively, which are indicated by the third arrow from the top in Figure 5.2 corresponding to the hyperfine transition $(v = 0,\ L = 0,\ F = 1,\ S = 0,\ J = 0) \rightarrow (v' = 0,\ L' = 1,\ F' = 1,\ S' = 0,\ J' = 1)$.

The hyperfine transition that is indicated by the second arrow from the top in Figure 5.2 corresponding to the transition $(v = 0,\ L = 0,\ F = 1,\ S = 1,\ J = 1) \rightarrow (v' = 0,\ L' = 1,\ F' = 1,\ S' = 1,\ J' = 0)$ was not clearly detected due to potentially lower initial population and relatively low transition strength. Instead, another strong transition around 6.051 MHz detuning corresponding to the hyperfine transition $(v = 0,\ L = 0,\ F = 0,\ S = 1,\ J = 1) \rightarrow (v' = 0,\ L' = 1,\ F' = 0,\ S' = 1,\ J' = 0)$ was observed. The measurements of this spectral range were repeated several times and the detailed results are illustrated in Figure 5.11 (g) $\sim$ Figure 5.12 (l). Then, an overview spectrum between 5.800 MHz and 6.350 MHz was obtained and is plotted in Figure 5.12 (m).

In addition, as shown in Figure 5.12 (n), a peak around -33.210 MHz was detected as well, which is indicated by the first arrow from the top in Figure 5.2, corresponding to the hyperfine transition $(v = 0,\ L = 0,\ F = 1,\ S = 2,\ J = 2) \rightarrow (v' = 0,\ L' = 1,\ F' = 1,\ S' = 2,\ J' = 1)$.

In atomic and molecular physics, the spectral resolution of spectroscopy is one of the most essential characteristics. In our work, if only the secular motion of the HD$^+$ ions is considered, the theoretical Doppler linewidth is approx. 55 $\sim$ 70 kHz when the ion ensemble is in the crystallized state (10 $\sim$ 15 mK), and approx. 150 $\sim$ 200 kHz in the liquid state (100 $\sim$ 200 mK). It should be noted that the large values result from the low mass of the HD$^+$ ion. At 10 $\sim$ 15 mK, the molecular ions are well confined along the trap axis and stay in the Lamb-Dicke regime in the transverse direction, since their secular motion in this direction is restricted by the trap electrodes to less than 0.1 mm, which is smaller than the terahertz wavelength (0.23 mm). In the axial direction, however, the ions are not strongly confined by the endcap electrodes of the trap, which yields their diffusive motion exceeding in length (typically 1.5 to 2.0 mm) the terahertz wavelength.

As shown in Figure 5.4, in this experiment, the terahertz radiation is employed diagonally into the ion trap. Thus, the Doppler broadening is not negligible in this work, even the ions are in the crystallized state (at relatively low temperature). Nevertheless, the linewidth of the Doppler broadening, fortunately, is smaller than the spacing between the hyperfine transitions originating from different ground hyperfine states relevant to this work, including the consideration of the Zeeman effect in an assumed magnetic field of 1 G. Therefore, the resolution of the hyperfine structure is permitted and not affected by the Doppler broadening, which is in principle advantageous in this experiment.

It can be seen from all those plots in Figure 5.10 $\sim$ Figure 5.12 that the observed linewidth in the spectra is on the order of magnitude of a few tens of kHz, from which the minimum and the second minimum values are ca. 2 kHz and 4 kHz around the -2.133 MHz and -2.140 MHz detunings (see Figure 5.10 (a), (b), and Figure 5.11 (c)), respectively, indicating that the Lamb-Dicke regime was reached in this experiment. Since the observed linewidth is smaller than the theoretical Doppler linewidth at 10 $\sim$ 15 mK, it can be inferred that the Doppler-free resolution at an even lower temperature than 10 mK of the ion ensemble was achieved in this experiment.

As mentioned above, the Zeeman effect plays an important role in the determination of the magnetic field B in the trap center which was assumed to be 1 G in this experiment. As a matter of fact, the plots in Figure 5.10 $\sim$ Figure 5.12 contain a lot of interesting information. For simplicity, we take the plot in Figure 5.11 (c) for analysis, since this hyperfine fundamental transition that is indicated by the first arrow from the right side of Figure 5.3 has relatively low Zeeman shift and is not affected by the other nearby transitions. As Figure 5.11 (c) shows, two peaks at -2.140 MHz and -2.133 MHz were detected. Considering that the theoretical value of -2.135 MHz ($B = 0$) and -2.138 MHz ($B = 1$ G), it can be concluded that the Zeeman effect was successfully observed and an upper limit of the magnetic field B in the trap center of 1.5 G was estimated, as the influence of the Doppler width is not conspicuous here.

It is noteworthy that in this experiment, several individual terahertz hyperfine fundamental transitions of HD^+ were successfully observed for the first time to our knowledge, however, on the other hand, all the spectra in the Figure 5.10 $\sim$ Figure 5.12 show inevitable signal fluctuations. See e.g. Figure 5.11 (h), Figure 5.12 (j), and Figure 5.12 (l) that are repeated measurements of Figure 5.11 (g), Figure 5.12 (i), and Figure 5.12 (k), respectively. It can be seen that the profiles of the plots are affected significantly by those fluctuations, which could be explained by the limited laser power, possibly imperfect spatial overlap of the involved radiations (including the terahertz wave, cooling lasers, and REMPD lasers), possibly a magnetic field gradient in the trap center, and relatively low population distribution in each initial hyperfine state.

5.6.2 Alternative strategy with frequency sweeping

To overcome the above-mentioned obstacles, an alternative strategy with frequency sweeping by using the method I (see subsubsection 5.5.3.1) initially and by the method II (see subsubsection 5.5.3.2) subsequently was implemented as a cross-check of those transitions.

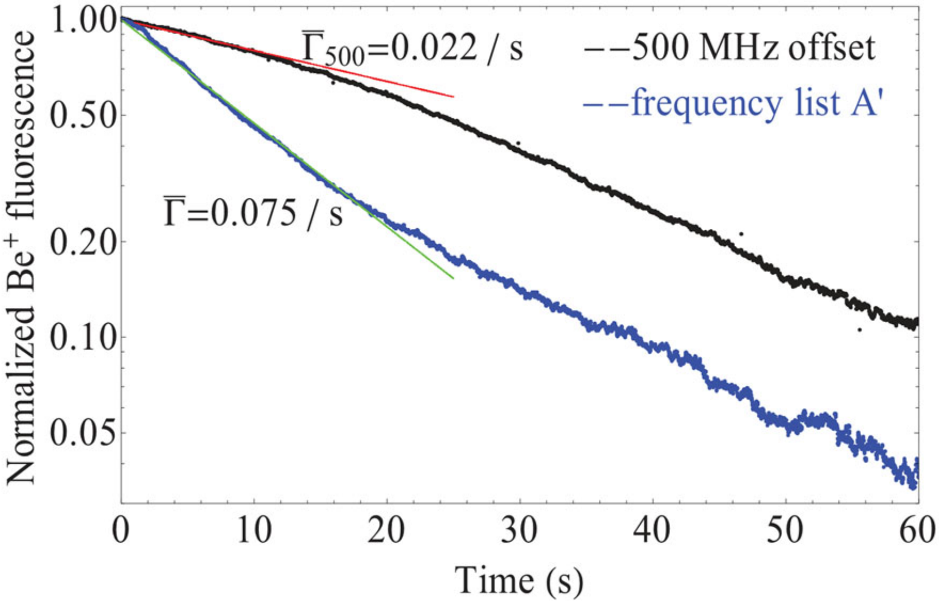

Figure 5.13: Be$^+$ fluorescence decay during the continuous secular excitation of the HD$^+$ ions (method I, liquid state) [91]. The signal recording starts after the rotational cooling lasers (5.5 μm and 2.7 μm) are switched off and the two REMPD lasers (1420 nm and 266 nm) and the terahertz radiation are turned on. Upper (black colored) trace: terahertz radiation is detuned 500 MHz away from resonance; lower (blue colored) trace: terahertz radiation on resonance. Each trace is averaged from 10 individual decay measurements. Exponential fits are performed to the first 10 seconds of each trace.

First, by using the method I, the measurements were performed in the liquid state of the cold ion ensemble, and the results are shown in Figure 5.13. Each trace is averaged from 10 individual decay measurements. With the terahertz wave frequency detuned by 500 MHz from the rotational resonant transition frequency $f_{0,theor}$ where no transition line exists, the upper trace (black) was obtained as the "background" signal without being influenced by terahertz rotational transitions. The REMPD process only dissociates the HD$^+$ ions in the $(v = 0, L = 1)$ level that has been depopulated by the 2.7 μm rotational cooling laser initially. As soon as the REPMD phase starts, this level receives population not only by terahertz excitation (if the terahertz frequency is near rotational resonance), but also by BBR-induced excitation from all the hyperfine states of the $(v = 0, L = 0)$ rovibrational ground level (rate ca. 0.09/s at 300 K). In addition, despite of the 5.5 μm rotational cooling that transfers the population from the $(v = 0, L = 2)$ rotational level to $(v' = 1, L' = 1)$ rovibrational level, the population is still present in the $(v = 0, L = 2)$ level, since it is transferred from higher-lying rotational levels, e.g. $(v = 0, L = 3)$ by BBR-stimulated emission (rate ca. 0.12/s) and spontaneous emission (rate ca. 0.06/s). Hence, a REMPD-induced HD^+ ions loss is inevitable.

The lower (blue) trace stands for the decay when the terahertz radiation is on resonance, using the frequency list A' of Table 5.1. By using a rate equation simulation with exponential fits performed to the first 10 seconds of each trace, the terahertz-transition-induced molecule number decay rate is calculated as 0.075/s, which is much higher than the BBR-induced decay rate of 0.022/s. Note that the decay in the presence of terahertz excitation contains the background decay.

The significant difference between these two decay rates shows that the signal of terahertz-induced-rotational excitation of HD^+ was clearly detected.

By using the same procedure, the measurements with smaller and larger frequency detunings relative to list A' (i.e. the two frequency lists B and C of Table 5.1) were also performed. As shown in Figure 5.14 (top), their decay rates do not differ remarkably from the background decay rates, thus an upper limit of the magnetic field in the trap of 1.5 G was deduced, which is consistent with the estimation by using the method II in subsection 5.6.1, as the influence of the Doppler width is not conspicuous here.

It is worth mentioning that the scheme of the method I provided us an effective approach to optimize experimental conditions: by applying laser rotational cooling and sweeping the selected terahertz frequencies, the signal-to-noise ratio has been dramatically increased; in the test measurements, by adjusting the alignment of only one wave beam each time, and meanwhile monitoring the real-time fluorescence decay, all the waves could be thus well focused on the trapped HD^+ ions.

Based on the results obtained in the liquid state ($100 \sim 200$ mK) by using the method I, a second set of measurements in the crystallized state ($10 \sim 15$ mK) of the ion ensemble by using method II were performed as well, and the results are shown in Figure 5.14 (bottom). Data points were taken with terahertz frequency at 500 MHz detuning and with the lists from A to E of Table 5.1 alternately. Again, a limited signal was observed with the far detuned terahertz radiation, since the BBR-induced excitation is significant within the REMPD time period of 3 seconds. The two close data points at frequency list A were taken with the same condition but on different days, which shows the reliability and reproducibility of the measurements, indicating that the rotational excitation induced by terahertz radiation has been clearly detected. For terahertz detunings of lists B and C, compared to the background signal, no significant excitation was observed. However, when reducing the detunings to half the values of lists B and C to lists D and E, the signal increases dramatically, which can be explained by a Doppler width of several 100 kHz or the presence of a magnetic field with values up to ca. 1.5 G, or a combination of both.

However, under the measurement conditions, the Doppler width is at most 70 kHz. Therefore, it can be concluded that the effect of the magnetic field on the hyperfine transition frequencies (Zeeman effect) was observed successfully.

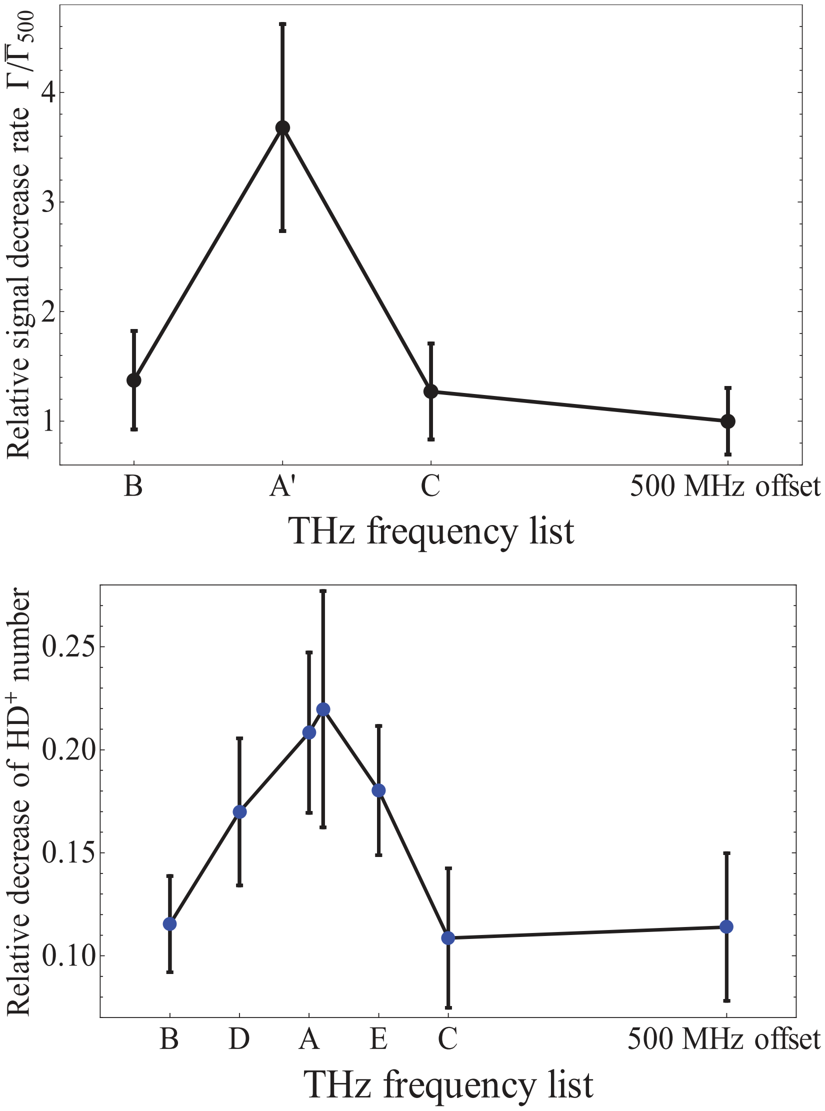

Figure 5.14: Frequency dependence of the terahertz-induced-rotational excitation of the HD$^+$ ions [91]. Top: ions are in the liquid state (100 ∼ 200 mK) and method I is used. $\bar{\Gamma}_{500}$ is the average decay rate when the terahertz radiation is detuned by 500 MHz. Each data point is the average of 9 individual decay measurements. Bottom: ions are well crystallized (10 ∼ 15 mK) and method II is used. Each data point results from 9 or 10 individual measurements. The two close points at frequency list A were taken with the same condition but on different days and are shown separated in the plot for clarity. In both plots, the error bars stand for the standard deviations of the data.

5.7 Conclusion and discussion

In this experiment, a pure rotational excitation $(v = 0, L = 0) \rightarrow (v' = 0, L' = 1)$ of a sympathetically cooled HD^+ molecular ion ensemble was observed. A scheme that is adapted to the features of the apparatus was applied to facilitate the experimentation. Due to the REMPD process that photodissociates the rotationally excited molecular ions, a procedure of cleaning the residual ions and loading of new HD^+ ions was implemented for each measurement cycle. Since the data acquisition rate is low and the number of HD^+ ions is also small, the rotational cooling for the preparation of a significant fraction (ca. 70%) of the HD^+ in the lower spectroscopic level $(v = 0, L = 0)$ was applied.

Based on this, a very first set of delicate measurements with the terahertz wave frequency detuned around −2.138 MHz, −9.069 MHz, 6.051 MHz, and −33.211 MHz from $f_{0,theor}$ was carried out. It is indicated from the obtained spectra that the Lamb-Dicke regime was reached and the Zeeman effect was successfully observed, from which, an upper limit of the magnetic field in the trap center of 1.5 G was estimated.

Since the signal-to-noise ratio of the individual frequency measurements was relatively low, terahertz radiation at four frequencies that nominally excites the four hyperfine states in the lower spectroscopic level was implemented as a double-check, and a clear rotational excitation was observed. Then, by applying the terahertz radiation detuned from the nominal resonance frequencies from 0.16 to 0.9 MHz (absolute) for the four frequencies, a significantly reduced but still observable excitation was detected, which can be explained by the presence of a magnetic field up to approx. 1.5 G. In addition, it is found that when the ions are in a crystallized state (at approx. $10 \sim 15$ mK) and well-confined in the trap, the contribution of secular ion motion to the linewidth is inconsequential.

Thus, by using two independent methods, it can be concluded that the fundamental rotational transition of HD^+ by terahertz radiation has been clearly detected, which is of significant importance, since it is the most fundamental dipole-allowed rotational transition of any molecule, and has not been observed before. It is worth mentioning that in this work, Doppler-free resolution with a fractional linewidth of 5×10^{-8} was achieved. To the best of our knowledge, it is the first time (January 2012) that a Doppler-free molecular ion transition was ever observed [91].

This experiment strongly motivated further development of the system and further investigation of the hyperfine transitions in our laboratory. Based on this work, a linewidth of 1×10^{-9} fractionally and 1.3 kHz absolute, an improvement of ca. 50-fold over the previous highest resolution in rotational spectroscopy, was later (2018) achieved in our laboratory [95]. In addition, by further measurements of the hyperfine components of the fundamental rotational transition, in 2020, an evaluation resulted in the most accurate test of a quantum-three-body prediction so far, at the level of 5×10^{-11} [96].

Finally, it is worth considering the extension of this work to the study of other molecular species. In molecular physics, those molecular ions in an electronic spin-singlet state are of high interest due to the simplified and narrow transitions. The related characterized parameters are the masses that would be significantly larger and the rotational constants that would be significantly smaller than the ones of HD^+, since an impressively lower transition frequency in the microwave regime would be deduced from the smaller rotational constant. In that case, the Lamb-Dicke regime will probably be effective and Doppler broadening will be suppressed even at not particularly low temperature, which is in principle advantageous. In addition, a smaller BBR-induced excitation rate (at 300 K) would be deduced from the smaller rotational constant as well, which would possibly make the REMPD process with near-zero background.

6 Transportable transfer cavity for QCL frequency controlling

Spectroscopic measurements of cold molecules such as HD$^+$ ions requires well controlling of the laser frequency. In our HD$^+$-project, as an optical pumping source, the QCL at a wavelength of 5.5 μm that transfers the HD$^+$ population to the rovibrational ground level ($v = 0, L = 0$) is important. Conventionally, the frequency of the QCL is broadened and stabilized to a gas absorption line which is mostly the case for a frequency-locking system and satisfies nearly all the requirements of our current spectroscopic tasks. However, for the future work of higher-resolution spectroscopy of HD$^+$, the QCL hyperfine pumping with fast and precise frequency control is highly demanded.

For this purpose, a so-called "transfer cavity" system that couples the QCL with a distributed-feedback (DFB) laser was developed. In this system, the QCL is frequency stabilized to the cavity, while the latter is locked to the DFB laser. Thus, by means of adjusting the frequency of the DFB laser, the related QCL frequency could be controlled correspondingly.

The whole setup of the transfer cavity system was initially built in our HD$^+$-laboratory ("HD$^+$-lab" for short). In order to test the stability, reliability, and accuracy of the system before applying in the HD$^+$-project, by using a frequency comb as a reference, a series of measurements were performed in our comb-laboratory ("comb-lab" for short) with positive results. Afterwards, the system was transported back to the HD$^+$-lab again for spectroscopic purposes. After calibration, the frequency tuning of the QCL at the wavelength of 5.5 μm was successfully realized.

Compared to the conventional scheme of manually locking and tuning the laser frequency with a frequency modulator, one obvious advantage of this novel scheme is that it can be programmed for various frequency detunings of the QCL including the value and the radiation time for each. Therefore, it is more efficient and more appropriate especially for the purpose of hyperfine pumping of HD$^+$.

In section 6.1 of this chapter, the theory of Pound-Drever-Hall (PDH) laser frequency stabilization that is the key technique for the transfer cavity system is introduced. In section 6.2, the schematic of the system is illustrated. In section 6.3, the involved lasers in the system are described. In section 6.4, the scheme and the results of the system frequency stability measurement with the assistance of a frequency comb are reported. In section 6.5, the results of the system frequency tunability measurement with the N_2O transmission line as a cross-check are shown. In section 6.6, the results of the frequency offset calibration between DFB and QCL are presented. In section 6.7, the results of the QCL hyperfine pumping for HD^+ ions by using the developed transfer cavity system are demonstrated, which prove that the system is valuable for the HD^+-project. Finally, a brief conclusion and discussion are given in section 6.8.

6.1 Theory of PDH laser frequency stabilization

PDH frequency stabilization [97, 98] is a useful technique to improve the frequency stability of lasers. The idea of this method is as follows: the frequency of one laser is measured by a cavity reflection or transmission and is then fed back to the laser source to suppress the frequency fluctuations. To discriminate the frequency fluctuations from the laser intensity fluctuations, a nulled lock-in detection is usually employed. Figure 6.1 shows the basic scheme of the laser frequency stabilization by using the PDH technique.

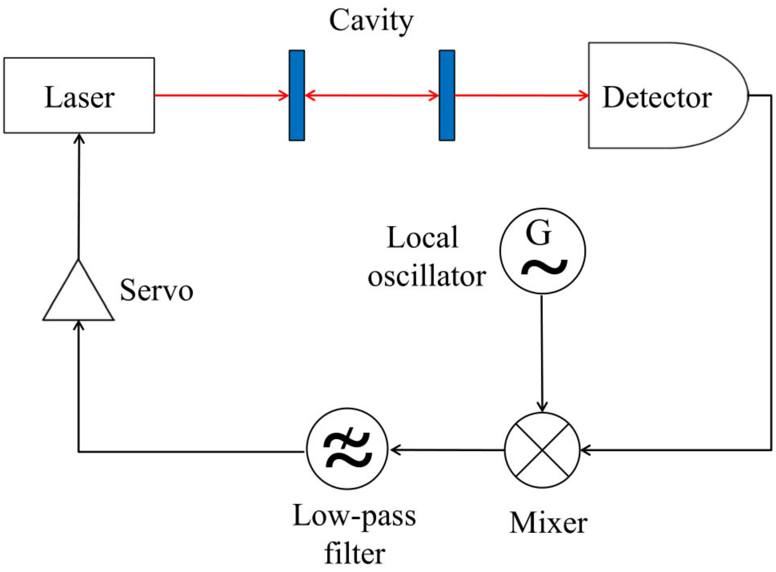

Figure 6.1: Basic scheme of the laser frequency stabilization by using PDH technique [97]. Red lines are optical paths while black lines are signal paths.

The electric field of the incident beam can be written by:

$$E(t) = E_0 e^{i\omega t}. \tag{6.1}$$

When the laser is phase modulated at a frequency Ω, its electric field becomes:

$$E(t) = E_0 e^{i(\omega t + \beta \sin \Omega t)}, \tag{6.2}$$

where β is the modulation depth (modulation index).

By using Bessel functions, this expression (Equation 6.2) can be expanded to:

$$\begin{aligned} E(t) &\approx [J_0(\beta) + 2iJ_1(\beta)\sin \Omega t]e^{i\omega t} \\ &= E_0[J_0(\beta)e^{i\omega t} + J_1(\beta)e^{i(\omega+\Omega)t} - J_1(\beta)e^{i(\omega-\Omega)t}]. \end{aligned} \tag{6.3}$$

Here, J_k ($k = 0$, 1) are the kth order Bessel functions. It can be seen that the wave sent to the cavity contains three parts: one carrier at a frequency of ω, and two sidebands at frequencies of $\omega \pm \Omega$. The power ratio of the carrier and the sidebands is determined by the modulation depth β. After coupling the beam into the cavity, the carrier and the sidebands independently interfere with the cavity resonator and the reflection (or transmission) from the cavity is subsequently detected by a fast photodiode. The light intensity detected can be described as [97]:

$$\begin{aligned} P(t) &= P_c\,|F(\omega)|^2 + P_s\,\{\,|F(\omega+\Omega)|^2 + |F(\omega-\Omega)|^2\,\} \\ &+2\sqrt{P_cP_s}\,\{\mathrm{Re}\,[F(\omega)F^*(\omega+\Omega) - F^*(\omega)F(\omega-\Omega)]\cos\Omega t \\ &+\mathrm{Im}\,[F(\omega)F^*(\omega+\Omega) - F^*(\omega)F(\omega-\Omega)]\sin\Omega t\,\} \\ &+(2\Omega \text{ terms}), \end{aligned} \tag{6.4}$$

where

$$F(\omega) = \frac{R(e^{i\omega/2\pi\nu} - 1)}{1 - R^2e^{i\omega/2\pi\nu}}. \tag{6.5}$$

Here, P_c and P_s represent the powers of the carrier and the sidebands, respectively. R is the reflectivity of the cavity mirror and $\nu = c/2L$ is the cavity free spectral range.

The output of the photodiode is mixed with a local oscillator's signal via a mixer, whose output contains both the DC (or very low frequency) and the modulation signal. After a low-pass filter, the modulation frequency is filtered out and the DC (or very low frequency) signal is sent to a servo amplifier. By measuring the derivative of the reflected intensity from the photodiode concerning frequency, the servo system will feed the variation back to the laser and hold it locking to the cavity.

6.2 Schematic of the transfer cavity system

In principle, a frequency modulator around the wavelength of 5.5 μm could be directly applied to shift the QCL laser frequency. However, such a frequency modulator is often expensive. On the other hand, the DFB lasers with frequency modulators around 1.5 μm, photodiodes for 5.5 μm and 1.5 μm, and several optical mirrors

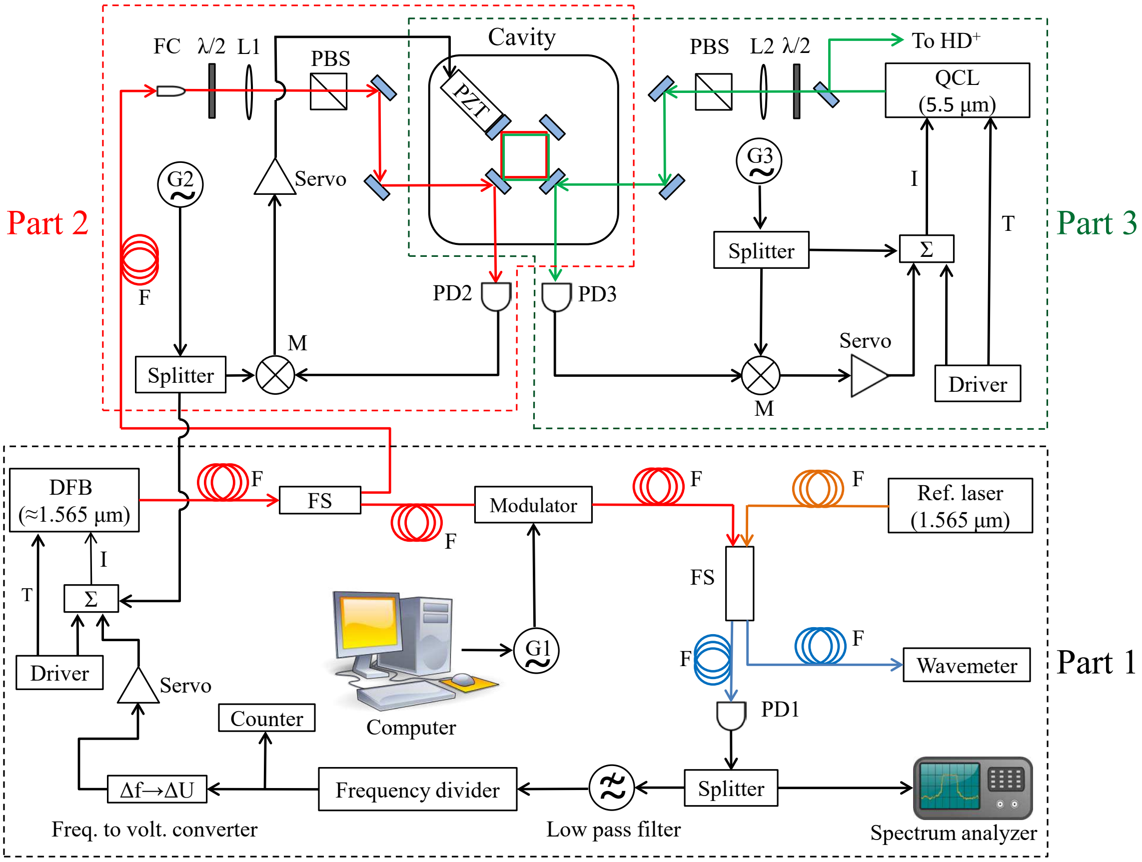

Figure 6.2: The schematic diagram of the transfer cavity. Part 1: One sideband of the DFB laser is locked to a reference laser. Part 2: The cavity is locked to the carrier of the DFB laser. Part 3: The QCL is locked to the cavity. Red: DFB laser at 1.565 μm; orange: reference laser at 1.565 μm; blue: beat notes between the DFB laser and the reference laser; green: QCL at 5.5 μm. F: optical fiber; FS: fiber splitter; I: current control; T: temperature control; Σ: adder; G: frequency generator; PD: photodiode; FC: fiber coupler; L: optical lens; PBS: polarization beam splitter; PZT: piezoelectric actuator; M: mixer.

including dichroic mirrors are already available in our laboratory. Thus, as an alternative method to achieve the same goal of the QCL frequency controlling, a transfer cavity system has been developed by using these already existing components.

Figure 6.2 shows a schematic diagram of the transfer cavity system that is composed of three parts.

Part 1: DFB laser locking system. After a 50:50 fiber splitter, a fiber-tailed DFB laser propagates partially to the cavity and partially to an electro-optic modulator

(EOM, Lucent 2623N) to generate a pair of sidebands of which their frequencies are controlled by a computer. By applying a reference laser that is phase-stabilized to a frequency comb with the same center frequency as the DFB laser, three phase-locked beat notes (one is from the DFB laser carrier, the other two are from the DFB sidebands with the reference laser, respectively) are monitored with a spectrum analyzer (Rohde & Schwarz, FS300, 9 kHz $\sim$ 3 GHz). A low-pass filter with a cutoff frequency of 400 MHz is used to let only the sideband that is at the lower frequency side pass through. By an electronic feedback loop, this sideband is locked to the reference laser. Thus, via adjusting the frequency of the generated DFB sideband by the computer, the carrier frequency could be correspondingly tuned.

Part 2: Cavity locking system. Figure 6.3 shows the ring cavity that is used in our system which consists of two plane mirrors M_1 and M_2 at a distance of 72 mm and two concave mirrors M_3 and M_4 (200 mm radii of curvature). The distance between M_1 and M_4 is 75 mm. M_1 and M_2 are used for coupling of the DFB laser and the QCL to the cavity, respectively. Mirror M_4 is mounted on a piezoelectric actuator.

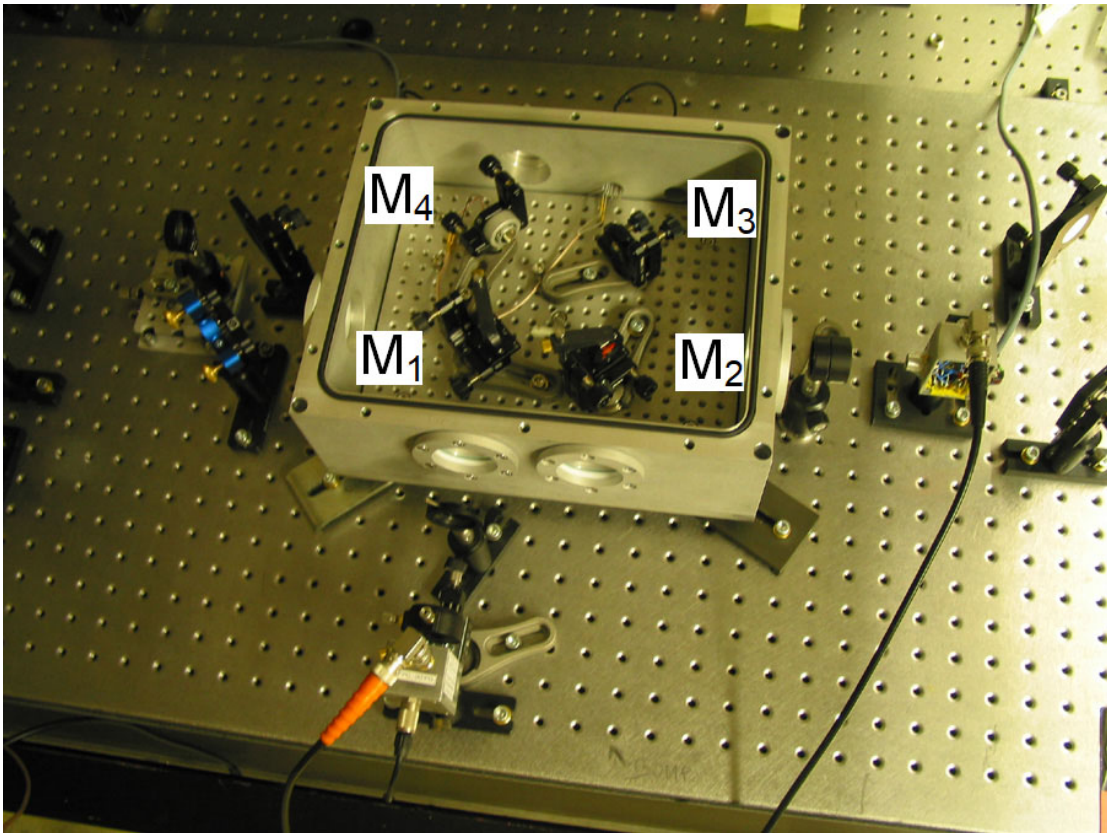

Figure 6.3: Photograph of the cavity.

As Figure 6.2 (Part 2) shows, a fiber coupler with a lens L1 is used to couple and collimate the DFB laser from the fiber to the free space. As a guiding beam, a fiber-tailed semiconductor laser at a wavelength of 532 nm is connected to the fiber coupler for alignment purposes and is then replaced with the DFB laser. The photodiode PD2 records the signals from the reflected light of the DFB laser from the mirror M_1 and the transmitted light of the DFB laser after the round trips in the ring cavity. Due to the linear-polarization dependence of the cavity, a $\lambda/2$-plate and a polarization beam splitter are inserted to increase the signal-to-noise ratio on the photodiode PD2. In this locking system, the piezoelectric actuator of the cavity that is connected with an electronic feedback loop is applied to stabilize the optical path length in the ring cavity to the DFB laser.

Part 3: QCL locking system. The QCL at a wavelength of 5.5 μm combined with a He-Ne laser as a guiding beam is the target laser that is planned to be frequency controlled by the system. By using a similar locking scheme as described in part 2, the frequency of the QCL is locked to the cavity.

Thus, the frequency of the QCL is ultimately controlled by the sideband generation of the DFB laser that is governed by a LabVIEW program in computer.

Figure 6.4 shows the working transfer cavity system that is employed in the HD$^+$-lab. By fixing all the functional components of the apparatus on a 120 cm × 60 cm breadboard, the system is designed to be transportable and could be applied to some other lasers in the future as well.

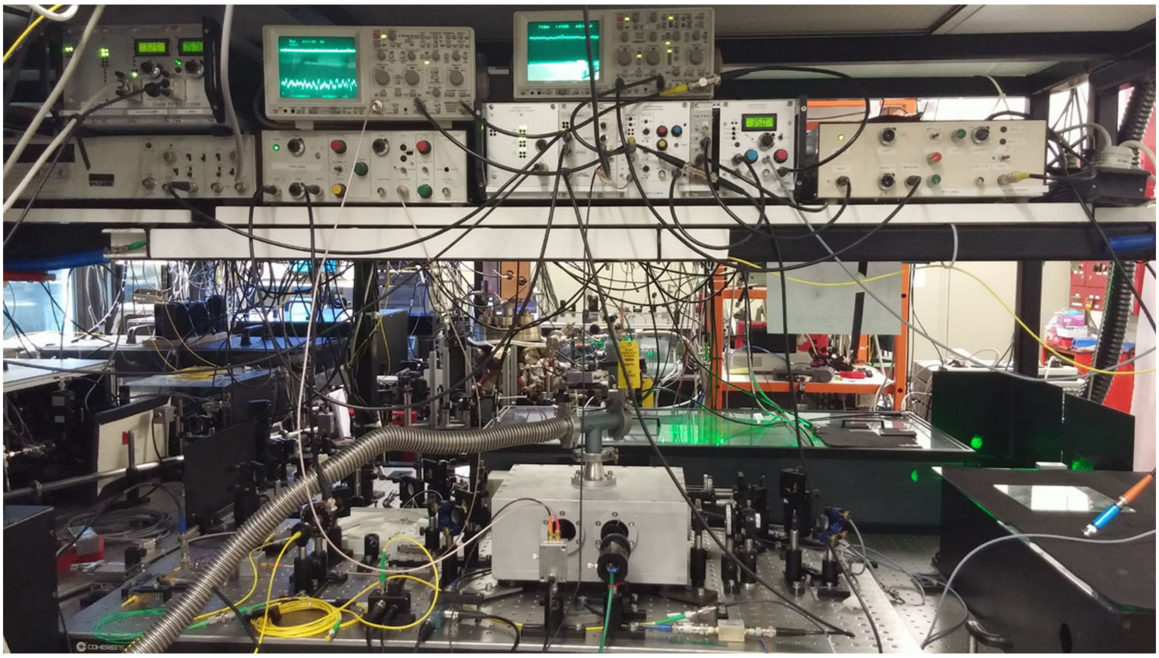

Figure 6.4: Photograph of the transfer cavity setup in the HD$^+$-lab.

6.3 The lasers

6.3.1 DFB laser and reference laser

The fiber-tailed DFB laser diode (Eblana Photonics, type EP1550-NLW-B) is driven by a laboratory self-made temperature and current module with the temperature set to 30.5 °C and the initial current set to 104 mA. The output power of the DFB laser is 7.6 mW.

The reference laser (Koheras BasiK) at a wavelength of 1564.603 nm with a max. output power of 10 mW is also fiber-tailed and has a narrow linewidth (ca. 3 kHz). Its frequency is tuned by a built-in piezo element and stabilized by an frequency comb. In this experiment, an output power of 2.5 mW of the laser is used, which is sufficient to make beat notes with the above-mentioned DFB laser.

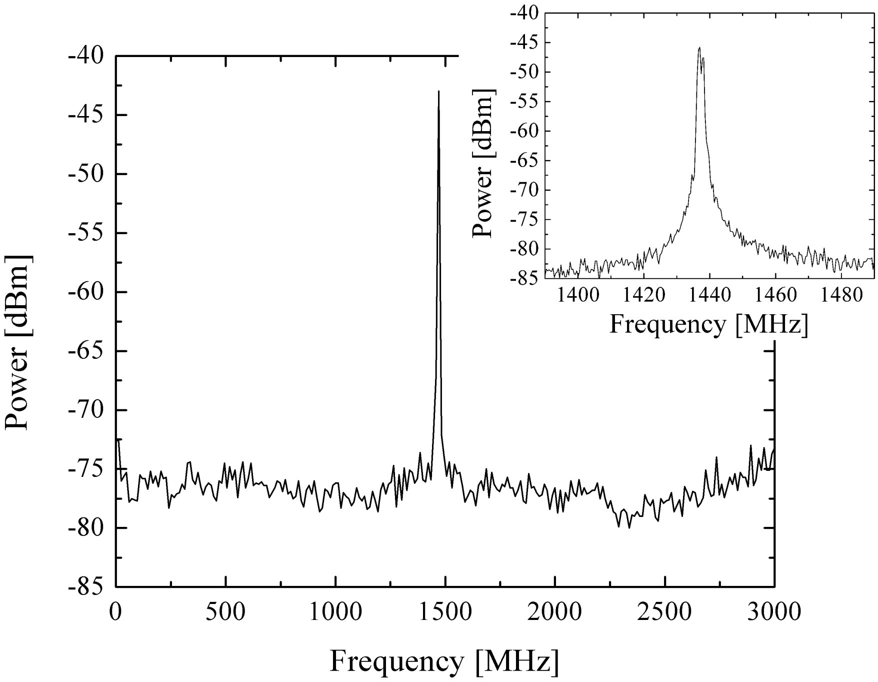

Figure 6.5: Beat note signal between the DFB laser (Eblana Photonics, type EP1550-NLW-B) and the reference laser (Koheras BasiK) measured by the spectrum analyzer when sideband generation is kept off. The inset shows the signal in a short frequency range measured by another day. Here, the beat note is used to determine the unknown DFB laser frequency, since the reference laser is already frequency stabilized by a frequency comb. A description of direct frequency measurement by counting beat notes between an unknown CW laser source and a frequency comb can be found in Ref. [99].

By using the scheme described in part 1 of section 6.2, the beat note signals are recorded by the spectrum analyzer when the sideband generation is kept off (see Figure 6.5) and on (see Figure 6.6). Here, for clarity, the beat notes of the carrier and the sidebands at the lower and higher frequency side of the DFB laser with the reference laser are denoted as “C”, “S1”, and “S2”, respectively, while the frequency generated by the generator is marked as “G”.

Since the frequency of the DFB laser diode is temperature and current dependent, the current of the DFB laser is adjusted (the temperature remains constant) until “S1” reaches 0 ∼ 400 MHz region. A low-pass filter is inserted to pass the signal of “S1” and block “G”, “C”, and “S2”. Consequently, by using an electronic feedback loop, the “S1” is locked to the reference laser.

Note: to avoid the occurrence of locking error, the frequency of “G” should not be set lower than the cutoff frequency of the low-pass filter, i.e. 400 MHz in this case.

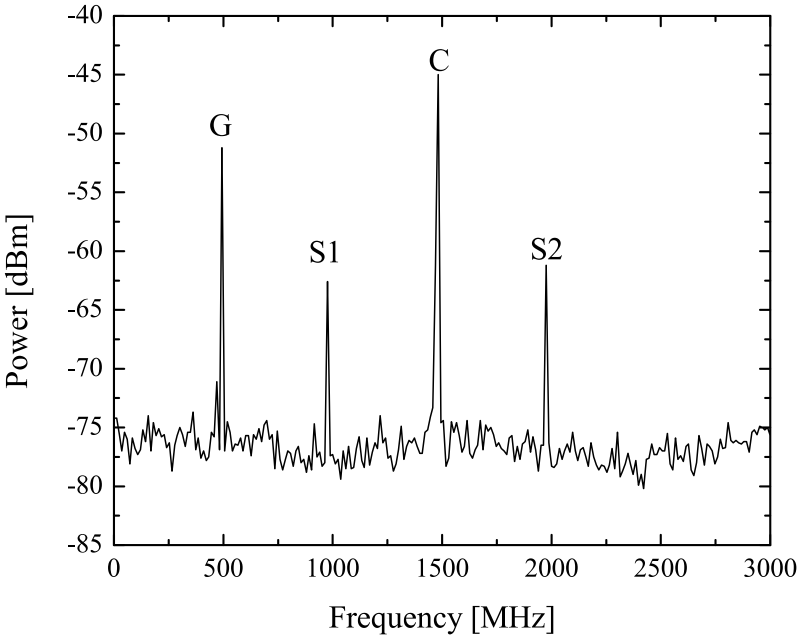

Figure 6.6: Beat note signal measured by the spectrum analyzer when sideband generation is kept on. C: carrier; S1: sideband at the lower frequency side; S2: sideband at the higher frequency side; G: frequency generated by the generator.

It is worth mentioning that to improve the frequency tunability of the transfer cavity system, the generator employed for the sideband generation is crucial, requiring a wide frequency tuning range without frequency jump. However, almost all the commercially available frequency generators, as is known, have several such "discontinuity points" during frequency sweeping especially in a large range, which is similar to the gear shift in automotive transmissions. By testing all the frequency generators that are available in our laboratory with the assistance of the spectrum analyzer, the synthesizer of Agilent HP 8341A shows no frequency jump in a relatively wide range between 2300 MHz and around 7000 MHz and is thus chosen for our application.

6.3.2 QCL (5.5 μm)

The 5.5 μm QCL (Alpes Lasers SA) is used as a repumping source for spectroscopy of HD^+. The laser chip is mounted on a thermoelectric cooler (TEC) that is controlled by a temperature control unit TCU 151 (Alpes Lasers SA). The temperature control range is from -30 to $+20$ °C with an accuracy of 0.1 °C. The laser chip with the TEC is operated in a laser housing with a water cooling system to remove the heat efficiently. The typical working temperature of the laser chip in this experiment is 5.0 °C. The current is provided by a commercial current source (ILX Lightwave, type LDX-3220) with a typical operating value of 432 mA.

As shown in Figure 6.7, by using an absorption line of ammonia (NH_3) as a reference, this QCL was previously stabilized to a frequency of 1823.53302 cm^{-1} which is the desired center frequency of the $(v = 0, L = 2) \rightarrow (v' = 1, L' = 1)$ rovibrational transition of HD^+ ion. In order to cover all the hyperfine transitions, the QCL frequency was broadened to 100 MHz, which satisfies nearly all the requirements of our previous spectroscopic tasks. However, with such a frequency locking scheme, the QCL frequency cannot be finely tuned for HD^+ hyperfine pumping purposes.

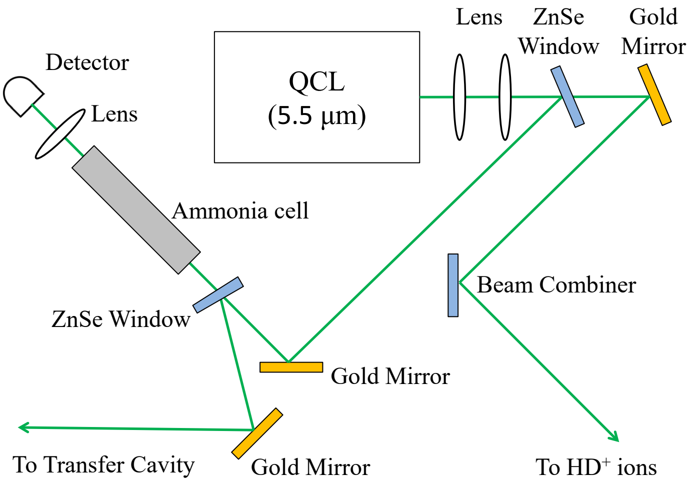

Figure 6.7: Schematic of the 5.5 μm QCL.

In order to combine this QCL to the transfer cavity system, a ZnSe window is inserted in front of the NH_3 gas cell (see Figure 6.7), which allows a portion of the laser to propagate to the transfer cavity system. Thus, the frequency of the QCL can be either locked to the gas cell or controlled by the transfer cavity system. This is also a good demonstration that the system could be applied to other lasers for frequency controlling purposes since all the functional components of the system are built on a breadboard to be transportable.

6.4 Frequency stability measurement

The whole system of the transfer cavity was initially developed in our HD^+-lab and subsequently transported in our comb-lab to test the frequency stability with the assistance of the frequency comb, which is an important step before applying it to the HD^+ spectroscopy project.

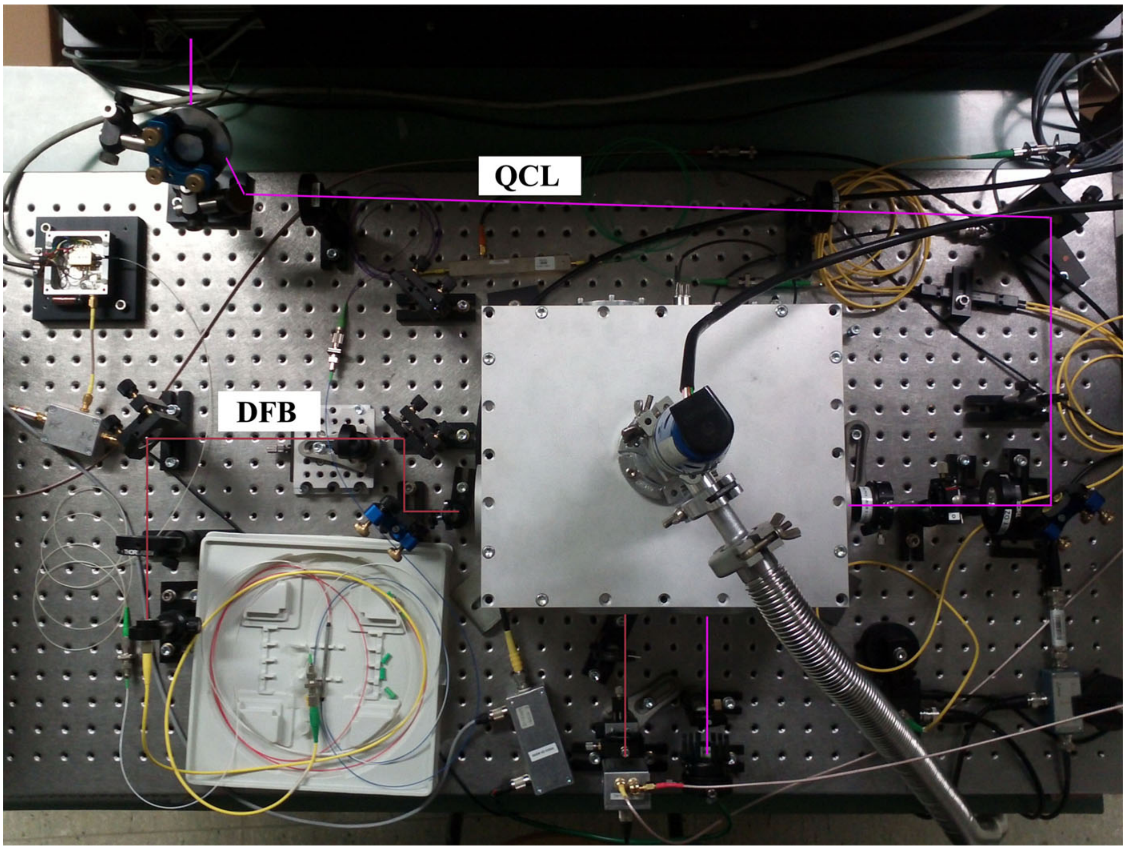

Figure 6.8: Photograph of the transfer cavity apparatus transported to the comb-lab. The DFB laser is drawn in red, while the QCL (5.4 μm) is in purple. In order to avoid the chromatic dispersion of the air, the cavity is operated in a vacuum chamber with a vacuum kept at 10^{-2} mbar. A frequency comb (not shown here) is used to measure the frequency of QCL precisely.

Instead of the involved QCL setup at a wavelength of 5.5 μm in HD$^+$-lab due to the inconvenience of transportation to the comb-lab, an alternative QCL at a wavelength of 5.4 μm built directly in the comb-lab was employed for the test purposes, thanks to an independent project of a laser spectrometer based on frequency comb metrology in our research group [100].

Figure 6.8 shows the transfer cavity setup that is transported to the comb-lab. For clarity, the DFB laser beam is colored in red while the QCL beam (5.4 μm) in purple. Due to the large wavelength difference between these two lasers, the cavity is installed in a vacuum chamber with a vacuum kept at 10^{-2} mbar to avoid the chromatic dispersion of the air.

6.4.1 Frequency comb

An optical frequency comb contains a huge number of "comb needles", shown in Figure 6.9. These "needles" are actually narrow-band laser modes of the frequency comb with fixed positions spread in the comb frequency range. The nth comb mode frequency f_n is given by:

$$f_n = f_{ceo} + n f_{rep} \tag{6.6}$$

with integer n, where f_{ceo} is the carrier-envelope offset frequency, while f_{rep} stands for the repetition rate of the comb.

In our laboratory, a home-modified frequency comb (Menlo Systems FC8004) based on a Ti:Sapphire short-pulse (fs) laser (Femtolasers FemtoSource Scientific 2000) has been used for several years. In this work, a new type of frequency comb (Menlo Systems FC1500-250-WG) is used to detect the QCL laser frequency more precisely. The key element of this new comb is a 250 MHz erbium-doped fiber oscillator with the spectral range broadened to near-infrared (NIR), i.e. 1050 $\sim$ 2100 nm. It generates the comb spectral structure with the repetition rate and can be remote-controlled by a computer program to realize a mode tuning. The carrier-envelope offset frequency is determined by a nonlinear interferometer. By using three EDFA modules and a supercontinuum generation module, this type of comb is much more compact and is made to be transportable.

For frequency stabilization, the comb is phase-locked to an optical reference with a linewidth of 1 Hz, while the optical reference is stabilized to an ultra-high-finesse ultra-low-expansion (ULE) cavity. In addition, a GPS-disciplined ultrastable hydrogen maser that produces a 10 MHz RF signal is used to actively stabilize the carrier-envelope offset frequency and the comb repetition rate.

To measure the frequency of a continuous-wave (CW) laser with the comb, a wavemeter is first applied to make a rough measurement. Then the corresponding comb modes are selected and heterodyned with the laser, while the other comb modes are suppressed by a diffraction grating in the laser beam pass or by suitable pass filters.

Subsequently, a frequency counter in the comb counts the beat notes by using a fast photodetector. Thus, the frequency of the CW laser is finally determined precisely.

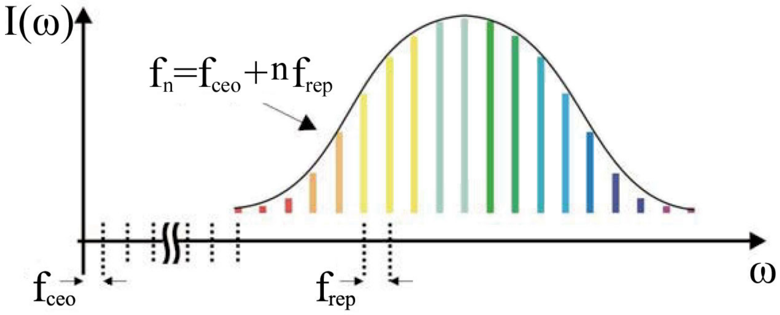

Figure 6.9: Schematic of the frequency comb spectrum. f_n, f_{ceo}, and f_{rep} are the mode frequency, the carrier-envelope offset frequency, and the repetition rate of the comb, respectively [99].

6.4.2 Scheme of frequency measurement with the frequency comb

When locked to the cavity, the frequency stability of the QCL reflects the stability of the total system. The schematic of the QCL frequency measurement is shown in Figure 6.10.

In this measurement, the new frequency comb (Menlo Systems FC1500-250-WG) is employed to detect the frequency fluctuation. Since its working spectral range is from 1050 nm to 2100 nm, nonlinear frequency conversion is applied by using the quantum phase matching (QPM) technique with an orientation-patterned gallium arsenide (OP-GaAs) crystal.

A sum-frequency at a wavelength of 1.2 μm is generated by the QCL and a fiber laser with the nonlinear-optical conversion in the OP-GaAs crystal, which can be described by:

$$\nu_{\text{SFG}} = \nu_{\text{QCL}} + \nu_{\text{fiber laser}}, \tag{6.7}$$

where ν_{SFG}, ν_{QCL}, and $\nu_{\text{fiber laser}}$ stand for the frequency of the sum-frequency, QCL, and the fiber laser.

The QCL (5.4 μm) is water cooled and temperature stabilized. The current is mainly controlled by a commercial current source (Wavelength Electronics, QCL1500). When the laser is locked to the transfer cavity, its frequency can be tuned by a feedback loop of the current modulation with a bandwidth of 1 MHz.

The fiber laser (wavelength at 1565.65 nm, linewidth 3 kHz) has an original output power of 10 mW and is divided into three parts. The first part is amplified by a 10-W EDFA (Keopsys) and is then delivered to the OP-GaAs crystal. The rest two are used for frequency stabilization purposes: one is sent to a wavemeter for frequency monitoring, while the other makes a beat note with the frequency comb. A feedback loop is applied to stabilize the frequency of the fiber laser with a signal-to-noise ratio of 40 dB.

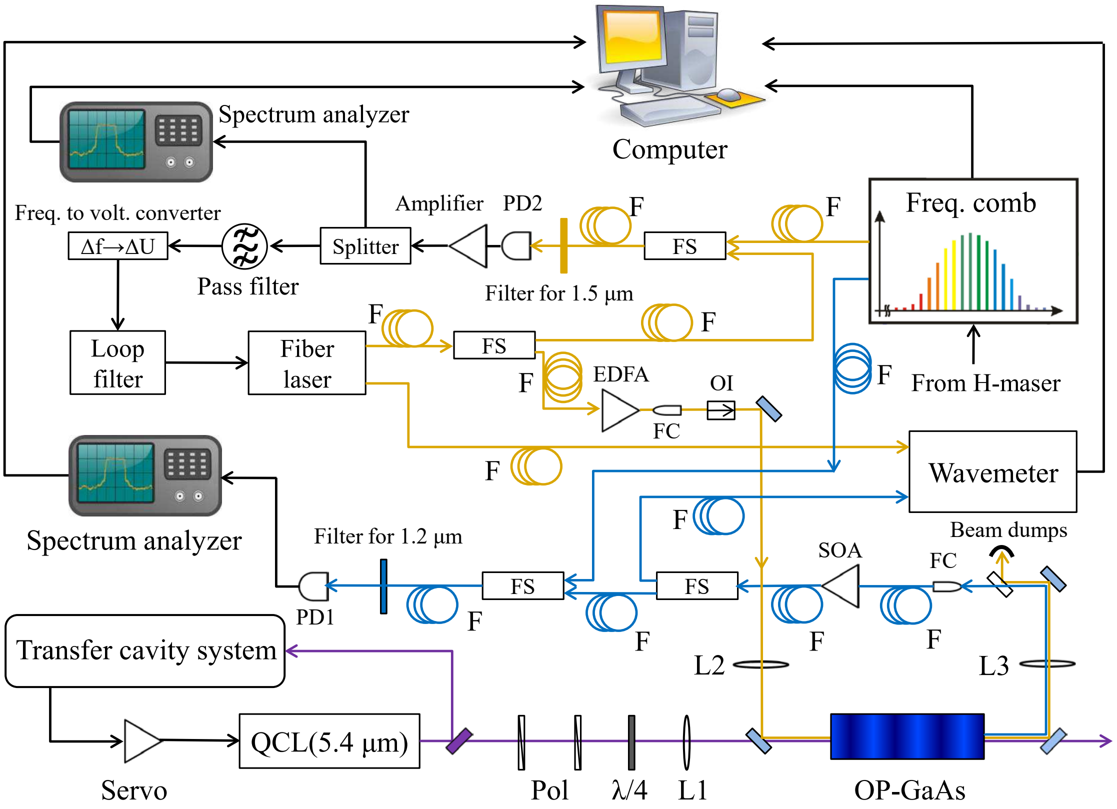

Figure 6.10: Schematic of the QCL frequency measurement with the frequency comb. Purple: QCL at 5.4 μm; yellow: fiber laser at 1.5 μm; blue: sum frequency at 1.2 μm. PD: photodiode; F: optical fiber; FS: fiber splitter; EDFA: erbium-doped fiber amplifier; FC: fiber coupler; OI: optical isolator; SOA: semiconductor optical amplifier; L: lens; Pol: polarizer. The orientation patterning period of the OP-GaAs crystal is 49.1 μm and the length of the crystal is 17 mm.

6.4.3 Results of frequency stability measurement

By using the scheme as shown in Figure 6.10, the frequency stability measurement has been performed. According to Equation 6.7, the frequency shift of the sum-frequency generation represents exactly the frequency stability of the QCL since the fiber laser is already stabilized by the comb.

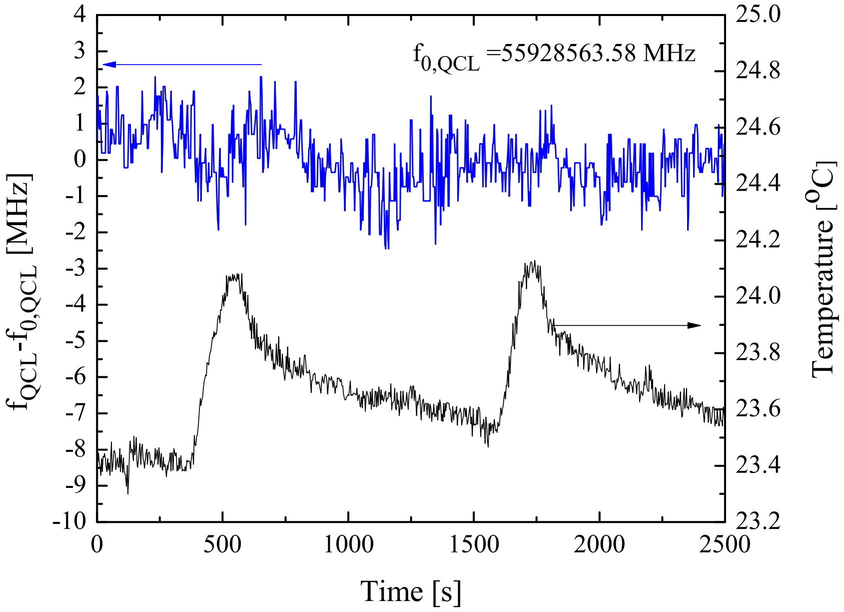

Figure 6.11: Temperature independence of QCL (5.4 μm) frequency. Left side: QCL frequency drift (in blue); right side: cavity temperature (in black). The cavity-heater is switched on and off alternatively to simulate the typical temperature fluctuation in the laboratory.

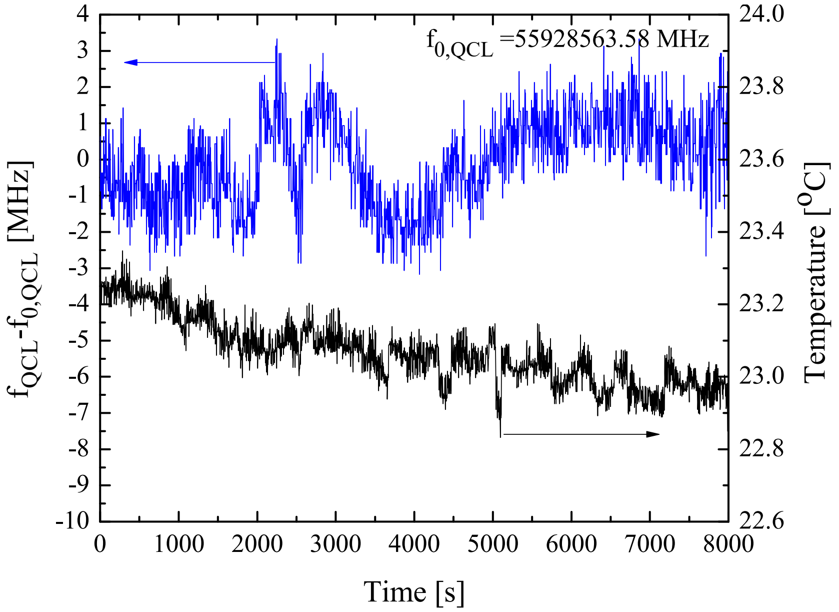

Figure 6.12: Long-term frequency stability of the QCL (5.4 μm). Left side: QCL frequency drift (in blue); right side: cavity temperature (in black). The cavity-heater is switched on at the beginning of the measurement and kept off for the remained measurement time.

The room temperature instability in our HD$^+$-lab where the transfer cavity system operates ultimately is typically less than 0.5 °C by using our laboratory self-made temperature stabilization system [38]. To simulate this fluctuation, a compact heater and a temperature sensor are installed separately inside the vacuum chamber in different corners to heat up the cavity and meanwhile record the temperature.

In the first measurement, the cavity-heater is switched on and off alternatively, causing the cavity temperature to change by ca. 0.7 °C (despite the temperature gradient in the cavity), which simulates the typical temperature fluctuation in the laboratory. Meanwhile, the frequency of the sum-frequency generation is recorded. As shown in Figure 6.11, the frequency fluctuation of the QCL within a range of ±2 MHz is irrelevant to the cavity temperature.

Normally, each experiment of HD$^+$ spectroscopy lasts for several hours. Therefore, as the second measurement, the long-term frequency stability of the transfer cavity system has been tested with the cavity-heater switched on at the beginning of the measurement and kept off for the remained measurement time. As can be seen in Figure 6.12, the frequency fluctuation of the QCL in a time scale of ca. 2.5 hours is within ±3 MHz, which is smaller than the HD$^+$ Doppler broadening and meets our requirement for the application in the HD$^+$-project.

6.5 Frequency tunability measurement

When locked to the transfer cavity, the QCL is ultimately frequency controlled by the DFB laser. The relation between the QCL frequency tuning Δf_{QCL} and the DFB frequency change Δf_{DFB} is given by:

$$\Delta f_{\mathrm{QCL}} = \frac{\lambda_{\mathrm{DFB}}}{\lambda_{\mathrm{QCL}}} \cdot \Delta f_{\mathrm{DFB}}. \tag{6.8}$$

Here, the dispersion effects could be neglected due to the vacuum conditions.

Figure 6.13 shows the result of the reflection scan of the cavity. At the wavelength of 5.5 μm, the cavity has a free spectral range of about 1 GHz with a width of the reflection peak of ca. 100 MHz, while at 1.5 μm, the free spectral range is approx. 300 MHz, which is in accordance with Equation 6.8. When locked to the cavity, the linewidth of the QCL is mainly determined by the jitter of those reflection peaks, which is estimated to be less than 10 MHz.

Note that this measurement is performed with the QCL at 5.5 μm in our HD$^+$-lab since it does not require special types of test equipment that are installed in our comb-lab.

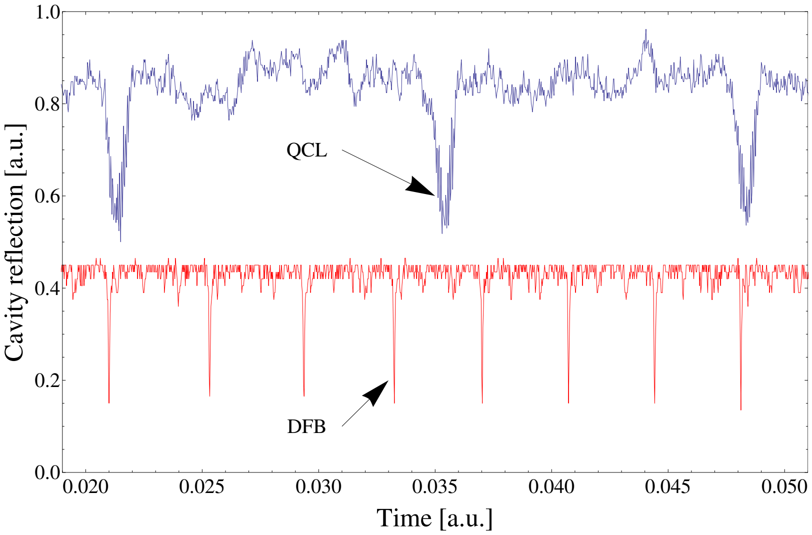

Figure 6.13: Reflection scan of the cavity at 5.5 μm (QCL, in blue) and 1.5 μm (DFB, in red).

To test the frequency tuning ability of the transfer cavity, the QCL (5.4 μm) in our comb-lab is connected to the system with the same test scheme as shown in Figure 6.10. In this measurement, the sidebands of the DFB laser are generated by a commercial synthesizer (HP8341) that has a relatively wide frequency tuning range from 2300 MHz to around 7000 MHz without frequency jump. The frequency tuning of the QCL (5.4 μm) is recorded by the frequency comb. As Figure 6.14 shows, the measurement starts with the QCL in a free-running mode. It can be seen that the QCL frequency drifts randomly without locking. When locked to the transfer cavity with the initial DFB sideband frequency set to 2350 MHz and the beat note signal of the carrier (see Figure 6.6) tuned to 2550 MHz, the QCL is stabilized to the zero-detuned frequency, denoted as $f_{0,\mathrm{QCL}}$. Afterwards, the DFB sideband frequency starts to sweep from 2350 MHz to 6810 MHz, leading to the corresponding QCL frequency tuning by 1.2 GHz. Finally, the measurement ends with a frequency jump due to the above-mentioned reason.

In this measurement, the QCL (5.4 μm) interrogates the transmission line of the nitrous oxide (N_2O) in a gas cell at 60 mbar. Thus, the transmission line is also recorded as a cross-check of the frequency tuning.

It should be pointed out that the frequency fast tuning ability of the system is extremely important since it is ultimately used to control the QCL (5.5 μm) for HD^+ hyperfine pumping purposes. To test this ability, by using the same procedure, the measurement is repeated by various sweeping time scales. It is found that as long as the DFB sideband frequency is within the above-mentioned range, the QCL frequency can be tuned immediately as the synthesizer (HP8341) sweeps and can be stabilized to the target frequency for several hours. One of the results is shown in Figure 6.15. It can be seen that the QCL frequency can be tuned fast within several seconds (or in an even shorter time scale, depending on the setting of the synthesizer). This measurement is repeated by three times, and the recorded transmission lines of N_2O show good system reliability.

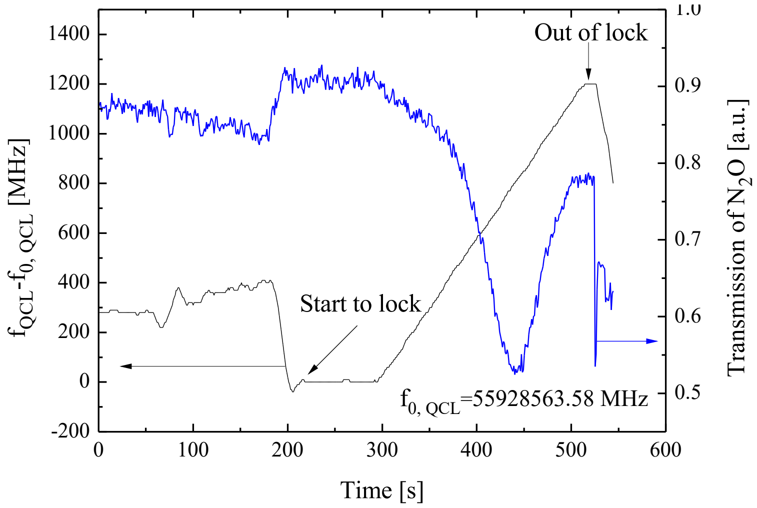

Figure 6.14: Frequency tuning ability of the transfer cavity. By sweeping the DFB sideband frequency from 2350 MHz to 6810 MHz, the QCL (5.4 μm) frequency can be tuned over a range of 1.2 GHz (left side, in black). As a cross-check, a transmission line of N_2O (right side, in blue) is recorded simultaneously.

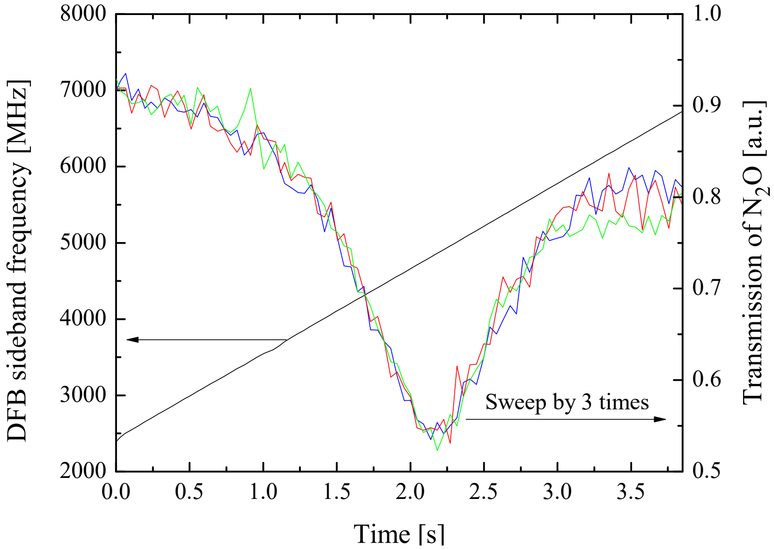

Figure 6.15: System reliability of the transfer cavity. Left side: the DFB sideband frequency is swept from 2350 MHz to 6810 MHz by three times within several seconds (in black); right side: the corresponding N_2O transmission lines (in blue, red, and green) are recorded and shows good reliability of the system.

6.6 Frequency calibration between DFB and QCL

According to Equation 6.8, in order to tune the QCL to a target frequency, the required corresponding DFB frequency can be calculated by:

$$f_{\mathrm{DFB}} = f_{\mathrm{DFB,0}} + \eta \times (f_{\mathrm{QCL}} - f_{\mathrm{QCL,0}}). \tag{6.9}$$

Here, the parameter $\eta = f_{\mathrm{DFB}}/f_{\mathrm{QCL}}$, where f_{DFB} and $f_{\mathrm{DFB,0}}$ are the target and original frequencies of DFB, while f_{QCL} and $f_{\mathrm{QCL,0}}$ are the corresponding frequencies of QCL, respectively.

After the test measurements were performed in the comb-lab, the whole transfer cavity system was transported back to the HD$^+$-lab. When the QCL (5.5 μm) is locked to the cavity and is used for hyperfine pumping of HD$^+$ in the $(v = 0,\ L = 2) \rightarrow (v' = 1,\ L' = 1)$ rovibrational transition, then $f_{\mathrm{QCL,0}}$ and f_{QCL} in Equation 6.9 could be defined as the spinless frequency of this transition (i.e. zero detuning with a calculated wave number of 1823.53302 cm^{-1}) and the desired detuning from the spinless transition frequency, respectively.

To precisely calculate f_{DFB} correspondingly, a frequency calibration between DFB and QCL is required. For this purpose, one approach is directly using the frequency comb, which was at that moment not available in the HD$^+$-lab. Therefore, an alternative method was performed as follows: since a small portion of the QCL (5.5 μm) interrogates the absorption line of the NH$_3$ gas (see Figure 6.7), the transmitted laser power after the NH$_3$ gas cell, as well as the lock-in signal, is recorded when scanning the QCL frequency by sweeping the sideband frequency of the DFB laser. As Figure 6.16 shows, the measurement was repeated twice, indicating the reliability and reproducibility of this method.

Here, at the zero-crossing point of the lock-in signal, the wave number of NH$_3$ is 1823.55698 cm^{-1} according to the database of HITRAN 2000. By reading the corresponding value of the DFB sideband frequency at this point (denoted as $f'_{\mathrm{DFB,0}}$) from the computer program, an expression similar to Equation 6.9 can be written as follows:

$$f_{\mathrm{DFB}} = f'_{\mathrm{DFB,0}} + \eta \times (f_{\mathrm{QCL}} - f'_{\mathrm{QCL,0}}). \tag{6.10}$$

Thus, a so-called “DFB frequency offset” in this case can be derived from Equation 6.9 and 6.10:

$$\begin{aligned} f_{\mathrm{DFB,offset}} &= f_{\mathrm{DFB,0}} - f'_{\mathrm{DFB,0}} \\ &= \eta \times (f_{\mathrm{QCL,0}} - f'_{\mathrm{QCL,0}}) \\ &= 3.505 \times (1823.55698\ \mathrm{cm}^{-1} - 1823.53302\ \mathrm{cm}^{-1}) \times c \\ &= 2517.7\ \mathrm{MHz}, \end{aligned} \tag{6.11}$$

where in this case, $\eta = 3.505$ and the light velocity $c = 29979245800$ cm/s. Thus, after calibration, Equation 6.9 could be written in the following form:

$$\begin{aligned} f_{\mathrm{DFB}} &= f'_{\mathrm{DFB},0} - f_{\mathrm{DFB,offset}} + \eta \times (f_{\mathrm{QCL}} - f_{\mathrm{QCL},0}) \\ &= f'_{\mathrm{DFB},0} - 2517.7\ \mathrm{MHz} + 3.505 \times (f_{\mathrm{QCL}} - f_{\mathrm{QCL},0}). \end{aligned} \tag{6.12}$$

Note that for different measurement days, the value of $f'_{\mathrm{DFB},0}$ might be different resulting from e.g. the slight change of the gas pressure of NH_3. Nevertheless, every time as soon as the QCL is locked to the transfer cavity, this procedure routine controlled by a computer program ensures a precise calibration and this effect from gas pressure change would be eliminated.

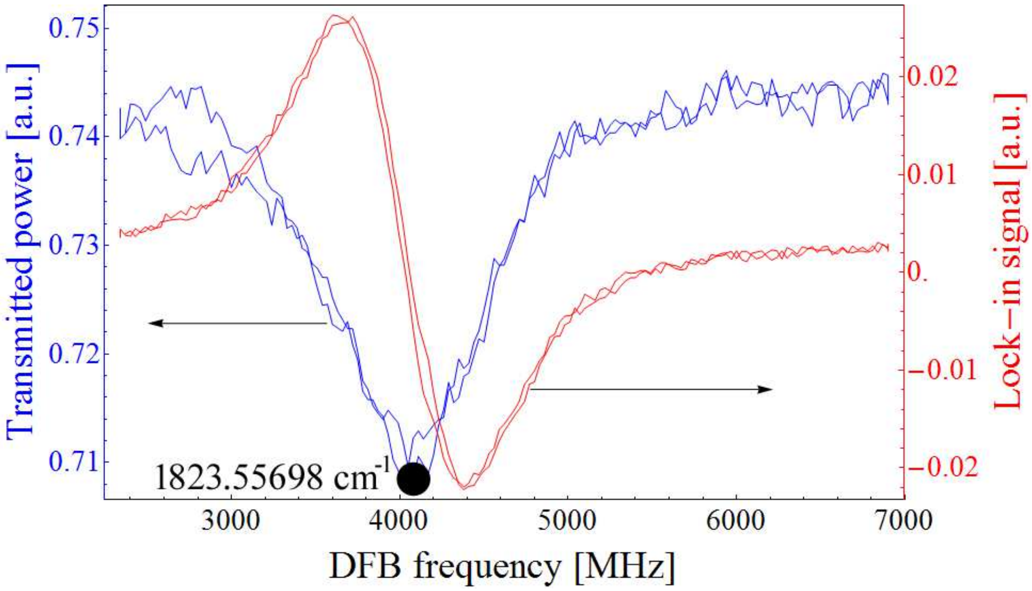

Figure 6.16: Transmitted laser power after the NH_3 gas cell with the gas pressure of 20 mbar.

6.7 QCL hyperfine pumping by using the transfer cavity

To test the reliability of the transfer cavity system, the frequency-controlled QCL was employed in the project of HD^+ spectroscopy.

Figure 6.17 shows the simplified energy levels of HD^+ ion with the $1+1'+1''$ REMPD scheme. When the HD^+ ions are sympathetically cooled by the atomic Be^+ ions, the molecular population is distributed among several rotational levels in the $v = 0$ manifold, while in other rovibraional levels including ($v = 1$, $L = 1$), there is no population without excitation. The QCL (5.5 μm) could nominally transfer the population from initial level ($v = 0$, $L = 2$) to the excited level ($v' = 1$, $L' = 1$). By using the REMPD lasers (i.e. 1475 nm and 266 nm), the population would be further transferred to the level ($v'' = 5$, $L'' = 2$) to be photodissociated.

Previously, the QCL was frequency broadened to 100 MHz and stabilized to resonance to cover almost all the dipole-allowed strong transitions. In the following experiment, the QCL is frequency controlled by the transfer cavity without broadening. Therefore, only when the QCL frequency addresses at least one hyperfine transition between the levels ($v = 0$, $L = 2$) and ($v = 1$, $L = 1$), the REMPD signal may be detected.

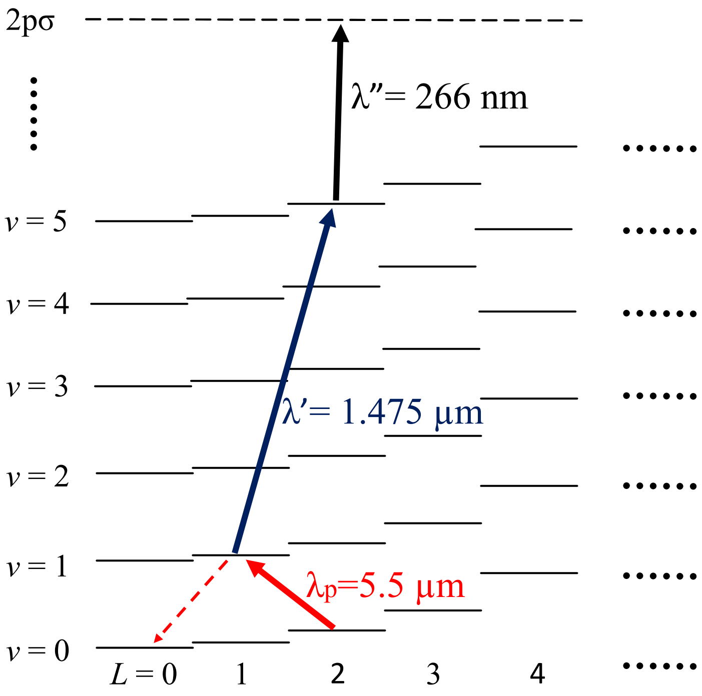

Figure 6.17: Simplified energy level scheme of molecular hydrogen ion HD$^+$ with relevant transitions for testing the reliability of the transfer cavity system. Full arrow: laser-induced transitions; dashed arrow: relevant spontaneous emission transition. The energy level differences are not to scale.

Figure 6.18 shows the energy diagram of the hyperfine states of the initial level ($v = 0$, $L = 2$) and the excited level ($v' = 1$, $L' = 1$). The hyperfine transitions at 1010.44 MHz and 1015.07 MHz detunings from the spinless transition frequency are chosen for QCL hyperfine pumping test purposes since these two low-Zeeman-shift transitions are far detuned from center frequency and are not affected by the other neighboring transitions (see Figure 7.2 (b) in chapter 7).

Similar to method II in subsection 5.5.3 (see Figure 5.8), the detection procedure is as follows: during the first secular excitation, all the lasers, including the REMPD lasers (i.e. 1475 nm and 266 nm) and the QCL with detuned frequency are initially blocked. Afterwards, all the lasers are unblocked to perform the $1 + 1' + 1''$ REMPD sequence for 20 seconds, followed by the second secular excitation to record the reduced Be$^+$ fluorescence level.

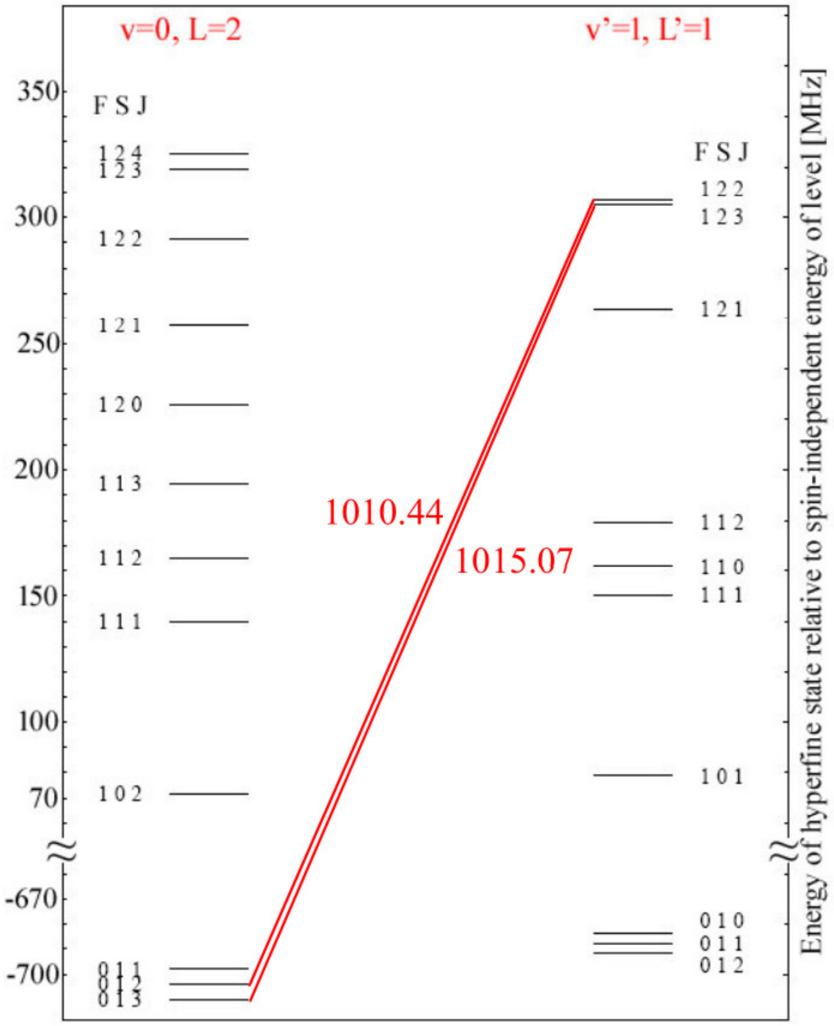

Figure 6.18: Energy diagram of the hyperfine states of HD$^+$ ion and relevant electric-dipole-allowed transitions in the zero magnetic field for testing the reliability of the transfer cavity system. Left side and right side show the hyperfine states in levels ($v = 0,\ L = 2$) and ($v' = 1,\ L' = 1$), respectively. The quantum numbers ($F,\ S,\ J$) are used to label the hyperfine states and each hyperfine state has a degeneracy factor of $(2J + 1)$.

The measured transition signal when the QCL frequency is near 1012 MHz detuning from the spinless frequency of the transition $(v = 0,\ L = 2) \rightarrow (v' = 1,\ L' = 1)$ will be shown in Figure 7.7 (b) in chapter 7 for demonstration purposes. The result reveals that the experimentally obtained spectrum is consistent with the theoretical calculation of 1010.44 MHz and 1015.07 MHz that contribute to the excitation, indicating that the transfer cavity system is able to control the QCL frequency and could be employed in the HD^+-project.

6.8 Conclusion and discussion

Under the motivation of performing QCL hyperfine pumping of HD^+, a transportable transfer cavity system was developed. The frequency stability and tunability of the system were measured with the reference of the frequency comb. Eventually, the system has been fully used in the spectroscopic study of doubly-spin-forbidden rovibrational transitions in HD^+, which will be described in chapter 7.

Since the system is built on a transportable breadboard and the cavity is held in a vacuum environment to avoid chromatic dispersion of the air for a large range of wavelengths, it is also applicable for frequency controlling of other lasers after calibration.

As mentioned in subsection 6.3.1, the frequency tuning range is mainly restricted to the generator applied for the sideband generation of the DFB laser. If a better generator or synthesizer is applied with a wider frequency sweeping range without a jump, the frequency tuning range would be in principle extended. Nevertheless, so far, the system satisfies the requirement well for the HD^+ hyperfine pumping purposes.

7 Spectroscopy of doubly-spin-forbidden transitions of HD$^+$ ions

Spectroscopic transitions in atoms and molecules in which the rotational angular momentum, nuclear spin, and total electronic spin are non-zero, show an abundant hyperfine structure. Due to the coupled angular momentum, the rovibrational transitions between energy levels are classified into allowed, spin-forbidden, and doubly-spin-forbidden transitions by the selection rules. The latter two are extremely weak and therefore exhibit very narrow natural linewidths. In the last few years, these weak transitions in atoms are of significant interest in the field of quantum optics and have been extensively studied towards several applications in quantum information processors [101], quantum simulators [102], and next-generation atomic clocks [103, 104], etc.

However, such transitions in molecules are much less reported, due to the enormous challenges to address them. In this work, by taking advantage of the developed transfer cavity system that is described in chapter 6, laser excitations of various doubly-spin-forbidden rovibrational transitions of molecular hydrogen ions HD$^+$ were performed. The HD$^+$ ions were sympathetically cooled by the atomic Be$^+$ ions to a secular temperature of approximately 10 mK. The weak transitions of HD$^+$ were driven by a QCL or a CW optical parametric oscillator (OPO). In the latter case, rotational cooling and hyperfine pumping by the QCL were employed additionally for the purpose of excitation signal enhancement. In both cases, the QCL was controlled by the transfer cavity system. For the transition detection, the method of REMPD was used.

In section 7.1, the hyperfine structure and the relevant hyperfine transitions including the doubly-spin-forbidden transitions of the lower and upper rovibrational levels of HD$^+$ ion are introduced. In section 7.2, the detection scheme of these weak transitions by using the REMPD method is shown. In section 7.3, the experimental apparatus including the OPO and QCL, as well as the measurement procedures, are described. Finally, the results of detection of the doubly-spin-forbidden hyperfine transitions are presented in section 7.4 and are further discussed in section 7.5.

It should be specially mentioned that due to the complexity of this experiment including the theoretical calculations and experimental preparations, this work would not be done without the theoretical support from Prof. S. Schiller and the good cooperation and teamwork from Dr. A. Borodin for operating the OPO and participating in the measurements.

7.1 Hyperfine structure of the lower and upper rovibrational levels

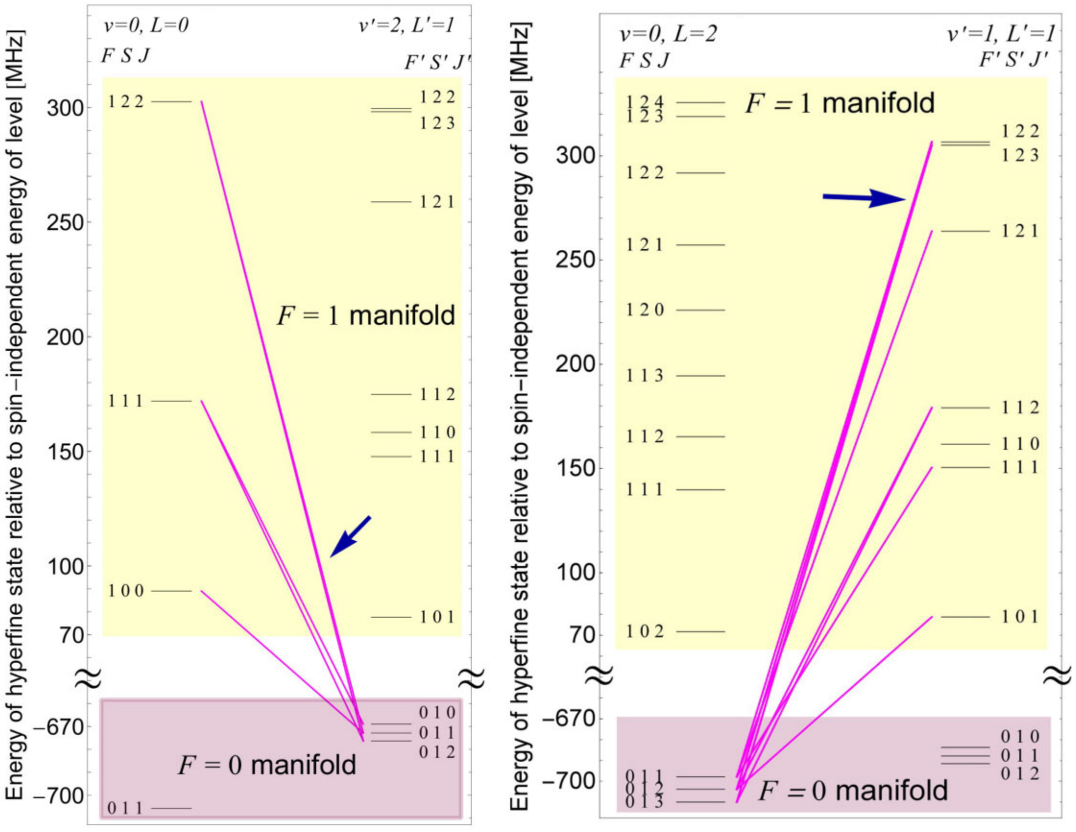

(a) (b)

Figure 7.1: Energy diagrams of the hyperfine states in the rovibrational levels of HD$^+$ ion with relevant transitions: (a) between $(v = 0, L = 0)$ and $(v' = 2, L' = 1)$; (b) between $(v = 0, L = 2)$ and $(v' = 1, L' = 1)$ [105]. The hyperfine states are labeled by the (in part approximate) quantum numbers (F, S, J).

Figure 7.1 illustrates the energy diagrams of the hyperfine states in the rovibrational levels relevant to the studied transitions. Panel (a) shows the rovibrational transitions between $(v = 0, L = 0)$ and $(v' = 2, L' = 1)$ levels. The first level has four hyperfine states: (0 1 1), (1 0 0), (1 1 1), and (1 2 2) that are labeled by the quantum numbers (F, S, J), while the second has 10 hyperfine states. This large number leads to rich hyperfine transitions. For each hyperfine state, the magnetic degeneracy factor is $(2J + 1)$ (not shown). The very weak F-manifold-dependent doubly-spin-forbidden transitions (with various values of both F and S) of strength larger than 3×10^{-5} are shown in pink. Due to the unperturbed (spin-independent) rovibrational transition frequency $f_{0,theor}$, these doubly-spin-forbidden transitions show (a) negative frequencies or (b) positive frequencies. The transitions indicated by the arrows are addressed by the OPO in the case (a) or the QCL in the case (b).

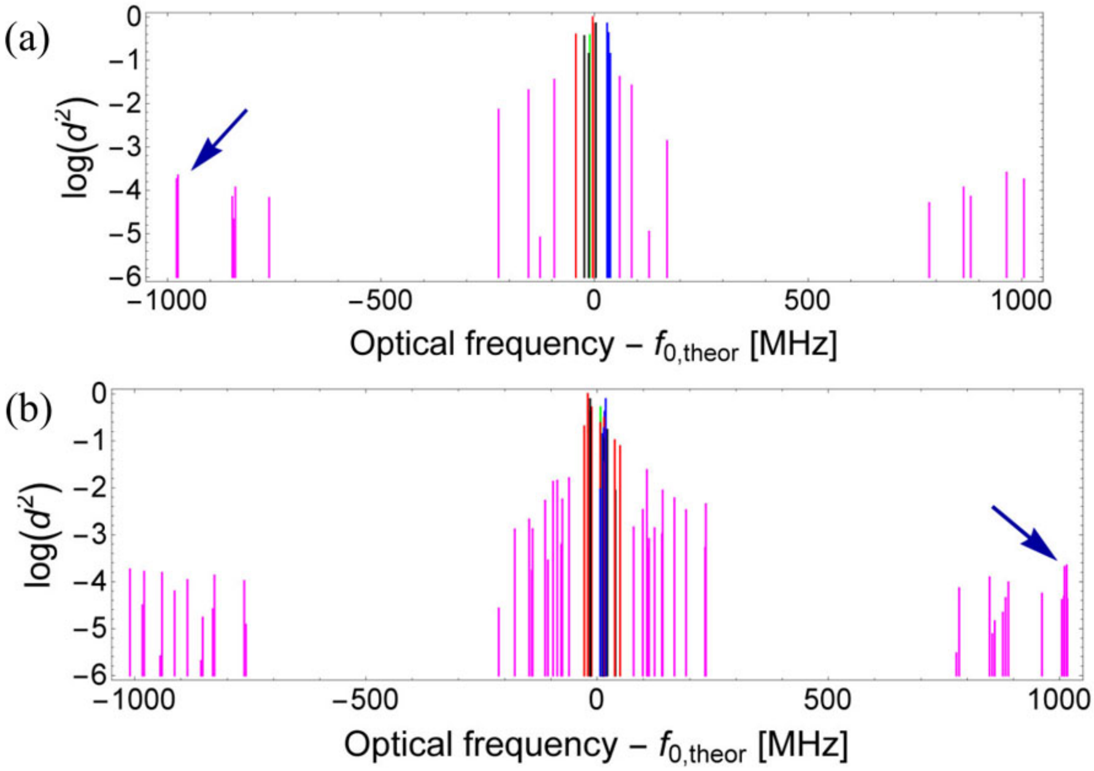

Figure 7.2: The frequencies of the various hyperfine transitions with the relative strengths [105]. Transition dipole moment squared (d^2) of the hyperfine transitions are normalized to that of the strongest hyperfine transition. Zero frequency is defined as the spinless rovibrational transition frequency $f_{0,theor}$. (a) Hyperfine transitions of $(v = 0, L = 0) \rightarrow (v' = 2, L' = 1)$ at 2.65 μm. (b) Hyperfine transitions of $(v = 0, L = 2) \rightarrow (v' = 1, L' = 1)$ at 5.5 μm. The magnetic field is zero. In these panels, all nearly forbidden transitions are shown in pink. The two transitions dominantly addressed by the OPO or the QCL are indicated by the arrows.

Figure 7.2 (a) shows the frequencies of the various hyperfine transitions with the relative strengths corresponding to Figure 7.1 (a). The strong ones among them are presented in red, green, blue, and black. In these spin-allowed transitions, the quantum numbers F and S do not change the value, while J changes by at most one unit. Their detunings from the corresponding spinless transition frequency $f_{0,theor}$ are relatively small (less than ±50 MHz), since the hyperfine Hamiltonians do not vary strongly with the vibrational and rotational quantum numbers, see Refs. [81]. Here, $f_{0,theor}$ is the rovibrational transition frequency in the absence of spin-related interactions.

In Figure 7.2 (a), hyperfine-state-dependent transitions (where at least one of the quantum numbers F and S changes the value) with detunings as large as ±1 GHz and strengths as small as 10^{-9} (normalized to the strongest transition) are partially arranged in pink. These transitions can be classified into two groups: (i) singly spin-forbidden transitions and (ii) doubly-spin-forbidden transitions. For the transitions in the first group, only the quantum number S changes while F remains. These transitions are confined inside the colored boxes in Figure 7.2 (a) with their detunings less than ±250 MHz and their strengths relatively weaker than the strongest one. As to the transitions in the second group, both quantum numbers S and F change values, which lead to detunings in the range of $700 \sim 1000$ MHz and $-700 \sim -1000$ MHz with their strengths significantly weaker than the singly spin-forbidden transitions.

The doubly-spin-forbidden transitions with negative detunings are colored in pink in Figure 7.1 (a). A subset of these transitions from the initial rovibrational state $(v = 0, L = 0, F = 1, S = 2, J = 2)$ are listed in Table 7.1.

Similarly, Figure 7.1 (b) shows the hyperfine structure of the rovibrational levels $(v = 0, L = 2)$ and $(v' = 1, L' = 1)$, while Figure 7.2 (b) presents the frequencies with relative strengths of the hyperfine transitions between those corresponding hyperfine states.

(F, S, J)		Detuning, $f - f_{0,theor}$ [MHz]	Relative strength
Lower state	Upper state		
(1, 2, 2)	(0, 1, 0)	−971.5	2×10^{-7}
	(0, 1, 1)	−975.4	2×10^{-4}
	(0, 1, 2)	−978.8	2×10^{-4}

Table 7.1: Precise detunings of the hyperfine transitions near −977 MHz detuning from the spinless frequency of the $(v = 0, L = 0) \rightarrow (v' = 2, L' = 1)$ rovibrational transition with respective transition strengths (relative to the strongest hyperfine transition) [105]. The second and third entries are the doubly-spin-forbidden transitions. The first one (with $\varDelta J = 2$) is extremely weak and does not contribute significantly to the detected signal.

7.2 Quantum state preparation

As mentioned in section 5.3, after the molecular HD$^+$ ions are loaded in the trap and thermalized with the BBR environment, without rotational cooling, the initial population of $(v = 0, L = 0)$ and $(v = 0, L = 2)$ levels are 0.10 and 0.27, respectively, which is in principle sufficient for detecting the hyperfine transitions of $(v = 0, L = 2) \rightarrow (v' = 1, L' = 1)$. However, for detecting the hyperfine transitions of $(v = 0, L = 0) \rightarrow (v' = 2, L' = 1)$, this initial population is too low.

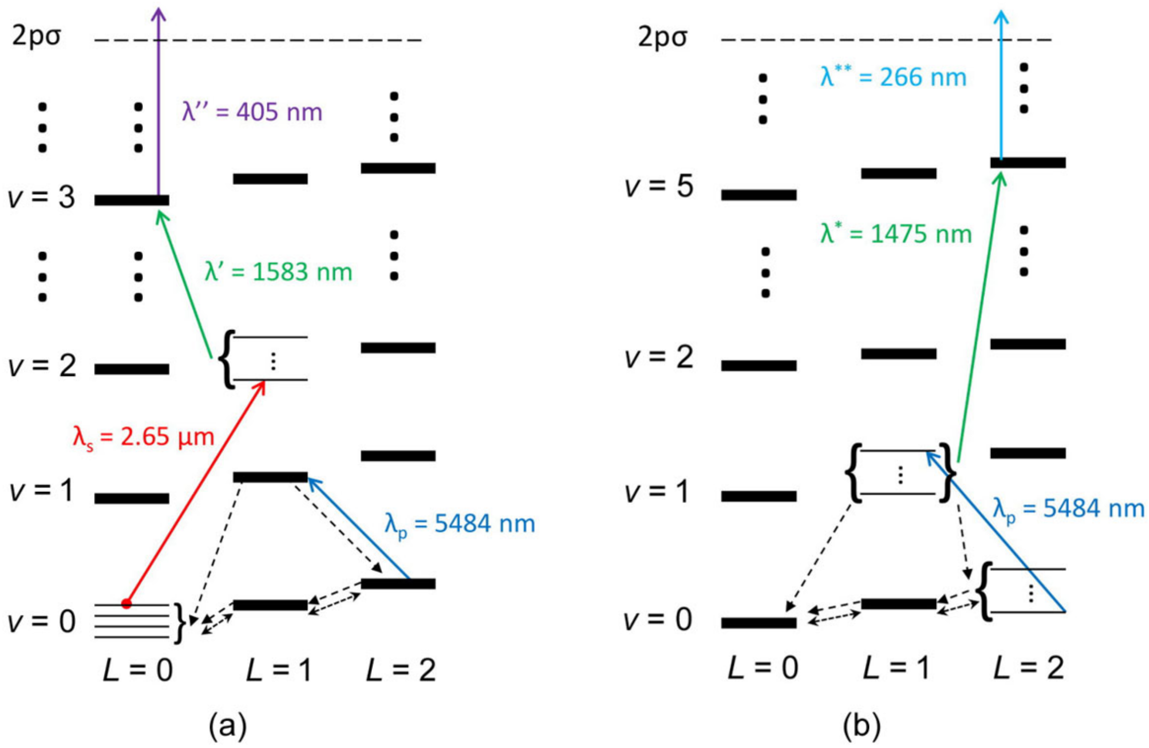

Figure 7.3: Schematic diagrams of energy levels of HD^+ with transitions relevant to this work [105]. Solid arrows represent laser-induced transitions; dashed arrows represent spontaneous emission transitions; dotted double arrows indicate BBR-induced transitions. The doubly-spin-forbidden hyperfine transitions, (a) between $(v = 0, L = 0)$ and $(v' = 2, L' = 1)$, excited by the OPO, is illustrated in red, and (b) between $(v = 0, L = 2)$ and $(v' = 1, L' = 1)$, excited by the QCL, is colored in dark blue. The REMPD process is implemented by cascaded radiations at (a) $\lambda' = 1583$ nm and $\lambda'' = 405$ nm or (b) $\lambda^* = 1475$ nm and $\lambda^{**} = 266$ nm, respectively. Rotational cooling is employed in the case (a) by an optical pumping at $\lambda = 5484$ nm and is not used in case (b), since in thermal equilibrium, the initial population in the level $(v = 0, L = 2)$ is approx. 27%, which is sufficient for spectroscopic purposes compared with the initial population of only approx. 10% in the level $(v = 0, L = 0)$ [92]. The QCL at $\lambda = 5484$ nm in case (b) is used for hyperfine-transition-detection purposes. The energy level differences are not to scale. Hyperfine structure is shown schematically only for the levels $(v = 0, L = 0)$, $(v = 0, L = 2)$, $(v' = 1, L' = 1)$, and $(v' = 2, L' = 1)$ that are relevant to this work.

Including the Zeeman substates, the rovibrational ground level $(v = 0, L = 0)$ carries altogether twelve quantum states. It is shown in our previous work [106] that when the rotational cooling by the 5.5 μm QCL takes place, among all the quantum states, even the hyperfine state $(F = 1, S = 2, J = 2)$ with the largest fraction possesses only approx. 20% of the total population. Therefore, for the spectroscopic study of doubly-spin-forbidden transitions with a higher signal-to-noise ratio and shorter overall measurement time, an effective quantum state preparation is required.

For this purpose, in the first step, a laser rotational cooling at $\lambda_p = 5484$ nm was applied [92, 107], which is indicated in Figure 7.3 (a) as a blue arrow. This optical pumping, controlled by the transfer cavity system, is used to transfer the population to the ground level $(v = 0, L = 0)$ via driving nearly all the strong transitions with near-zero detuning. After the optical pumping, approx. 60% of the molecular HD$^+$ ions will be in the ground level. Concomitantly, the population in each hyperfine state of the ground level would be increased by the optical pumping, e.g, approx. 20% of the population would be in the hyperfine state $(F = 1, S = 2, J = 2)$ [106].

In the second step, the hyperfine pumping was implemented to increase the population in a particular hyperfine state. For example, as shown in Figure 7.1 (a), the transitions driven by the OPO are used to transfer the population from the $F = 1$ manifold of the $(v = 0, L = 0)$ level to $F' = 0$ manifold of the rovibrational level $(v' = 2, L' = 1)$, from which the population is transferred into the vibrational ground levels $(v'' = 0, L'' = 1)$ and $(v'' = 0, L'' = 3)$ via cascaded spontaneous emission, and then into $(v''' = 0, L''' = 0)$ and $(v''' = 0, L''' = 2)$ by BBR and spontaneous emission. Thus, the residual population in the upper three hyperfine states $(1\,0\,0)$, $(1\,1\,1)$, and $(1\,2\,2)$ that are labeled by the quantum numbers (F, S, J) of the ground level $(v = 0, L = 0)$ could be transferred to the lowest-energy hyperfine state $(0\,1\,1)$ of the same ground level (see Figure 7.1 (a)).

In addition, the QCL performing the rotational cooling in the first step could be subsequently tuned to weak transitions and used as a hyperfine pumping source, since it is controlled by the transfer cavity and thus can be tuned rapidly by a computer program. As shown in Figure 7.1 (b), the population is transferred from the $F = 0$ manifold of the $(v = 0, L = 2)$ level to $F' = 1$ manifold of the rovibrational level $(v' = 1, L' = 1)$, from which the population is further transferred into the ground level $(v'' = 0, L'' = 0)$ via spontaneous emission.

Since spontaneous emission and BBR take place predominantly between strong transitions, i.e. spin-allowed transitions (without changing F and S), the population of the $F = 0$ manifold of the $(v = 0, L = 0)$ level will be accumulated after a number of intermediate pumping steps.

7.3 Experimental method

7.3.1 Overview

A schematic of the experimental setup and laser beams for spectroscopy of doubly-spin-forbidden rovibrational transitions is shown in Figure 7.4. Similar to the project of terahertz spectroscopy of HD$^+$ ions that is described in chapter 5, the UV cooling laser at 313 nm enters from the right to the vacuum chamber to cool down the atomic Be$^+$ ions, after which the HD$^+$ ions are sympathetically cooled to a secular temperature as low as approximately 10 mK, where the Doppler broadening for 2.7 μm and 5.5 μm radiations are ca. 5 MHz and 3 MHz, respectively [106]. The REMPD lasers ($\lambda' = 1583$ nm and $\lambda'' = 405$ nm, or $\lambda^* = 1475$ nm and $\lambda^{**} = 266$ nm according to different schemes in Figure 7.3) propagate from the left. In order to study the doubly-spin-forbidden transitions as shown in Figure 7.1, a CW OPO at 2.65 μm and a transfer-cavity-controlled QCL at 5.5 μm are employed to drive those transitions. In addition, this QCL is used as a rotational cooling source and a hyperfine pumping source as well. For signal detection, the method of REMPD is applied.

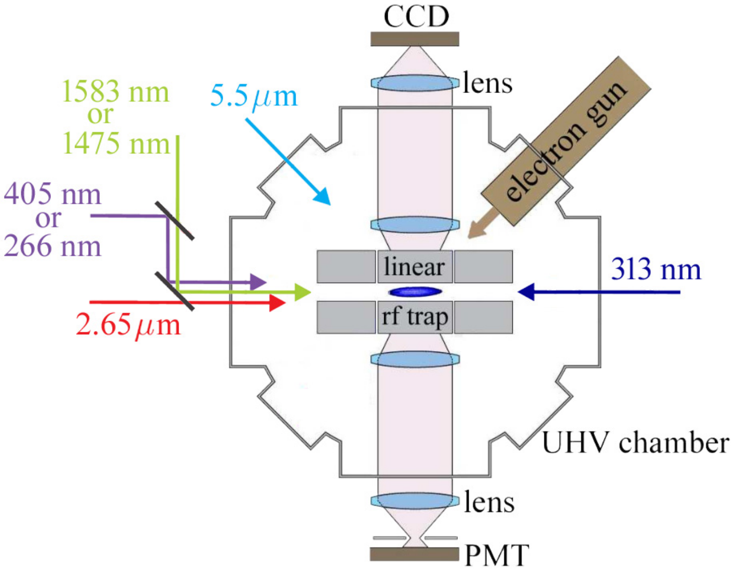

Figure 7.4: Schematic of the setup and laser beams for spectroscopy of doubly-spin-forbidden rovibrational transitions [105]. CCD: charge-coupled device; PMT: photomultiplier tube. Dimensions are not to scale.

7.3.2 OPO

The rovibrational transition frequency of the $(v = 0, L = 0) \rightarrow (v' = 2, L' = 1)$ transition of the molecular HD$^+$ ion is $f_{0,theor} = 113.014969$ THz (2.65 μm). For this wavelength, the currently available CW laser sources, e.g. DFB-type diode laser, would not have sufficient power for the present spectroscopic study. Therefore, a home-made CW singly-resonant OPO [108] pumped by a 9-W infrared (IR) laser at a wavelength of 1064 nm, with a resonant (signal) wavelength of 1.8 μm, and an idler wavelength of 2.65 μm is applied.

In this work, the OPO's idler radiation is coupled into a 3-m long, single-mode ZBLAN optical fiber (FiberLabs Inc.), delivered to the experimental setup, and collimated by a metal-coated off-axis parabolic reflective collimator (Thorlabs, Inc.). About a power of 10 mW is available in front of the vacuum chamber window. The laser beam is focused into the trap center with a beam diameter of approx. 200 μm.

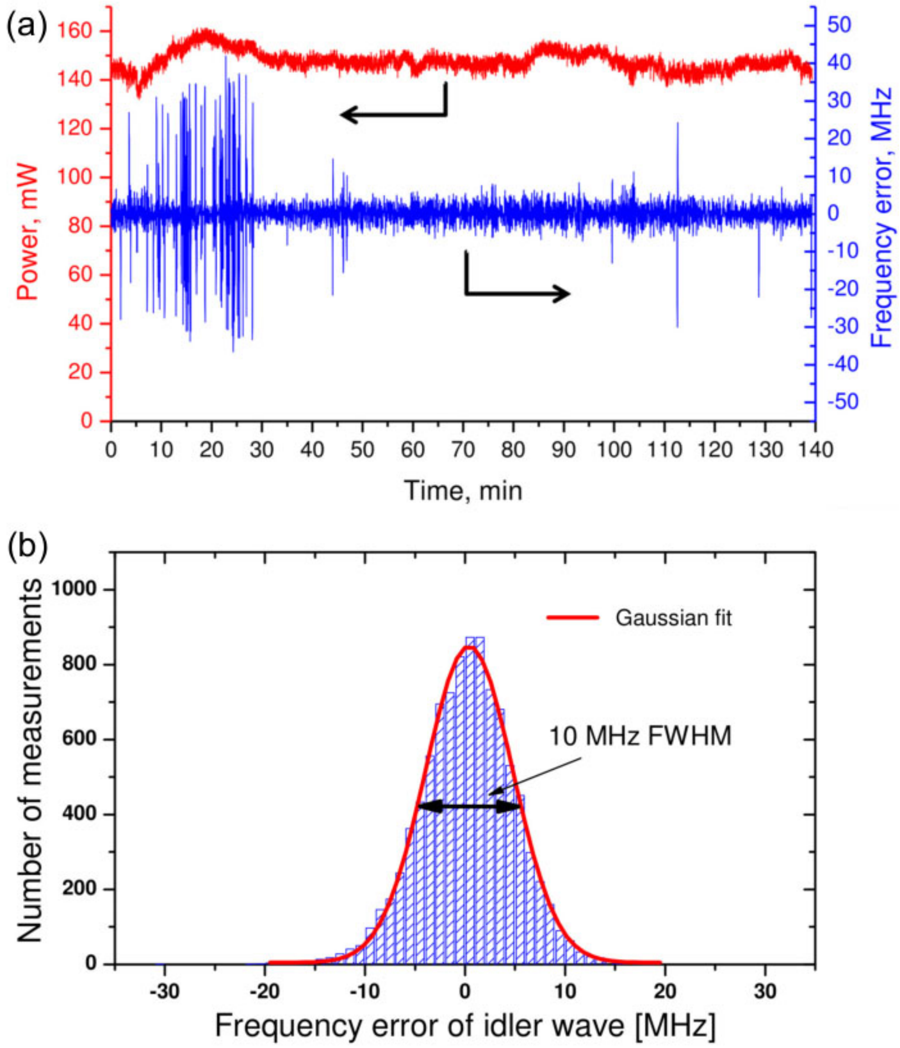

Figure 7.5: Frequency stabilization of the CW OPO [105]. (a) Stability of the idler frequency and output power. (b) Histogram of the idler frequency error while the frequency of OPO is stabilized. The measurement duration is approx. 60 min.

The frequency stabilization of the idler radiation (2.65 μm) of the OPO is achieved by means of the thermal lock method. Due to the lack of mid-IR wavemeter, a near-IR wavemeter (High Finesse Angstrom WS-7 IR) is used instead to record the pump (1.06 μm) and signal (1.8 μm) wavelengths λ_{pump} and λ_{signal}, after which the idler frequency $f_{idler} = c/\lambda_{pump} - c/\lambda_{signal}$ is computed in real-time by the LabVIEW program. By applying a digital feedback system based on the error signal that is converted from the deviations of the idler frequency from the goal frequency, the pump laser frequency is adjusted accordingly to suppress the frequency drift. Thus, the frequency stabilization of the idler radiation is realized. As is illustrated in Figure 7.5, the fluctuation is within ±5 MHz relative to the goal frequency. Note that the accuracy of the wavemeter is tested by using a frequency comb that is locked to a GPS-disciplined ultrastable hydrogen maser and is routinely checked by the 1.5 μm radiation from our 313 nm UV cooling laser source, since this radiation is frequency-stabilized with an iodine line that contributes an adequate frequency reference.

7.3.3 QCL based on the transfer cavity system

The 5.5 μm QCL (Alpes Lasers SA) was previously frequency stabilized to a gas (NH_3) absorption line and could not be finely tuned. Since the transfer cavity system has been successfully developed, in this spectroscopic studies of doubly-spin-forbidden transitions of HD^+ ions, the QCL is frequency controlled by the new system. Taking advantage of the precise and fast tuning by the computer program, it is used not only as a driving source for detecting the hyperfine transitions between $(v = 0, L = 2)$ and $(v' = 1, L' = 1)$ levels of HD^+, but also as a rotational cooling source (to excite all the strong transitions) and hyperfine pumping source (to drive the corresponding weak transitions) for detecting the hyperfine transitions between $(v = 0, L = 0)$ and $(v' = 2, L' = 1)$ levels. A detailed description of the QCL has been given in chapter 6.

7.3.4 Measurement procedures

Similar to the terahertz spectroscopic measurements of HD^+ ions (see section 5.5), the REMPD process took place to detect the doubly-spin-forbidden transitions in this work.

First, the method I (see subsubsection 5.5.3.1) was used to detect the target transitions of HD^+ ions preliminarily, which is an effective approach to test the experimental conditions including optimizing the alignment of all involved laser beams and checking the validness of the desired laser frequencies.

Then, the method II (see subsubsection 5.5.3.2) was applied to detect the target doubly-spin-forbidden hyperfine transitions. During the laser excitation of those transitions and the REMPD process, the secular excitation was kept off to ensure that the HD$^+$ ions remain at a low secular temperature (approx. $10 \sim 15$ mK).

7.4 Results

7.4.1 Preliminary excitation of the transitions

As a preliminary test, the excitation of the $(v = 0, L = 0) \rightarrow (v' = 2, L' = 1)$ rovibrational transition by the OPO with a power of approx. 10 mW and a frequency of nearly zero detuned from the spinless transition frequency $f_{0,theor}$ of HD$^+$ ions was tested. The strong transitions that are shown as colored lines at the center of Figure 7.2 (a) were driven. By using the method I, the corresponding fluorescence decay signals were recorded and presented in Figure 7.6.

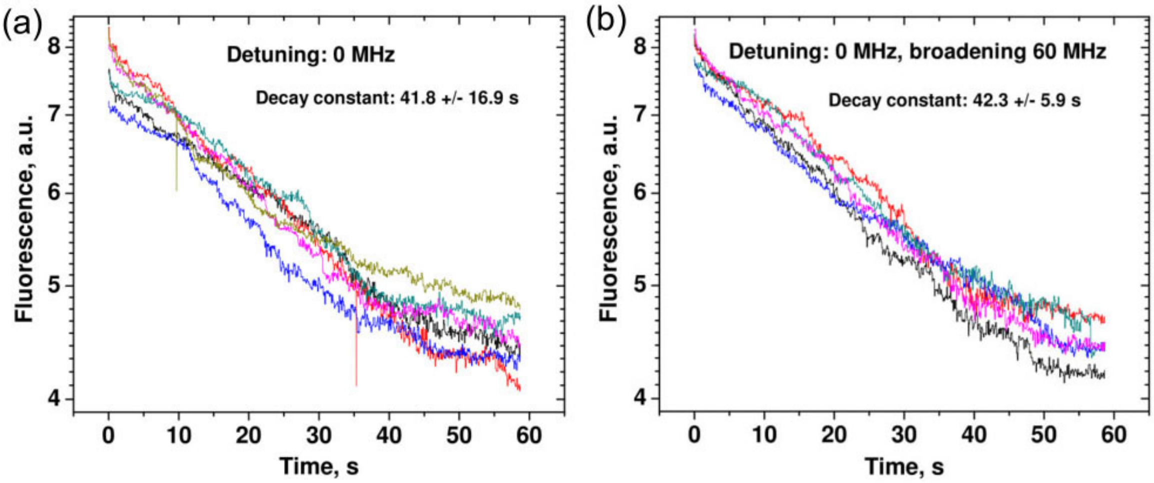

Figure 7.6: Fluorescence decay signals as a function of time for detection of the rovibrational transition $(v = 0, L = 0) \rightarrow (v' = 2, L' = 1)$ in HD$^+$ molecular ions by the OPO [105]. (a) The OPO frequency is stabilized to 0 MHz detuning from $f_{0,theor}$ without broadening. (b) The OPO is broadened by ±30 MHz additionally. Both cases indicate nearly the same average decay constant, however, case (b) shows smaller decay fluctuations, which would be interpreted as the influence of moderate frequency broadening that averages out the residual frequency instability.

Compared with case (a), the OPO radiation in case (b) is additionally broadened by approx. ±30 MHz via sweeping the pump laser frequency, which yields the signal fluctuations in case (b) approx. three times smaller than in case (a), since the moderate frequency broadening averages out the residual frequency instability. In addition, it is noticed that both cases (a) and (b) indicate nearly the same average decay constant, from which it can be evaluated that the HD$^+$ ion number decreases with a relatively low rate of 0.02 s^{-1}. Nevertheless, the excitation of the $(v = 0, L = 0) \rightarrow (v' = 2, L' = 1)$ transition is observed as a preliminary investigation for detecting the hyperfine transitions.

On the other hand, the excitation of $(v = 0, L = 2) \rightarrow (v' = 1, L' = 1)$ transition has been already implemented in the terahertz spectroscopic study of HD$^+$ (see chapter 5), which could be regarded as the preparation for detecting the hyperfine transitions between those two levels.

7.4.2 Detection of the doubly-spin-forbidden hyperfine transitions

Based on the analysis and all the preparations including the above-mentioned quantum state preparation, the spectra of the doubly-spin-forbidden hyperfine transitions in the HD$^+$ molecular ions were finally measured and demonstrated in Figure 7.7.

The detections were performed by using the measurement procedure of method II with the time interval of the REMPD process extended from three seconds to five seconds (see Figure 5.8). Each data point in Figure 7.7 is the average of ten individual measurements with the error bars of the standard deviation.

The total time required for data acquisition of the spectra would be approximately 10 hours for (a) and 16 hours for (b) of Figure 7.7, since each individual measurement cycle contains many steps, i.e. molecular ion loading, cleaning, rotational cooling, hyperfine pumping, transition excitation, REMPD, data recording, and ion removal, etc.

Figure 7.7 (a) shows the spectrum in the $(v = 0, L = 0) \rightarrow (v' = 2, L' = 1)$ transition when the OPO frequency is detuned to near −977 MHz from the spinless transition frequency and stabilized without additional broadening. It can be seen that this hyperfine transition is clearly observed compared with the background signal. When the OPO frequency is detuned large enough away from −977 MHz, e.g. at −1027 MHz and −927 MHz, the signal merges into the background level. However, when reducing the detunings to half of those values, e.g. at −1002 MHz and −952 MHz, the signal increases to half of the maximum value of the −977 MHz detuning, indicating a linewidth of approx. 40 MHz. The error bar of the measurement is approx. ±5% resulting from the instability of the power and frequency of the OPO (see Figure 7.6), the power fluctuation of the cooling laser at 313 nm, the variation of the number of ions in background loss, etc.

Compared with the theoretical calculation that is indicated by the blue arrow in Figure 7.2 (a), this detected excitation comes from the contributions of three doubly-spin forbidden transitions (listed in Table 7.1) that are detuned to −971.5 MHz,

-975.4 MHz, and -978.8 MHz, with the relative transition strength of 2×10^{-7}, 2×10^{-4}, and 2×10^{-4} for each, respectively.

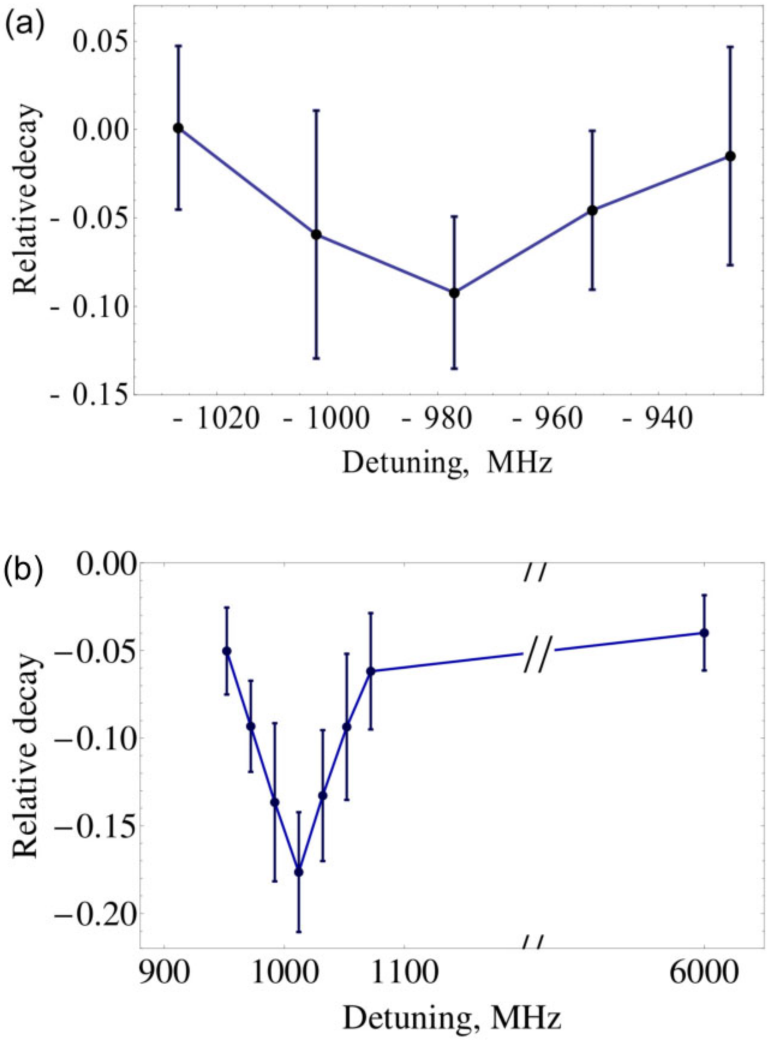

Figure 7.7: Spectra of the doubly-spin-forbidden hyperfine transitions in HD$^+$ molecular ions [105]. (a) Spectrum in the $(v = 0, L = 0) \rightarrow (v' = 2, L' = 1)$ overtone transition, driven by the OPO that is detuned and stabilized to the target frequency near -977 MHz without additional broadening. (b) Spectrum in the $(v = 0, L = 2) \rightarrow (v' = 1, L' = 1)$ fundamental vibrational transition, driven by the QCL that is detuned near $+1010$ MHz without additional broadening.

Theoretically, for the demonstrated hyperfine transition shown in Figure 7.7 (a), an ideal maximum ion number relative decay of ca. -0.25 would be expected after the rotational cooling and hyperfine pumping. This is the fraction of all HD$^+$ molecular ions that are photodissociated via the employed transitions. However, experimentally, the maximum fractional decay signal obtained is ca. -0.10 ± 0.05. Considering that the spectroscopic lower state contains approx. 20% of all HD$^+$ ions after the rotational cooling, it can be evaluated that approx. 50% of the relevant population is excited during the transition-induced-excitation interval of five seconds, i.e. an excitation rate of ca. 0.14 s^{-1}. The difference compared to the theoretical expectation would be explained by the actually available laser power of the OPO, the possibly imperfect spatial overlap between the focused OPO beam and the HD$^+$ molecular ions, and the limited excitation by the REMPD laser at 1583 nm.

Note that the spectrum of Figure 7.7 (a) could be experimentally detected only after the quantum state preparation, i.e. transferring the residual population in the three hyperfine states (1 1 1), (1 0 0), and (0 1 1) that are labeled by the quantum numbers (F, S, J) of the ground level $(v = 0, L = 0)$ to the hyperfine state (1 2 2) of the same ground level (see Figure 7.1 (a)) by means of the rotational cooling and hyperfine pumping before REPMD. Thanks to the performance of the transfer-cavity-controlled QCL, this quantum state preparation has been eventually realized. Since this procedure is controlled by a computer program, by only changing the corresponding frequency list, the quantum state preparations for the other hyperfine states, i.e. (1 1 1), (1 0 0), and (0 1 1) of the ground level are implemented as well. Thus, all the hyperfine transitions between $(v = 0, L = 0)$ and $(v' = 2, L' = 1)$ levels could be detected.

By the similar measurement procedures, the doubly forbidden transitions between $(v = 0, L = 2)$ and $(v' = 1, L' = 1)$ levels driven by the QCL were also detected. Compared with the above-presented measurements of the hyperfine transitions for $(v = 0, L = 0) \to (v' = 2, L' = 1)$, this experiment is relatively straightforward since the performance of the OPO is not required and the desired QCL frequency could be controlled by the computer-based transfer cavity. In addition, as mentioned in section 5.3, after the molecular HD$^+$ ions are loaded in the trap, without rotational cooling and hyperfine pumping, the initial population of $(v = 0, L = 2)$ level is 0.27, which is in principle already sufficient for detecting the hyperfine transitions of $(v = 0, L = 2) \to (v' = 1, L' = 1)$ when considering the relatively fast BBR-induced population redistribution to the $(v = 0, L = 2)$ level. Therefore, the quantum state preparation, in this case, is doable but not highly demanded.

As a demonstration, one of the doubly forbidden transitions that is near +1000 MHz detuning relative to the spinless transition frequency is shown in Figure 7.7 (b). Compared with the theoretical calculation that is indicated by the blue arrow in Figure 7.2 (b), this detected excitation reflects the contributions from at least two doubly-spin forbidden transitions that are detuned to +1010 MHz and +1015 MHz, with the relative transition strength of 2×10^{-4} for each, respectively. The linewidth of this measured transition is ca. 70 MHz, which is caused mainly by the frequency instability and the power fluctuation of the QCL.

7.5 Conclusion and discussion

In this work, the doubly-spin-forbidden transitions between $(v = 0, L = 2)$ and $(v' = 1, L' = 1)$, and between $(v = 0, L = 0)$ and $(v' = 2, L' = 1)$ rovibrational levels of HD$^+$ molecular ions were successfully excited and observed.

The former transition was driven by the frequency-tunable QCL and the signal has been clearly detected, due to the sufficiently high initial population and the relatively simple scheme for detection.

The latter transition was driven by the CW OPO with frequency stabilized by a digital feedback system based on a wavemeter. Due to the relatively low initial population, the rotational cooling and hyperfine pumping by sweeping the frequencies of the OPO and QCL were implemented to realize the quantum state preparation. Consequently, a relatively low but still observable excitation signal was detected. It is found that even when the OPO operates at full power yielding its laser intensity at the trap center of ca. 30 W/cm^2, the transition rate induced by this intensity is still lower than the spontaneous emission rate from the upper rovibrational level (ca. 32 s^{-1}), indicating that the home-made OPO which has a relatively high power at the wavelength of 2.65 μm among all the currently available CW laser sources in our laboratory is still not robust enough. Nevertheless, this doubly-spin-forbidden hyperfine transition has been observed with the quantum state preparation. Based on this result, if a more powerful CW source at 2.65 μm is available in the future, together with some further improvements, the signal-to-noise ratio would be increased.

It should be mentioned that the QCL was fully used in this work not only as a driving source, but also as a rotational cooling source and hyperfine pumping source for detecting the hyperfine transitions. Since it is frequency controlled by the transfer cavity system, the success of this spectroscopic study proves the usefulness of the system.

8 Summary and outlook

This work presents various results and applications in the field of cold atoms and molecules, with the aim of high-resolution spectroscopy of the molecular hydrogen ion HD^+.

Since the HD^+ ions are sympathetically cooled by the laser-cooled Be^+ ions, for the first step, in order to perform an effective and stable laser cooling of the atomic Be^+ ions, a compact frequency-stabilized tunable UV source at 313 nm with high power up to 100 mW was employed instead of a previous sophisticated and large UV radiation system. Throughout the whole work of spectroscopic measurements of Be^+ ions and HD^+ ions, the novel system offered long-term stability of more than ten hours, which was sufficient for one complete spectrum measurement.

By adjusting the frequencies of the cooling and repumping laser, the process of Coulomb crystallization of a beryllium ensemble was studied. By carefully controlling during the loading of Be^+ ions and HD^+ ions, ion crystals with various sizes including extremely small sizes can be obtained, e.g. a mixed-species linear ion chain that contains about 40 cooled Be^+ ions and 3 HD^+ ions. Such a mixed-species linear ion chain could be used for the molecular quantum state preparation for quantum information processing by implementing new cooling schemes for the vibrational motion of the extended ion chain. Furthermore, the vibrational trap mode spectrum of the two-species ion chain could be studied by quantum logic techniques.

In principle, trapping a “Coulomb-pair” that is composed of only one single Be^+ ion and one single HD^+ ion is possible by further improvement of the controlling system for ion loading procedure or the geometry of trap electrodes or both. In that case, the space charge effects, Doppler effects, coupling effects, as well as collisions between Be^+ and HD^+ ion species that occasionally lead to resonance frequency shift and line broadening, would be significantly reduced.

In this work, the medium-sized crystal that normally contains about 1500 Be^+ ions and about $150 \sim 200$ HD^+ ions was used for spectroscopic measurements. Due to the current detection scheme of REMPD, the crystal with relatively large numbers of ions enables a good signal-to-noise ratio.

Precise spectroscopy of cold atoms and molecules requires understanding and controlling the local magnetic field. For this purpose, based on a large number of Raman spectroscopic measurements of Be^+ ions, the conditions of the zero magnetic field, as well as the relations between the magnetic fields and the currents of Helmholtz coils in all three dimensions, have been found. Compared with the conventional measurement by a magnetic sensor, the method of Raman spectroscopy in this work has several advantages: first, opening the vacuum chamber could be avoided, which potentially brings pollutants into the vacuum chamber and takes weeks long to pump to the same ultra-high vacuum environment; second, the magnetic field that is determined from the spectra is intrinsically more precise than the one from the conventional method, since an imprecision of location occurs in the latter case.

Although there exists possibly a magnetic field gradient in the trap center, the magnetic field measurement has important significance for the followed spectroscopic work of HD^+ or other trapped ion species in our laboratory. It predicted the spectra and helped us greatly to analyze the behavior of the particles more pertinently including the Zeeman effect.

Based on this work, excitation of the fundamental rotational transition $(v = 0, L = 0) \rightarrow (v' = 0, L' = 1)$ of HD^+ at 1.3 THz by using two experimental methods was performed, and significant transition frequencies were recorded. In addition, the BBR-induced rotational excitation was also observed. It is indicated from the obtained spectra that the Lamb-Dicke regime was reached and the Zeeman effect was successfully observed, from which, an upper limit of the magnetic field in the trap center of 1.5 G was estimated. It is for the first time to clearly detect the fundamental rotational transition of HD^+ by terahertz radiation, which is of the utmost importance, since it is the most fundamental dipole-allowed rotational transition of any molecule, and has not been observed before. It should be mentioned that in this work, Doppler-free resolution with a fractional linewidth of 5×10^{-8} was achieved. To the best of our knowledge, it is the first time (January 2012) that a Doppler-free molecular ion transition was ever observed [91].

The results strongly motivated further development of the system and further investigation of the hyperfine transitions of HD^+. As a result, a linewidth of 1×10^{-9} fractionally and 1.3 kHz absolute, an improvement of ca. 50-fold over the previous highest resolution in rotational spectroscopy, was later (2018) achieved in our laboratory [95]. In addition, by further measurements of the hyperfine components of the fundamental rotational transition, in 2020, an evaluation resulted in the most accurate test of a quantum-three-body prediction so far, at the level of 5×10^{-11} [96].

Generally, as an optical pumping source applied in spectroscopic studies of HD^+, the QCL at a wavelength of 5.5 μm is extremely important, because it transfers the HD^+ population to the rovibrational ground level $(v = 0, L = 0)$. Conventionally, the frequency of the QCL is broadened and stabilized to a gas absorption line, which satisfies nearly all the requirements of our current spectroscopic tasks. However, for the future work of higher-resolution spectroscopy of HD^+, the QCL hyperfine pumping is highly demanded, which requires a fast and precise frequency control. For this purpose, a so-called “transfer cavity” system that couples the QCL with a DFB laser was developed. In this system, the QCL was frequency stabilized to the cavity, while the latter was locked to the DFB laser. Thus, by means of adjusting the frequency of the DFB laser, the related QCL frequency could be controlled correspondingly.

For demonstration purposes, the QCL frequency was controlled by this system and tuned to near 1012 MHz offset from the spinless frequency of the transition $(v = 0,\ L = 2) \rightarrow (v' = 1,\ L' = 1)$ of HD$^+$. Thus, the QCL was used as a driving source and the doubly-spin-forbidden transition between $(v = 0, L = 2)$ and $(v' = 1, L' = 1)$ levels of HD$^+$ was clearly detected, which agreed with the theoretical calculation of 1010.44 MHz and 1015.07 MHz that contribute to the excitation. Since the system is designed to be transportable, it is also applicable for frequency controlling of other lasers after calibration. Currently, with this system, the QCL frequency tuning range is 1.2 GHz, which is restricted to the property of the generator applied for the sideband generation of the DFB laser. If a better generator or synthesizer is applied in the future with a wider frequency sweeping range without a jump, the frequency tuning range would be in principle extended. Nevertheless, so far, the system satisfies the requirement well for the HD$^+$ hyperfine pumping purposes.

As mentioned above, one of the most important purposes of developing this transfer cavity system is the QCL hyperfine pumping of HD$^+$. For demonstration, by together applying a frequency-tunable OPO, the QCL was used as a hyperfine pumping source to drive the corresponding weak transitions between $(v = 0, L = 2)$ and $(v' = 1, L' = 1)$ levels of HD$^+$. Thus, the quantum state preparation to a specific hyperfine state of HD$^+$ has been realized. Subsequently, the doubly-spin-forbidden transition between $(v = 0, L = 0)$ and $(v' = 2, L' = 1)$ levels of HD$^+$ was detected as well. Due to an inadequate laser intensity of the OPO and possibly imperfect spatial overlap between the laser beam and the HD$^+$ ions, the signal is relatively low but still observable. By further improving the alignment of all the involved lasers and increasing the laser power intensities, the signal-to-noise ratio would be increased.

On the other hand, in principle, by only applying traditional optical pumping rather than QCL hyperfine pumping, the doubly-spin-forbidden transition between $(v = 0, L = 0)$ and $(v' = 2, L' = 1)$ levels of HD$^+$ could be detected. However, in practical experiments, it is very difficult especially in the initial phase of the test measurements when totally no signal is observed due to the above-mentioned reasons. In this case, the QCL hyperfine pumping increases the possibility to find the signal that we are looking for, and makes it possible to improve the signal.

Through these experiments, it reveals the importance of the quantum state preparation for high-resolution spectroscopy. It is useful to consider the extension of this work to other atomic and molecular species.

9 Publications

J. Shen, A. Borodin, M. Hansen, and S. Schiller. Observation of a rotational transition of trapped and sympathetically cooled molecular ions. *Phys. Rev. A*, 85: 032519, 2012.

J. Shen, A. Borodin, and S. Schiller. A simple method for characterization of the magnetic field in an ion trap using Be^+ ions. *Eur. Phys. J. D*, 68: 359, 2014.

U. Bressel, A. Borodin, J. Shen, M. Hansen, I. Ernsting, S. Schiller. Manipulation of Individual Hyperfine States in Cold Trapped Molecular Ions and Application to HD^+ Frequency Metrology, *Phys. Rev. Lett.*, 108: 183003, 2012.

S. Vasilyev, A. Nevsky, I. Ernsting, M. Hansen, J. Shen, S. Schiller. Compact all-solid-state continuous-wave single-frequency UV source with frequency stabilization for laser cooling of Be^+ ions. *Appl. Phys. B*, 103: 27-33, 2011.

PHYSICAL REVIEW A **85**, 032519 (2012)

Observation of a rotational transition of trapped and sympathetically cooled molecular ions

J. Shen, A. Borodin, M. Hansen, and S. Schiller
Institut für Experimentalphysik, Heinrich-Heine-Universität Düsseldorf, 40225 Düsseldorf, Germany

(Received 16 January 2012; published 29 March 2012)

We demonstrate rotational excitation of molecular ions that are sympathetically cooled by laser-cooled atomic ions to a temperature as low as approximately 10 mK. The molecular hydrogen ions HD^+ and the fundamental rotational transition $(v = 0, N = 0) \rightarrow (v' = 0, N' = 1)$ at 1.3 THz, the most fundamental dipole-allowed rotational transition of any molecule, are used as a test case. This transition has not been observed before. Rotational laser cooling was employed in order to increase the signal, and resonance-enhanced multiphoton dissociation was used as detection method. The black-body-radiation-induced rotational excitation is also observed. The extension of the method to other molecular species is briefly discussed.

DOI: 10.1103/PhysRevA.85.032519 PACS number(s): 33.20.Bx

I. INTRODUCTION

High-resolution laboratory rotational spectroscopy of molecules is an important and very well-developed technique in molecular physics. It has provided extensive data on and insight into the structure and dynamics of molecules and has several applications, including the identification of molecular species in interstellar clouds. In the recent past, the accessible spectral region has been extended from the microwave region to the terahertz (submillimeter wavelength) region, thanks to the development of appropriate terahertz radiation sources attaining useful power levels. Continuous-wave, narrow-linewidth terahertz radiation, suitable for high-resolution molecular spectroscopy, is available from backward-wave oscillators or via frequency upconversion using Schottky diodes [1,2] or semiconductor superlattices [3,4].

The resolution of rotational spectroscopy has been increased beyond the Doppler limit by several techniques, such as molecular beams [5], velocity-class selection [6], Lamb-dip spectroscopy, and two-photon spectroscopy [7]. For example, sub-Doppler spectral lines with widths of approximately 15 kHz around 100 GHz [8] and 30–40 kHz at 0.7–1 THz [9,10] have been reported. However, the resolution of such methods is limited by transition time broadening and/or pressure broadening. In order to eventually overcome these limitations, it is interesting to explore a fundamentally different regime: trapping cold (<1 K) molecules in an interaction-free (ultra-high-vacuum) environment and localization to submillimeter extension. Then, transition time broadening and pressure broadening, as well as Doppler broadening, may be strongly reduced or even eliminated altogether. This regime may be reached with cold neutral molecules stored in e.g. optical traps or with cold molecular ions in radio-frequency traps. The production methods of cold molecules have been reviewed elsewhere; see, for example, Refs. [11,12].

In this work, we take a step toward applying high-resolution rotational spectroscopy on cold molecules: we demonstrate rotational excitation on sympathetically cooled and strongly confined molecular ions, using here secular temperatures as low as 10–15 mK. Our spectroscopic technique is a destructive one, resonance-enhanced multiphoton dissociation (REMPD). The particular implementation used here is $1 + 1' + 1''$ REMPD, where the molecule absorbs sequentially three photons of different energies. In our work, the transitions induced by each photon corresponds to the three main energy scales of a molecule: rotational (here ca. 1 THz), vibrational (here: overtone, ca. 200 THz), and electronic (ca. 1100 THz).

With respect to the temperature of the ions and the detection method, our work is complementary to the recent demonstration of terahertz rotational spectroscopy of trapped, helium-buffer-gas-cooled H_2D^+ and D_2H^+ ions at kinetic ion temperatures of approximately 24 K, where Doppler broadening is limiting the linewidth to approximately 1 MHz [13].

II. THE HD^+ MOLECULE AND THE SPECTROSCOPIC TECHNIQUE

The molecule we consider here, HD^+, is the most fundamental molecule with electric dipole-allowed rotational transitions [14]. Its potential as a test system for molecular quantum mechanics and for novel fundamental physics studies has been described previously [14–19]. Vibrational spectroscopy of sympathetically cooled HD^+ with the highest resolution of any molecular ion to date has recently been reported by us [20]. Pure rotational transitions have so far been observed only for the last and penultimate vibrational levels, $v = 21, 22$, close to the dissociation limit [21,22], where their $N = 0 \rightarrow N' = 1$ transition frequencies lie in the microwave range (ca. 50 and 9.4 GHz, respectively). Here we report on the rotational transition in the $v = 0$ ground vibrational level, at much higher frequency. The rovibrational transition frequencies have been calculated *ab initio* with high precision [18,19], greatly facilitating the experimental search. The $(v = 0, N = 0) \rightarrow (v' = 0, N' = 1)$ fundamental rotational transition studied here occurs at $f_{0,\,\mathrm{theor}} = 1\,314\,925.752$ MHz ("spinless" value, i.e., excluding hyperfine energy contributions), with an estimated theoretical error of approximately 2 kHz [23]. The $f_{0,\,\mathrm{theor}}$ value includes (among others) a contribution of approximately 48.8 MHz from relativistic effects (order α^2) and approximately −9.4 MHz from QED effects of order α^3.

An important aspect of this work is the use of laser rotational cooling [24]; see Fig. 1. It is used to transfer most of the molecular population, initially distributed among several rotational levels in $v = 0$, into the rovibrational ground state $(v = 0, N = 0)$ and it also empties the spectroscopy target state $(v' = 0, N' = 1)$. It modifies the difference in fractional population of the lower and upper spectroscopy levels, from

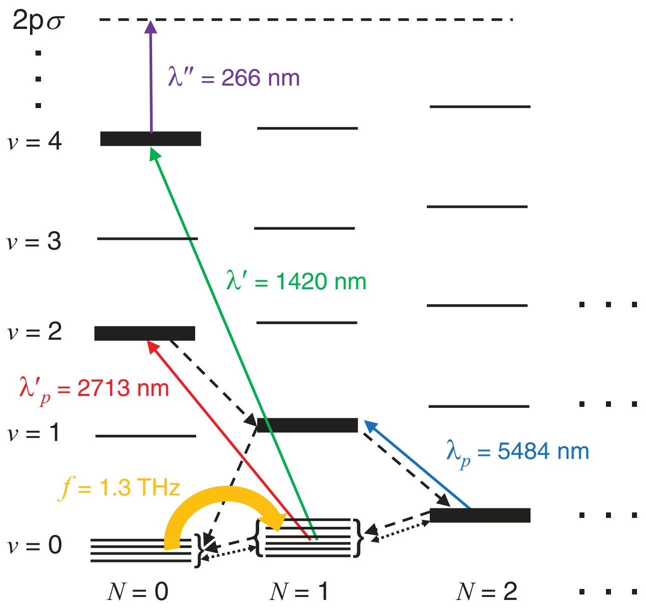

FIG. 1. (Color online) Simplified energy level scheme of HD$^+$ with transitions relevant to this work. Full thin arrows, laser-induced transitions; dashed arrows, some relevant spontaneous emission transitions; and dotted double arrows, some relevant black-body-radiation-induced transitions. The terahertz wave (thick arrow) is tuned so that the four hyperfine states in ($v = 0$, $N = 0$) are excited to corresponding hyperfine states in ($v' = 0$, $N' = 1$). Resonant laser radiation at λ' (1420 nm) and nonresonant radiation at λ'' (266 nm) transfer the rotationally excited molecules to a vibrationally excited level ($v'' = 4$, $N'' = 0$) and then further to electronically excited molecular states (predominantly 2pσ), from which they dissociate. Rotational cooling is performed by radiation at λ_p (5.5 μm) and λ'_p (2.7 μm). The level energy differences are not to scale. Hyperfine structure is indicated very schematically for the levels ($v = 0$, $N = 0, 1$) and as thick lines for some other participating levels. The waves at λ', λ'', λ_p, λ'_p have relatively large spectral linewidths.

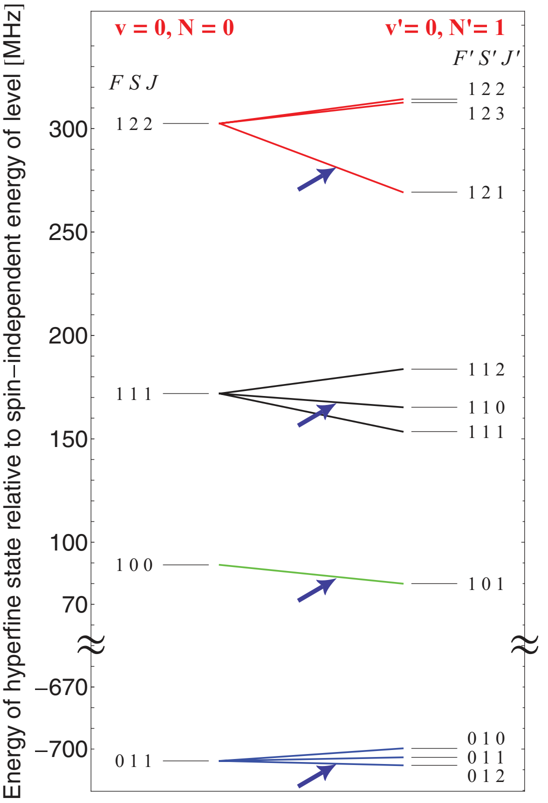

FIG. 2. (Color online) Energy diagram of the hyperfine states and main electric-dipole transitions in zero magnetic field. Left side, rovibrational ground level ($v = 0$, $N = 0$); right side, rotationally excited level ($v' = 0$, $N' = 1$). The hyperfine states are labeled by the (in part approximate) quantum numbers (F, S, J). The degeneracy factor of each hyperfine state is $(2J + 1)$. Transitions that do not change the quantum numbers F, S are relatively strong and are indicated, starting from the top of the figure, by red, black, green, and blue lines. The four transitions addressed consecutively in this work are indicated by arrows.

approximately -0.15 in thermal equilibrium to approximately 0.7, and thus significantly increases the detectable signal.

The hyperfine structure and the Zeeman effect of the lower and upper rovibrational levels are important aspects in the rotational spectroscopy [25,26]. As Fig. 2 shows, the ground state possesses four hyperfine states and 12 magnetic substates (with magnetic quantum number J_z). In the region occupied by the ions in our apparatus, the magnetic field is nonzero, lifting the magnetic degeneracy. The spectrum contains a large number of transitions with relatively large transition dipole moments; see Fig. 3. Most transitions, even the $\Delta J_z = 0$ ones, shift by approximately 100 kHz or more in a field of strength 1 G. Exceptions include five (strong) $J_z = 0 \to J'_z = 0$ transitions, whose quadratic Zeeman shifts in 1 G are at most 6.2 kHz in absolute value [26]. From each lower hyperfine state there is at least one such transition; the state ($F = 0, S = 1, J = 1, J_z = 0$) has two. Three of them are indicated by the first, third, and fourth arrows (from the top) in Fig. 2. A fourth is the hyperfine transition ($F = 1, S = 1, J = 1, J_z = 0$) $\to$ ($F' = 1, S' = 1, J' = 2, J'_z = 0$). Its transition frequency $f = f_{0,\,\mathrm{theor}} + 11.78$ MHz is close to other transition frequencies and is therefore not considered suitable for the present work. Instead, we use the ($F = 1, S = 1, J = 1, J_z = 0$) $\to$ ($F' = 1, S' = 1, J' = 0, J'_z = 0$) transition (second arrow from the top in Fig. 2), which, however, exhibits a much larger quadratic Zeeman effect (78 kHz at 1 G). The magnetic field in the trap region is not spatially constant in direction and magnitude, so some line broadening can be expected.

The theoretical Doppler linewidth, considering only secular motion, is approximately 55–70 kHz for the lowest temperatures used here (10–15 mK) and approximately 150–200 kHz if the ion ensemble is in the liquid state (100–200 mK). Note that the values are relatively large due to the low mass of the HD$^+$ ion. At 10–15 mK, the molecular ions are well confined along the axis of the trap and their motion in transverse direction is restricted to a range smaller than the terahertz wavelength (0.23 mm). In the axial direction, the confinement is not as strong, since diffusive motion of the ions is still occurring along the crystal axis, which exceeds in length (ca. 1.5 mm) the terahertz wavelength. Thus, Doppler broadening may still be present in our experiment, even at the lowest temperatures. The terahertz source [27] has a linewidth below

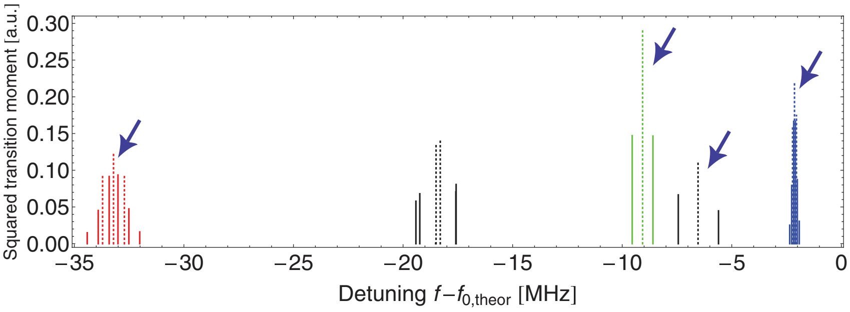

FIG. 3. (Color online) Section of the theoretical stick spectrum of the rotational transition in the frequency range relevant to this work, showing the Zeeman splittings and shifts in a 1 G magnetic field. Dashed lines are π transitions; full lines are σ transitions. $f_{0,\,\mathrm{theor}}$ is the theoretical "spinless" transition frequency. The four terahertz frequencies of list A (see Table I) are indicated by the arrows. The colors used correspond to those used in Fig. 2.

100 Hz and subhertz absolute frequency stability, values that are not relevant in comparison to other line-broadening effects.

The Doppler linewidth is smaller than the typical spacing between hyperfine transitions originating from different ground hyperfine states, even in the presence of a magnetic field on the order of 1 G. This is in principle advantageous, since it could permit resolution of the hyperfine structure. However, detecting individual hyperfine lines would also lead to a small signal-to-noise ratio: The individual hyperfine levels each contain only a fraction of the total population. If a statistical population distribution were produced by action of the black-body radiation field (BBR) and of the rotational cooling lasers, each substate would contain 1/12 of the total population, this fraction being typically 20 to 30 molecules. The individual populations are likely to vary significantly in time, requiring the collection of substantial data and averaging. We do not attempt to do so here and in order to obtain a sufficiently strong rotational excitation signal we have applied the following strategy.

We irradiate the molecules sequentially on terahertz frequencies corresponding to strong hyperfine transitions. Different frequency sets are used; see Table I. Each frequency from a set is irradiated for 200 ms and is meanwhile frequency-modulated by ±2 kHz at a 5 Hz rate. The list is repeated several times for a total of 3 s or more, depending of the excitation approach used.

The frequency lists include three of the five above mentioned low-Zeeman-shift $J_z = 0 \to J'_z = 0$ transitions, which originate from three of the four hyperfine states of $(v = 0, N = 0)$, and the respective frequency values have been chosen to correspond to an assumed magnetic field of 1 G. As mentioned above, the chosen transition starting from the fourth hyperfine state $(F = 1, S = 1, J = 1)$ has a substantial quadratic Zeeman effect. We therefore attempt to compensate for the lack of precise knowledge of the magnetic field distribution by exciting at four distinct frequencies, corresponding to the shifts induced by the magnetic field values 0.25, 0.5, 0.75, and 1 G (the detuning for 0 G is −6.617 MHz). Altogether, this list of frequencies (denoted by A'; see Table I) should nominally excite four of the twelve Zeeman substates. However, in the presence of a significant Doppler broadening, more substates (with larger Zeeman shifts) will be addressed. Indeed, the frequencies necessary to excite all Zeeman substates of the ground hyperfine states fall into ranges of approximately ±0.5, ±1, 0, ±0.22 MHz at 1 G, relative to the frequencies of the list A'. These spreads have a partial overlap with the Doppler broadening at the higher molecular temperatures (100–200 mK) employed here.

In order to obtain information about the detuning dependence of the rotational excitation, we also apply "detuned-frequency lists." Lists labeled B and C are detuned to smaller and larger frequencies, respectively, relative to list A' (relative detunings of list B: −1.782, −1.311, −0.704, −0.327 MHz, relative detunings of list C: 1.803, 1.443, 0.714, 0.326 MHz). The detunings are larger than the shift induced by the Zeeman effect in a 1 G field. Lists D and E have relative detunings approximately half as large as those of lists B and C, respectively (list D: −0.891, −0.655, −0.352, −0.163 MHz, list E : 0.901, 0.722, 0.357, 0.163 MHz). Finally, list A is also used, which is a simplified version of list A'. Frequency modulation is used in all cases.

III. EXPERIMENTAL APPARATUS AND PROCEDURE

A schematic of our apparatus [28] is shown in Fig. 4. The ultra-high vacuum (UHV) chamber houses a linear ion trap driven at 14.2 MHz. HD gas is loaded into the chamber by opening a piezoelectric valve, after which it is ionized by an

TABLE I. Frequency lists used for excitation of the rotational transition. f_i is the terahertz frequency.

	Frequency $f_i - f_{0,\,\mathrm{theor}}$ (MHz)						
Lower hyperfine level $(F,\,S,\,J)$	(1,2,2)	(1,1,1)				(1,0,0)	(0,1,1)
List A'	−33.211	−6.597	−6.578	−6.558	−6.539	−9.069	−2.138
List A	−33.211	−6.539				−9.069	−2.138
List B	−34.993	−7.850				−9.773	−2.465
List C	−31.408	−5.096				−8.355	−1.812
List D	−34.102	−7.194				−9.421	−2.301
List E	−32.310	−5.817				−8.712	−1.975
500-MHz detuning	500						

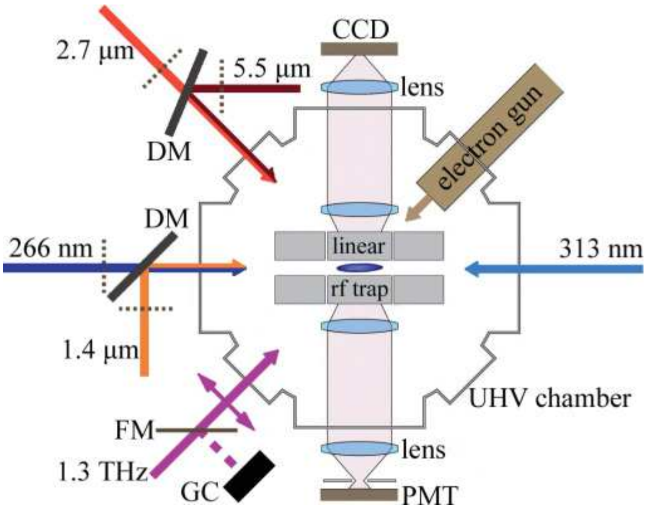

FIG. 4. (Color online) Schematic of the apparatus and beams. GC, Golay cell; FM, flip mirror; DM, dichroic mirror; and dotted lines, electrically controlled laser beam shutters. The double arrow indicates the polarization of the terahertz wave. Not to scale.

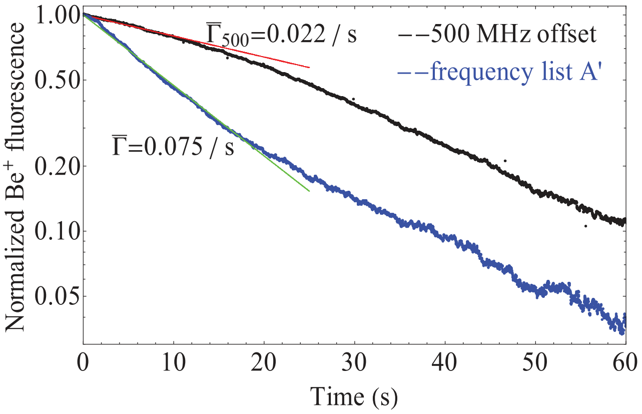

FIG. 5. (Color online) Atomic fluorescence signal during continuous secular excitation of the HD$^+$ ions (method I, liquid state). The time axis starts after the 2.7 μm rotational cooling laser is turned off and the two REMPD lasers and terahertz radiation are turned on. The upper (black) trace, where the terahertz radiation is detuned from resonance, shows the molecular ion number decay due mainly to the effect of BBR-induced rotational excitation. Lower (blue) trace is for terahertz radiation on resonance. Each trace is the average of 10 individual decays. The lines are exponential fits to the first 10 s of the data.

electron gun. The laser radiation for REMPD enters from the left and the 313 nm cooling radiation [29] enters from the right. The rotational cooling radiation enters diagonally. The terahertz source is positioned close to the vacuum chamber and its wave is focused into the chamber center by a concave paraboloidal mirror oriented at right angle to the beam. With a manual flip mirror, the wave can be sent to a Golay cell detector for power-monitoring purposes. The terahertz source has been described previously [27]. It is driven at the 72nd subharmonic of the desired frequency, near 18 GHz. This signal is provided by a microwave synthesizer, which is frequency locked to a global positioning system (GPS)-referenced hydrogen maser. The first REMPD laser is a diode laser emitting at the wavelength $\lambda = 1420$ nm and exciting the $(v = 0, N = 1) \rightarrow (v' = 4, N' = 0)$ transition. The second REMPD laser excitation is nonresonant and is provided by a resonantly frequency-doubled 532 nm laser. Initially, a Be$^+$ ion crystal is produced in the trap. Typically, the same Be$^+$ ion crystal is used for several hours of experimentation.

The molecular sample preparation routine starts by frequency stabilization of the cooling laser to a frequency a few tens of MHz to the red of the frequency for optimal Be$^+$ cooling, using a hyperfine transition of molecular iodine as reference. Then, a small amount of HD gas is let into the chamber and ionized by the electron gun. Both HD$^+$ ions as well as heavy impurity ions are generated, trapped, and quickly sympathetically cooled. In order to remove these impurity ions, the DC quadrupole potential is briefly increased, reducing the quasipotential strength in one transverse direction. The heavy ions then escape from the trapping region. This ends the preparation procedure; the produced cold HD$^+$ sample contains typically approximately 300 molecules.

The acquisition of one data point proceeds as follows: (i) The terahertz excitation is initially effectively kept off by detuning the frequency by 500 MHz from the rotational resonance, and the REMPD lasers are also blocked. (ii) The rotational cooling laser beams are unblocked, and a repeated secular frequency scan (740–900 kHz) is activated and kept on during the remainder of the measurement cycle (method I). The heating of the molecular ions heats the Be$^+$ ions sympathetically and spectrally broadens their 313 nm absorption line. This leads to a substantial increase of the cooling-laser-stimulated atomic fluorescence, due to the laser's relatively large detuning from atomic resonance. The fluorescence signal level is indicative of the initial number of HD$^+$ in the ion ensemble. (iii) For a duration $T_c = 35$ s, the rotational cooling takes place, after which the 2.7 μm rotational cooling laser is blocked (not the 5.5 μm laser). (iv) The REMPD lasers are unblocked and simultaneously the terahertz frequency scan is initiated. The resulting molecule loss reduces the heating and thus the atomic fluorescence signal. (v) The change in fluorescence as a function of time is followed until the signal essentially reaches the level in the absence of molecules. (Figure 5 displays the first 60 s only.) The secular excitation is kept on all the time. This concludes acquisition of one data point.

In an alternative measurement mode (method II), the secular scan activated in step (ii) to obtain a normalization signal is turned off after a few seconds while the rotational cooling continues. At the end of step (iii), both rotational cooling lasers are blocked. In step (iv), the terahertz source and the REMPD lasers are turned on only for 3 s. Immediately afterward, in step (v) the secular excitation is turned on again and the reduced fluorescence level is recorded during a few seconds. The ratio of the two fluorescence levels defines our signal and gives approximately the relative decrease in HD$^+$ number after REMPD.

At the end of either procedure, residual HD$^+$ and product ions are removed from the trap by applying the following cleaning procedure. (In method II, we do not "reuse" the remaining molecules, as we prefer to excite molecular samples prepared in the same way each time.) The cooling laser is detuned by a few 100 MHz to the red of the atomic cooling transition, causing melting of the crystal into a liquid. A secular excitation frequency scan covering the frequencies of HD^+ and lighter ions is turned on. The cooling laser is briefly blocked and unblocked several times. Light ions are thereby ejected from the trap. The secular excitation is turned off and the system is ready for a new molecule loading.

IV. RESULTS AND DISCUSSION

The first set of measurements was taken in the liquid state using method I. Figure 5 shows two atomic fluorescence traces. The upper (black, “background”) trace was obtained with the terahertz wave frequency detuned by 500 MHz from $f_{0,\,\mathrm{theor}}$, a value where no transition line exists. The REMPD only dissociates molecules in the ($v = 0, N = 1$) level. This level has initially been depopulated by the 2.7 μm rotational cooling laser, which is favorable for the purpose of the spectroscopy. As soon as the spectroscopy phase starts, the level receives population not only by terahertz rotational excitation (if the frequency is near resonance), but also by BBR-induced excitation from all hyperfine states of the ground rovibrational level (rate ca. 0.09/s at 300 K). In addition, the population still present in the ($v = 0, N = 2$) level or reaching it from higher-lying rotational levels is transferred into ($v = 0, N = 1$) by BBR-stimulated emission (rate ca. 0.12/s) and spontaneous emission (rate ca. 0.06/s). Therefore, a REMPD-induced molecule loss is always present.

A rate equation simulation yields a BBR-induced molecule number decay rate that depends on REMPD laser intensities and reaches ca. 0.075/s in the limit of very high intensities. After partial optimization of the UV dissociation laser alignment onto the ion crystal and therefore maximization of its intensity, we observed values of ca. 0.04/s at 25 s after the REMPD laser was turned on. The rate at this time rather than at 0 s is considered since at 0 s the number of molecules present is larger and this may lead to some saturation of the secular excitation signal. We explain the difference compared to the theoretical maximum by the actually available laser power and possibly imperfect REMPD laser beams overlap. With an improved alignment of the UV laser, an increase of the BBR-induced decay rate to ca. 0.060/s was observed.

The lower (blue) trace represents the decay in the presence of resonant terahertz radiation, using frequency list A'. We observe a large difference in the initial rate of signal decrease as compared to the background trace. Note that the decay occurring in the presence of resonant terahertz radiation also contains the background decay.

We also performed measurements with the two frequency lists B and C, for which the frequencies were detuned from those of list A' by different amounts for the four hyperfine states. As Fig. 6 (top) shows, the decay rates do not differ significantly from the background decay rates, and we can therefore deduce an upper limit for the magnetic field of 1.5 G, as the influence of the Doppler width is not significant here.

A second set of measurements was taken with method II; see Fig. 6 (bottom). Here, the terahertz radiation is applied only when the ion ensemble is well crystallized, at temperatures of approximately 10–15 mK. Data points were taken alternately at 500 MHz detuning, with list A, with list B (D), and with list C (E). Again, a finite (background) signal is observed when the terahertz radiation is far detuned, since BBR excites the rotational transition significantly on the used time scale of 3 s. Irradiation with the frequency list A provides a clear signal that rotational excitation induced by terahertz radiation takes place. We find again no significant difference in the rotational excitation efficiency for the detunings of lists B and C, compared to the background measurement. However, reducing the detunings to half the values (lists D and E) shows an increase of signal. This increase can be explained by the presence of a magnetic field of ca. 1 G or a Doppler width of several 100 kHz, or a combination of both. However, the Doppler width is at most 70 kHz under the operating conditions, and therefore we conclude that we observed the effect of the magnetic field on the hyperfine transition frequencies.

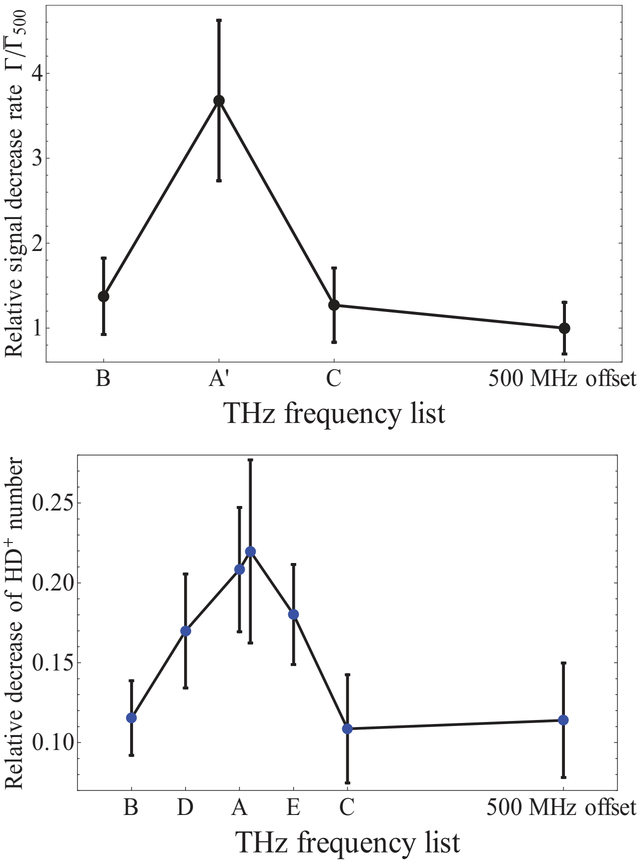

FIG. 6. (Color online) Frequency dependence of the rotational excitation. Top, in the liquid state, at ca. 100–200 mK, using method I. $\bar{\Gamma}_{500}$ is the average decay rate when the terahertz radiation frequency is detuned by 500 MHz. Each data point results from nine individual decays. Bottom, in the crystallized state, at 10–15 mK, using method II. Each data point represents the mean of nine or ten measurements. The two close points were taken with the same list A on different days and are shown separated for clarity. The error bars in both plots show the standard deviations of the data, not of the mean. The lines are guides for the eye.

V. CONCLUSION

We observed a pure rotational excitation of a sympathetically cooled molecular ion ensemble. In order to facilitate the observation, we applied a scheme adapted to the particularities of the apparatus. As the available detection scheme is a destructive one that employs photodissociation of the rotationally excited molecules, a new molecular ion loading cycle has to be implemented for each data point, and the data acquisition rate is very low. The number of ions sympathetically cooled is also small. Therefore, the preparation of a significant fraction (ca. 70%) of the molecular ions in the lower spectroscopic level was essential. Even so, the detection of a rotational transition originating from a single hyperfine state has too low of a signal-to-noise ratio. This is also due to the concurrent process of BBR-induced rotational excitation, which yields a finite background signal (decay rate) in connection with the photodissociation.

We therefore applied terahertz radiation at four frequencies that nominally excite the four hyperfine states in the lower spectroscopic level. This allowed a clear observation of the rotational excitation, using two different methods. By applying terahertz radiation detuned from the nominal resonance frequencies by amounts varying from 0.16 to 0.9 MHz (absolute) for the four frequencies, we found a significantly reduced but still observable excitation. This can be explained by the presence of a magnetic field with values up to approximately 1 G. In comparison, the contribution of secular ion motion to the linewidth when the ions are at approximately 10 mK and well-confined is negligible.

There is a strong motivation for further development of the method demonstrated here, since a resolution of the hyperfine structure of HD^+ and an accurate measurement of the hyperfine transition frequencies would represent a significant test of the *ab initio* calculations of this molecule. Possible improvements are the application of hyperfine state preparation techniques, recently demonstrated [20], and accurate control of the magnetic field in the trap region.

Finally, it is useful to consider the extension of this work to other molecular species. These can be characterized by their mass and their rotational constant, which are to a certain extent related. For many species, the masses will be significantly larger and the rotational constants significantly smaller than in the case of HD^+. The smaller rotational constant will lead to a significantly smaller transition frequency, in the microwave regime. It is likely that the Lamb-Dicke regime will then be effective, in particular if the microwave propagation direction is along the narrow width of the molecular ion ensemble, and Doppler broadening would be absent altogether. The smaller rotational constant will also lead to a smaller black-body-radiation excitation rate (at 300 K), which is very favorable, since it will make possible REMPD with near-zero background. The experimentally demonstrated fraction of molecules in the ground state obtained by applying rotational cooling on such heavier molecules is so far significantly below the level used here on HD^+ [30], but simulations [31] show that similar levels should be achievable with appropriate laser cooling schemes and laser systems. Hyperfine structure and Zeeman shift coefficients will be molecule-specific. Molecular ions in an electronic spin singlet state are particularly interesting, as they would have a reduced number of hyperfine states, of Zeeman substates, and much reduced linear Zeeman shift coefficients, simplifying and narrowing the spectrum. Thus, the extension of rotational spectroscopy of sympathetically cooled molecular ions to other species appears very promising.

ACKNOWLEDGMENTS

This work was funded by the DFG (Project Schi 431/11-1) and by an equipment grant of the Heinrich-Heine-Universität. We thank F. Lewen for the loan of equipment and V. Korobov for communication of unpublished results. We are indebted to B. Roth and T. Schneider for their contributions in the initial phase of this study.

---

[1] F. Lewen, S. P. Belov, F. Maiwald, T. Klaus, and G. Winnewisser, Z. Naturforsch. A **50**, 1182 (1995).
[2] A. Maestrini, J. Ward, G. Chattopadhyay, E. Schlecht, and I. Mehdi, Frequenz—J. RF Engineer. **62**, 118 (2008).
[3] F. Klappenberger, K. F. Renk, P. Renk, B. Rieder, Y. I. Koshurinov, D. G. Pavelev, V. Ustinov, A. Zhukov, N. Maleev, and A. Vasilyev, Appl. Phys. Lett. **84**, 3924 (2004).
[4] C. P. Endres, F. Lewen, T. F. Giesen, S. Schlemmer, D. G. Paveliev, Y. I. Koschurinov, V. M. Ustinov, and A. E. Zhucov, Rev. Sci. Instrum. **78**, 043106 (2007).
[5] See, e.g., H. W. Kroto, *Molecular Rotation Spectra* (Wiley, London, 1975).
[6] S. Carocci, A. Di Lieto, A. Menciassi, P. Minguzzi, and M. Tonelli, J. Mol. Spectrosc. **175**, 62 (1996).
[7] L. A. Surin, B. S. Dumesh, F. S. Rusin, G. Winnewisser, and I. Pak, Phys. Rev. Lett. **86**, 2002 (2001).
[8] G. Cazzoli, L. Dore, C. Puzzarini, and S. Beninati, Phys. Chem. Chem. Phys. **4**, 3575 (2002).
[9] G. Winnewisser, S. P. Belov, Th. Klaus, and R. Schieder, J. Mol. Spectrosc. **184**, 468 (1997).
[10] V. Ahrens, F. Lewen, S. Takano, G. Winnewisser, S. Urbana, A. A. Negirev, and A. N. Koroliev, Z. Naturforsch. A **57**, 669 (2002).
[11] R. Krems, B. Friedrich, and W. C. Stwalley, eds., *Cold Molecules* (CRC Press, Boca Raton, FL, 2009).
[12] I. W. M. Smith, ed., *Low Temperatures and Cold Molecules* (World Scientific Publishing, Singapore, 2008).
[13] O. Asvany, O. Ricken, H. S. P. Müller, M. C. Wiedner, T. F. Giesen, and S. Schlemmer, Phys. Rev. Lett. **100**, 233004 (2008).
[14] W. H. Wing, G. A. Ruff, W. E. Lamb, and J. J. Spezeski, Phys. Rev. Lett. **36**, 1488 (1976).
[15] A. Carrington, I. R. McNab, and C. A. Montgomerie, J. Phys. B **22**, 3551 (1989).
[16] J. C. J. Koelemeij, B. Roth, A. Wicht, I. Ernsting, and S. Schiller, Phys. Rev. Lett. **98**, 1730024 (2007).

[17] S. Schiller and V. Korobov, Phys. Rev. A **71**, 032505 (2005).
[18] V. I. Korobov, Phys. Rev. A **74**, 052506 (2006).
[19] V. I. Korobov, Phys. Rev. A **77**, 022509 (2008).
[20] U. Bressel *et al*., to appear in Phys. Rev. Lett. (2012).
[21] A. Carrington, C. A. Leach, A. J. Marr, R. E. Moss, C. H. Pyne, and T. C. Steimle, J. Chem. Phys. **98**, 5290 (1993).
[22] A. Carrington, I. R. McNab, C. A. Montgomerie, and J. M. Brown, Mol. Phys. **66**, 1279 (1989).
[23] V. I. Korobov (private communication).
[24] T. Schneider, B. Roth, H. Duncker, I. Ernsting, and S. Schiller, Nat. Phys. **6**, 275 (2010).
[25] D. Bakalov, V. I. Korobov, and S. Schiller, Phys. Rev. Lett. **97**, 243001 (2006).
[26] D. Bakalov, V. I. Korobov, and S. Schiller, J. Phys. B **44**, 025003 (2011).
[27] S. Schiller, B. Roth, F. Lewen, O. Ricken, and M. Wiedner, Appl. Phys. B **95**, 55 (2009).
[28] P. Blythe, B. Roth, U. Fröhlich, H. Wenz, and S. Schiller, Phys. Rev. Lett. **95**, 183002 (2005).
[29] S. Vasilyev, A. Nevsky, I. Ernsting, M. Hansen, J. Shen, and S. Schiller, Appl. Phys. B **103**, 27 (2011).
[30] P. Staanum, K. Højbjerre, P. Skyt, A. Hansen, and M. Drewsen, Nat. Phys. **6**, 271 (2010).
[31] See the Supplemental Materials in Ref. [24].

PRL **108,** 183003 (2012) PHYSICAL REVIEW LETTERS week ending 4 MAY 2012

Manipulation of Individual Hyperfine States in Cold Trapped Molecular Ions and Application to HD$^+$ Frequency Metrology

U. Bressel, A. Borodin, J. Shen, M. Hansen, I. Ernsting, and S. Schiller
Institut für Experimentalphysik, Heinrich-Heine-Universität Düsseldorf, Universitätsstr. 1, 40225 Düsseldorf, Germany

(Received 20 November 2011; published 3 May 2012)

Advanced techniques for manipulation of internal states, standard in atomic physics, are demonstrated for a charged molecular species for the first time. We address individual hyperfine states of rovibrational levels of a diatomic ion by optical excitation of individual hyperfine transitions, and achieve controlled transfer of population into a selected hyperfine state. We use molecular hydrogen ions (HD$^+$) as a model system and employ a novel frequency-comb-based, continuous-wave 5 μm laser spectrometer. The achieved spectral resolution is the highest obtained so far in the optical domain on a molecular ion species. As a consequence, we are also able to perform the most precise test yet of the *ab initio* theory of a molecule.

DOI: 10.1103/PhysRevLett.108.183003 PACS numbers: 37.10.Pq, 33.15.Mt, 33.15.Pw, 42.50.Xa

Cold trapped molecules [1,2] currently represent an intense field of activity relying on sophisticated methods of molecule production, translational and internal cooling, spectroscopy and sensitive detection. Many applications, such as chemical reaction studies [3,4], tests of molecular quantum theory [5], fundamental physics [6,7] and quantum computing [8] would benefit strongly from the availability of advanced manipulation techniques, already standard in atomic physics. These are not straightforward for molecules, and for charged molecules have not been demonstrated yet. Production methods for molecular ions (usually, e.g., by electron impact ionization) and, if heteronuclear, their interaction with the blackbody radiation of the surrounding vacuum chamber, usually lead to significant population of a substantial number of internal states. A first, important step in the manipulation of internal states of molecular ions is population transfer between rotational states (heteronuclear molecules usually being cold vibrationally, i.e., are all in the $v = 0$ ground vibrational state). It has been demonstrated that a significant fraction (ca. 75%) of an ensemble of diatomic molecular ions can be pumped into the vibrational and rotational ground level ($v = 0, N = 0$) [9,10]; see Fig. 1.

For a general diatomic molecule, however, this pumping is usually not capable of preparing molecules in a single quantum state, because spin interactions generate a hyperfine structure with several states in each rovibrational level. For example, a diatomic molecule with one unpaired electron ($s_e = 1/2$), and nuclei with nuclear spins $I_1 = 1/2$ and $I_2 = 1$ (such as HD$^+$) has 4 hyperfine states in zero magnetic field if the rotational angular momentum is $N = 0$, but 10 if $N = 1$, and 12 if $N \geq 2$; see Fig. 2(a). The ability to address selectively molecules in one particular hyperfine state (or even in a single quantum state with a particular magnetic quantum number J_z) and to transfer molecules from one hyperfine state to another are clearly important tools of a molecular quantum toolbox that can be part of a full quantum state preparation procedure.

Complicating the addressing, the number of strong transitions between two given rovibrational levels (v, N), (v', N') is equal to the larger of the two numbers of hyperfine states, i.e., potentially high, and with only small differences in transition frequency. Figure 2(b) shows as an example the case of the fundamental vibrational transition $(v = 0, N = 0) \rightarrow (v' = 1, N' = 1)$ in HD$^+$, where 10 strong transitions occur over a range of about 60 MHz ([11,12]). Addressing a single hyperfine state in a multispin molecule thus requires a spectroscopy that can resolve individual hyperfine lines in the spectrum.

In this work, our approach is based on one-photon laser excitation of the fundamental vibrational transition $(0, 0) \rightarrow (1, 1)$ at the wavelength λ_f, see Fig. 1. The relatively low transition frequency, $\lambda_f > 2.5$ μm for diatomics, in combination with the low secular kinetic energy $k_B T_{\mathrm{sec}}$ achievable by sympathetic cooling, yields a Doppler broadening $\Delta\nu_D$ of the transitions that is smaller than many line spacings. This provides the desired quantum state selectivity for addressing some of the hyperfine states, using strong transitions. For our test case HD$^+$, $\lambda_f = 5.1$ μm, $T_{\mathrm{sec}} \simeq 10$ mK, $\Delta\nu_D \simeq 3$ MHz. Additionally, excitation of weak transitions [which violate the approximate selection rules $\Delta F = 0$, $\Delta S = 0$, see Fig. 2(b)], provides selectivity for all hyperfine states, since for these transitions the frequency spacings are larger. Compared to the use of a pure rotational excitation $(0, 0) \rightarrow (0, 1)$ [13] or a microwave transition within a rovibrational level, the use of a vibrational transition has the advantage that the excitation may be followed by a much faster spontaneous decay from (1,1), either back into the ground rovibrational level (rate approx. 6 s^{-1}) or into the relatively long-lived rotational level ($v'' = 0$, $N'' = 2$) (rate approx. 12 s^{-1}). This allows reasonably rapid pumping of the molecule (possibly after repeated absorption and spontaneous emission events) into

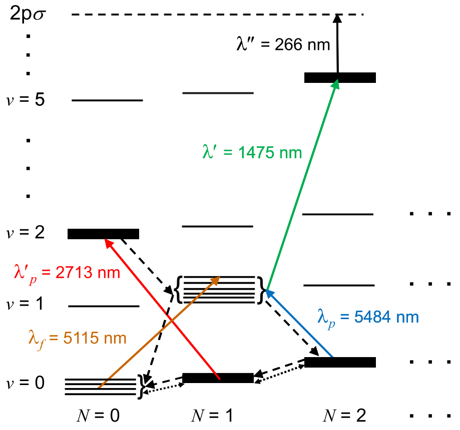

FIG. 1 (color online). Schematic energy level scheme of HD$^+$ with transitions relevant to this work. Hyperfine structure is shown schematically only for the ($v = 0$, $N = 0$) and (1,1) levels as lines, but is implied for all other levels as well (thick bars). Full lines: laser-induced transitions, dashed lines: some relevant spontaneous emission transitions; dotted lines: some blackbody induced transitions. The spectrally narrow wave λ_f selectively excites molecules from a particular hyperfine state ($v = 0, N = 0, F, S, J$) to a single hyperfine state ($1,1, F', S', J'$) Quantum state preparation is performed by irradiating alternatly the appropriately tuned waves λ_f and λ_p, in conjunction with spontaneous emission from the level (1,1). Resonant laser radiation at λ' and nonresonant radiation at λ'' is used to detect that hyperfine-state-selective excitation to the (1,1) level has occurred, by transferring the excited molecules to the electronically excited molecular state $2p\sigma$ from which they dissociate. Initially, rotational cooling is performed by radiation at λ_p and λ'_p. The level energy differences are not to scale. The waves at λ', λ'', λ_p, λ'_p, have large spectral linewidths and do not excite hyperfine state selectively.

another long-lived state, a necessary condition for efficient quantum state preparation, as shown below.

The experiment is performed on ensembles of HD$^+$ ions trapped in a linear quadrupole radio-frequency trap (14.2 MHz), sympathetically translationally cooled by co-trapped, laser-cooled Beryllium atomic ions [14] and rotationally cooled by lasers. The HD$^+$ molecule is of interest since it is a fundamental quantum system that allows precision measurements of QED effects and fundamental constants [5]. Our laser system consists of four subsystems: a $\lambda_f = 5.1$ μm laser spectrometer referenced to an atomic frequency standard [15] (see Supplemental Materials [16]), a reliable, frequency-stabilized fiber-laser-based 313 nm laser for cooling of Beryllium ions [17], a rotational cooling laser system (a $\lambda_p = 5.5$ μm quantum cascade laser and, for part of the measurements, a $\lambda'_p = 2.7$ μm diode laser), and a pair of lasers (λ, λ') for resonance-enhanced multiphoton dissociation (REMPD); see Fig. 1. Rotational cooling [9] is a crucial tool here, as it significantly increases the fractional population of molecules in the lower rovibrational level

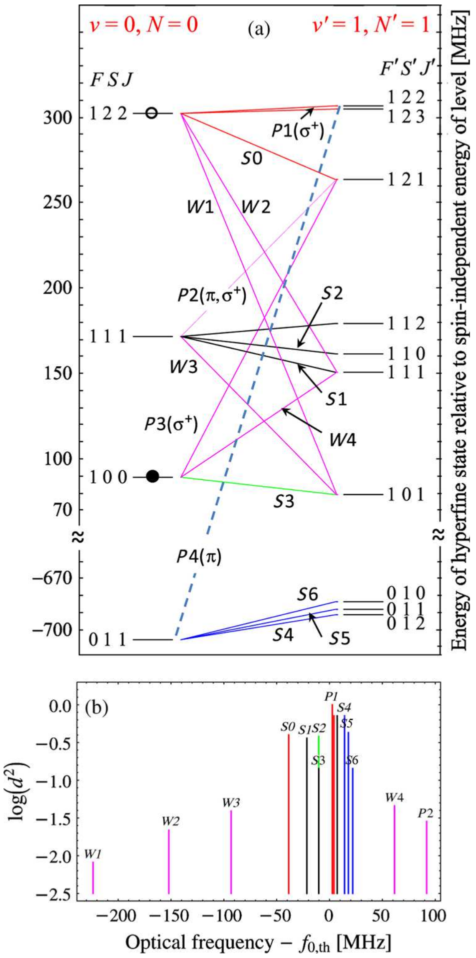

FIG. 2 (color online). (a) Energy diagram of the hyperfine states and main electric-dipole transitions in zero magnetic field. (b) Stick spectrum of the transitions (in zero magnetic field; values of the squared transition moment d^2 are normalized to the strongest transition). The states are labeled by the quantum numbers (F, S, J). Weak transitions are shown in pink [12]. Very weak transitions are not shown, except for $P4$ (dashed). The "spin-independent" transition frequency $f_{0,\mathrm{th}}$ is the value if nuclear and electron spin were zero. $S0$, $S1$, $S2$, $S3$, $S4$, $S5$, $S6$, $W1$, $W2$, $W3$, $W4$, $P2$ are transitions studied here ("W, S, P" mean "weak", "strong", and "pumping", respectively). All were observed except $S4$. $W1$, $W3$ are the transitions used here to achieve population transfer from the hyperfine states ($v = 0$, $N = 0$, $F = 1$, $S = 2$, $J = 2$, J_z) (empty circle) and ($0,0,1,1,1,J'_z$) into the hyperfine state ($0,0,1,0,0,J''_z$) (filled circle). $P1$, $P2$, $P3$, and $P4$ are proposed optical pumping transitions (with indicated polarizations) for preparation of the molecule in the single quantum state ($0, 0, 1, 2, 2, J_z = +2$) (one of the Zeeman states in the open circled hyperfine state).

($v = 0, N = 0$), from ca. 10% to 60%–75%. The possibility provided by our laser system to measure the HD$^+$ fundamental vibrational transition frequency $f = c/\lambda_f$ also allows us to perform a precise comparison with the *ab initio* theory of the molecular hydrogen ion.

Hyperfine-resolved rovibrational transitions are induced by the $\lambda_f = 5.1\ \mu$m radiation tuned precisely to individual transitions. We then detect (without hyperfine-state selectivity) the population of the goal vibrational level ($v' = 1, N' = 1$), by $1 + 1'$ resonance-enhanced multiphoton dissociation (REMPD) [18]; see Fig. 1. Together, this represents a three-photon ($1 + 1' + 1$”) REMPD process. The reduction of the HD^+ number by the REMPD process is our spectroscopic signal [18].

Figure 3 shows the obtained hyperfine-state resolved spectrum. All theoretically predicted and addressed hyperfine transitions were observed; only the (nominally strong) transition $S4$ is barely detected, for unknown reason. Transition $W4$, which originates from a lower hyperfine state with only a small fractional population ($J = 0$, thus statistically containing only 5%–6% of all molecules), could only be made clearly evident using a preceding hyperfine pumping step (see below). Each of the 4 hyperfine states of the lower level was selectively addressed, and 5 of the 12 upper level hyperfine states were selectively populated. We also observed the line at −10.2 MHz, which contains two nearly coinciding transitions $S2$ and $S3$, but originating from different ground hyperfine states. The remaining strong transitions (including the line marked $P1$ in Fig. 2) were also observed, but their small spacing prevents complete resolution, and they are not reported in the Fig. 3.

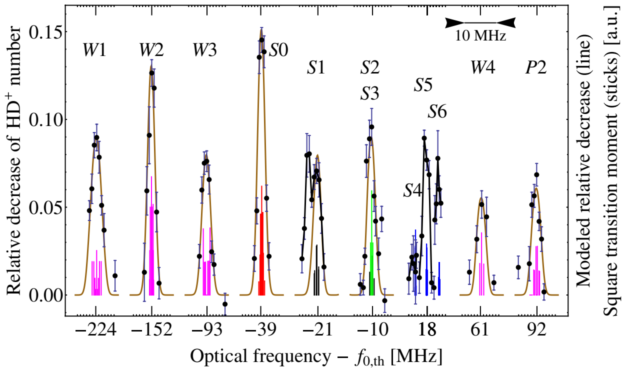

FIG. 3 (color online). Observed hyperfine spectrum of the $(v = 0, N = 0) \longrightarrow (1, 1)$ fundamental rovibrational transition in cold trapped HD^+ ions. The effective intensity times irradiation duration product of the $5.1\ \mu$m radiation varied from line to line, and was adapted to avoid saturation. Brown lines are the result of fitting $f_{0,\mathrm{exp}}$, the individual line amplitudes, the Doppler temperature (9.5 mK) and the average magnetic field (0.8 G). The sticks are for illustration purpose and show the theoretical squared transition dipole moments for the Zeeman components at 0.8 G, assuming exciting radiation polarized at 45° to the magnetic field. They are scaled by different factors for presentation purpose. Color coding is as in Fig. 2. $S4$, $S6$ were taken at high intensity-irradiation time product, $S5$ at a lower value. The side peak of $S1$ is probably due to an ion micromotion sideband of $S2/S3$. The $W4$ line required hyperfine-state optical pumping for its detection (see Fig. 4).

We demonstrate hyperfine-state manipulation by optical pumping of individual hyperfine-state populations into a goal state. As a goal state we choose ($v = 0$, $N = 0$, $F = 1$, $S = 0$, $J = 0$, $J_z = 0$) which is nondegenerate ($J = 0$) and thus a single quantum state (filled circle in Fig. 2). After rotational cooling, we apply the following sequence twice: $W1$ line (3 s), rotational repumping (λ_p and λ'_p simultaneously for 5 s), $W3$ line (3 s). A final 10 s of rotational repumping is performed before the spectroscopic excitation. The $W1$ and $W3$ transitions excite population from two initial hyperfine states (0, 0, 1, 2, 2, J_z), (0, 0, 1, 1, 1, J'_z) (without J_z selectivity) into the state (1, 1, 1, 0, 1, J''_z). This state has dominant spontaneous decay to the goal state (green line $S3$ in Fig. 2). We find clear evidence that this hyperfine-state preparation is taking place by observing the transition $W4$ starting from the goal state by REMPD; see Fig. 4. This transition is not observable in our experiment without the preparation procedure, since then the population in the lower hyperfine state is too low.

Our hyperfine-state resolved spectrum represents the highest-resolution optical spectrum of any molecular ion so far [5,19,20]. This enables an accurate comparison of experimental frequencies with *ab initio* theory. We

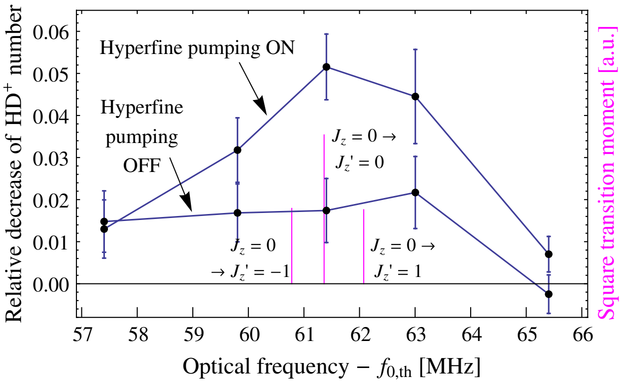

FIG. 4 (color online). Demonstration of hyperfine-state manipulation. The transition $W4$ shown here is observed only when hyperfine optical pumping is implemented. This transition represents the excitation from a single quantum state, $(0,0,1,0,0,J_z = 0)$. Data shown were taken alternating measurements preceded by hyperfine optical pumping (upper data points joined by line) and not (lower data points). The intensity of the $5.1\ \mu$m laser radiation was set to its maximum both during hyperfine pumping on the $W1$ and $W3$ transitions and subsequent detection of the $W4$ transition. Irradiation time on the $W4$ transition was 3 s. Rotational cooling by the $2.7\ \mu$m and $5.5\ \mu$m laser was used. The zero level corresponds to the relative decrease measured when the $5.1\ \mu$m spectroscopy laser was blocked. The three sticks show, for illustration purposes, the theoretical transition frequencies and strengths in a 0.8 G magnetic field and radiation polarized at 45° to the magnetic field. The shift of the central component is −0.05 MHz relative to the zero-field frequency.

obtain two hyperfine-state separations in the ground state, $\Delta f_{0,0,a} = (E(0,0,1,2,2) - E(0,0,1,1,1))/h$ and $\Delta f_{0,0,b} = (E(0,0,1,1,1) - E(0,0,1,0,0))/h$, from the measured transition frequency combinations $f(S1) - f(W2)$, $f(W3) - f(W1)$, $f(P2) - f(S0)$, and from $f(W4) - f(S1)$, $f(P3) - f(P2)$, respectively. In addition, two excited state splittings, $\Delta f_{1,1,c} = (E(1,1,1,2,1) - E(1,1,1,1,1))/h$ and $\Delta f_{1,1,d} = (E(1,1,1,1,1) - E(1,1,1,0,1))/h$ are similarly obtainable by suitable frequency combinations. A fit of these hyperfine-state separations to the data (fitting also the spin-independent frequency) yields agreement with the *ab initio* results $(\Delta f_{0,0,a}, \Delta f_{0,0,b}, \Delta f_{1,1,c}, \Delta f_{1,1,d}) = (130.60(1), 82.83(1), 113.33(1), 71.68(1))$ MHz [11,21], with deviations (experimental minus theoretical) of $(-0.22(0.13), 0.28(0.38), -0.13(0.15), 0.27(0.19))$ MHz. The values in inner parentheses being the experimental uncertainties. The two measured hyperfine separations of the ground state also allow determining the two hyperfine constants $E_4(0,0)$, $E_5(0,0)$ [11] which fully describe the hyperfine structure of the ground state [12]. Our fit yields $(E_4(0,0), E_5(0,0)) = (906(17), 142.33(25))$ MHz, whereas the theory values are $(925.38(1), 142.29(1))$ MHz [11,21].

Assuming instead that the hyperfine energies are given by the theoretical values (this assumption being strengthened by the agreement of hyperfine theory and experiment for large-v levels [11,22]), we can fit an overall frequency correction to the spectra $W1$, $W2$, $W3$, $S0$, $S1$, $S2 + S3$, $W4$, $P2$. We obtain the spin-independent frequency $f_{0,\mathrm{exp}} = 586\,050\,52.00$ MHz, with combined statistical and systematic error of 0.064 MHz (see Supplemental Material [16]). The theoretical value is $f_{0,\mathrm{th}} = 586\,050\,52.139(11)(21)$ MHz, where the first error is due to the uncertainty of the fundamental constants and the second is the theoretical error in the evaluation of the QED contributions [21,23,24]. The difference between experimental and theoretical results is -2.0 times the combined theoretical plus experimental error. The relative experimental uncertainty of 1.1×10^{-9} represents the most accurate test of molecular theory to date. In particular, our measurement is the first molecular measurement sufficiently accurate to be explicitly sensitive to the QED contributions of order α^5 (relative to the nonrelativistic contribution to the transition frequency), calculated as 0.109(21) MHz for the transition studied here [21,24].

Based on the technique demonstrated here, we can propose a realistic optical pumping procedure for preparing most of the population in a single quantum state (v, N, F, S, J_z), i.e., with well-defined projection of the total angular momentum. Under typical conditions, the relative statistical occupation of any individual quantum state in $(v = 0, N = 0)$ is only $\simeq (1/12) \times (60\%–75\%) \simeq 5\%–6\%$ under rotational cooling by a single laser (λ_p) or two lasers (λ_p, λ_p'). Exciting sequentially the four transitions $P4$ $[(0,0,0,1,1) \rightarrow (1,1,1,2,2)]$, $P3$, $P2$, $P1[(0,0,1,2,2) \rightarrow (1,1,1,2,3)]$ in a weak magnetic field and with polarizations chosen as indicated in Fig. 2(a) will cause transfer of the population of all Zeeman quantum states of (0, 0) to the single Zeeman quantum state (0, 0, 1, 2, 2, $J_z = +2$), via spontaneous emission processes from (1, 1, 1, 2, $J' = \{1,2\}$, J_z'), which dominantly occur on strong transitions [red lines in Fig. 2(a)]. These excitations should be interleaved with rotational cooling (lasers λ_p, λ_p'), which also serves as repumper following spontaneous decay into ($v'' = 0$, $N'' = 2$). The optical pumping procedure should take a few ten seconds and lead to 60%–70% fractional population in the goal state.

In summary, we have shown that it is possible to address and prepare individual hyperfine states in cold, trapped diatomic molecular ions even in presence of a complex spin structure. A midinfrared laser spectrometer controlled by an atomic standard-referenced frequency comb, and sufficiently low ion kinetic energies were two important aspects. The observed, Doppler-limited, transition linewidths (3 MHz) are the lowest obtained to date on a molecular ion species in the optical domain [note that they scale as (molecule mass)$^{-1/2}$]. We also observed, for the first time to our knowledge, weakly allowed hyperfine transitions using optical excitation. As one application, we were able to directly determine the population fraction of molecules, in particular, hyperfine states. The largest value we found was 19%, clearly indicating the effectiveness of our rotational cooling. We also demonstrated excitation of a transition from a single quantum state. Since our test molecule HD$^+$ is the simplest heteronuclear molecule and is excited from the rovibrational ground state, this study represents the first precision measurement of the most fundamental electric-dipole allowed rovibrational transition of any molecule [19]. A comparison of theory with experiment showed that (i) the hyperfine energies of small-v, N rovibrational levels agree within deviations of less than 0.3 MHz and (ii) the spin-independent energy agrees within 2 times the relative error of 1.1×10^{-9}.

We are grateful to B. Roth, T. Schneider, A. Yu. Nevsky, and S. Vasilyev for help and support, and to V. Korobov for important discussions. Funding was provided by DFG project Schi 431/11-1.

[1] *Cold Molecules*, edited by R. Krems, B. Friedrich, and W. C. Stwalley (CRC Press, Boca Raton, 2009).

[2] *Low Temperatures and Cold Molecules*, edited by I. W. M. Smith (World Scientific Publishing, Singapore, 2008).

[3] B. Roth, P. Blythe, H. Wenz, H. Daerr, and S. Schiller, Phys. Rev. A **73**, 042712 (2006).

[4] P. F. Staanum, K. Højbjerre, R. Wester, and M. Drewsen, Phys. Rev. Lett. **100**, 243003 (2008).

[5] J. C. J. Koelemeij, B. Roth, A. Wicht, I. Ernsting, and S. Schiller, Phys. Rev. Lett. **98**, 173002 (2007).

[6] S. Schiller and V. Korobov, Phys. Rev. A **71**, 032505 (2005).
[7] H. Müller *et al.*, Phys. Rev. A **70**, 076004 (2004).
[8] D. DeMille, Phys. Rev. Lett. **88**, 067901 (2002).
[9] T. Schneider, B. Roth, H. Duncker, I. Ernsting, and S. Schiller, Nature Phys. **6**, 275 (2010).
[10] P. Staanum, K. Højbjerre, P. S. Skyt, A. K. Hansen, and M. Drewsen, Nature Phys. **6**, 271 (2010).
[11] D. Bakalov, V. I. Korobov, and S. Schiller, Phys. Rev. Lett. **97**, 243001 (2006).
[12] D. Bakalov, V. I. Korobov, and S. Schiller, J. Phys. B **44**, 025003 (2011).
[13] J. Shen, A. Borodin, M. Hansen, and S. Schiller, Phys. Rev. A **85**, 032519 (2012).
[14] P. Blythe, B. Roth, U. Fröhlich, H. Wenz, and S. Schiller, Phys. Rev. Lett. **95**, 183002 (2005).
[15] U. Bressel, I. Ernsting, and S. Schiller, Opt. Lett. **37**, 918 (2012).
[16] See Supplemental Materials at http://link.aps.org/supplemental/10.1103/PhysRevLett.108.183003 for details.
[17] S. Vasilyev, A. Nevsky, I. Ernsting, M. Hansen, J. Shen and S. Schiller, Appl. Phys. B **103**, 27 (2011).
[18] B. Roth, J. C. J. Koelemeij, H. Daerr, and S. Schiller, Phys. Rev. A **74**, 040501-4 (2006).
[19] The $(0, 1) \leftrightarrow (1, 0)$ transition has been measured in an ion beam experiment, with a linewidth ≥ 7 MHz and a frequency uncertainty $\simeq 21$ MHz, W. H. Wing *et al.*, Phys. Rev. Lett. **36**, 1488 (1976); J. J. Spezeski, Ph.D. dissertation, Yale University, 1977.
[20] H. C. Miller, M. Al-Za'al, and J. W. Farley, Phys. Rev. Lett. **58**, 2031 (1987).
[21] V. I. Korobov, (private communication).
[22] A. Carrington, I. R. McNab, C. A. Montgomerie-Leach, and R. A. Kennedy, Mol. Phys. **72**, 735 (1991).
[23] V. I. Korobov, Phys. Rev. A **74**, 052506 (2006).
[24] V. I. Korobov, Phys. Rev. A **77**, 022509 (2008).

SUPPLEMENTAL MATERIALS

Addressing and manipulation of individual hyperfine states in cold trapped molecular ions and application to HD$^+$ frequency metrology

U. Bressel, A. Borodin, J. Shen, M. Hansen, I. Ernsting, S. Schiller
Institut für Experimentalphysik, Heinrich-Heine-Universität Düsseldorf, Universitätsstr. 1, 40225 Düsseldorf, Germany

1. General features of hyperfine structure

We consider a diatomic molecule with total electron spin s, nuclei with nuclear spins I_1, I_2, in a rotational level N. The spin degeneracy is lifted (only partially in zero magnetic field) into a number of hyperfine states by the electron spin - nuclear spin interaction ($\sim \mathbf{s} \cdot \mathbf{I_i}$) and/or the electron spin - rotation interaction ($\sim \mathbf{s} \cdot \mathbf{N}$). In HD$^+$, the (approximate) quantum numbers (F, S, J) correspond to the couplings $\mathbf{F} = \mathbf{s} + \mathbf{I_p}$, $\mathbf{S} = \mathbf{F} + \mathbf{I_d}$, $\mathbf{J} = \mathbf{S} + \mathbf{N}$. The electron spin - nuclear spin interactions determine the main splittings in a given ro-vibrational level, resulting in 4 singlets (if $N = 0$) or in 4 multiplets (if $N \neq 0$). In the latter case, the electron-spin rotation interaction determines the splitting strength within the multiplets [1].

The line splittings in the transition spectrum, Figure 2b arise because in the lower and upper levels (i) the strengths of the electron spin-nuclear spin interactions and of the electron spin - rotation interaction differ, and (ii) the rotational angular momenta N, N' differ. The density of lines in the spectrum is essentially independent of whether the transition is a fundamental vibrational transition, an overtone transition ($\Delta v = v' - v > 1$) (e.g. [2]), or a pure rotational transition ($\Delta v = 0$).

2. 5.1 µm laser spectrometer

The spectroscopy radiation was generated by frequency-mixing in a nonlinear optical crystal two near-infrared lasers which are individually referenced to a conventional frequency comb [3]. The generated wavelength, 5.1 µm, extends the coverge provided so far by sources with absolute frequency measurement capability [4, 5].

We use two continuous-wave lasers, a Nd:YAG laser (1064 nm, ca. 6 W) stabilized to a Doppler-free resonance in molecular iodine via its second-harmonic wave at 532 nm, and a 1344 nm home-built external cavity quantum-dot diode laser (QD-ECDL). The main part of the 1344 nm wave is resonantly enhanced in a ring resonator containing a periodically poled MgO:LiNbO$_3$ crystal with poling period 25.4 µm, appropriate for difference frequency generation of 5.1 µm radiation. The 1064 nm wave is focused and overlapped with the 1344 nm wave in the crystal, but not resonated. Although the crystal strongly absorbs the generated 5.1 µm radiation, an output power of up to 0.1 mW is generated. Small fractions of the 1064 and 1344 nm waves are sent via an unstabilized single-mode optical fiber to another laboratory containing the femtosecond Ti:sapphire frequency comb, where both frequencies are measured. The 1344 nm laser is actively frequency-stabilized to a mode of the frequency comb. The 1064 nm wave frequency is continuously measured by the comb. The comb itself is stabilized to a hydrogen maser or ultra-stable quartz oscillator, both referenced to GPS.

Tunable, frequency-stable 5.1 µm radiation is produced by amplitude modulating the diode laser output wave with an integrated-optic modulator at a variable radio-frequency Ω before sending the wave to the resonator. This generates two sidebands, and the resonator length is stabilized to resonate one of the two, generating a single frequency at 5.1 µm. By changing the modulation frequency Ω, the 5.1 µm radiation can be smoothly and precisely frequency-tuned over 460 MHz. We determined the spectral width of the 5.1 µm radiation as $\Gamma_f \simeq 0.68\,\mathrm{MHz}$. The frequency instability (Allan deviation) of this radiation is constant at ca. 23 kHz for integration times τ up to 10 s, dropping to 4 kHz at $\tau = 800\,\mathrm{s}$. Both linewidth and instability are significantly lower than the Doppler width of the HD$^+$ hyperfine transitions studied here. The absolute frequency uncertainty of the 5.1 µm radiation is less than 10 kHz when averaged over 1 h.

3. Procedures and analysis

Each data point in a spectrum measurement is acquired from one loading of HD$^+$ ions into a laser-cooled Be$^+$ ion cluster. Figure A1 shows an example.

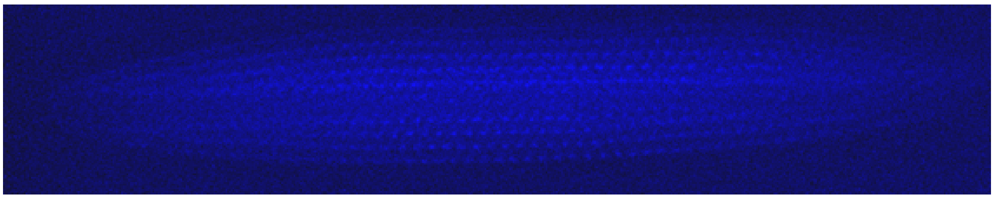

Figure A1: CCD image of a typical Beryllium ion Coulomb cluster with embedded HD$^+$ ions (darker region along the long axis), as used in the experiment.

From molecular dynamics (MD) simulation of ion cluster fluorescence images [6] we deduce an upper limit for the secular temperature $T_{sec} \leq 15\,\mathrm{mK}$. After loading, the molecules are rotationally cooled by $\lambda_p \simeq 5.5\,\mu$m radiation (and, for some measurements, also $\lambda_p{}' = 2.7\,\mu$m radiation) for 30 s, transferring about 60% (75%) of the molecules into the ($v = 0$, $N = 0$) ro-vibrational ground level. This population is spread over the four hyperfine states. Then, the rotational pumping laser waves are blocked and the $5.1\,\mu$m spectroscopy radiation is applied along the trap axis for 3 - 30 s, simultaneously with a 1475 nm diode laser (ca. 1 mW) driving the ($v' = 1$, $N' = 1$) $\to$ ($v'' = 5$, $N'' = 2$) overtone transition, and a 266 nm laser (ca. 25 mW) that dissociates the molecules in the latter state.

The number of trapped HD$^+$ ions is measured by excitation of their secular motion before the rotational cooling and after the (partial) photodissociation. Excitation of the secular motion heats up all ions and therefore changes the Be$^+$ fluorescence rate, which is detected by a photomultiplier. The relative decrease in the photomultiplier signal is the signal of interest, the excited molecule fraction. As the spectroscopy source linewidth is 0.7 MHz, we made frequency steps of typically 0.8 MHz when scanning through the lines. One data point could be recorded on average every 3 min. This limited the number of data points per frequency value that could be taken. We performed between 4 and 25 measurements per frequency point. Typically, one hyperfine transition required one day of measurement. Background level measurements were performed in the same way, with the 5.1 µm laser blocked. Alignment of the 5.1 µm laser with the ion cluster varied from day to day, which was compensated by adjusting the power.

The typical standard deviation of the relative decay data taken at a given optical frequency (not of the mean) is 0.02. This is due primarily to the low number of HD$^+$ ions loaded into the ion cluster (a few hundred) and the low relative population in a particular hyperfine state (only a fraction $\simeq (0.6 - 0.75)\,p_J$, where $p_J = (2J + 1)/12$ in a particular hyperfine state J, for $N = 0$), which is further reduced during the REMPD phase (λ_p, $\lambda_p{}'$ lasers off) by the competing black-body-radiation driven excitation ($v = 0$, $N = 0$) $\to$ (0, 1). The overall small numbers lead to significant statistical fluctuations in the number of ions actually prepared into a particular initial hyperfine state after optical pumping, and in the fraction excited and dissociated. As a consistency check, we found that the maximum observed dissociated fractions (at high intensity and on resonance) did not exceed p_J. For example, for line S0, we observed (19.4±1.4)% ion number reduction, for lines S2+S3, (16.4±2.8)%. Note that the values shown in Figure 3 are lower because there, lower intensities were used in order to avoid saturation broadening.

The smallest observed full-width-half-maximum linewidths are $\simeq$ 3.0 MHz. Assigning this to be due to Doppler broadening only, the value yields an upper limit of 15 mK for the secular temperature, consistent with the MD simulations.

The observable spectrum may be modeled, including the effects of finite secular temperature, finite laser linewidth, finite population in the lower level, the effect of unresolved Zeeman splittings by the non-zero magnetic field in the ions' region [7], and black-body-radiation induced excitation to (0, 1). In order to simplify the analysis, in the experiment we chose laser power and irradiation times such that significant saturation and concomitant broadening of the signals was avoided, i.e. the linear absorption regime was maintained. We furthermore take into account: (i) from independent measurements we have some knowledge about the magnetic field: an upper limit of ca. 1 G [8]; (ii) the laser linewidth does not contribute strongly to the total linewidth, and we may therefore use an effective Doppler temperature for modeling the lineshape; (iii) the overlap between the focused spectroscopy beam (ca. 0.5 mm waist) and the ion cloud was not constant over the time span covering all hyperfine line measurements; (iv) the effect of black-body-induced excitation (0, 0) $\to$ (0, 1) represents a reduction in maximum observable signal. Thus, we fit an effective product of intensity and irradiation time to each transition spectrum in order to reproduce the signal levels. We used a simplified model of the magnetic field inhomogeneity in the ions' volume. We find a good fit for an average magnetic field of 0.8 G and (9.5 ± 1) mK temperature. The statistical error for the spinless frequency $f_{0,th}$ is obtained from a Monte Carlo simulation as 60 kHz.

4. Systematic errors

Due to the slow data rate of this experiment, measurements of systematics were not possible. However, the well-developed theory of the HD^+ molecule allows relying on theoretical results to estimate upper limits for various systematic errors. Those due to light shift, black-body shift [9], electric quadrupole shift [10], and Stark shift [11, 12], are theoretically estimated to be less than 10 kHz. The only potential significant effect is the Zeeman effect. The sticks in Figures 3, 4 show the splittings expected for the typical magnetic field value in our trap [7]. These unresolved splittings could lead to a shift of the centers of the lines but we find that the weighted mean frequency of the magnetic components of any line shifts weakly with magnetic field (e.g. less than ca. 10 kHz for line S0 at 1 G). We modeled the influence of the imprecisely known magnetic field on the fitted spin-independent frequency and estimate an error of 13 kHz from this effect. In order to obtain the spin-independent frequency from our measurements, we use the theoretical prediction of the hyperfine energies. The influence of their theoretical errors onto the fitted spin-independent frequency is conservatively assumed to be 10 kHz. The error of the optical frequency measurements is less than 10 kHz. Similar considerations are applied to the fit of the hyperfine splittings.

5. Theoretical transition frequencies

The theoretical frequency of any particular hyperfine transition arises from three contributions. The main contribution is non-relativistic, 58 604 301.269 MHz, determined by the solution of the Schrödinger equation [13] and whose error (11 kHz) comes dominantly from the uncertainties of the electron-proton and proton-deuteron mass ratios m_e/m_p, and m_p/m_d [14]. A second contribution, 750.870 MHz, is from relativistic and QED effects [15], with estimated theoretical uncertainty of 21 kHz [16]. The sum of these two contributions is the spin-independent frequency $f_{0,th}$. The third is the hyperfine contribution [1], e.g. -38.685 MHz for transition S0. Improved values for the hyperfine constants and Bethe logarithm communicated recently by V. Korobov have been used here. The influence of these improved values as compared to the published ones on the results presented here is small in comparison with the experimental uncertainties. The theoretical uncertainty of the hyperfine contributions to the transition frequencies is less than 10 kHz [16].

6. Hyperfine state preparation

The re-pumping suggested acts predominantly on the strong, non-spin-state changing transitions. P2 is a weak transition, P3, P4 are very weak transitions. The transition dipole moments of the latter are so small [7] that a quantum cascade laser (typical output power level 10 mW) could be used for obtaining usefully large rates. Such a laser could be frequency-stabilized to a spectrometer of the type developed here, using the beat note with it as an error signal.

An additional rotational cooling laser that depletes the ($v = 0$, $L = 3$) level by exciting from it to the (1, 2) or (2, 2) level could enable an even higher population fraction in the goal hyperfine state.

In a similar way, any other Zeeman states of the ground vibrational level could in principle be populated to a high fraction.

It is recognized that variations of the above scheme can also be used to achieve similar population fractions in individual quantum states of the ($v = 0$, $N = 1$) level.

---

[1] D. Bakalov, *et al.*, Phys. Rev. Lett. **97**, 243001 (2006)
[2] B. Roth, *et al.*, Phys. Rev. A **74**, 040501 (2006)
[3] U. Bressel, I. Ernsting, and S. Schiller, Opt. Lett. **37**, 918 (2012)
[4] Wavelengths shorter than 4.4 µm were obtained in: P. Cancio, S. Bartalini, S. Borri, I. Galli, G. Gagliardi, G. Giusfredi, P. Maddaloni, P. Malara, D. Mazzotti and P. De Natale, Appl. Phys. B **102**, 255 (2011)
[5] For wavelengths near 10.6 µm, see A. Amy-Klein, A. Goncharov, M. Guinet, C. Daussy, O. Lopez, A. Shelkovnikov, and C. Chardonnet, Opt. Lett. **30**, 3320 (2005)
[6] C. B. Zhang, D. Offenberg, B. Roth, M. A. Wilson, and S. Schiller, Phys. Rev. A **76**, 012719 (2007)
[7] D. Bakalov, *et al.*, J. Phys. B: At. Mol. Opt. Phys. **44**, 025003 (2011)
[8] J. Shen, A. Borodin, M. Hansen, and S. Schiller, Phry. Rev. A **85**, 032519 (2012);
[9] J.-Ph. Karr, S. Kilic, and L. Hilico, J. Phys. B **38**, 853 (2005);
[10] A. K. Bhatia and R. J. Drachman, Phys. Rev. A. **61**, 032503 (2000);

[11] R. E. Moss and L. Valenzano, Mol. Phys. **100**, 1527 (2002)
[12] D. Bakalov and S. Schiller, to appear in Hyperfine Interactions (2012)
[13] V.I. Korobov, Phys. Rev. A **74**, 052506 (2006)
[14] P.J. Mohr, B.N. Taylor, and D.B. Newell (2011), "The 2010 CODATA Recommended Values of the Fundamental Physical Constants" (Web Version 6.0). This database was developed by J. Baker, M. Douma, and S. Kotochigova. Available: http://physics.nist.gov/constants. National Institute of Standards and Technology, Gaithersburg, MD 20899
[15] V.I. Korobov, Phys. Rev. A **77,** 022509 (2008)
[16] V. I. Korobov, private communication (2010)

Appl Phys B
DOI 10.1007/s00340-011-4435-1

Applied Physics B
Lasers and Optics

Compact all-solid-state continuous-wave single-frequency UV source with frequency stabilization for laser cooling of Be^+ ions

S. Vasilyev · A. Nevsky · I. Ernsting · M. Hansen ·
J. Shen · S. Schiller

Received: 26 October 2010 / Revised version: 13 December 2010

Abstract A compact setup for generation, frequency stabilization, and precision tuning of UV laser radiation at 313 nm was developed. The source is based on frequency quintupling of a C-band telecom laser at 1565 nm, amplified in a fiber amplifier. The maximum output power of the source at 313 nm is 100 mW. An additional feature of the source is the high-power output at the fundamental and the intermediate second- and third-harmonic wavelengths. The source was tested by demonstration of laser cooling of Be^+ ions in an ion-trap apparatus. The output of the source at the third-harmonic wavelength (522 nm) was used for stabilization of the laser frequency to molecular iodine transitions. Sub-Doppler spectroscopy and frequency measurements of hyperfine transitions in molecular iodine were carried out in the range relevant for the Be^+ laser cooling application.

1 Introduction

Single-frequency UV laser sources are used in a variety of research related to high-resolution spectroscopy of atoms, molecules and ions. As an example from quantum optics, the beryllium ion, laser cooled on the 2s → 2p transition at a wavelength of 313 nm, is a workhorse of quantum computing, precision spectroscopy of atomic and molecular ions via sympathetic cooling, and of the quantum logic optical clock [1–5], and is of interest for the nuclear structure of its isotopes [6, 7]. The UV laser source required for such experiments should be as simple, reliable, and compact as possible, so as to keep the complexity of the experiments manageable.

Single-frequency lasers directly emitting at wavelengths around 313 nm do not exist. Second-harmonic generation (SHG) of a dye laser at 626 nm is a straightforward solution but is expensive. Sum-frequency generation (SFG) of a Ti:Sapphire laser (650–1100 nm) and a frequency doubled Nd-doped laser (532 nm) allows one to cover the UV range between 293 and 358 nm using SFG in LBO or BBO nonlinear crystals. Such a source, employing SFG in a doubly-resonant enhancement cavity has been previously developed and used for Be^+ cooling [8]. Similar to the dye laser solution, the drawbacks of this approach are high initial and maintenance costs of the lasers, high complexity and bulkiness of the optical setup, the necessity to stabilize the frequency of two laser sources.

A much simpler and cost-efficient all-solid-state solution is SHG of diode-laser (DL) emission. This approach became of practical use with an advent of high-power DL amplifiers. UV laser sources based on frequency doubling or quadrupling of DL MOPAs (master oscillator power amplifier) are now commercially available. Unfortunately, the 313 nm wavelength cannot be addressed in this way for lack of DLs with reasonably high power at subharmonic wavelengths of 626 nm and 1252 nm. A feasible solution is using a 939 nm DL MOPA, followed by SHG and SFG stages. However the UV output power from such a system would be much lower than that from the system described below.

Due to remarkable progress in the fiber laser technology, reliable and cost-efficient near-IR fiber lasers and amplifiers with high spectral purity and high output power are now available [9, 10]. Currently, high-power cw ytterbium (Yb) and erbium (Er) doped fiber lasers are used success-

---

S. Vasilyev (✉) · A. Nevsky · I. Ernsting · M. Hansen · J. Shen · S. Schiller
Institut für Experimentalphysik, Heinrich-Heine-Universität Düsseldorf, Universitätsstr. 1, 40225 Düsseldorf, Germany
e-mail: Sergey.Vasilyev@uni-duesseldorf.de
url: http://www.exphy.uni-duesseldorf.de
Fax: +49-211-8113116

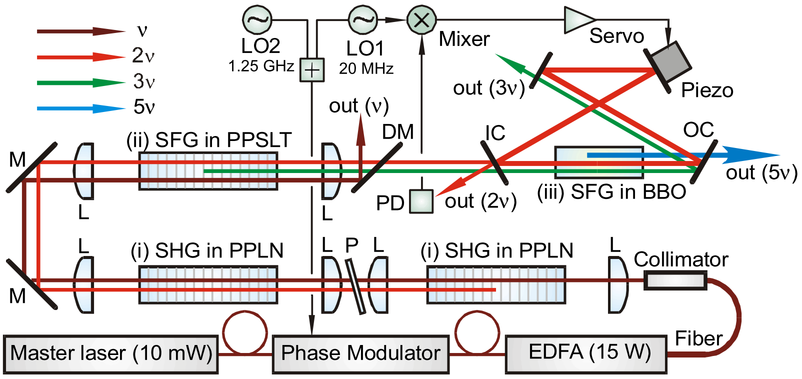

Fig. 1 Schematic of the setup for frequency quintupling of the 1565 nm laser. L: lenses, M: mirrors, DM: dichroic mirror, P: Brewster plate for phase mismatch compensation (see text), IC/OC: input and output couplers of the enhancement cavity PD: photodetector, out (ν, 2ν, 3ν, 5ν): output beams at fundamental, second, third and fifth-harmonic wavelength. The third-harmonic output, out (3ν) is delivered to the frequency stabilization system (see Sect. 3)

fully as a starting point for a various kinds of nonlinear frequency conversion [11–14]. The high (and easily scalable) fiber laser power can be combined with the performance of modern nonlinear materials based on quasi-phase-matching (QPM). First commercial systems for nonlinear frequency conversion of fiber lasers are appearing.

By a convenient coincidence, the 313 nm UV wavelength, relevant for Be^+ cooling, is a fifth harmonic of the 1565 nm IR wavelength, which is within the range of the Er-doped fiber lasers, and within the C-band of fiber-optic communication. Consequently a variety of active and passive components are mass produced and easily available for this wavelength.

An apparent drawback of the UV generation by quintupling of the 1565 nm radiation, is the relatively large number of nonlinear frequency conversion stages, and hence the relatively low overall conversion efficiency. However, this can be compensated by increase (at a reasonable cost) of the fiber laser power at the fundamental wavelength.

In this paper we report on a UV source based on quintupling of the IR laser and suitable for laser cooling of Be^+ ions. A narrowband telecom laser is amplified to 15 W in an Er-doped fiber amplifier (EDFA) and then the fifth harmonic (5H) of the fundamental frequency is generated in a chain of nonlinear crystals. The main advantage of the source is the compact and robust design, owing to the reliability of the fiber laser components. The footprint of the quintupling setup is less than 0.2 m^2, where the seed laser at the fundamental wavelength, the EDFA, and the auxiliary fiber components can be located in a rack rather than on the optical table. A UV output power of 100 mW was reached using an enhancement cavity in the last frequency conversion stage. A UV power of 2 mW was measured without the enhancement cavity, i.e. using an all-single-pass configuration of the frequency conversion setup. This simplified source is especially robust and can be used for less power demanding applications.

The intermediate third-harmonic output of the source (522 nm) provides a convenient means for laser frequency stabilization since molecular iodine is an excellent and well-studied reference for laser wavelengths in the green. We implemented a system for frequency stabilization and precision tuning of the UV output frequency around the Be^+ cooling transition. The frequency of the UV source can be stabilized to various hyperfine components in the spectrum of molecular iodine and in addition can be continuously and precisely offset-tuned by a double-pass AOM frequency shifter.

The developed UV source was integrated in our experimental apparatus for laser cooling of Be^+ ions and sympathetic cooling of molecular ions and was successfully tested during long-term (multi-hour) experiments.

2 Nonlinear frequency conversion setup

The schematic of the setup for frequency quintupling of the infrared laser at 1565 nm is shown in Fig. 1. A master laser, a single-frequency Er-doped distributed-feedback (DFB) fiber laser module (Koheras K80-153-12), was amplified in a 15-W polarization-maintaining EDFA (IPG EAR-15K-C-LP-SF-UD). A fiber-optic phase modulator was placed in-between the master laser and the amplifier to produce two sets of sidebands, used for the enhancement cavity locking (modulation frequency: 20 MHz), and for producing a Be^+ repumper wave (modulation frequency: 1.25 GHz).

Frequency conversion of the fundamental laser frequency (ν) to the fifth harmonic (5ν) was realized in the following stages: (i) single-pass SHG ($\nu + \nu \rightarrow 2\nu$) in a cascade of two 50-mm long periodically poled lithium niobate crystals (PPLN, Deltronic); (ii) single-pass SFG ($\nu + 2\nu \rightarrow 3\nu$) in the 30-mm long periodically poled magnesium doped lithium tantalate crystal (PPSLT, HCP); (iii) SFG ($2\nu + 3\nu \rightarrow 5\nu$) in a 10-mm long BBO crystal (Ekspla). The BBO crystal was placed in the enhancement cavity in order to increase the UV output power (this frequency conversion stage can also be of single-pass type, for low-power applications). All nonlinear crystals were temperature stabilized within 0.1°C. Simple plano-convex (PCX) lenses were used for the beam focusing and collimation.

In our opinion, the chosen sequence of frequency conversions and of the intermediate wavelengths is well balanced. The PPLN and PPSLT crystals are resistant to "photorefractive damage" under high-power irradiation at intermediate second- and third-harmonic wavelengths. The third-harmonic output at 522 nm can be used for frequency stabilization of the source, as will be discussed below. The overall optical design of the source is rather simple and hence robust. All frequency conversions but one are of single-pass type and no laser beam combining is needed. The use of the single-pass arrangement with very efficient QPM nonlinear crystals, in combination with the cavity-enhanced arrangement for the BBO crystal, is a good compromise between simplicity and performance of the UV source. The footprint of the frequency conversion setup is 0.6 m × 0.3 m and could be further reduced.

The first (SHG) step of frequency conversions is done in a cascade of two nonlinear crystals [15]. Theoretically, this provides up to a factor 4 increase of the SHG efficiency. Dispersion in the refocusing lenses in-between the two crystals and in the air introduces a phase mismatch between the fundamental and the second-harmonic waves at the front end of the second crystal in the cascade. A Brewster plate (P in Fig. 1) was used in the setup to compensate and adjust the phase mismatch (e.g. a 1° tilt of the 3-mm thick glass plate corresponds to a π phase shift between the two waves while the chromatic aberration introduced by the plate is minuscule).

The measured second-harmonic (SH) power at the output of the cascade as a function of laser power at fundamental wavelength (pump, 1565 nm) is shown in Fig. 2a (left vertical axis). The maximum SH power of 7.7 W corresponds to 53% pump conversion efficiency. The dashed curve on the plot (right vertical axis) illustrates the enhancement of the SH power in the cascade with respect to the single-crystal SHG. Use of the cascade results in 330% SHG enhancement at low pump power. The difference between measured value and the theoretical limit (400%) can be explained by chromatic aberrations of the PCX lenses that were used for the refocusing. The decrease of the enhancement factor with increase of the pump power can be attributed to the various power-induced wavefront distortions and to the pump depletion. The measured output power of the source at the third-harmonic (TH) wavelength is shown in Fig. 2b by the green curve (left vertical axis). At 15 W pump power, 1.2 W TH output and 8% conversion efficiency were reached.

For the resonant SFG, we used a standard bow-tie enhancement cavity, with two plane and two curved mirrors (50 mm radii of curvature). A plane-parallel cut and antireflection-coated BBO crystal was located between the curved mirrors in the 30 µm waist of the cavity mode. The cavity was designed to resonate with only one of the two input waves, the second harmonic at 783 nm. The third harmonic traverses the crystal in a single pass and then is being delivered to the frequency stabilization system (see Fig. 1). This arrangement was chosen to minimize the interference between the enhancement cavity and the frequency stabilization system, which relies on the third-harmonic output (i.e. the enhancement cavity and the laser frequency can be scanned and locked independently).

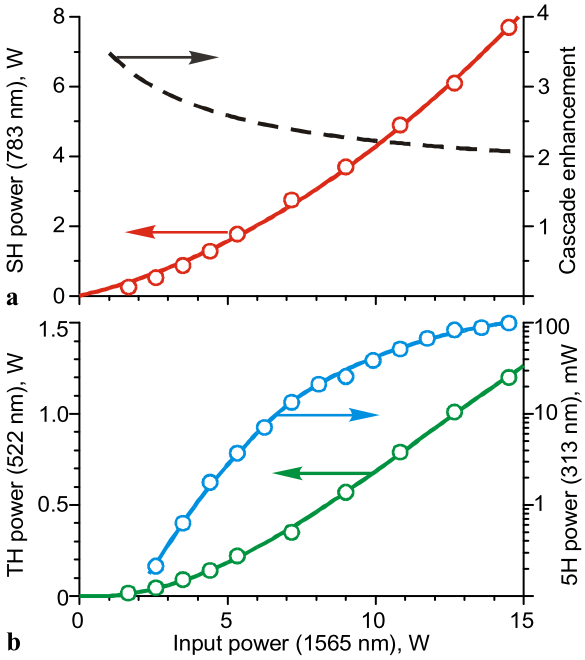

Fig. 2 Output power of the source at second, third and fifth-harmonic wavelength (SH, TH, 5H, respectively) vs. input power at fundamental wavelength. Part (**a**): *left axis*—SH power, *right axis*—enhancement factor of the two-crystal cascade (see text). Part (**b**): *left axis*—TH power, *right axis*—5H power (1 minute average) in logarithmic scale

The cavity was locked to the master laser using the standard Pound–Drever–Hall (PDH) technique [16, 17]. The sidebands for the PDH lock (20 MHz) we generated in the fiber-optic phase modulator. The modulator was placed between the master laser and the EDFA (see Fig. 1) and modulates the fundamental wave. The sidebands are maintained during the frequency conversions, as the phase-matching bandwidths of the nonlinear crystals are large enough.

The dependence of the UV fifth-harmonic (5H) output power on the input pump power is shown in Fig. 2b by the blue curve (right vertical axis). A logarithmic scale is used to make the plot more illustrative. As can be seen, the considerable level of 100 mW 5H output has been reached. Comparison with the 2 mW power measured for the single-pass conversion in the BBO crystal, shows that the enhancement factor of approx. 50 was obtained by using the enhancement cavity approach.

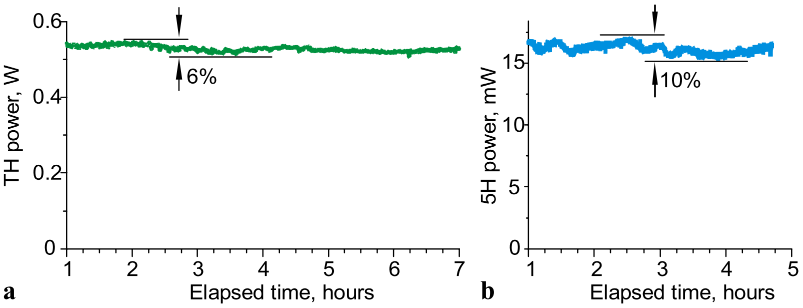

Fig. 3 Output power of the source at third-harmonic (TH) and fifth-harmonic (5H) wavelengths during long-term operation. Both measurements were started after 1 hour warming up of the setup

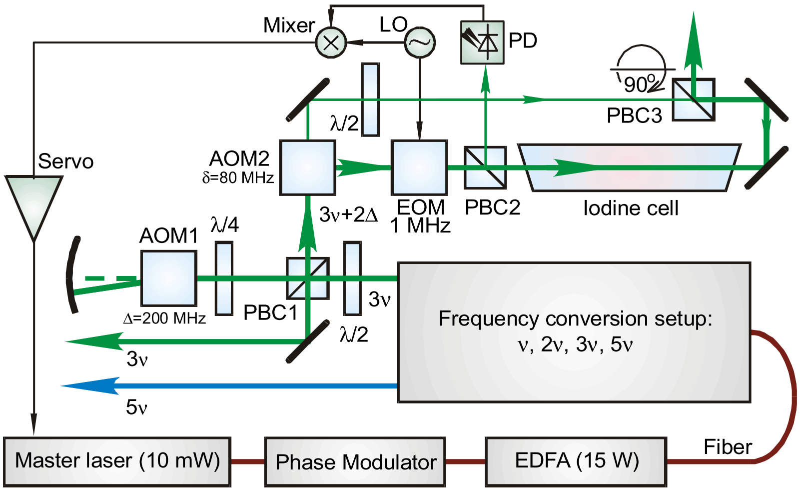

Fig. 4 Schematic of the setup for frequency stabilization and tuning of the UV source. $3\nu, 5\nu$ are the output beams at third and fifth-harmonic wavelength, PBC polarization beam splitter cubes (the PBC3 is rotated by 90° with respect to the PBC2, to reflect the pump beam and transmit the probe beam), $\lambda/2$, $\lambda/4$ wave plates, AOM acoustooptic modulators (AOM1 is used for fine frequency tuning), EOM: electrooptic modulator, PD: photodetector

The characterization of the power stability of the setup was carried out at a fundamental pump power reduced to 9 W. This pump power level corresponds to 15–20 mW 5H output power, which is more than sufficient for our Be^+ cooling setup. The output power stability at the TH wavelength is illustrated in Fig. 3a. The measurement was started after one hour warming up of the setup. The observed fluctuations of the TH power are mainly due to instability of the laser power at fundamental wavelength and due to temperature instabilities of the nonlinear crystals. No evidence of photorefractive damage of the QPM crystals was observed during the tests. No active control of the phase-matching between the fundamental and SH waves in the SHG cascade (adjustment of the plate P, see Fig. 1) was needed. Figure 3b shows the power stability of the fifth-harmonic UV output. This measurement was also started after one hour warming up. The observed fluctuations of the 5H power are within 10%.

If desired, the UV output power can be actively stabilized e.g. by polarization control of the fundamental wave, or by control of the phase shift in the SHG cascade (adjustment of the tilt of the plate P). Another, all-electronic, means for the power stabilization would be splitting of some laser power at fundamental wavelength from the central frequency to auxiliary sidebands, produced by the fiber-optic phase modulator (already included in the system).

The large margin of power (100 mW maximum output vs. several mW actually required for laser cooling applications) is an advantage in the practical use of the source. Temperature-induced misalignments and possible degradation of the BBO crystal and of other components can be compensated (to some extent) by an increase of the pump power at fundamental wavelength. Thus the source can be operated without maintenance during a longer time.

3 Frequency stabilization of the UV source

The frequency of the UV source was stabilized using molecular iodine as a reference. A schematic of the setup for frequency stabilization and tuning of the source is shown in Fig. 4. A fraction of the source's output at the third-harmonic wavelength (3ν) is split on the polarization beam splitter cube (PBC1) and sent to the double-pass acoustooptic frequency shifter (AOM1) with central frequency $\Delta = 200$ MHz and ±50 MHz bandwidth. The frequency-shifted beam ($3\nu + 2\Delta$) is sent to the second AOM (AOM2 at 80 MHz) to produce the pump and the probe inputs for the Doppler-free frequency modulation transfer spectroscopy setup (FMTS, [18]) with the 15 cm long temperature stabilized iodine cell. The pump beam is modulated at 1 MHz by the electro optic modulator (EOM). The demodulated error signal is fed back to the master laser via the servo amplifier. Thus the master laser's frequency can be locked to the hyperfine structure (hfs) components of molecular iodine transitions via the third-harmonic output of the source. The frequency of the fifth-harmonic UV output of the source (5ν) is related to the reference frequency of the hfs component (ν_{I2}) by the formula: $5\nu = (5/3) \cdot (\nu_{I2} - 2\Delta - \delta/2)$, where Δ is the modulation frequency of AOM1 and δ is the modulation frequency of AOM2. The UV output frequency can be fine-tuned by tuning the frequency Δ within the bandwidth of AOM1.

The absorption spectrum of molecular iodine in the wavelength range relevant for Be^+ cooling is shown in Fig. 5a. The measurement was carried out with the iodine cell at 10°C. The absorption lines were assigned using the atlas of Gerstenkorn and Luc [19]. By coincidence, the absorption line P58(2-49) is located rather close to the 521.888 nm TH wavelength (arrow on the plot), which corresponds to the 313.133 nm 5H UV wavelength (the Be^+ cooling transition [6]).

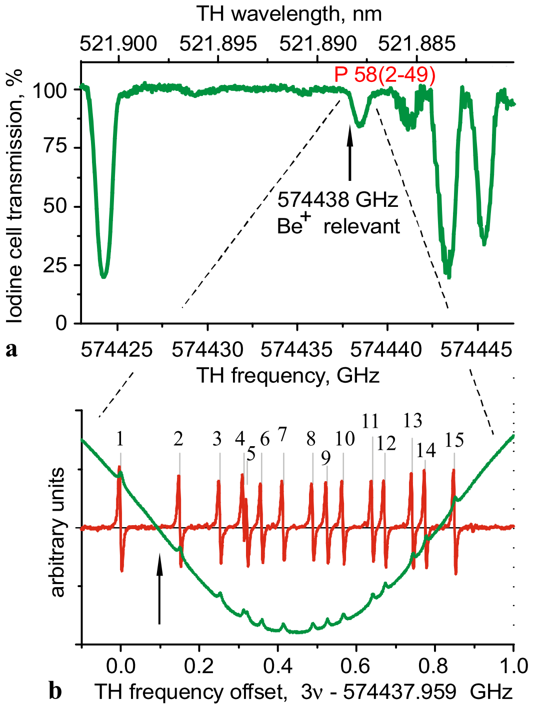

Fig. 5 (**a**) Absorption spectrum of molecular iodine in the range relevant for the Be^+ laser cooling applications (15 cm long iodine cell at 10°C). (**b**) A sub-Doppler survey of the absorption line at 521.888 nm (15 cm long iodine cell at 30°C). Doppler background with hfs Lamb dips (*green*) and the demodulated error signal (*red*)

Figure 5b, red line illustrates the Doppler-free FMTS signal of this convenient line. The green line in the plot shows the Lamb dips of the hfs components on the Doppler background. The P58 line is relatively weak. Therefore the iodine cell was kept at 30°C temperature in order to increase the population of the ground level and, as a result, to improve signal to noise ratio of the generated FMTS error signals.

We determined the absolute frequencies of the hfs components using a femtosecond frequency comb. It is based on a Ti:Sapphire laser (Femtosource Scientific 200) and a commercial comb kit (MenloSystems, FC 8004), modified in-house. The frequency comb's repetition rate and the carrier envelope frequency were locked to an active hydrogen maser (Vremya-Ch), itself steered to GPS on long time scales. The master laser was locked to a particular hfs component. The 1565 nm fundamental wave of the setup was superimposed with the comb on a beat line. The heterodyne beat note between the laser wave and the nearest comb mode was detected with a low-noise photodetector. The detected beat note was filtered, amplified by a tracking oscillator and measured by means of a dead-time-free frequency counter. The results of the measurements are summarized in Table 1. The estimated uncertainty of the frequency values is about 500 kHz as we did not take into account various systematic effects.

The frequency stability of the source was characterized when the master laser was locked to the a1 hfs component. The Allan deviation of the laser frequency is shown in Fig. 6 and the insert shows the beat signal scatter during 1-hour measurement. The Allan deviation of the laser frequency is below 1 kHz for integration times between 2 and 40 seconds. The linear drift (approx. 18 Hz/s) is attributed mainly to the DC offset variation of the locking electronics. It can be removed by temperature stabilization of the critical electronic components (RF mixer, input amplifier). The instability of the iodine cell temperature results in fluctuations of the laser frequency on a time scale of few hundred seconds.

Table 1 Frequencies of the hfs components of the P58(2-49) molecular iodine absorption line. The estimated uncertainty of the frequency values is 500 kHz

hfs line	Freq. (GHz)	hfs line	Freq. (GHz)	hfs line	Freq. (GHz)
a1	574437.959	a6	574438.318	a11	574438.600
a2	574438.110	a7	574438.373	a12	574438.631
a3	574438.212	a8	574438.448	a13	574438.702
a4	574438.273	a9	574438.485	a14	574438.735
a5	574438.281	a10	574438.525	a15	574438.809

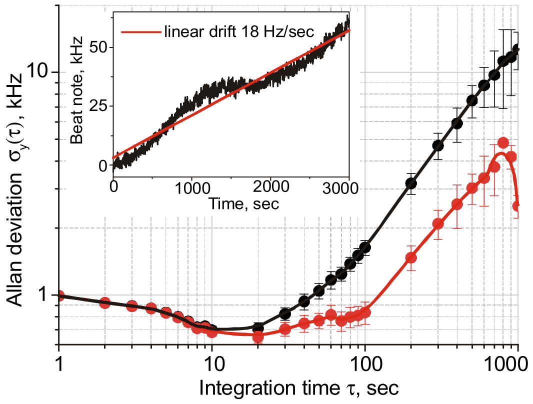

Fig. 6 Allan deviation of the frequency of the master laser (15665 nm) stabilized to the a1 hfs component. *Black*: the deviation is calculated with the linear drift taken into account, *red*: the linear drift is removed. *Inset*: the beat signal scatter

The long-term drift, 250 kHz over 1 h at 313 nm, is much less than the natural linewidth of the Be^+ cooling transition. For Be^+ laser cooling, the frequency of the source can be stabilized using the hfs components of the P58(2-49) iodine transition as a reference. The gap between an iodine reference frequency and a desired frequency can be bridged by the double-pass AOM frequency shifter. The spacing between hfs components (30–150 MHz) is within the bandwidth of the frequency shifter (200 MHz). Hence the UV output wavelength of the source can be precisely set and adjusted over a 1.5 GHz range.

4 Application of the UV source to laser cooling of Be^+

The UV source was developed with the goal of a reliable source for laser cooling of beryllium. Thus, it was tested using our apparatus for laser cooling of Be^+ ions and sympathetic cooling of molecular ions. Details of the setup and the method to obtain trapped laser-cooled Be^+ ions are described in [3]. In brief, we trap a few thousand Be^+ ions in a linear quadrupole radio-frequency trap driven at 14 MHz. The trap is enclosed in a UHV chamber kept below 10^{-10} mbar. To load Be^+ ions into the trap, atoms are thermally evaporated from a beryllium wire, and ionized by an electron beam. Ensembles of Be^+ ions can be brought to temperatures of $\approx$10 mK by Doppler laser cooling at 313 nm. At these temperatures, the beryllium ions arrange themselves in an ordered state referred to as a Coulomb crystal. The fluorescence of Be^+ ions at 313 nm is monitored by a photomultiplier tube and by a CCD camera.

The UV source was operated at 10–20 mW output power, a typical level for our Be^+ cooling setup. The source was locked to the most red-shifted hfs component (a1) of the P58 transition during the loading of the Be^+ ions into the trap. That corresponds to $\approx$1 GHz red detuning from the central frequency of the cooling transition and allows for more efficient cooling of hot ions. Subsequently, the UV frequency was tuned toward the cooling transition frequency. We observed the crystallization of the Be^+ ions cloud when the source's frequency was locked to the a4–a8 hfs components.

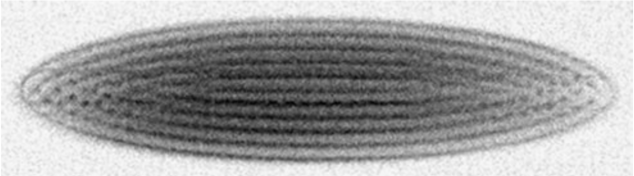

Fig. 7 CCD image of a Be^+ ion crystal

The $^2S_{1/2}$ ground state of the $^2S_{1/2} \leftrightarrow {}^2P_{3/2}$ cooling transition has a hyperfine splitting of 1.25 GHz. The excited $^2P_{3/2}$ state can decay into either of the two hyperfine levels of the ground state. Therefore a 'repumper' laser wave, with the frequency detuning of 1.25 GHz from the 'main' wave is required for more efficient laser cooling. The repumper sidebands in the source's UV output were produced by phase modulation of the master laser at the fundamental wavelength (LO2 in Fig. 1).

An example of a generated Be^+ ion crystal is illustrated in Fig. 7. A characteristic shell-like structure can be clearly seen in the image.

5 Conclusion

In conclusion, we developed a complete setup for generation, frequency stabilization, and precision tuning of UV laser radiation at 313 nm. We tested the source by demonstration of successful laser cooling of Be^+ ions in our ion-trap apparatus.

The setup includes a compact nonlinear frequency conversion stage for quintupling of the high-power IR output of the fiber amplifier seeded by a low-power narrow-linewidth telecom master laser at 1565 nm. The output power of the source at 313 nm is 100 mW when pumped with 15 W at the 1565 nm fundamental wavelength.

The frequency stabilization stage allows for locking the master laser to hfs components of molecular iodine via the third-harmonic output of the source at 522 nm. The source's frequency is fine-tunable by an acoustooptic frequency shifter. We measured the frequencies of the hfs components of P58(2-49) transition in molecular iodine, relevant for Be^+ laser cooling application. The use of iodine as frequency reference means that the source can be operated without the need of a wavelength meter. The frequency stability of the source is, by a considerable margin, sufficient for Be^+ laser cooling.

Features of the source are compactness, robustness, usability, an important use of reliable fiber-optic components.

The source can be transported from one lab to another and reconnected to the fiber laser and to the electronics rack in a matter of minutes. Only little adjustments of the optical setup are required after the transportation because all frequency conversion stages but one are single-pass. The warm-up time is short, about an hour.

With such properties, the source can become a workhorse for laser cooling of Be^+ and similar applications, such as the measurement of linewidths of atomic transitions. A significant amount of source's output at the intermediate wavelengths (1565 nm, 783 nm, 522 nm) remains available. This can be used for other applications; in particular, the third-harmonic output (1 W at 522 nm) can be frequency doubled to produce 260 nm, which is often needed for (non-resonant) photodissociation of atoms or molecules, e.g. in our own experiments on spectroscopy of HD^+. Thus, the UV source becomes multi-purpose. Possible improvements are active stabilization of the UV output power and increased frequency stability.

The developed setup can be used as a building block for a more sophisticated multi-wavelength UV source for cooling of ions into the quantum ground state of motion in an ion trap using the Raman sideband cooling technique [20].

Acknowledgement This research is partly supported by the Deutsche Forschungsgemeinschaft DFG within the project SCHI 431/13-1.

References

1. C. Langer, R. Ozeri, J.D. Jost, J. Chiaverini, B. DeMarco, A. Ben-Kish, R.B. Blakestad, J. Britton, D.B. Hume, W.M. Itano, D. Leibfried, R. Reichle, T. Rosenband, T. Schaetz, P.O. Schmidt, D.J. Wineland, Phys. Rev. Lett. **95**, 060502 (2005)
2. T. Rosenband, D.B. Hume, P.O. Schmidt, C.W. Chou, A. Brusch, L. Lorini, W.H. Oskay, R.E. Drullinger, T.M. Fortier, J.E. Stalnaker, S.A. Diddams, W.C. Swann, N.R. Newbury, W.M. Itano, D.J. Wineland, J.C. Bergquist, Science **319**, 1808 (2008)
3. P. Blythe, B. Roth, U. Fröhlich, H. Wenz, S. Schiller, Phys. Rev. Lett. **95**, 183002 (2005)
4. J.C.J. Koelemeij, B. Roth, A. Wicht, I. Ernsting, S. Schiller, Phys. Rev. Lett. **98**, 173002 (2007)
5. B. Roth, U. Fröhlich, S. Schiller, Phys. Rev. Lett. **94**, 053001 (2005)
6. T. Nakamura, M. Wada, K. Okada, A. Takamine, Y. Ishida, Y. Yamazaki, T. Kambara, Y. Kanai, T.M. Kojima, Y. Nakai, N. Oshima, A. Yoshida, T. Kubo, S. Ohtani, K. Noda, I. Katayama, V. Lioubimov, H. Wollnik, V. Varentsov, H.A. Schuessler, Phys. Rev. A **74**, 052503 (2006)
7. W. Nörtershäuser, D. Tiedemann, M. Žáková, Z. Andjelkovic, K. Blaum, M.L. Bissell, R. Cazan, G.W.F. Drake, Ch. Geppert, M. Kowalska, J. Krämer, A. Krieger, R. Neugart, R. Sánchez, F. Schmidt-Kaler, Z.-C. Yan, D.T. Yordanov, C. Zimmermann, Phys. Rev. Lett. **102**, 062503 (2009)
8. H. Schnitzler, U. Fröhlich, T.K.W. Boley, A.E.M. Clemen, J. Mlynek, A. Peters, S. Schiller, Appl. Opt. **41**, 7000 (2002)
9. A. Tünnermann, T. Schreiber, F. Röser, A. Liem, S. Höfer, H. Zellmer, S. Nolte, J. Limpert, J. Phys. B, At. Mol. Opt. Phys. **38**, S681 (2005)
10. Y. Jeong, J. Nilsson, J.K. Sahu, D.N. Payne, R. Horley, L.M.B. Hickey, P.W. Turner, IEEE J. Sel. Top. Quantum Electron. **13**, 546 (2007)
11. A. Henderson, R. Stafford, Opt. Express **14**, 767 (2006)
12. M. Vyatkin, A. Dronov, M. Chernikov, S.V. Popov, J.R. Taylor, D.V. Gapontsev, V.P. Gapontsev, in *Conference on Lasers and Electro-Optics/Quantum Electronics and Laser Science and Photonic Applications Systems Technologies, Technical Digest (CD)* (Optical Society of America, Washington, 2005), paper CThZ6
13. T. Sudmeyer, Y. Imai, H. Masuda, N. Eguchi, M. Saito, S. Kubota, Opt. Express **16**, 1546 (2008)
14. S. Vasilyev, S. Schiller, A. Nevsky, A. Grisard, D. Faye, E. Lallier, Z. Zhang, A.J. Boyland, J.K. Sahu, M. Ibsen, W.A. Clarkson, Opt. Lett. **33**, 1413 (2008)
15. R. Thompson, M. Tu, D. Aveline, N. Lundblad, L. Maleki, Opt. Express **11**, 1709 (2003)
16. R.W.P. Drever, J.L. Hall, F.V. Kowalski, J. Hough, G.M. Ford, A.J. Munley, H. Ward, Appl. Phys. B **31**, 97 (1983)
17. E.D. Black, Am. J. Phys. **69**, 79 (2001)
18. A. Arie, S. Schiller, E.K. Gustafson, R.L. Byer, Opt. Lett. **17**, 1204 (1992)
19. S. Gerstenkorn, P. Luc, *Atlas du Spectre D'absorption de la Molécule D'iode* (Laboratoire Aimé Cotton, CNRS II, Paris, 1978)
20. M.D. Barrett, B. DeMarco, T. Schätz, V. Meyer, D. Leibfried, J. Britton, J. Chiaverini, W.M. Itano, J.D. Jost, B. Jelenkovic, C. Langer, T. Rosenband, D.J. Wineland, Phys. Rev. A **68**, 042302 (2003)

Bibliography

[1] J. D. Weinstein, R. Carvalho, T. Guillet, B. Friedrich, and J. M. Doyle. Magnetic trapping of calcium monohydride molecules at millikelvin temperatures. *Nature*, 395:148–150, 1998.

[2] A. Fioretti, D. Comparat, A. Crubellier, O. Dulieu, F. Masnou-Seeuws, and P. Pillet. Formation of Cold Cs_2 Molecules through Photoassociation. *Phys. Rev. Lett.*, 80:4402–4405, 1998.

[3] M. Tarbutt, H. Bethlem, J. Hudson, V. Ryabov, V. Ryzhov, B. Sauer, G. Meijer, and E. Hinds. Slowing Heavy, Ground-State Molecules using an Alternating Gradient Decelerator. *Phys. Rev. Lett.*, 92:173002, 2004.

[4] M. Wewer and F. Stienkemeier. Molecular versus excitonic transitions in PTCDA dimers and oligomers studied by helium nanodroplet isolation spectroscopy. *Phys. Rev. B*, 67:125201, 2003.

[5] S. Dürr, T. Volz, A. Marte, and G. Rempe. Observation of Molecules Produced from a Bose-Einstein Condensate. *Phys. Rev. Lett.*, 92:020406, 2004.

[6] S. A. Rangwala, T. Junglen, T. Rieger, P. W. H. Pinkse, and G. Rempe. Continuous source of translationally cold dipolar molecules. *Phys. Rev. A*, 67:043406, 2003.

[7] M. Greiner, C. A. Regal, and D. S. Jin. Emergence of a molecular Bose-Einstein condensate from a Fermi gas. *Nature*, 426:537–540, 2003.

[8] S. Jochim, M. Bartenstein, A. Altmeyer, G. Hendl, S. Riedl, C. Chin, J. Denschlag, and R. Grimm. Bose-Einstein Condensation of Molecules. *Science*, 302:2101–2103, 2003.

[9] D. J. Larson, J. C. Bergquist, J. J. Bollinger, W. M. Itano, and D. J. Wineland. Sympathetic cooling of trapped ions: A laser-cooled two-species nonneutral ion plasma. *Phys. Rev. Lett.*, 57:70–73, 1986.

[10] R. E. Drullinger, D. J. Wineland, and J. C. Bergquist. High-resolution optical spectra of laser cooled ions. *Appl. Phys.*, 22:365–368, 1980.

[11] J. P. Karr, S. Patra, J. C. J. Koelemeij, J. Heinrich, N. Sillitoe, A. Douillet, and L. Hilico. Hydrogen molecular ions: new schemes for metrology and fundamental physics tests. *J. Phys.: Conference Series*, 723:012048, 2016.

[12] J. D. Prestage, R. L. Tjoelker, and L. Maleki. Atomic Clocks and Variations of the Fine Structure Constant. *Phys. Rev. Lett.*, 74:3511–3514, 1995.

[13] V. I. Korobov. Bethe logarithm for the hydrogen molecular ion HD^+. *Phys. Rev. A*, 70:012505, 2004.

[14] F. Riehle and J. Helmcke. Optical Frequency Standards Based on Neutral Atoms and Molecules. *Frequency Measurement and Control: Advanced Techniques and Future Trends*, 79:95–129, 2001.

[15] D. Gerlich and S. Schlemmer. Deuterium fractionation in gas-phase reactions measured in the laboratory. *Planet. Space Sci.*, 50:1287–1297, 2002.

[16] D. DeMille. Quantum Computation with Trapped Polar Molecules. *Phys. Rev. Lett.*, 88:067901, 2002.

[17] F. Lewen, S. P. Belov, F. Maiwald, Th. Klaus, and G. Winnewisser. A Quasi-Optical Multiplier for Terahertz Spectroscopy. *Z. Naturforsch. A*, 50:1182–1186, 1995.

[18] A. Maestrini, J. Ward, G. Chattopadhyay, E. Schlecht, and I. Mehdi. Terahertz Sources Based on Frequency Multiplication and Their Applications. *Freq.*, 62:118–122, 2008.

[19] F. Klappenberger, K. F. Renk, P. Renk, B. Rieder, Yu. I. Koshurinov, D. G. Pavelev, V. Ustinov, A. Zhukov, N. Maleev, and A. Vasilyev. Semiconductor-superlattice frequency multiplier for generation of submillimeter waves. *Appl. Phys. Lett.*, 84:3924, 2004.

[20] C. P. Endres, F. Lewen, T. F. Giesen, S. Schlemmer, D. G. Paveliev, Y. I. Koschurinov, V. M. Ustinov, and A. E. Zhucov. Application of superlattice multipliers for high-resolution terahertz spectroscopy. *Rev. Sci. Instrum.*, 78:043106, 2007.

[21] L. A. Surin, B. S. Dumesh, F. S. Rusin, G. Winnewisser, and I. Pak. Doppler-free two-photon millimeter wave transitions in OCS and CHF_3. *Phys. Rev. Lett.*, 86:2002–2005, 2001.

[22] S. Carocci, A. Di Lieto, A. Menciassi, P. Minguzzi, and M. Tonelli. High-Resolution Rotational Spectroscopy of CH_3I Using a Novel Doppler-Free Technique. *J. Mol. Spectrosc.*, 175:62–67, 1996.

[23] H. W. Kroto. Molecular Rotation Spectra. *John Wiley & Sons, Ltd.*, 1975.

[24] G. Cazzoli, L. Dore, C. Puzzarini, and S. Beninati. Millimeter- and submillimeter-wave spectrum of $C^{17}O$. Rotational hyperfine structure analyzed using the Lamb-dip technique. *Phys. Chem. Chem. Phys.*, 4:3575–3577, 2002.

[25] G. Winnewisser, S. P. Belov, T. Klaus, and R. Schieder. Sub-Doppler measurements on the rotational transitions of carbon monoxide. *Abstracts of OSU International Symposium on Molecular Spectroscopy 1990-1999*, 1997.

[26] V. Ahrens, F. Lewen, S. Takano, G. Winnewisser, Š. Urban, A. A. Negirev, and A. N. Koroliev. Sub-Doppler Saturation Spectroscopy of HCN up to 1

THz and Detection of J= 3→ 2 (4→ 3) Emission from TMC1. *Z. Naturforsch. A*, 57:669–681, 2002.

[27] R. Krems, B. Friedrich, and W. C. Stwalley. Cold Molecules: Theory, Experiment, Applications. *CRC Press*, 2009.

[28] I. W. M. Smith. Low Temperatures and Cold Molecules. *Imperial College Press*, 2008.

[29] W. H. Wing, W. E. Lamb, Jr., G. A. Ruff, and J. J. Spezeski. Observation of the infrared spectrum of the hydrogen molecular ion HD^+. *Phys. Rev. Lett.*, 36:1488–1491, 1976.

[30] V. I. Korobov. Leading-order relativistic and radiative corrections to the rovibrational spectrum of H_2^+ and HD^+ molecular ions. *Phys. Rev. A*, 74:052506, 2006.

[31] V. I. Korobov. Relativistic corrections of $m\alpha^6$ order to the rovibrational spectrum of H_2^+ and HD^+ molecular ions. *Phys. Rev. A*, 77:022509, 2008.

[32] S. Schiller and V. I. Korobov. Tests of time independence of the electron and nuclear masses with ultracold molecules. *Phys. Rev. A*, 71:032505, 2005.

[33] A. Carrington and R. A. Kennedy. Vibration-rotation spectroscopy of the HD^+ ion near the dissociation limit. *Mol. Phys.*, 56:935–975, 1985.

[34] J. C. J. Koelemeij, B. Roth, A. Wicht, I. Ernsting, and S. Schiller. Vibrational Spectroscopy of HD^+ with 2-ppb Accuracy. *Phys. Rev. Lett.*, 98:173002, 2007.

[35] P. Wolfgang and S. Helmut. Ein neues Massenspektrometer ohne Magnetfeld. *Z. Naturforsch. A*, 8, 1953.

[36] R. E. March, R. J. Hughes, and J. F. J. Todd. Quadrupole storage mass spectrometry. *Wiley Interscience Publications*, 1989.

[37] L. Hornekær. Single- and multi-species Coulomb ion crystals: Structures, dynamics and sympathetic cooling. *PhD thesis*, University of Århus, 2000.

[38] U. Bressel. High-resolution vibrational spectroscopy of cold molecular hydrogen ions. *PhD thesis*, Heinrich-Heine-Universität Düsseldorf, 2011.

[39] M. Drewsen and A. Brøner. Harmonic linear Paul trap: Stability diagram and effective potentials. *Phys. Rev. A*, 62:045401, 2000.

[40] W. Schnitzler. Development of an experiment for trapping, cooling and spectroscopy of molecular hydrogen ions. *PhD thesis*, Universität Konstanz, 2001.

[41] B. Roth, P. Blythe, and S. Schiller. Motional resonance coupling in cold multispecies Coulomb crystals. *Phys. Rev. A*, 75:023402, 2007.

[42] C. B. Zhang, D. Offenberg, B. Roth, M. A. Wilson, and S. Schiller. Molecular-dynamics simulations of cold single-species and multispecies ion ensembles in a linear Paul trap. *Phys. Rev. A*, 76:012719, 2007.

[43] J. D. Prestage, A. Williams, L. Maleki, M. J. Djomehri, and E. Harabetian. Dynamics of charged particles in a Paul radio-frequency quadrupole trap. *Phys. Rev. Lett.*, 66:2964–2967, 1991.

[44] Vladimir L. Ryjkov, XianZhen Zhao, and Hans A. Schuessler. Simulations of the rf heating rates in a linear quadrupole ion trap. *Phys. Rev. A*, 71:033414, 2005.

[45] H. G. Dehmelt. Radiofrequency Spectroscopy of Stored Ions I. *Adv. At. Mol. Phys.*, 3:53–72, 1968.

[46] H. G. Dehmelt. Radiofrequency Spectroscopy of Stored Ions II. *Adv. At. Mol. Phys.*, 5:109–154, 1969.

[47] W. M. Itano, J. C. Bergquist, J. J. Bollinger, and D. J. Wineland. Cooling methods in ion traps. *Phys. Scr.*, T59:106–120, 1995.

[48] T. W. Hänsch and A. L. Schawlow. Cooling of gases by laser radiation. *Opt. Commun.*, 13:68–69, 1975.

[49] D. J. Wineland and H. Dehmelt. Proposed 10^{14} $\delta\nu < \nu$ laser fluorescence spectroscopy on Tl^+ mono-ion oscillator III (sideband cooling). *Bull. Am. Phys. Soc.*, 20:637, 1975.

[50] V. S. Letokhov, M. A. Ol'shanii, and Yu B. Ovchinnikov. Laser cooling of atoms: a review. *J. Eur. Opt. Soc. B*, 7:5–40, 1995.

[51] C. S. Adams and E. Riis. Laser cooling and trapping of neutral atoms. *Prog. Quant. Electron.*, 21:1–79, 1997.

[52] P. Bowe, L. Hornekær, C. Brodersen, M. Drewsen, J. S. Hangst, and J. P. Schiffer. Sympathetic Crystallization of Trapped Ions. *Phys. Rev. Lett.*, 82:2071–2074, 1999.

[53] D. Kielpinski, B. E. King, C. J. Myatt, C. A. Sackett, Q. A. Turchette, W. M. Itano, C. Monroe, D. J. Wineland, and W. H. Zurek. Sympathetic cooling of trapped ions for quantum logic. *Phys. Rev. A*, 61:032310, 2000.

[54] C. B. Zhang. Production and sympathetic cooling of complex molecular ions. *PhD thesis*, Heinrich-Heine-Universität Düsseldorf, 2008.

[55] S. Stenholm. The semiclassical theory of laser cooling. *Rev. Mod. Phys.*, 58:699–739, 1986.

[56] H. J. Metcalf and P. van der Straten. Laser Cooling and Trapping. *Springer-Verlag*, 1999.

[57] C. Cohen-Tannoudji. Atomic Motion in Laser Light. Fundamental Systems in Quantum Optics. *Elsevier Science Publishers*, 1992.

[58] C. Monroe, D. M. Meekhof, B. E. King, S. R. Jefferts, W. M. Itano, D. J. Wineland, and P. Gould. Resolved-Sideband Raman Cooling of a Bound Atom to the 3D Zero-Point Energy. *Phys. Rev. Lett.*, 75:4011–4014, 1995.

[59] J. J. Sakurai, S. F. Tuan, and E. D. Commins. Modern Quantum Mechanics, Revised Edition. *Am. J. Phys.*, 63:93–95, 1995.

[60] B. H. Bransden and C. J. Joachain. Physics of Atoms and Molecules. *Longman Scientific & Technical*, 1983.

[61] W. L. Slattery, G. D. Doolen, and H. E. DeWitt. Improved equation of state for the classical one-component plasma. *Phys. Rev. A*, 21:2087–2095, 1980.

[62] J.P. Hansen. Statistical Mechanics of Dense Ionized Matter. I. Equilibrium Properties of the Classical One-Component Plasma. *Phys. Rev. A*, 8:3096–3109, 1973.

[63] D. H. E. Dubin and T. M. O'Neil. Trapped nonneutral plasmas, liquids, and crystals (the thermal equilibrium states). *Rev. Mod. Phys.*, 71:87–172, 1999.

[64] E. L. Pollock and J. P. Hansen. Statistical Mechanics of Dense Ionized Matter. II. Equilibrium Properties and Melting Transition of the Crystallized One-Component Plasma. *Phys. Rev. A*, 8:3110–3122, 1973.

[65] D. Offenberg. Studies of trapped, cooled ion ensembles. *PhD thesis*, Heinrich-Heine-Universität Düsseldorf, 2009.

[66] B. Roth. Production, Manipulation and Spectroscopy of Cold Trapped Molecular Ions. *Habilitationsschrift*, Heinrich-Heine-Universität Düsseldorf, 2007.

[67] C. Wunderlich, G. Morigi, and D. Reiß. Simultaneous cooling of axial vibrational modes in a linear ion trap. *Phys. Rev. A*, 72:023421, 2005.

[68] P. O. Schmidt, T. Rosenband, C. Langer, W. M. Itano, J. C. Bergquist, and D. J. Wineland. Spectroscopy Using Quantum Logic. *Science*, 309:749–752, 2005.

[69] J. Shen, A. Borodin, and S. Schiller. A simple method for characterization of the magnetic field in an ion trap using Be^+ ions. *Eur. Phys. J. D*, 68:359, 2014.

[70] S. Vasilyev, A. Nevsky, I. Ernsting, M. Hansen, J. Shen, and S. Schiller. Compact all-solid-state continuous-wave single-frequency UV source with frequency stabilization for laser cooling of Be^+ ions. *Appl. Phys. B*, 103:27–33, 2011.

[71] R. J. Thompson, M. Tu, D. C. Aveline, N. Lundblad, and L. Maleki. High power single frequency 780 nm laser source generated from frequency doubling of a seeded fiber amplifier in a cascade of PPLN crystals. *Opt. Express*, 11:1709–1713, 2003.

[72] A. Yoshizawa, R. Kaji, and H. Tsuchida. Generation of polarisation-entangled photon pairs at 1550 nm using two PPLN waveguides. *Electron. Lett.*, 39:621–622, 2003.

[73] R. Boyd. Nonlinear Optics. *Academic Press*, 2003.

[74] V. A. Yerokhin. Hyperfine structure of Li and Be^+. *Phys. Rev. A*, 78:012513, 2008.

[75] D. J. Wineland, J. J. Bollinger, and W. M. Itano. Laser-Fluorescence Mass Spectroscopy. *Phys. Rev. Lett.*, 50:628–631, 1983.

[76] J. Park, Z. Yan, H. Loh, S. Will, and M. Zwierlein. Second-scale nuclear spin coherence time of ultracold ^{23}Na^{40}K molecules. *Science*, 357:372–375, 2017.

[77] L. Hilico, N. Billy, B. Grémaud, and D. Delande. Ab initio calculation of the J = 0 and J = 1 states of the H_2^+, D_2^+ and HD^+ molecular ions. *Eur. Phys. J. D*, 12:449–466, 2000.

[78] J. Crassous, F. Monier, J. Dutasta, M. Ziskind, C. Daussy, C. Grain, and C. Chardonnet. Search for Resolution of Chiral Fluorohalogenomethanes and Parity-Violation Effects at the Molecular Level. *ChemPhysChem*, 4:541–548, 2003.

[79] H. Müller, S. Herrmann, A. Saenz, A. Peters, and C. Lämmerzahl. Tests of Lorentz invariance using hydrogen molecules. *Phys. Rev. D*, 70:076004, 2004.

[80] C. A. Leach and R. E. Moss. Spectroscopy and Quantum Mechanics of the Hydrogen Molecular Cation: A Test of Molecular Quantum Mechanics. *Annu. Rev. Phys. Chem.*, 46:55–82, 1995.

[81] D. Bakalov, V. I. Korobov, and S. Schiller. High-precision calculation of the hyperfine structure of the HD^+ ion. *Phys. Rev. Lett.*, 97:243001, 2006.

[82] H. Araki. Quantum-Electrodynamical Corrections to Energy-Levels of Helium. *Prog. Theor. Phys.*, 17:619–642, 1957.

[83] J. Sucher. Energy Levels of the Two-Electron Atom to Order α^3 ry; Ionization Energy of Helium. *Phys. Rev.*, 109:1010–1011, 1958.

[84] R. D. Ray and P. R. Certain. Hyperfine Structure in the Infrared Spectrum of HD. *Phys. Rev. Lett.*, 38:824–826, 1977.

[85] A. Carrington. Microwave Spectroscopy at the Dissociation Limit. *Science*, 274:1327–1331, 1996.

[86] D. Bakalov, V. I. Korobov, and S. Schiller. Magnetic field effects in the transitions of the HD^+ molecular ion and precision spectroscopy. *J. Phys. B*, 44:025003, 2011.

[87] E. A. Colbourn and P. R. Bunker. Accurate theoretical vibration-rotation energies and transition moments for HD^+, HT^+, and DT^+. *J. Mol. Spectrosc.*, 63:155–163, 1976.

[88] Z. Amitay, D. Zajfman, and P. Forck. Rotational and vibrational lifetime of isotopically asymmetrized homonuclear diatomic molecular ions. *Phys. Rev. A*, 50:2304–2308, 1994.

[89] R. A. Hegstrom. ***g*** factors and related magnetic properties of molecules. Formulation of theory and calculations for H_2^+, HD^+, and D_2^+. *Phys. Rev. A*, 19:17–30, 1979.

[90] V. I. Korobov. *(private communication).*

[91] J. Shen, A. Borodin, M. Hansen, and S. Schiller. Observation of a rotational transition of trapped and sympathetically cooled molecular ions. *Phys. Rev. A*, 85:032519, 2012.

[92] T. Schneider, B. Roth, H. Duncker, I. Ernsting, and S. Schiller. All-optical preparation of molecular ions in the rovibrational ground state. *Nat. Phys.*, 6:275–278, 2010.

[93] S. Schiller, B. Roth, F. Lewen, O. Ricken, and M. C. Wiedner. Ultra-narrow-linewidth continuous-wave THz sources based on multiplier chains. *Appl. Phys. B*, 95:55–61, 2008.

[94] M. Tadjeddine and G. Parlant. Computed photodissociation cross sections of HD^+, and Franck-Condon factors for the ionization of HD. *Mol. Phys.*, 33:1797–1803, 1977.

[95] S. Alighanbari, M. G. Hansen, V. I. Korobov, and S. Schiller. Rotational spectroscopy of cold and trapped molecular ions in the Lamb–Dicke regime. *Nat. Phys.*, 14:555–559, 2018.

[96] S. Alighanbari, G. S. Giri, F. L. Constantin, V. I. Korobov, and S. Schiller. Precise test of quantum electrodynamics and determination of fundamental constants with HD^+ ions. *Nature*, 581:152–158, 2020.

[97] E. D. Black. An introduction to Pound–Drever–Hall laser frequency stabilization. *Am. J. Phys.*, 69:79–87, 2000.

[98] A. Arie, S. Schiller, E. K. Gustafson, and R. L. Byer. Absolute frequency stabilization of diode-laser-pumped Nd:YAG lasers to hyperfine transitions in molecular iodine. *Opt. Lett.*, 17:1204–1206, 1992.

[99] I. Ernsting. Entwicklung und anwendung eines frequenzkamm-basierten lasersystems für die präzisions-spektroskopie an ultrakalten molekülen und atomen. *PhD thesis*, Heinrich-Heine-Universität Düsseldorf, 2009.

[100] M. Hansen, I. Ernsting, S. Vasilyev, A. Grisard, E. Lallier, B. Gérard, and S. Schiller. Robust, frequency-stable and accurate mid-IR laser spectrometer based on frequency comb metrology of quantum cascade lasers up-converted in orientation-patterned GaAs. *Opt. Express*, 21:27043–27056, 2013.

[101] M. ŠAŠURA and V. BUŽEK. Cold trapped ions as quantum information processors. *J. Mod. Opt.*, 49:1593–1647, 2002.

[102] H. Häffner, C. F. Roos, and R. Blatt. Quantum computing with trapped ions. *Phys. Rep.*, 469:155–203, 2008.

[103] T. Rosenband, D. B. Hume, P. O. Schmidt, C. W. Chou, A. Brusch, L. Lorini, W. H. Oskay, R. E. Drullinger, T. M. Fortier, J. E. Stalnaker, S. A. Diddams, W. C. Swann, N. R. Newbury, W. M. Itano, D. J. Wineland, and J. C. Bergquist. Frequency Ratio of Al^+ and Hg^+ Single-Ion Optical Clocks; Metrology at the 17th Decimal Place. *Science*, 319:1808–1812, 2008.

[104] N. Hinkley, J. A. Sherman, N. B. Phillips, M. Schioppo, N. D. Lemke, K. Beloy, M. Pizzocaro, C. W. Oates, and A. D. Ludlow. An Atomic Clock with 10^{-18} Instability. *Science*, 341:1215–1218, 2013.

[105] A. Borodin, J. Shen, and S. Schiller. Observation of doubly-spin-forbidden rovibrational transitions in cold trapped molecular ions. *Submitted to Phys. Rev. A.*

[106] U. Bressel, A. Borodin, J. Shen, M. Hansen, I. Ernsting, and S. Schiller. Manipulation of Individual Hyperfine States in Cold Trapped Molecular Ions and Application to HD^+ Frequency Metrology. *Phys. Rev. Lett.*, 108:183003, 2012.

[107] P. Staanum, K. Højbjerre, P. Skyt, A. Hansen, and M. Drewsen. Rotational laser cooling of vibrationally and translationally cold molecular ions. *Nat. Phys.*, 6:271–274, 2010.

[108] C. Wellers, A. Borodin, S. Vasilyev, D. Offenberg, and S. Schiller. Resonant IR multi-photon dissociation spectroscopy of a trapped and sympathetically cooled biomolecular ion species. *Phys. Chem. Chem. Phys.*, 13:18799–18809, 2011.

Acknowledgement

The work presented in this doctoral thesis would not have been possible without the support and assistance from numerous people.

First of all, I would like to thank my supervisor, Prof. Stephan Schiller for introducing me to the institute, giving me the opportunity to research on this very interesting and challenging topic, guiding and encouraging me throughout my research period. Many skills obtained from him will benefit me for my future career life.

Many thanks to:

Bernhard Roth for introducing me to the interesting research field and his guidance for the experiment. He was always ready to answer my questions. His good humour brought us countless happiness.

Tobias Schneider for the great help in solving problems especially with the theoretical calculations. He taught me many useful skills and was always ready to help.

Sergey Vasilyev for the contribution to building the novel UV cooling laser setup. He introduced me to various lasers and was a reliable guide for frequency stabilization.

Ingo Ernsting for working with the frequency comb before and during the spectroscopic measurements.

Qunfeng Chen for answering my questions and helping me to solve problems.

Michael Hansen for supporting me so much in data obtaining and analyzing in the measurement runs.

Andrii Borodin for the good cooperation and teamwork especially for operating the OPO, participating in the measurements of doubly-spin-forbidden rovibrational transitions in HD^+, and providing me with constructive discussions.

Alexander Nevsky, Ulf Bressel, Christian Wellers, Soroosh Alighanbari, Eugen Wiens, and Akobuije Chijioke for their continuous interest in this work and giving me many useful suggestions.

Peter Dutkiewicz, Rita Gusek, Heinrich Hoffmann, Dmitri Iwaschko, and Ulrich Rosowski for the assistance on electronics and mechanics, and for their great patience to teach me the German language during the lunches and coffee breaks.

Prof. Wolfgang Behmenburg for his friendship and kindness, and his interest in this work.

Beate Rödding for her great patience and kindness whenever I needed help.

Most importantly, I would like to thank my wife Chunli who made so many sacrifices for our family and supporting me continuously. I thank my daughter Jiuzhang, who managed to come into this world and brought me the courage to finish my doctoral work. I am also grateful to my parents for their constant support and encouragement throughout my life.